Biaxial Wrinkling of Thin-Walled GFRP Webs in Cell-Core Sandwiches

THÈSE N^{O} 5185 (2011)

PRÉSENTÉE LE 19 OCTOBRE 2011

À LA FACULTÉ ENVIRONNEMENT NATUREL, ARCHITECTURAL ET CONSTRUIT
LABORATOIRE DE CONSTRUCTION EN COMPOSITES
PROGRAMME DOCTORAL EN STRUCTURES

ÉCOLE POLYTECHNIQUE FÉDÉRALE DE LAUSANNE

POUR L'OBTENTION DU GRADE DE DOCTEUR ÈS SCIENCES

PAR

Behzad DEHGHAN MANSHADI

acceptée sur proposition du jury:

Prof. J. Zhao, président du jury
Prof. T. Keller, Dr A. Vasilopoulos, directeurs de thèse
Prof. L. A. Carlsson, rapporteur
Prof. M. Motavalli, rapporteur
Prof. I. Smith, rapporteur

ÉCOLE POLYTECHNIQUE
FÉDÉRALE DE LAUSANNE

Suisse
2011

To my great parents
and
my lovely wife, Zohreh

Preface

Sandwich panels composed of thin face sheets and a core material constitute material-tailored structural components for fiber-reinforced polymer (FRP) composite materials. The FRP face sheets bear the bending moment while the core – usually a foam or honeycomb material – is subjected to shear. In civil engineering applications, the core material normally has to be reinforced due to large spans (e.g. in roof constructions) or heavy concentrated loads (e.g. in bridge construction). This reinforcement consists of a core-integrated grid of FRP webs that bear the shear forces. The function of the core material is thus limited to the prevention of wrinkling in the compressed web or face sheet laminates. This type of structure is known as a cell-core sandwich.

A major failure mode of sandwich structures is wrinkling of the compressed face sheets. This source of failure is well known and reliable models exist to predict the wrinkling load. Wrinkling, however, can also occur in the webs of cell-core sandwiches. Since this type of structure is still new and therefore not yet well investigated, models to predict wrinkling in the webs due to shear do not yet exist. Wrinkling is caused by the compression diagonal, which is crossed by a transverse tension stress field. The effect of such transverse tension stress fields on the wrinkling load of laminates is as yet unexplored. This thesis focuses on this phenomenon, which is of great importance for the reliable and economic design of cell-core sandwiches.

I would like to thank the Swiss Innovation Promotion Agency CTI (Grant No. 9121.1 PFIW-IW) and industry partners Scobalit Composites, Winterthur, Switzerland and Ernst Basler & Partner AG, Zurich, Switzerland for their support of this project, and the EPFL Laboratory of Applied Mechanics and Reliability for the use of its experimental facilities.

Prof. Dr. Thomas Keller

CCLab Director and thesis director

Summary

Fiber-reinforced polymer (FRP) sandwich structures offer several advantages compared to structures made of traditional materials, such as high specific strength, good corrosion resistance, low thermal conductivity and rapid component installation. In this context, glass fiber-reinforced polymer (GFRP) cell-core sandwiches composed of outer GFRP face sheets, a foam core and a grid of GFRP webs integrated into the core to reinforce shear load capacity are well suited for load-bearing applications in civil engineering i.e. in bridge deck and roof construction.

Despite the great potential of these structural concepts, the use of heterogeneous materials in FRP sandwiches results in more complex failure mechanisms compared to conventional structural components and lack of knowledge regarding the prediction of failure modes makes the design of structural components difficult. This is one of the major disadvantages limiting the acceptance of cell-core sandwiches in civil engineering applications. One of the critical failure modes of cell-core sandwich structures is wrinkling in the webs.

A great deal of information exists concerning the phenomenon of skin wrinkling failure of sandwich laminates loaded in compression but comparatively little on wrinkling in the webs of sandwich structures where the pure compression loading is complicated by supplementary transverse tension. The purpose of this research is to develop an appropriate model for the prediction of wrinkling in the webs of cell-core sandwich structures.

Two new approaches were developed to predict the wrinkling loads of webs. The first approach examines the wrinkling behavior in webs as an in-plane biaxial compression-tension buckling problem according to the rotated stress field theory. In this regard, extensive experimental, numerical and analytical studies were performed to investigate the interaction between the compression and tension stress tensors during the buckling/wrinkling instability phase of GFRP plates and sandwich panels subjected to biaxial compression-tension loading.

The investigations demonstrated that the transverse tension in the biaxial compression-tension set-up induced two simultaneous counteracting effects: a stabilizing and a lateral contraction effect. The stabilizing effect tends to push the plate back to the median plane and thereby delays the onset of buckling/wrinkling instability. In contrast, lateral contraction accelerates the bending of the plate, which leads to a significant decrease in buckling/wrinkling loads. In composite plates, the first effect predominates and increases the buckling loads while in sandwich panels the second effect is dominant and decreases the wrinkling loads.

Using the second approach, the wrinkling behavior of foam-filled web-core panels was modeled by applying an improved mixed-mode interaction formula in which two approximate models are developed based on the energy method in order to determine the critical loads when the pure shear and bending stresses act independently on the web.

The application of both approaches to a real case study, the GFRP cell-core sandwich roof of the Novartis Campus Main Gate Building proved that they are sufficiently accurate to be used as valid tools assisting the optimum design of sandwich structures whereas existing models result in too conservative predictions.

Keywords: Sandwich structures; Composite laminates; Failure mode; Buckling; Wrinkling; Shear forces; Biaxial compression-tension tests; Mathematical models.

Résumé

Les structures réalisées en panneaux sandwich à base de matériaux composites (FRP) présentent de nombreux avantages face aux structures réalisées en matériaux traditionnels, dont une résistance spécifique élevée, une bonne résistance à la corrosion et une basse conductivité thermique. Dans ce contexte, les structures sandwich composées de laminés extérieurs en polymères renforcés par des fibres de verre (GFRP), d'un noyau en mousse et d'une grille d'âmes en GFRP intégrées à l'intérieur du noyau permettant d'augmenter la résistance à l'effort tranchant, sont adaptées aux applications structurelles dans le génie civil telles que dans la construction de tablier de ponts et de toitures de bâtiments.

Malgré le grand potentiel de ces concepts structuraux, l'utilisation de matériaux hétérogènes dans les sandwichs en FRP conduit à des mécanismes de rupture plus complexes que ceux des éléments structuraux conventionnels. De plus, le manque de connaissances quand à la prédiction des mécanismes de rupture rend leur conception difficile. Ce désavantage majeur empêche l'acceptation des structures sandwich renforcé par des âmes intérieures dans les applications de génie civil. Un des modes de rupture critique de ces sandwichs est le voilement de âmes intérieures.

De nombreuses études traitent du voilement des laminés extérieurs d'un sandwich sollicités en compression mais peu d'information est disponible quant au voilement des âmes intérieures de structures en sandwich dans lesquelles la compression est accompagnée par une traction transversale. L'objectif de cette recherche est de développer un modèle de prédiction du voilement des âmes de renforcement des sandwichs.

Deux nouvelles approches permettant de prédire les charges de voilement des âmes ont été développées. La première approche étudie le phénomène du voilement des âmes comme un problème de flambage d'un élément sous un état de sollicitation biaxiale de compression/traction dans son plan. Cette étude applique la théorie de rotation des champs de contraintes. Des nombreuses études expérimentales, numériques et analytiques ont été réalisées afin de comprendre l'interaction des tenseurs contraintes de compression et de traction lors des phénomènes d'instabilité de flambage et de voilement des laminés en GFRP et des éléments sandwich sollicités en compresion-traction biaxial respectivement.

Les investigations ont démontré que la traction transversale appliquée dans les essais de compression/traction biaxiale a deux effets simultanés qui se compensent, un effet stabilisateur et un effet de contraction latérale. L'effet de stabilisation a tendance à faire revenir le laminé à son plan moyen et retarde ainsi les phénomènes d'instabilité de flambage et de voilement. Par contre, la contraction latérale accroît la flexion du laminé réduisant de manière significative les charges de flambage et de voilement. Dans les laminés en matériaux composites le premier effet est prédominant et augmente les charges de flambage alors que dans les panneaux en sandwich le deuxième effet s'impose et réduit les charges de voilement.

Dans la deuxième approche, le comportement face au voilement des âmes intérieures du sandwich a été modélisé par une formule d'interaction intégrant deux modèles basés sur la méthode énergétique et déterminants les charges critiques sous un état de cisaillement pure et de flexion.

Les deux approches ont été appliquées à un cas réel : la toiture du bâtiment de réception du campus Novartis à Bâle, structure sandwich à âmes intérieures réalisée en GFRP. Les analyses réalisées démontrent que les deux approches développées permettent d'optimiser le dimensionnement des structures sandwich alors que les modèles actuellement utilisés mènent à des prédictions trop conservatrices.

Mots clés: Structures en sandwich; Laminés en composites; Mode de rupture; Voilement; Effort tranchant; Essais de compression/traction biaxiales; Modèles mathématiques.

Acknowledgments

Over the past three and a half years, I have received support and encouragement from many different people and it is truly difficult to list all of them in one small space, but here I would like to acknowledge those who have made a particularly important contribution.

First, I would like to express my most sincere gratitude to my thesis director Prof. Dr. Thomas Keller for giving me the opportunity to work on this research project, his support, guidance and our rich discussions. Moreover, I would like to express my deepest gratitude to my thesis co-director, Dr. Anastasios P. Vassilopoulos, who also supervised my thesis and supported me with his sympathetic encouragements and recommendations to overcome the difficulties encountered during these years.

I would also like to acknowledge the following exceptional sources of support:

- The Swiss Innovation Promotion Agency CTI (Grant No. 9121.1 PFIW-IW);
- Industry partners Scobalit Composites, Winterthur, Switzerland and Ernst Basler & Partner AG Zurich, Switzerland for their generous donation of the experimental materials and their technical support;
- The EPFL Laboratory of Applied Mechanics and Reliability (LMAF), in particular Prof. Dr. Ioannis Botsis, the Director of the LMAF laboratory, for use of the biaxial testing system.

I wish to express my thanks to the thesis defense committee for the time and effort they devoted to reading and evaluating the thesis and also for their expert suggestions: Prof. Dr. Leif A. Carlsson, University of Florida, USA; Prof. Dr. Ian Smith, Director, Applied Computing and Mechanics Laboratory (IMAC), EPFL; Prof. Dr. Masoud Motavalli, Director, Structural Engineering Research Laboratory, EMPA, Switzerland; and Prof. Dr. Jian Zhao, Director, LMR-EPFL, President of the jury.

The whole team of technicians at IS EPFL for their steadfast support: Sylvain Demierre for always providing intelligent and practical solutions for experimental testing and measuring problems and above all his sense of humor; François Perrin and Roland Gysler for preparing the specimens and biaxial experimental set-up, Patrice Gallay for manufacturing mechanical elements of “Swiss Made” quality, and generally for their incredible patience in listening to requests in my poor French. The help provided by Gérald Rouge and Gilles Guignet was also essential for this work.

I would like to thank my colleagues at CCLab–EPFL: Dr. Julia de Castro for the expert suggestions concerning civil engineering applications and her helpful comments regarding my PhD oral exam presentation; Omar Moussa for his friendship and helping me to improve my English language skills; all the former and current CCLab members: Dr. Erika Schaumann, Dr. Yu Bai, Dr. Ye Zhang, Roohollah Sarfaraz, Moslem Shahverdi, Michael Osei-Antwi, Carlos Pascual Agullo, Wie Sun, and Ping Zhu, for their friendship and for creating a pleasant atmosphere that broadened my understanding of other cultures; and Magdalena Schauenberg for her efficient administrative assistance.

Many thanks to those who helped me to prepare the thesis document: Prof. Keller and Dr. Anastasios P. Vassilopoulos (for their careful reading, valuable remarks and interesting suggestions); Margaret Howett for her meticulous English corrections; Carlos Pascual Agullo for converting the English abstract into the French “résumé”, and Dr. Julia de Castro for correcting and improving the résumé.

And last but not least, I wish to express my sincerest thanks to my wife, my family, my in-laws, my uncle and my late aunt for their great support, not forgetting my friends from all over the world for their encouragement.

Contents

1 Introduction

1.1. Context and motivations

Sandwich structures are an attractive concept since, thanks to an appropriate choice of materials and geometry, constructions with high stiffness-to-weight ratios can be achieved, and for this reason they are currently used primarily in aerospace and marine applications. Now the advantages of using GFRP materials in sandwich construction, i.e. insensitivity to frost and de-icing salts, low thermal conductivity and short installation times, are also being explored in civil applications, e.g. building and bridge construction. In this context, foam-core-based sandwich structures, reinforced by an internal grid of webs and denominated cell-core sandwiches, are well suited for transverse load-bearing applications i.e. bridge deck and roof construction. Keller et al. (2008) showed that GFRP composites assembled in large-scale cell-core sandwich structures enable the prefabrication of lightweight and function-integrated roof structures for rapid on-site installation, as shown in Figure 1.1. In this particular building, structural functions, building physics functions (thermal insulation, waterproofing), and architectural functions (complex shapes) were all integrated into sandwich components.

Requirements for building applications, e.g. roof construction, include thermal insulating performance, which leads to the use of thin and widely spaced webs to avoid large conductive thermal losses across the panels. The thin webs of cell-core sandwich structures are relatively long panels that are susceptible to wrinkling, a local buckling failure in the sandwich webs due to the compression components of the stress tensors resulting from shear, normal and bending loads. The fundamental failure mechanism "web wrinkling" is similar to compressive skin wrinkling, a skin failure caused by the core's inability to support a skin loaded in compression. Web wrinkling, however, is different because of the combination of in-plane tensile and compressive

stresses in the web. As shown in Figure 1.2, in the case of web wrinkling, the laminate is not only subjected to uniaxial compression, but also to transverse tension. Web wrinkling can thus be considered as an in-plane biaxial compression-tension wrinkling problem and consists of interaction between the compression and transverse tension stress fields.

Figure 1.1. Novartis Campus Main Gate Building with GFRP cell-core sandwich roof (Keller et al. 2008).

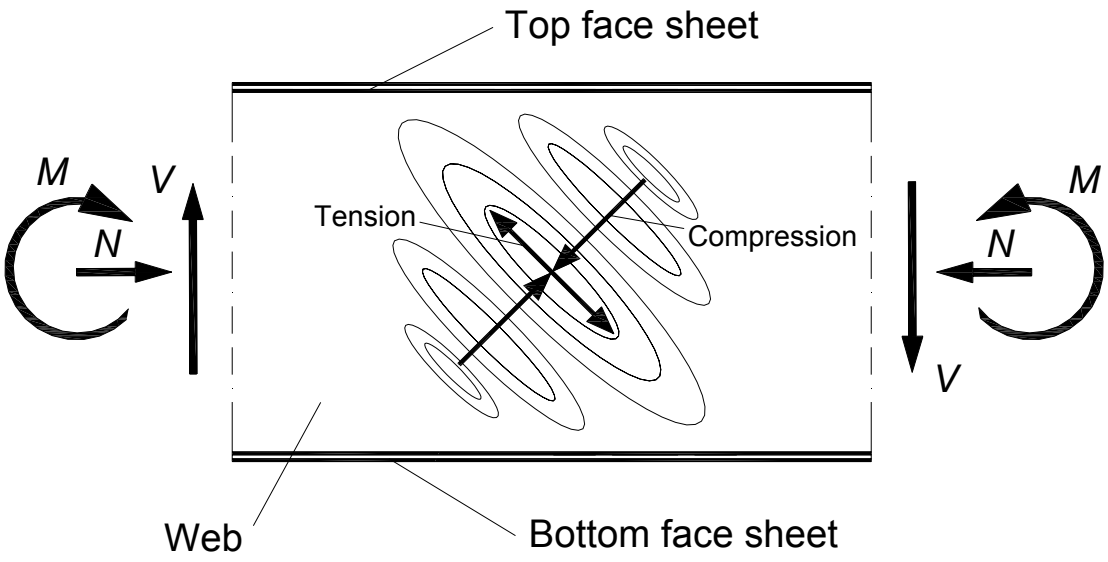

Figure 1.2. Buckling mode in webs of sandwich beams.

Due to the strict stiffness requirements for civil applications and the uncertain post-wrinkling behavior in webs, the initial web wrinkling is considered a limiting failure mode in design. Therefore, an understanding of web wrinkling as a biaxial compression-tension problem is critical for developing optimum designs that efficiently meet all the necessary requirements.

Numerous theoretical models and experimental data exist concerning uniaxial compression wrinkling (Plantema 1966, Allen 1969, Ley et al. 1999) and biaxial compression-compression wrinkling (Fagerberg and Zenkert 2005-a&b, Birman and Bert 2004, Hadi and Matthews 2000, Vonach and Rammerstorfer 2000-a&b, Sullins et al. 1969). However, this knowledge is not directly applicable to web wrinkling, concerning which only a small amount of information is available. An experimental study on the shear wrinkling of GFRP sandwich stiffener webs was performed by Lake et al. (2007). Modeling was attempted by modifying the common uniaxial wrinkling model (Hoff and Mautner 1945, and Ley et al. 1999) but no satisfying result was achieved. Furthermore, the distribution of the stresses in the webs, i.e. the effect of tension, could not be identified from the experiments.

An analytical investigation of the wrinkling of foam-filled web-core sandwich panels in the case of pure shear loading was performed by Briscoe et al. (2010). The web was modeled as a simply supported plate resting on a Pasternak elastic foundation under pure shear stresses. The applicability of the plate buckling model to web-core panels under a distributed load was demonstrated; nevertheless, the model was not accurate compared to finite element modeling. No experimental validation was performed and the interaction between the compression and transverse tension stress fields could not be captured. Indeed, in cell-core sandwich structures, the face sheets provide rotational resistances to the webs, which depends on material properties and geometric parameters such as web spacing and face sheet thickness. Therefore, assuming simply supported boundary conditions for the web at the juncture of the web and face sheets leads to considerably conservative results. Moreover, in a more realistic case, a web-core panel is subjected not only to shear stresses but also to in-plane bending stresses and the influence of bending stresses can be significant assuming, as did Briscoe et al. (2010), that the face sheet thickness is of the same order as the web thickness.

1.2. Objectives

The aim of this research is to develop models for the accurate prediction of the wrinkling (local buckling) behavior of webs in cell-core sandwich structures. In order to achieve this, the following objectives have been defined:

- investigate the wrinkling/buckling of webs as an in-plane biaxial compression-tension instability problem;
- understand and quantify the influences of transverse tension on web buckling/wrinkling behavior and the corresponding effect of core material;
- develop a mixed-mode local/global buckling model for long orthotropic plates that are stabilized by a relatively thick elastic foam and subjected to combined pure bending and shear loads;
- investigate the application of the developed models to the design of webs in GFRP cell-core sandwich beams;

1.3. Methodology

The methodology used to attain the objectives is as follows:

- state–of–the art concerning cell-core sandwiches in civil engineering applications, failure modes in sandwich structures and mechanism of wrinkling failure in these structures;
- survey of analytical and experimental investigation concerning wrinkling failure of sandwich structures under uniaxial and biaxial loads;
- investigate the wrinkling of webs in cell-core sandwiches as:
    - biaxial compression-tension local buckling problem,
    - mixed-mode buckling problem;
- experimental investigation of the buckling of GFRP plates and wrinkling of GFRP sandwiches subjected to biaxial compression-tension loading;

- analytical and numerical modeling of stress fields in experimentally examined GFRP plates;
- analyses of experimental buckling/wrinkling investigation and modeling;
- modeling of the transition from buckling of GFRP plate to wrinkling of GFRP sandwiches and the effect of the transverse tension load throughout the transition;
- numerical investigation to define the boundary conditions in web panels at the juncture between webs and face sheets in cell-core sandwich structures;
- development of a mixed-mode interaction model for local/global buckling of long orthotropic plates that are stabilized by a relatively thick elastic foam and subjected to combined pure bending and shear loads;
- investigation of the applicability of the developed models to the webs of cell-core sandwich beams using the design example of GFRP cell-core sandwich roof (Keller et al. 2008);

1.4. Thesis organization

The research presented in this thesis is divided into four main parts: the first concerns the state of the art review. The second part is dedicated to the approach in which the wrinkling of cell-core sandwich webs is treated as a biaxial compression-tension local buckling problem. This part consists of the experimental, numerical, and analytical investigation of the buckling/wrinkling of GFRP plates and sandwiches subjected to biaxial compression-tension loading. The third part deals with the development of a new approach, a mixed-mode interaction buckling model, in order to predict the wrinkling of cell-core sandwich webs. In this approach, the webs are investigated as long orthotropic plates that are stabilized by relatively thick elastic foam and subjected to combined pure bending and shear loads. In the last main part, the applicability of the developed approaches for the prediction of the wrinkling loads in the thin-walled webs of cell-core sandwiches is investigated. In this context, the GFRP cell-core sandwich roof (Keller et al. 2008) is selected as a design example. The general organization of the thesis is shown in Figure 1.3.

The following is a summary of the chapter contents:

Chapter 2: The state–of–the art introduces the general principles of sandwich structures, the use of GFRP sandwiches in civil constructions, and the most common failure modes in sandwich structures. Wrinkling failure modes as the most frequent failures of cell-core sandwich structures with thin face sheets and webs are introduced. A review of existing models for the prediction of wrinkling under uniaxial and biaxial loading conditions as well as a specific investigation concerning wrinkling in sandwich webs follow. Concluding remarks provide the justification for researching the wrinkling of thin-walled GFRP webs in cell-core sandwiches.

Chapter 3: Experimental investigations of the biaxial compression-tension buckling and wrinkling of GFRP plates and sandwich panels reveal the effect of transverse tension on the buckling behavior of structural components, e.g. thin-walled webs in FRP girders or cell-core sandwiches, which are subjected to biaxial compression-tension stress fields. Experiments establish a comprehensive experimental database for a better understanding of the interaction between the compression and transverse tension stress fields and the development of analytical models for the prediction of the instability loads under these biaxial stress fields.

Chapter 4: The analytical and numerical modeling of the experimental set-up provides the in-plane stress field of the orthotropic plates and sandwich panels subjected to biaxial compression-tension loading. The resulting in-plane stress field aids the development of an analytical model for simulation of the buckling and wrinkling behavior of orthotropic FRP plates stabilized by a thick foam and subjected to biaxial compression-tension in-plane loading. The model allows the evaluation of the positive and negative effects of increasing the transverse tension load on buckling and wrinkling loads and of the influence of the relative stiffness between plate and foam core on these positive and negative effects. Furthermore, the analytical modeling simulates the transition from buckling to wrinkling by increasing the foam density.

Chapter 5: The prediction of the buckling behavior in the orthotropic web panels of cell-core sandwich structures is carried out using two approaches. The first approach is based on a mixed-mode interaction formula to simulate the buckling of orthotropic webs subjected to combined shear and bending loads. The second approach treats the local buckling behavior of cell-core panels as a biaxial compression-tension buckling problem. The applicability of the developed

approaches in the prediction of the wrinkling loads in the thin-walled webs of GFRP cell-core sandwich beams is investigated. The case study concerns the sandwich beams tested by Keller et al. 2008 during the design of the GFRP cell-core sandwich roof structure for the Novartis Campus Main Gate Building.

Chapter 6: The conclusions and major findings of the research are summarized. Suggestions for future research areas are also formulated.

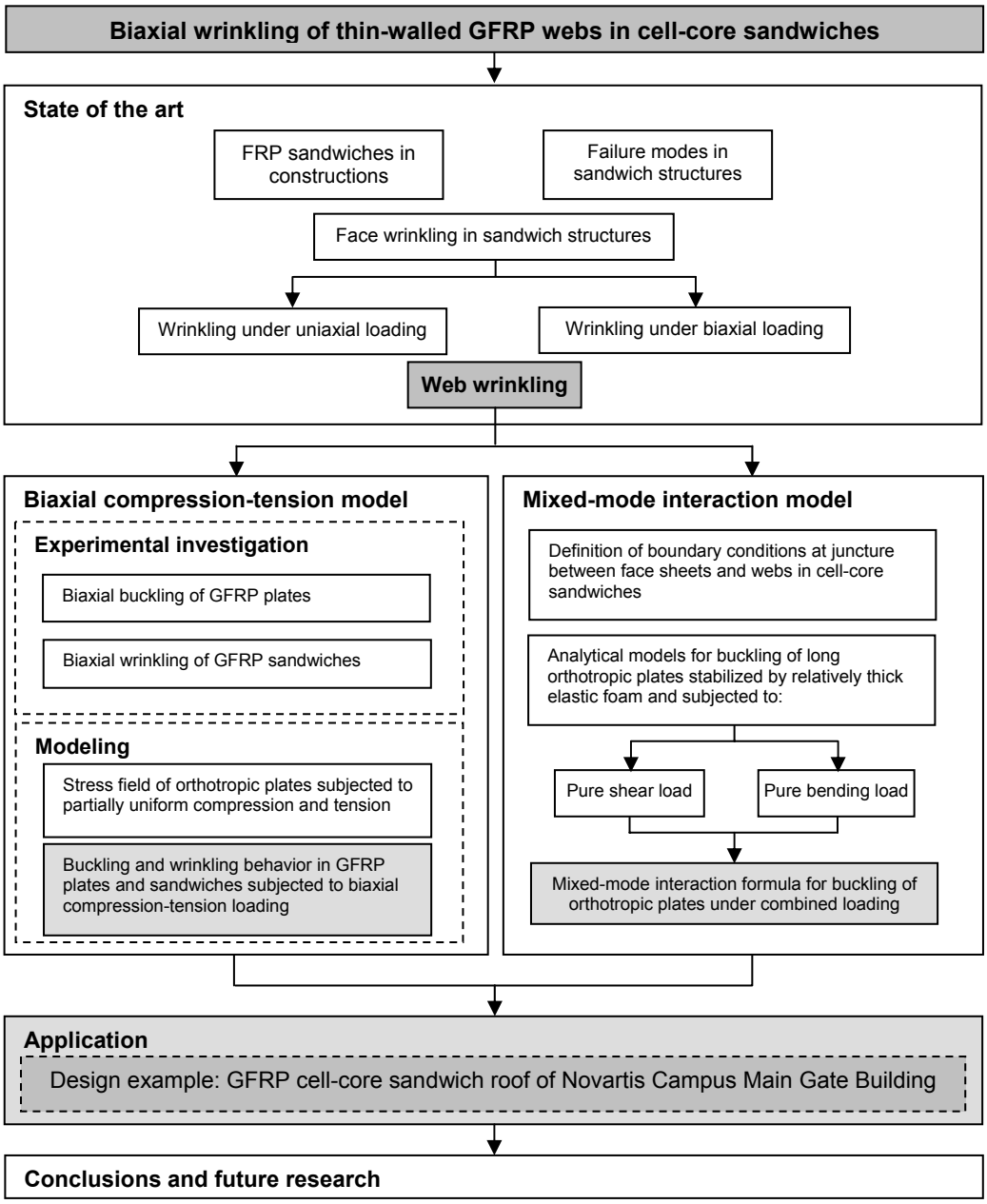

Figure 1.3. Thesis methodology and organization.

2 State of the Art

The proposed approach for predicting the wrinkling of webs in cell-core sandwich structures is based on a detailed analysis of the state–of–the art in the relevant field. First, the concept of sandwich structures is introduced and FRP sandwich structures in civil applications for lightweight high performance bridges and multifunctional buildings are extensively discussed. Then a short review of common failure modes in sandwich structures is presented. Being the most frequent failures in cell-core sandwich structures with thin face sheets and webs, different wrinkling failures modes are described and a survey of existing models developed for the prediction of wrinkling under uniaxial and biaxial loading conditions is provided. Since the final objective of the thesis is to study the wrinkling of webs in cell-core sandwich structures, the state–of–the art review concentrates on research in which web wrinkling is specifically investigated.

2.1. Introduction

A sandwich structure is defined as a layered construction formed by bonding two thin stiff face sheets to a relatively thick lightweight core as shown in Figure 2.1. The face sheets provide practically all the overall bending and in-plane extensional rigidity of the sandwich. The core serves to position the faces at locations removed from the neutral axis, provides virtually all the transverse shear rigidity of the sandwich, and stabilizes the face sheets against local buckling. Thus the structural sandwich concept is quite similar to that of a conventional I beam. The sandwich core plays a role which is analogous to that of the I beam web while the sandwich face sheets perform a function very similar to that of the I beam flanges. The face sheets commonly consist of metal, e.g. aluminum alloys, or composite material, e.g. carbon or glass fiber-reinforced composite, while the core material comes in several forms such as honeycomb cores, foam cores, balsa wood, corrugated cores, or truss cores.

The sandwich is an attractive structural design concept in applications requiring high bending stiffness and strength combined with low weight, for example aeronautical structures, high-speed marine craft and racing cars, since, with the proper choice of materials and geometry, constructions with high stiffness-to-weight ratios can be achieved.

Figure 2.2 shows the benefits that can be obtained in terms of stiffness-to-weight ratio by combining the core and skin materials rather than using one single material. The oblique lines represent constant stiffness-to-weight ratio. By choosing a material with properties that lie somewhere between those of the core and skin materials, only the grey zone can be covered. By combining the materials in sandwich panels, a zone with higher stiffness-to-weight ratio is obtainable (Ashby and Brechet 2003).

In addition to weight advantages, other economical advantages are vital for the potential use of sandwich construction in many applications. Sandwich material combinations with monolithic construction are even more advantageous in cost-sensitive applications than in weight-critical applications (Pflug and Verpoest 2006). Sandwich construction using a low-cost core material is not only lightweight but also cost effective, especially since the advancement and automation of production processes enable lightweight sandwich panels to be produced at lower cost (Rion 2008).

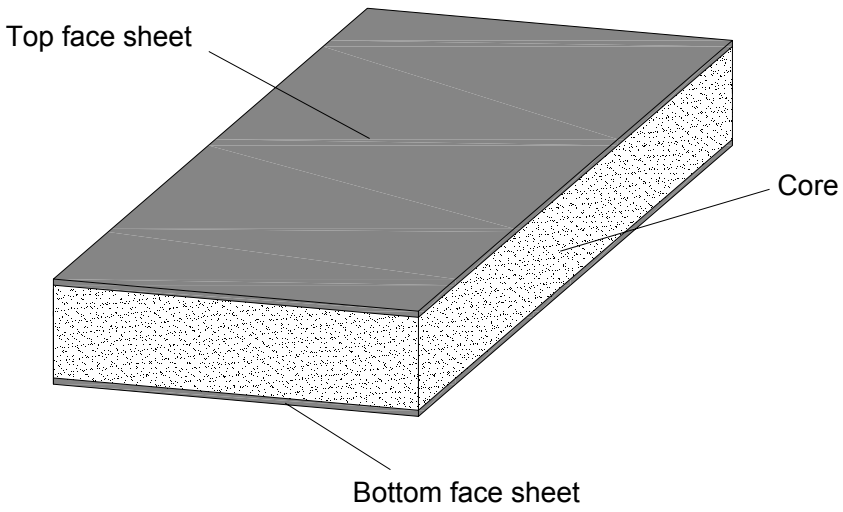

Figure 2.1. Typical sandwich construction.

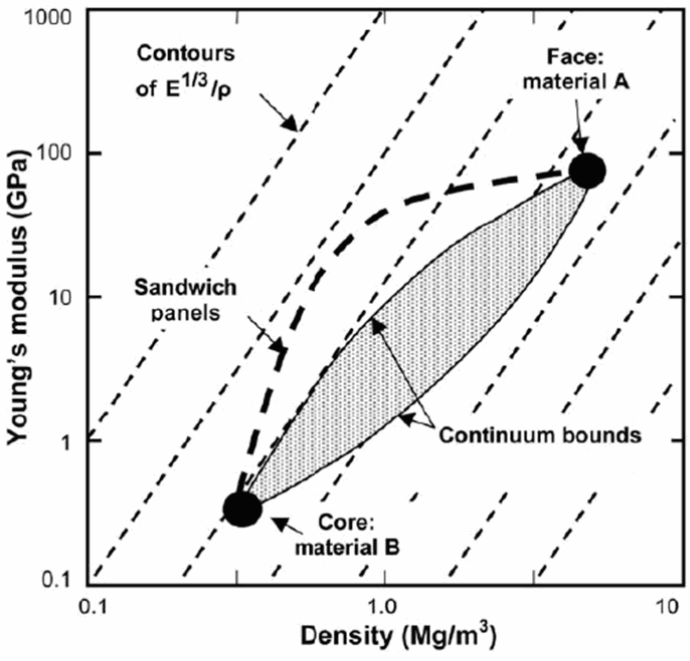

Figure 2.2. Optimal stiffness-to-weight ratio (Ashby and Brechet 2003).

The use of sandwich construction in aerospace vehicles is certainly not a recent innovation. The concept of the structural sandwich beam - the separation of stiff faces by a lightweight core - dates back to the 1820s (Zenkert 1995), but the systematic use of sandwich beams and sandwich panels as structural elements began in the middle of the 20th century during the Second World War on the British Mosquito aircraft. The sandwich was in the form of plywood faces of birch bonded to a balsa wood core, leading to the extensive use of sandwich structures in airplanes. More exhaustive information on the history of sandwich construction can be found in the introduction sections of the standard literature on sandwich structures (Allen 1969, Plantema 1966, Zenkert 1995, Vinson 1995). Motivated by improvements in manufacturing processes, adhesives, core and face materials as well as analysis techniques driven by the aerospace industry, sandwich construction has entered a wide field of applications in other areas of lightweight design such as naval engineering, the transportation industry, sports industry, and civil engineering.

2.2. FRP sandwiches in civil construction

Fiber-reinforced polymer (FRP) composites are promising construction materials that are increasingly used in civil engineering applications. The applications can be classified into three

broad areas. The first is the construction of new structures such as bridges and columns built exclusively of FRP. These structures have been proved to be durable and very resistant to environmental hazards. A second, and more common, application is the repair and rehabilitation of damaged or deteriorating structures. Thirdly, FRPs have been used in non-structural architectural or aesthetic applications such as cladding, roofing, flooring and partitions.

Over the past 15 years, a significant amount of research has been carried out to investigate the use of FRP decks for replacement of existing deteriorated bridge decks and for new bridge constructions (Zureick et al. 1995, Ehlen 1999, GangaRao et al. 1999, Alampalli et al. 2002, Bakis et al. 2002, Hutcheson and Sheppard 2003, Keller 2003, Williams et al. 2003, Stoll et al. 2004, Keller 2006, Alagusundaramoorthy et al. 2006, Kos and Stoll 2008, Robinson and Kosmatka 2008). Since raw material costs are high in comparison to traditional materials such as steel, concrete, or aluminum, FRP products had difficulty competing. Despite large potential benefits (i.e. environmental durability, rapid installation, reduced deadweight in superstructures), acquisition costs rule the bridge market (Kos and Stoll 2008). Two types of FRP products have been competing in this area in the last decades: sandwich and adhesively-bonded pultruded shapes. FRP decks produced by adhesively-bonded pultruded shapes include EZ Span (Atlantic Research), Superdeck (Creative Pultrusions), DuraSpan (Martin Marietta Materials) and ASSET (Fiberline Composite). The pultruded shapes are typically aligned transverse to the traffic flow direction. Figure 2.3 is a schematic diagram of the DuraSpan pultruded deck system. Pultruded decks were favored due to technology automation and production quality.

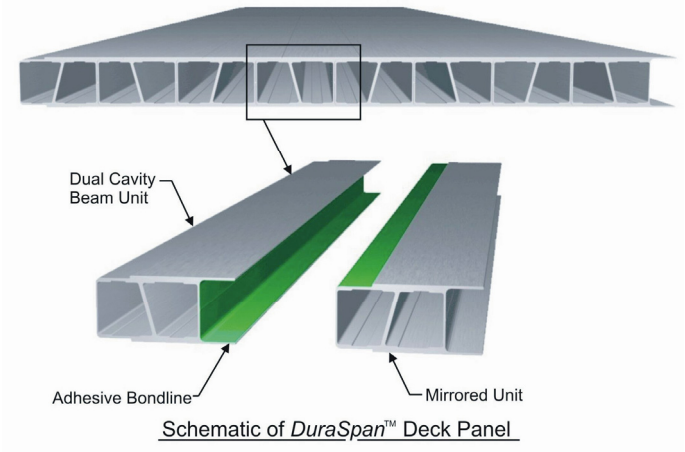

Figure 2.3. DuraSpan® deck system by Martin Marietta Composites, Inc.

Sandwich decks meet the high strength and stiffness requirements at a minimum unit weight. They are made of bonded core materials, separating strong, stiff and low-density face sheets. The entire deck is made to act compositely. A great advantage of this type of construction is its flexibility for designing structures to meet varied depths and deflection requirements. Robust sandwich constructions capable of bearing loads can be made especially when high strength cores are used. A major problem experienced with this type of construction is that the production line is not automated as the pultruded production is and therefore a high degree of manual labor is required, especially when high strength cores are used. Furthermore, delamination and debonding are the most common failure modes observed due to certain manufacturing defects. Recently, some companies e.g. Webcore Technologies Inc., have made advances in core manufacturing automation in which the automated process creates a core sheet of uniform thickness. The sheets are manufactured using consolidating pressure so there are no gaps between webs and core materials, which greatly enhances the core-to-skin bonds in sandwich panels. Several bridges have been constructed in various parts of the world using lightweight FRP sandwich decks. Some noteworthy examples are No-Name Creek Bridge Kansas 1996, Bonds Mill Lift Bridge - an electrically operated lift bridge in England 1998, Bennett's Creek FRP Bridge New York 1998, Composite Army Bridge (CAB) developed and tested at the University of California-San Diego 1999, and a short-span FRP sandwich deck Summit County, Ohio 2006.

In building construction, however, FRP composites have not yet had the same success, even though they also offer promising material properties for this domain. GFRPs, for instance, have the added benefit of low thermal conductivity that enables GFRP load-bearing components to act as insulating elements in addition to their structural functions. Furthermore, GFRP elements can be translucent or transparent and come in a range of colors. The possibility of integrating these different functions into individual building components can allow the merging of traditionally separated and layered structural and facade components into a function-integrated, single-layer building envelope (Keller et al. 2008). This re-opens the option of using the architectural concepts of the "Bauhaus" or modern architectural style that was lost in the 1970s, after the first oil crisis. That is, the structure must no longer be wrapped and hidden by the insulation facade for energy saving reasons and can function as a visible, architectural feature. This function-integrated envelope concept was developed in the 1950s and 60s for small single-storey GFRP

housing units and revived in the late 1990s. An example of this is the Eyecatcher Building, see Figure 2.4, constructed in 1999 in Switzerland (Keller 2003). In this building, the GFRP load-bearing structure is integrated into the facade layer and penetrates the latter without forming thermal bridges. Further, Keller et al. (2008) showed that GFRP composites assembled in large-scale cell-core sandwich structures enable the prefabrication of lightweight and function-integrated roof structures for rapid on-site installation, as shown in Figure 2.5. In this particular building, structural functions, building physics functions (thermal insulation, waterproofing), and architectural functions (complex shapes to fulfill high aesthetic requirements) were integrated into sandwich components.

The structural sandwich concept in the aforementioned examples is commonly an FRP cell-core sandwich which is composed of outer FRP face sheets, a foam core and a grid of FRP webs integrated into the core to reinforce the shear load capacity. Therefore, it has a transverse and longitudinal web configuration making it look like a box, as can be seen from Figure 2.6. Lately, the feasibility of the fabrication and structural performance of sandwich panels composed of a polyurethane core, GFRP skins and different GFRP web configurations has been investigated by Fam and Sharaf (2010). They demonstrated that, by integrating webs into the core panel, strength and stiffness can be substantially enhanced, by 44-140%, depending on the web configuration.

Figure 2.4. The Eyecatcher Building (Keller 2003).

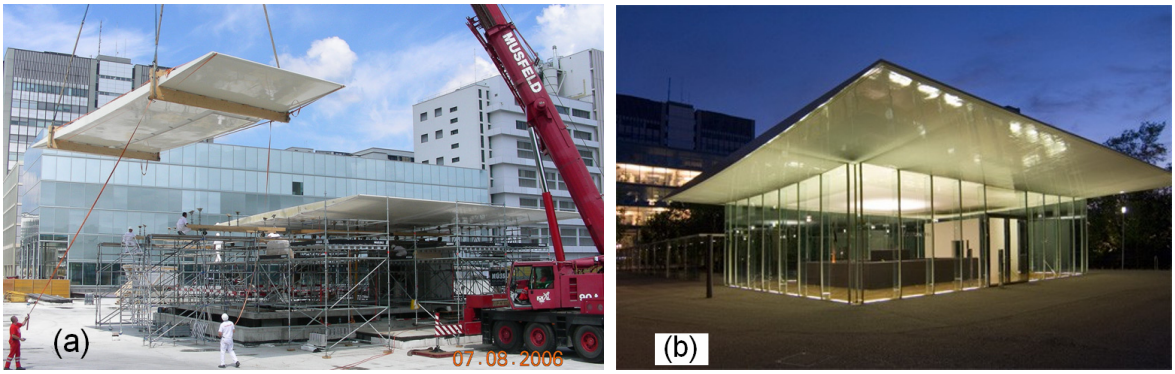

Figure 2.5. (a) Roof assembly at construction site (Keller et al. 2008); (b) Novartis Campus Main Gate Building with GFRP sandwich roof.

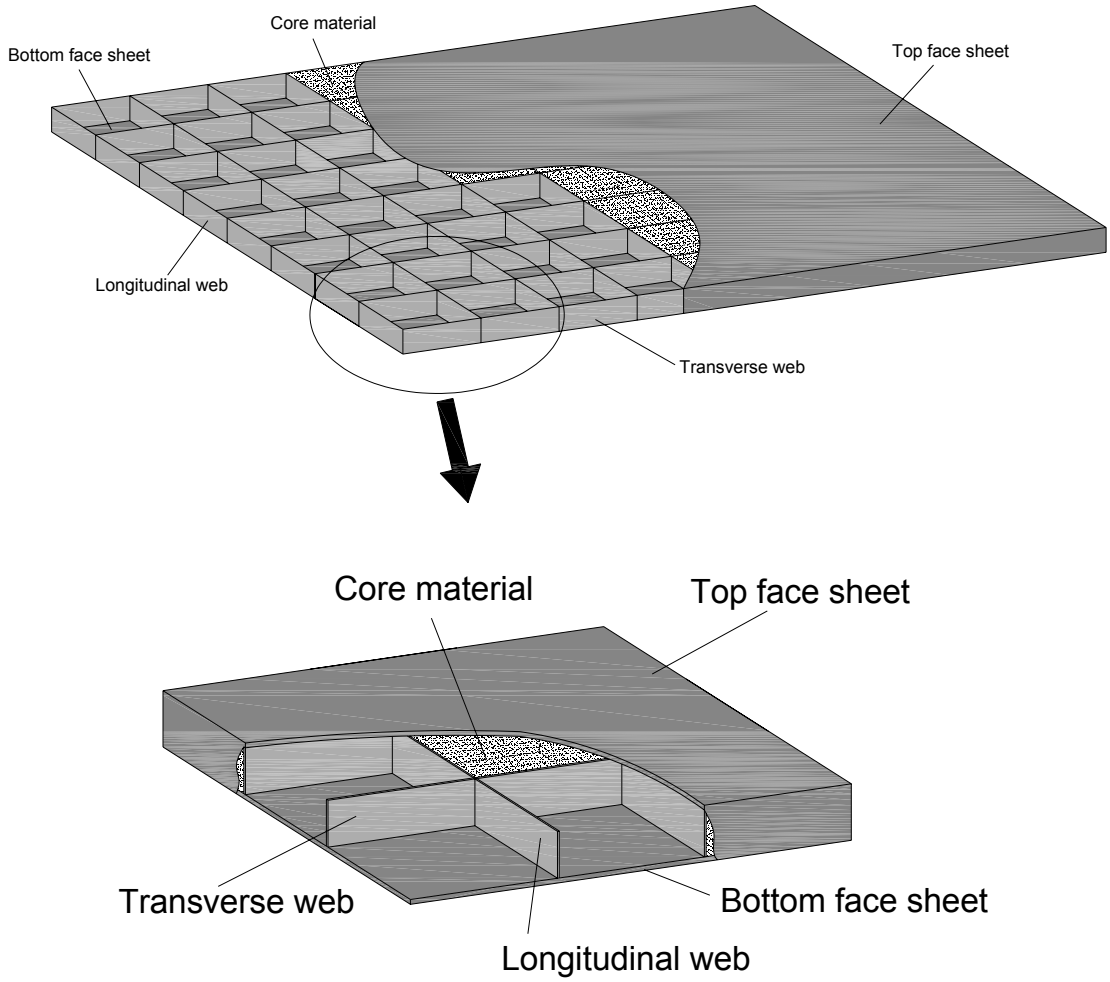

Figure 2.6. Cell-core sandwich system (for clarity purposes, face sheet and core material are only partially displayed).

2.3. Failure modes in sandwich structures

The use of heterogeneous materials, high stiffness and strength FRP laminates as the face layers, and soft materials such as polyurethane foam or honeycomb as the core, means that sandwich components can be used in material-tailored designs. However, this heterogeneity results in more complex failure mechanisms than those that occur with conventional structural elements (e.g. steel, concrete, wood etc.). Face sheet compressive failure, adhesive bonding failure, indentation failure, wrinkling, and core shear failure are common failure modes that occur in sandwich constructions (Sullins et al. 1969, Petras and Sutcliffe 1999, and Daniel and Gdoutos 2002). The

most common failure modes are summarized in Figure 2.7 with a brief description in the following.

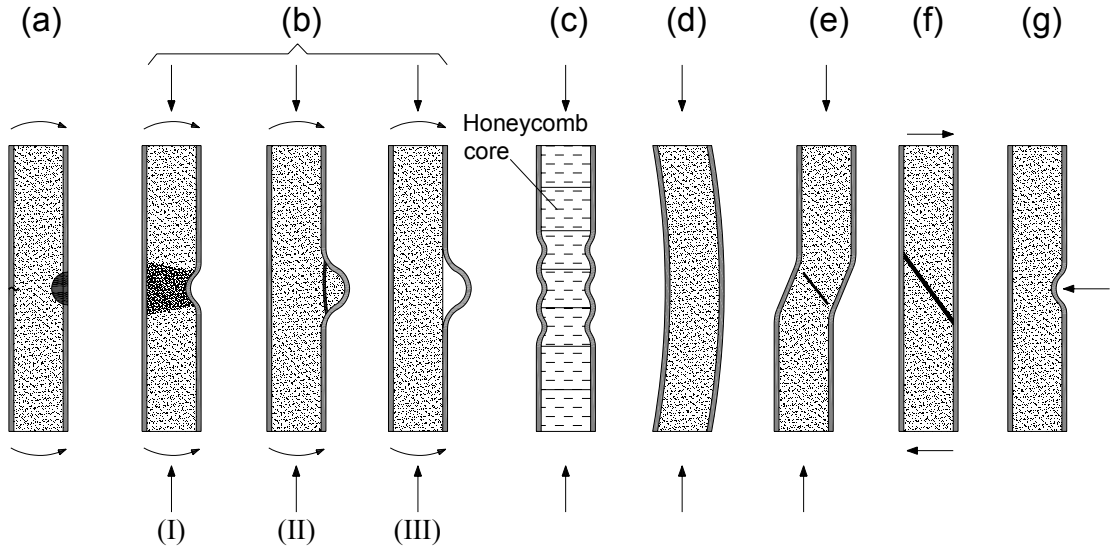

Figure 2.7. Typical failure modes of sandwich panels (according to Sullins et al. 1969 and Rion 2008).

(a) Tensile and compressive face sheet failure

This failure mode occurs when the maximum stress in the face sheet reaches the yield or fracture strength of the skin under either tension or compression.

(b) Face wrinkling

Wrinkling is a failure mode due to local face sheet instability. The skin buckles and forms waves with short wavelengths. This mode occurs frequently in sandwich panels with thin skins and a relatively low-density core (Gdoutos et al. 2003) and is therefore of primary importance for light sandwich structures. As shown in Figure 2.7(b), final failure followed by face wrinkling will usually be either crushing of the core (Figure 2.7(b)–I), tensile rupture of the core (Figure 2.7(b)–II), or tensile rupture of the core-to-face sheet bond (Figure 2.7(b)–III). However, thanks to appropriate selection of the adhesive system, it can reasonably be assumed that the tensile bond strength will exceed both the tensile and compressive strengths of the core and thus the ultimate failure will certainly be in the core. In the following sections, the wrinkling failure mechanism and the relevant existing models for prediction of this failure are elaborated.

(c) Face dimpling

This is a localized mode of instability that occurs in sandwiches with discontinuous cores such as honeycomb or corrugated core. As shown in Figure 2.7(c), in the regions directly above each core cell, the face sheet buckles with the cell walls acting as edge supports. This type of instability is often observed in sandwiches comprising relatively large cells and thin faces. The progressive growth of these buckles can eventually lead to the buckling mode identified above as face wrinkling.

(d) Global buckling

The general instability mode is shown in Figure 2.7(d) and usually occurs in panels with relatively stiff face sheets and thin cores. The phenomenon involves overall bending of the composite wall coupled with transverse (normal to face sheets) shear deformations. Buckling of the sandwich beams is very similar to ordinary Euler buckling theory. The difference is that instability may also occur due to shear in the sandwich beam (Rion 2008).

(e) Shear crimping

Shear crimping is a special form of general instability in which the buckle wavelength is very short due to a low transverse shear modulus of the core; nevertheless it is often referred to as a local mode of failure. This failure is a sudden phenomenon instantly followed by core shear failure or a shear failure in the core-to-face sheet bond.

(f) Core shear failure

This failure mode may occur when the shear stresses in the core exceed the shear strength of the core. Note that for some core materials such as honeycomb core the shear strength changes according to the loading direction.

(g) Core indentation

Although the strength and stiffness of the sandwich structures are very high, thin skins bonded to the core, which has low compressive strength, are highly sensitive to local loads that can easily indent the skins.

2.4. Face wrinkling in sandwich structures

Face wrinkling has traditionally been treated as a local, short-wavelength buckling phenomenon that is one of a number of possible buckling modes exhibited by sandwich structures. There are several different modes of wrinkling, as shown in Figure 2.8, (Sullins et al. 1969, Ley et al. 1999, Fagerberg 2003). The occurrence of the different wrinkling modes depends on sandwich geometry (thickness of components) and material properties (in particular core materials).

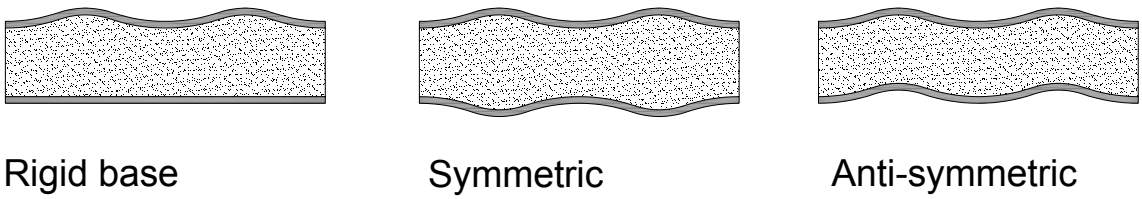

Figure 2.8. Wrinkling instability modes.

In the first mode "rigid base", short-wavelength buckling waves occur only on one face sheet of the sandwich. This mode appears when the sandwich is under bending and only one face sheet is under compression, or if the sandwich has unsymmetric face sheets, one with a higher buckling load than the other. In the second mode, the wrinkling of the face sheets is symmetric with respect to the middle surface of the sandwich and is a special case of rigid base wrinkling at a smaller distance to the rigid plane. The third mode is the anti-symmetric, or in some literature "snake", mode where the two face sheets wrinkle in phase, anti-symmetric with respect to the middle surface of the sandwich. This mode is common for anisotropic core materials where the shear stiffness is considerably lower than the Young's modulus (perpendicular to the face sheet), e.g. honeycombs, and for sandwich configurations with a thin core. If the core is sufficiently stiff and thick, which is the case for most sandwich structures used in civil applications, wrinkling in an anti-symmetric mode does not occur at any wavelength. Therefore, the present research is focused on the symmetric mode, which corresponds to wrinkling of a plate resting on relatively thick core materials. In this framework, a detailed review of analytical approaches for the

wrinkling of sandwiches under uniaxial and biaxial loading conditions is presented in the following.

2.4.1. Wrinkling under uniaxial loading

The first reported works on sandwich face wrinkling were published in the early 1940s by Gough et al. (1940) and Williams et al. (1941). The results of these investigations are in essence covered by the following (Ley et al. 1999). They started by modeling the wrinkling of uniaxially loaded flat sandwiches and treated the face sheet as an ordinary beam or strut supported by a relatively thick core foundation and disregarding transverse shear deformations (a reasonable assumption for a thin composite or metal face), as shown in Figure 2.9.

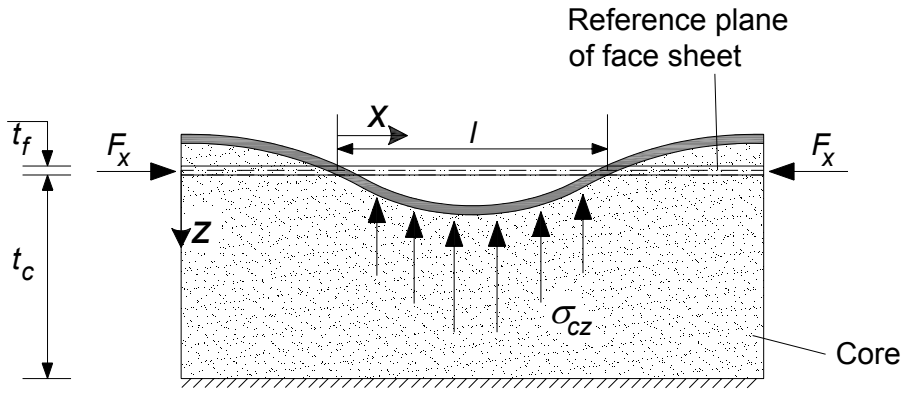

Figure 2.9. Uniaxial wrinkling, 2-D model.

The wrinkling deflection wave is assumed as being a periodic wave with the (half) wavelength, l, see Figure 2.9. For a beam on elastic foundation in bending, the governing differential equation is then written as follows

$$D_f \frac{d^4 w_f}{dx^4} + F_x \frac{d^2 w_f}{dx^2} - \sigma_{cz} = 0 \tag{2.1}$$

where w_f is the defection function of the beam (face sheet), D_f is the bending stiffness of the face sheet alone, F_x is the compressive load acting on the face sheet and σ_{cz} is the support pressure from the core due to compressive deformation in the core. Note that in Eq. (2.1) two transverse shear deformations of the core and the corresponding stresses were assumed negligible, which can

also be added in the general form. In wrinkling the displacements of the face sheets are transmitted to the core in which they damp out rapidly in the thickness direction. Numerous theoretical models and experimental data exist concerning uniaxial compression wrinkling (Gough et al. 1940, Cox and Riddell 1945, Hoff and Mautner 1945, Williams 1947, Hemp 1948, Yusuff 1955, Plantema 1966, and Allen 1969) which consist of different assumptions regarding the decay of the transverse deformation in the core and several different solution approaches. Although the approaches are different they yield approximately the same result and the differences are mainly due to varying assumptions regarding the decay of the transverse core deformation. Ley et al. (1999) made an extensive review of the most commonly used models, their advantages and disadvantages and their agreement with experimental data.

In the following, a short introduction to five of the most commonly used theories for uniaxial face wrinkling together with their derivations is presented. Three of the models are based on the solution of the governing differential equations, while the others are based on energy methods.

(a) Winkler foundation model

In the Winkler foundation model, the simplest one, the continuous elastic medium of the core is modeled as a set of parallel elastic springs (Zenkert 1995). Therefore, since there is no decay in linear elastic deformation, σ_{cz} is constant in Eq. (2.1). Indeed, this approach assumes a core with the modulus perpendicular to the faces (E_c) but with no out-of-plane shear stiffness, i.e. G_c = 0. According to Hooke's law, the stress in springs (core) is proportional to the face sheet deflection, and can be written as

$$\sigma_{cz}(x,z) = -K_z w_c(x,0) = -K_z w_f \tag{2.2}$$

in which K_z is the so-called "foundation modulus" and $w_c(x,z)$ is the transverse deformation in the core. Since the stress is constant through the core thickness and core shear is disregarded, the wrinkling wave, $w_c(x,z)$, damps out linearly through the core. It further has to be equal to zero at the symmetry plane and can therefore be written as

$$w_c(x,z) = w_f\left(1-\frac{z}{t_c}\right) \tag{2.3}$$

For the core as a continuous medium with no out-of-plane shear stiffness, i.e. G_c = 0, it can be written that:

$$\varepsilon_z = \frac{dw_c}{dz} \tag{2.4}$$

$$\sigma_{cz} = E_c \varepsilon_z \tag{2.5}$$

where ε_z is the strain of the core in *z*-direction (perpendicular to the face sheet). Integrating Eqs. (2.2) to (2.5) results in:

$$K_z = \frac{E_c}{t_c} \tag{2.6}$$

Finally, Eq. (2.1) is solved by assuming a sinusoidal deflection function of the face sheet, w_f, in *x*-direction as follows:

$$w_f = A \sin\left(\pi x / l\right) \tag{2.7}$$

where *A* is the deflection amplitude. Inserting this into Eq. (2.1) results in F_x as a function of the wavelength *l*. The minimization of F_x with respect to *l* leads to the critical compressive force:

$$F_{Winkler} = 2\sqrt{D_f K_z} = 0.577\sqrt{\frac{E_f {t_f}^3 E_c}{t_c(1-{\upsilon_f}^2)}} \tag{2.8}$$

where υ_f and E_f are the Poisson ratio and Young's modulus of the face sheet, respectively.

(b) Hoff – Mautner's model

The next common model to be assessed is that presented by Hoff and Mautner (1945) and the solution is obtained based on the minimum potential energy method. In this model, assuming the face forms a sinusoidal wrinkling wave (see Eq. (2.7)), the wave damps out linearly in the core through the depth of *h*; therefore it is expressed as:

$$w_c(x,z) = \frac{A(h-z)}{h} \sin\frac{\pi x}{l} \tag{2.9}$$

Combining Eqs. (2.4) and (2.5), the perpendicular (tensile/compressive) stress in the core can be expressed as $\sigma_{cz} = E_c \, \partial w_c / \partial z$. If the displacements are assumed only in the *z*-direction and no

displacement in the *x*-direction is assumed, i.e. u_c=0, then the core shear stress is obtained as follows:

$$\tau_{cxz} = G_c\left(\frac{\partial w_c}{\partial x} + \frac{\partial u_c}{\partial z}\right) = G_c\frac{\partial w_c}{\partial x} \tag{2.10}$$

The total potential energy equation can be attained by

$$\Pi = U_f + U_c + \Omega \tag{2.11}$$

where U_f, U_c, and Ω are the strain energy of the face sheet, the strain energy in the core and the work of the external force F_x, respectively. They are obtained as follows:

$$U_f = \frac{D_f}{2}\int_0^l\left(\frac{d^2 w_f}{dx^2}\right)^2 dx \tag{2.12}$$

$$U_c = \frac{1}{2E_c}\int_0^l\int_0^h {\sigma_{cz}}^2 dxdz + \frac{1}{2G_c}\int_0^l\int_0^h {\tau_{cxz}}^2 dxdz \tag{2.13}$$

$$\Omega = -\frac{1}{2}\int_0^l F_x\left(\frac{d^2 w_f}{dx^2}\right)^2 dx \tag{2.14}$$

Minimizing the total potential energy with respect to A, F_x will be obtained as a function of the wavelength l and h. The minimization of F_x with respect to l and h leads to the critical compressive stress as follows:

If $h<t_c/2$:

$$\sigma_{Hoff} = 0.91\sqrt[3]{E_f E_c G_c} \tag{2.15}$$

If $h \geq t_c/2$ (thin core) then:

$$\sigma_{Hoff} = 0.817\sqrt[3]{\frac{E_f E_c t_f}{t_c}} + 0.166G_c\left(\frac{t_c}{t_f}\right) \tag{2.16}$$

Hoff and Mautner (1945) found that the prediction of the wrinkling load trends agreed very well with tests but suggested that in practical cases the load should be predicted using the conservative formula:

$$\sigma_{Hoff} = 0.5 \sqrt[3]{E_f E_c G_c} \tag{2.17}$$

This is the formula used today in a large part of the industry and is often designated Hoff's formula.

(c) Plantema's model

The solution method in Plantema's model (Plantema 1966) is similar to the one described for Hoff and Mautner's model. The only difference is that this model assumes exponential deformation decay in the core so that:

$$w_c(x,z) = Ae^{-kz} \sin\frac{\pi x}{l} \tag{2.18}$$

where k is an unknown model parameter. The total potential energy method as described by Eqs. (2.11) to (2.14) is derived. Minimizing the total potential energy with respect to A gives F_x as a function of the wavelength l and k. The minimization of F_x with respect to l and k leads to the critical compressive force. In the case of anisotropy of the face sheets, the critical wrinkling load is derived as:

$$P_{Plantema} = \frac{3}{2} \sqrt[3]{2 D_f E_c G_c} \tag{2.19}$$

If the face sheet is isotropic Eq. (2.19) can be rewritten as:

$$\sigma_{Plantema} = 0.85 \sqrt[3]{E_f E_c G_c} \tag{2.20}$$

As can be seen, this result is very close to that obtained by Hoff and Mautner for the thick core cases.

(d) Allen's model

Allen (1969), similarly to previous models, assumed a thin beam (the face sheet) under compressive end loads, continuously supported by an elastic core, which extends infinitely on one side of the beam, see Figure 2.9. Hence, the differential equation with the assumption of having a homogeneous beam or plate in bending is given by Eq. (2.1). It is also assumed that the core is isotropic and a sinusoidal wrinkling wave in the face sheet occurs, see Eq. (2.7). Then, by considering that the stress in the core has to satisfy Airy's stress function, it follows:

$$\sigma_{cz} = -\frac{a'}{l} A \sin\frac{\pi x}{l} \tag{2.21}$$

while $a' = \dfrac{2\pi E_c}{(3-v_c)(1+v_c)}$ and v_c is the Poisson ratio of the core.

Solving the differential equation of (2.1) by having the core stress, Eq. (2.21) and deflection function, Eq. (2.7), F_x is again attained as a function of the wavelength l. The minimization of F_x with respect to the wavelength leads to the critical compressive force, which is presented as:

$$P_{Allen} = 0.88 \sqrt[3]{D_f a'^2} \tag{2.22}$$

If the face sheet is isotropic with $G_c = E_c/2(1+v_c)$, the critical stress is obtained as

$$\sigma_{Allen} = 0.78 \sqrt[3]{E_f E_c G_c} \tag{2.23}$$

(e) Gutierrez – Webber's model

This model (Gutierrez and Webber 1980), which is an extension of the previous model by Webber et al. (1976), deals with the wrinkling of the orthotropic face sheet under compression when the sandwich panel is loaded in bending. The solution is obtained by numerical analysis based on solving the equilibrium differential equations.

The equilibrium equations for the core, when the displacement in the *x*-direction, u_c, is assumed as non-zero, are written as:

$$\sigma_{cz} = -z\frac{d\tau_{cxz}}{dx} + \sigma_{z=0} \tag{2.24}$$

$$w_c = -\frac{z^2}{2E_c}\frac{d\tau_{cxz}}{dx} + z\frac{\sigma_{z=0}}{E_c} \tag{2.25}$$

$$u_c = z\frac{\tau_{cxz}}{G_c} + \frac{z^3}{6E_c}\frac{d^2\tau_{cxz}}{dx^2} - \frac{z^2}{2E_c}\frac{d\sigma_{z=0}}{dx} \tag{2.26}$$

where $\sigma_{z=0}$ is the stress in the core at z=0 and is therefore a function of x only. The z-axis is defined differently from the one in Figure 2.9. Figure 2.10 illustrates the model used for the development of the equations.

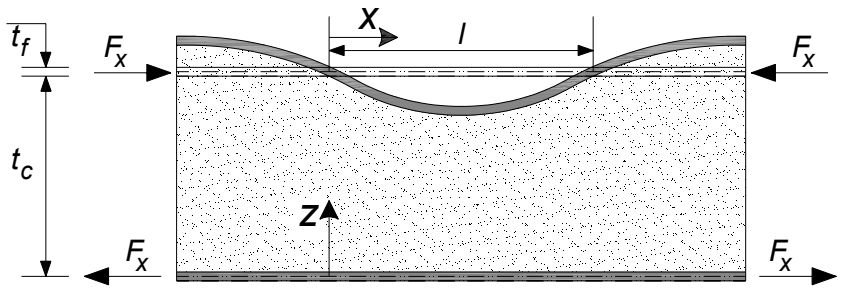

Figure 2.10. Wrinkling of face sheet of sandwich beam under bending moment.

The equilibrium equations for the top face sheet (under compression) at $z=t_c$ are as follows:

$$A'\frac{d^2u_f}{dx^2} - B'\frac{d^3w_f}{dx^3} = \left(\tau_{cxz}\right)_{z=t_c} \tag{2.27}$$

$$B'\frac{d^3u_f}{dx^3} - D'\frac{d^4w_f}{dx^4} - F_x\frac{d^2w_f}{dx^2} = \left(\sigma_{cz}\right)_{z=t_c} \tag{2.28}$$

where the coefficients A', B', D' are defined with the ABD matrix of the laminated face presented in Webber et al. (1976). Furthermore, u_f and w_f are the displacements of the face sheet in x- and z-directions which are equal to u_c and w_c at $z=t_c$. So Eqs. (2.24) to (2.26) can be integrated into Eqs. (2.27) and (2.28) and by suitable differentiation and substitution, an eighth order differential equation is obtained. By considering that the wrinkled face has a sinusoidal shape with a half wavelength l similar to the one presented in Eq. (2.7) and solving the eighth order differential equation numerically, the minimum wrinkling wavelength, l, can be calculated. The value of l giving the lowest load corresponds to the critical wavelength and gives the critical wrinkling load of the beam. Note that the model considered that the face sheet in tension remains flat and unstrained during the wrinkling of the skin under compression.

2.4.2. Wrinkling under biaxial loading

Two general approaches exist for dealing with the wrinkling of face sheets subjected to biaxial or multiaxial loads. The first approach involves the results from the uniaxial compression wrinkling being extrapolated to biaxial cases. The procedure usually starts with the calculation of the maximum principal face sheet compressive stress. This stress is then compared to an allowable stress derived using the uniaxial compression wrinkling models. In the second approach, 2-D

deflection functions used for the uniaxial compression wrinkling are extended to 3-D deflection functions describing the face sheet deformation as a plate under general conditions. Therefore, the stresses and strains of core and face sheets are determined for (x, y, z) space. The governing differential equations and/or the energy derivations are solved for a 3-D problem under general conditions. In the following, five existing models for the biaxial compression-compression wrinkling of rectangular sandwich panels are discussed. Three of them employ the first approach and the others the second.

(a) Sullins' model

The first reported discussion regarding wrinkling under multi-axial load was attributed to Sullins et al. (1969) with certain recommendations as follows: first, calculate the principal stresses σ_1 and σ_2, either by means of analytical or numerical methods. If only one of the principal stresses is in compression, then disregard the tension stress and treat the problem as one-dimensional. If both principal stresses are in compression then use the following interaction formula to determine the wrinkling strength:

$$\left(\frac{\sigma_1}{\sigma_{1cr}}\right)+\left(\frac{\sigma_2}{\sigma_{2cr}}\right)^3 \le 1 \qquad (2.29)$$

with $\sigma_1 > \sigma_2$ and the critical stresses σ_{1cr} and σ_{2cr} being the one-dimensional wrinkling stresses calculated in the directions of the principal stresses. The interaction model is taken from analyses and tests concerning the global buckling of sandwich panels with isotropic face sheets and, without physical justification, proposed for use in the case of wrinkling as well.

(b) Fagerberg–Zenkert's model

The model proposed by (Fagerberg 2000, Fagerberg and Zenkert 2005-a) is to evaluate the wrinkling load of anisotropic sandwich panels by using one of the uniaxial wrinkling theories and then calculating the wrinkling stress in every direction of the panel, assuming cylindrical bending and disregarding any special plate effects. The method is based on the assumption that the wrinkling first occurs at the angle φ where the ratio of the applied load P_φ and sustainable wrinkling load $P_{\varphi,cr}$ reaches a global maximum. The P_φ may be found in any coordinate system by simple transformation of the external applied loads N_x, N_y and N_{xy}, and P_φ is then simply taken as the compressive load perpendicular to the wrinkling wave defined at an angle φ, see Figure 2.11.

By disregarding the influence of the extension-bending coupling matrix in orthotropic laminates, the $P_{\varphi,cr}$ is easily estimated by inserting the first value of the bending stiffness matrix into the uniaxial Plantema formula, Eq. (2.19), which is written as follows:

$$P_{\varphi,cr} = \frac{3}{2}\sqrt[3]{2D_{\varphi 11}E_c G_c} \tag{2.30}$$

where $D_{\varphi 11}$ is the bending stiffness of the face sheet determined in the same direction as P_{φ}. This method provides a possibility to find the angle between the applied load and the wrinkling waves. This proposed method is easy to apply and according to (Fagerberg and Zenkert 2005-a) gives a good prediction of the critical wrinkling load. However, since the method uses the uniaxial wrinkling models, this means it assumes the wrinkling wave to be an infinite sine wave and therefore it does not take into account the interaction effects of the transverse shear and compression or tension.

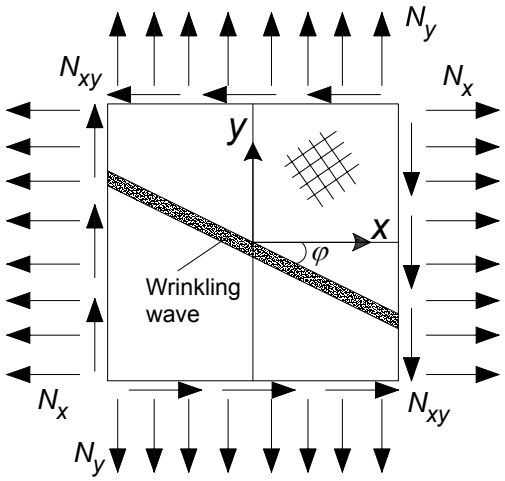

Figure 2.11. An anisotropic sandwich plate subjected to multiaxial in-plane loading.

(c) Vonach–Rammerstorfer's model

In this model (Vonach and Rammerstorfer 2000-a, Vonach and Rammerstorfer 2000-b, Vonach 2001), by considering wrinkling as a local short-wave buckling phenomenon, the face sheet is assumed as being in a homogeneous stress state prior to buckling and its length and width are assumed to be infinite. Therefore, the deformation pattern is also assumed to be an infinite sine

wave. In the case of orthotropic plates, the deformation pattern of the wrinkled face layer is also a single sine wave, but its orientation will generally not coincide with the direction of the major principal compressive stress due to the influence of orthotropy. In this model, it is assumed that as long as the core exhibits transversely isotropic behavior and the plane of isotropy coincides with the face layer, the core has no influence on the direction of the wave pattern. As shown in Figure 2.12, the coordinate system of the axes of orthotropy is denoted as (x, y, z) system, whereas the (r, s, z) system is oriented in the wave-pattern direction, which is at an angle φ to the material axes. This is expressed as:

$$w_f = w_{c\ at\ z=0} = w^* \sin\left(\frac{\pi(x\cos\varphi + y\sin\varphi)}{l}\right) \tag{2.31}$$

where the half wavelength l and the wave angle φ are the unknowns to be derived.

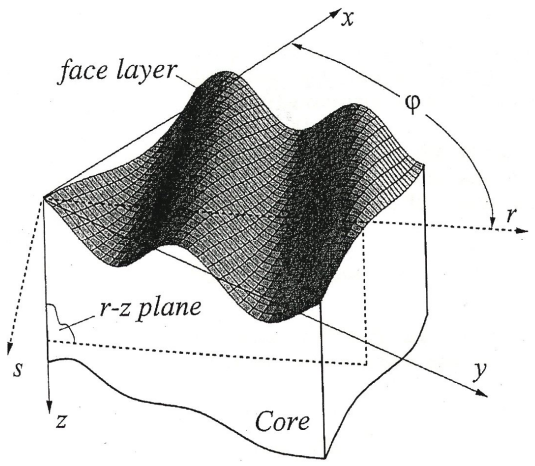

Figure 2.12. Geometry of wrinkling problem (Vonach and Rammerstorfer 2000-a).

Then by considering that the stress in the core has to satisfy Airy's stress function, the amplitude of the transverse displacement w^* at the interface has been calculated as

$$w^* = \sigma^c_{z,0}\frac{l}{\pi K_z} \tag{2.32}$$

This equation gives the relationship between the stress amplitude $\sigma^c_{z,0}$ and the deformation amplitude at the interface in the transverse direction, both of which are distributed sinusoidal. K_z

is the "foundation modulus" (see Winkler foundation model in Section 2.4.1). Therefore $l/\pi K_z$ represents the inverse foundation stiffness of the core, depending on the wavelength l, which can be inserted into the differential equation of the face layer. In this model, the face layer has been modeled as an orthotropic plate with the material axes in the x-, y- and z-directions as follows:

$$B_x^f \frac{\partial^4 w_f}{\partial x^4} + 2B_{xy}^f \frac{\partial^4 w_f}{\partial x^2 \partial y^2} + B_y^f \frac{\partial^4 w_f}{\partial y^4} + P_x \frac{\partial^2 w_f}{\partial x^2} + 2P_{xy} \frac{\partial^2 w_f}{\partial x \partial y} + P_y \frac{\partial^2 w_f}{\partial y^2} + w_f \frac{\pi}{l} K_z = 0 \qquad (2.33)$$

in which the various B^f denote the plate stiffness parameters and the quantities P_x, P_y and P_{xy} are the compressive normal and shear forces per unit width acting in the face layer. Using the definition of w_f in Eq. (2.31), the compressive force $P_x^*(l,\phi)$ for a nontrivial solution of Eq. (2.33) can be derived as follows:

$$P_x^*(l,\varphi) = \frac{(\frac{\pi}{l})^2 \left(B_x^f \cos^4\varphi + 2B_{xy}^f \sin^2\varphi\cos^2\varphi + B_y^f \sin^4\varphi \right) + \frac{l}{\pi} K_z}{\cos^2\varphi + 2\left(\frac{P_{xy}}{P_x}\right)\sin\varphi\cos\varphi + \left(\frac{P_y}{P_x}\right)\sin^2\varphi} \qquad (2.34)$$

The critical compressive force is obtained by minimizing $P_x^*(l,\varphi)$ with respect to the two unknown variables, l and φ, which requires a numerical method to solve two nonlinear equations simultaneously. In fact, the latter two models are analogous; Vonach-Rammerstorfer's model follows the same approach as Fagerberg-Zenkert's model with different solution methods. The Vonach-Rammerstorfer's model is limited to a certain parameter range and cannot easily include honeycombs cores. Moreover, since this model, like the previous one, assumes the wrinkling wave to be an infinite sine wave, it does not take into account the interaction effects of the transverse shear and compression or tension on the local wrinkling wave.

(d) Birman–Bert's model

Birman and Bert (2004) have presented some analytical modeling for the wrinkling of composite-facing sandwich panels subjected to biaxial compression-compression loading. In this study, two possible modes of wrinkling are considered. The first is represented by a long sine wave that may be perpendicular to the direction of one of the applied compression loads or inclined relative to the load direction by an angle of φ. This is based on the same approach used in the latter two

models. In this context, a comparison of different solutions obtained using three different uniaxial wrinkling models (Winkler foundation model, Hoff-Mautner's model and Plantema's model) was made. It was concluded that Plantema's model was more appropriate than the Hoff's and Winkler foundation models since it predicted more conservative combinations of wrinkling stresses than the other models. The second wrinkling mode in symmetrical laminated face sheets is represented by rectangular wrinkles oriented along the load direction. In this mode, the face sheet is assumed as being an infinite plate (compared to the short length of the rectangular wrinkles) subjected to compression-compression loading. The solutions are provided based on three models of deformation decay in the core (Winkler model, Hoff-Mautner's model and Plantema's model). Then the resulting formulations are numerically solved only for the case of unidirectional compression of the sandwich structure.

(e) Hadi–Matthew's model

The model proposed by Hadi and Matthews (2000) is a development of the unified theory of Benson-Mayers (Benson and Mayers 1967) from isotropic sandwich panels to the buckling of anisotropic sandwich panels. The model calculates symmetrical and anti-symmetrical buckling simultaneously and thus provides results for overall buckling and wrinkling. The model is constructed based on the minimum potential energy principle, which is solved by the Raleigh-Ritz method. In this solution, the strain energy of the face sheets is calculated in the general form comprising membrane strains and plate curvatures. Moreover, the core is assumed to be an anti-plane core, in which core stiffness along the face sheet is disregarded. Therefore the strain energy of the core can be given as a summation of shear strain energy and normal transverse strain energy. Extra strain energy due to the continuity condition between the face sheets and core is defined. Satisfying the continuity requirement between the face sheets and core gives the strain energy in the adhesive. Then the external work due to shear and normal loads is calculated. Note that all three displacements in *x*-, *y*- and *z*-directions (*u*, *v*, and *w*) for two face sheets are considered. Finally, the total energy, Π, of the system is the summation of the calculated energies. The displacement functions of the sandwich plate are assumed as being:

$$(u_m, v_m, w_m) = \sum_{i=1}^{\infty}\sum_{j=1}^{\infty} C_{ij}^{m} f(i,x) g(j,y) \tag{2.35}$$

where f and g can be either sinusoidal or co-sinusoidal functions, based on the boundary conditions, i and j are half-wavelength integers that represent the number of waves for sinusoidal or co-sinusoidal functions in x- and y-directions and C_{ij}^{m} are undetermined coefficients. Fulfilling the Ritz condition, which states that the total energy of the system should be stationary, $\partial \Pi / \partial C_{ij}^{m} = 0$, results in 10 simultaneous equations in C_{ij}^{m}, m=1,2,….,10. Indeed, the stability criterion of a sandwich plate is reduced to the generalized eigen-value problem of the type $[P']\{C\} = N_x[Q']\{C\}$ where $[P']$ is the square matrix with size $10ij$ that represents the structure stiffness matrix and $[Q']$ is the stress stiffness matrix. The values of i and j should be increased to 100 in order to be able to predict wrinkling modes.

2.4.3. Wrinkling and initial imperfection

In models such as those described above, face sheets were assumed to be perfectly flat and wrinkling was treated as a bifurcation problem where no out-of-plane deflections were permitted until a certain compressive load was reached where the face sheets would buckle locally in a symmetric or anti-symmetric mode. It is well known, however, that due to imperfections inherent in the fabrication process, such as tolerances of core machining, local variation in thickness of the adhesive bond, or irregularities in the composite face sheet lamination, the fabricated structures exhibit low amplitude waviness. Since the wrinkling is assumed to be a local instability with short wavelength, the actual wrinkling load is very much affected by any initial imperfections or waviness of the face sheet (Hoff and Mautner 1945, Yussuf 1960, Gutierrez and Webber 1980, Sullins 1969, Kassapoglou et al. 1995).

While no accurate measurements of the waviness are provided, some design guidelines and handbooks recommend certain waviness ratios (ratio of waviness amplitude to face sheet thickness) that, combined with a waviness analysis, seem to present a reasonable agreement with test results (Sullins 1969, Kassapoglou et al. 1995). For example, as presented by (Sullins 1969), it was found that the factors preceding the cube root expression in Eqs. (2.15), (2.17), (2.20) and (2.23) from between 0.5 to 0.9 reduce to low numbers such as 0.05 to 0.1 in the case of high waviness. The reason for proposing Eq. (2.17) by Hoff and Mautner (1945) as a conservative formula to be used in the industry is mainly based on the initial imperfections. As discussed in

Plantema (1966), the effect of initial imperfections can be taken into account by reducing the wrinkling strength to approximately 80% of the theoretical value.

Furthermore, Fagerberg and Zenkert (2005-b) performed an investigation in which the panel strength was predicted by a model taking the initial imperfections into account. It was found that using this model as a basis for the wrinkling analysis provides a better foundation for failure analysis than the ordinary stability analysis and it also allows the determination of which type of failure mode (compressive failure of face sheet, core crushing, tensile rupture of core, etc.) is likely to be the ultimate failure. The prediction model was based on the derivation carried out by Timoshenko and Gere (1963) for the buckling of a strut or plate with an initial imperfection and subsequently proved by Allen (1969) to be valid for plates resting on an elastic foundation. In Section 4.3.2, the analytical model is explained in more detail and used for modeling the experimental results.

2.4.4. Wrinkling and finite element modeling

Experimental investigation simulating wrinkling failure under certain boundary conditions (in particular for biaxial loading conditions) is very difficult and costly since it requires extremely precise set-ups and automations. Therefore, with the development of computer power over the last 30 years, most of the research works (Fagerberg 2000 & 2003, Fagerberg and Zenkert 2005-a, Vonach and Rammerstorfer 2000-a&b, Vonach 2001, Birman and Bert 2004, Hadi and Matthews 2000, Lake et al. 2007, Brisco et al. 2010) published in the wrinkling field seek to perform finite element (FE) modeling and use it for validation of their analytical solutions. In this regard, there are certain common points that should be considered:

- In a 2-D model the face sheet should be modeled with beam elements and the core with membrane elements. In a 3-D model the face should be modeled with shell elements and the core with solid (brick) elements (Fagerberg 2003 and Vonach 2001).
- The use of two types of element with a different number of nodal degrees of freedom is sometimes questioned. However, the mathematical error will be small compared to the case in which the thin face sheets and relatively thick core are modeled with only one type of element. In this situation, a large number of elements are required to avoid a too-high element aspect ratio and distortion.

- To achieve a satisfactory estimate, the element length should be shorter than half the wrinkling wavelength. If the shape of the wrinkling wave is also important and a better estimation is needed, a minimum of four elements per wavelength should be used.
- The core should consist of at least four elements through its thickness. The sides of the core elements should be of equal lengths, forming a square in 2-D or cube in 3-D. If fewer elements are used through the core thickness, buckling modes might be missed and/or predictions will be erroneous.
- Elements with quadratic shape functions are preferred over elements with linear shape functions. Models with quadratic shape function elements simulate buckling modes with a high number of waves much better than models with linear shape function elements, even if the number of elements is fewer.

Note that in FE softwares (e.g. ANSYS), wrinkling loads are predicted by linear elastic buckling analysis since they do not differentiate between buckling and wrinkling in the eigen-value solution.

2.5. Web wrinkling

As explained in Sections 2.4.1 and 2.4.2, a large amount of information is available on the phenomenon of the skin wrinkling failures of sandwich panels loaded in uniaxial compression (Plantema 1966, Allen 1969, Ley et al. 1999) and biaxial compression–compression wrinkling (Fagerberg and Zenkert 2005-a, Birman and Bert 2004, Hadi and Matthews 2000, Vonach and Rammerstorfer 2000-a&b, Sullins et al. 1969). However, this knowledge is not directly applicable to web wrinkling, for which only a small amount of information is available. The thin webs of cell-core sandwich structures are relatively long panels that can be subjected to combined shear, normal, and bending loads, see Figure 1.2.

The fundamental failure mechanism of web wrinkling is similar to compressive skin wrinkling, a skin failure caused by an inability of the core to support a skin loaded in compression. Web wrinkling, however, is different since the pure compression loading case is complicated by the supplementary tensile stresses. As shown in Figure 1.2, in the case of web wrinkling, the laminate is not only subjected to uniaxial compression, but also to transverse

tension. The existing biaxial models presented in Section 2.4.2, except Hadi–Matthews's model, are based on the assumption that the face sheet is an infinite plate (compared to the short length of rectangular wrinkles) and thus the wrinkling load is independent of the boundary conditions and has an associated harmonic mode shape. This assumption is not always applicable to web wrinkling, as wrinkles might occur close to the corners of the rectangular webs where the maximum stresses appear due to combined shear and bending loading. In addition, the models assumed the wrinkling waves as being infinite sine waves with very short wavelength and therefore do not take into account the interaction effects of the transverse compression or tension stresses. This is a serious limitation if the models are to be applied in the prediction of web wrinkling. In fact, when the relative stiffness of the foam and the bending stiffness of the web are low, web wrinkling with a relatively long wavelength occurs. In this situation, the size of the wrinkles becomes comparable to the dimension of webs, and thus the contribution of transverse stresses as well as the effect of the boundary conditions can be very significant. The only model that does not have these limitations is the Hadi–Matthews's model; however, this model is an eigen-value solution that requires a huge calculation effort to predict wrinkling modes. In this context, little recent research has been devoted to web wrinkling in composite sandwiches.

An experimental study of the shear wrinkling of GFRP sandwich stiffener webs was performed by Lake et al. (2007). Modeling was attempted by modifying the common uniaxial wrinkling model (Hoff and Mautner 1945). The authors proposed a model in which the Young's modulus of the face sheet, E_f, in formulations such as Eqs. (2.15), (2.17), (2.20) and (2.23) are replaced by the shear modulus of the web. However, no satisfying result was obtained. Furthermore, the distribution of the stresses in the webs, i.e. the effect of transverse tension, could not be identified from the experiments.

An analytical investigation of the wrinkling of foam-filled web-core sandwich panels for the case of pure shear loading was performed by Briscoe et al. (2010). The web was modeled as a simply supported plate resting on a Pasternak elastic foundation under pure shear stresses. No experimental validation was performed and the interaction between the compression and transverse tension stress fields could not be captured. The applicability of the plate-buckling model to webs in cell-core sandwich beams under distributed load was demonstrated; nevertheless, the model was not accurate compared to finite element modeling. Part of the

inaccuracy results from the simple support assumption. Indeed, in cell-core sandwich structures, the face sheets provide substantial rotational resistances to the webs that depend on material properties and geometric parameters such as web spacing and face sheet thickness. Therefore, assuming simply supported boundary conditions for the web at the juncture of the web and face sheets may lead to considerably conservative results. Moreover, in a more realistic case, a web-core panel is subjected not only to shear stresses but also to in-plane bending stresses and the influence of the bending stresses can be significant when face sheet and web thicknesses are similar, which is commonly the case in cell-core sandwich structures and was also assumed by Briscoe et al. (2010).

2.6. Summary and justification of objectives

The detailed literature review shows that research on wrinkling failure in sandwich structures has concentrated on experimental, numerical and analytical studies of compressive wrinkling of isotropic face sheets under uniaxial compression loading and the presented models assume different functions for the decay of the transverse deformation in different types of core materials. The existing models are based on either the solution of the governing differential equations, or energy methods. Although the approaches are different they yield approximately the same result and the differences are mainly due to varying assumptions concerning the decay of the transverse core deformation.

Since the face sheet is assumed to be isotropic, these models always assumed that the wrinkling occurs perpendicular to the compression loads and that they could treat the problem as a unixial problem. However, for anisotropic face sheets, this is not the case. The wrinkling wave can be at an angle to compression loads and therefore the problem changes to a multiaxial problem even if the external compression load is uniaxial. Two general approaches are proposed for these cases. The first approach involves the results from the uniaxial compression wrinkling being extrapolated to biaxial cases. In the second approach, 3-D deflection functions are considered for describing the face sheet deformation as a plate under general conditions. Therefore, the governing differential equations and/or the energy derivations are derived and solved in general forms. Several models based on these two approaches were developed for the predication of biaxial compression-compression wrinkling of rectangular sandwich panels.

However, the validation of the proposed models is limited to FE modeling since experimental investigations simulating biaxial conditions require highly precise set-ups and test machines.

Although the fundamental mechanism of web wrinkling is similar to compressive skin wrinkling, they are different since the pure compression loading case is accompanied by complementary transverse tensile stresses. Most existing models assume that the wrinkling waves are infinite sine waves with very short wavelength and therefore they do not take into account the interaction effects of the transverse compression or tension stresses. Consequently, exploring the effect of transverse tension in the buckling or wrinkling behavior of structural components, e.g. thin-walled webs in FRP girders or cell-core sandwiches, requires experimental investigations of the biaxial buckling and wrinkling of GFRP plates and sandwich panels subjected to biaxial compression-tension loading (see Sections 3.2 and 3.3). Experiments can provide a comprehensive database for a better understanding of the interaction between the compression and transverse tension stress fields and aid the development of analytical models for the prediction of instability loads under biaxial stress fields.

Moreover, earlier models assumed the face sheet as being an infinite plate and thus their solutions for wrinkling loads are not independent of boundary conditions. This assumption is not applicable to web wrinkling, as wrinkles might occur close to the corners of the rectangular webs where the maximum stresses exist due to the combined shear and bending loading. The only model that does not make these assumptions is the Hadi–Matthews's model which is based on the general form of the eigen-value buckling solution. This model requires huge computational efforts for wrinkling load predictions however. Therefore, development of a new analytical model for simulation of the buckling and wrinkling behavior of orthotropic FRP plates and sandwich panels subjected to biaxial compression-tension in-plane loading is needed (see Section 4.3). The model should cover not only the buckling of plates but also the wrinkling of sandwich panels. This allows evaluation of the effects of the transverse tension on buckling and wrinkling in the biaxial compression-tension stress field (see Sections 4.3.5 and 4.3.6).

The literature review on the application of FRP composite sandwiches showed that cell-core sandwiches are increasingly used in civil engineering applications and have now entered into the domain of building construction (Keller et al. 2008) as a promising structural concept. Due to the strict stiffness requirements for civil applications, the initial web buckling is considered a

limiting failure mode in the design of cell-core sandwich structures. Therefore, the accurate prediction of web wrinkling, as one of the common failures in cell-core sandwiches, is crucial for developing optimum designs that meet all the strict requirements.

Little research has been recently devoted particularly to web wrinkling in composite sandwiches. An experimental study of the shear wrinkling of GFRP sandwich stiffener webs was performed by Lake et al. (2007). Modeling was attempted by modifying the common uniaxial wrinkling model, which was not successful. Another analytical investigation of the wrinkling of foam-filled web-core sandwich panels was performed by Briscoe et al. (2010). The model was not accurate compared to finite element modeling because of two important assumptions. Assuming simply supported boundary conditions for the web at the juncture of the web and face sheets might lead to considerably conservative results. The boundary condition of the web-core panels should be evaluated according to the interaction between the webs and face sheets in the presence of the core material (see Section 5.3). The second assumption was that the web core was only subjected to shear stresses while, in a more realistic case, a web-core panel is subjected not only to shear stresses but also to in-plane bending stresses. The influence of bending stresses can be significant in local instabilities and should be taken into account in the prediction of the wrinkling behavior of webs in cell-core sandwiches (see Sections 5.4 and 5.5).

3 Experimental investigation

3.1. Overview

This chapter is dedicated to the experimental investigations carried out for simulating the biaxial compression-tension wrinkling of GFRP sandwich panels. In a first step buckling of GFRP plates was considered (which may be seen as a special case of wrinkling – with a low number of waves) before the more complex wrinkling was studied. Details of the experimental set-up are given and the main results of experimental investigations are summarized. The influence of an increasing transverse tension load on the buckling and post-buckling and wrinkling behavior is investigated for plates and sandwich panels with different fiber architectures in order to also investigate the effect of different orthotropic stacking sequences. Experiments establish an appropriate database for better understanding of the interaction between the compression and transverse tension stress fields in buckling and wrinkling instabilities.

3.2. Biaxial buckling of GFRP plates

3.2.1. Introduction and objectives

The structural FRP composite components used in the civil engineering field are mainly girders and cellular slabs for bridge decks (Upadyay and Kalyanaraman 2003, Keller and Schollmayer 2004). In many cases, webs of open- or closed-girder cross sections are thin and therefore sensitive to shear buckling (Barbero and Raftoyiannis 1993). According to the rotated stress field theory, developed by Höglund (1997) for the shear buckling of steel and aluminum plate girders, substantial post-buckling strength can develop via a tension membrane stress field anchored in the surrounding flanges and/or transverse stiffeners. In a pure state of shear, the absolute values of

the principal membrane stresses σ_1 (tension) and σ_2 (compression) are identical as long as no buckling occurs. After web buckling, stresses are redistributed and tension stresses increase significantly, while compression stresses increase much less, as shown in Figure 3.1. Without web stiffeners, the inclination of the post-buckling stresses, ϕ, decreases with increasing shear strength to shear buckling stress ratio. Shear buckling thus can be considered as an in-plane biaxial compression-tension buckling problem. The diagonal compression stresses are crossed by transverse tension stresses which increase in the post-buckling stage.

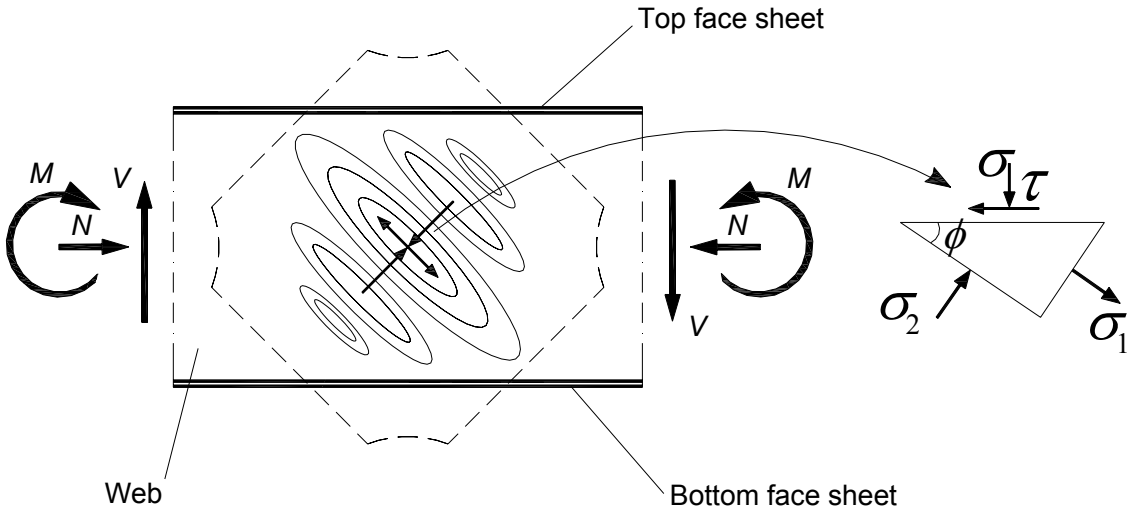

Figure 3.1. Stress state and buckling mode in girder webs (according to Höglund 1997), location of experimental specimens.

Although several analytical and numerical studies have been carried out on the buckling and post-buckling of flat composite panels subjected to general loading conditions (Leissa 1983, Reddy 1997, Ungbhakorn and Singhatanadgid 2006, Shufrin et al. 2008), few included experimental results and corresponding model validation. Moreover, despite the fact that composite structures are exposed to combined loading, most experimental studies are limited to uniaxial compressive loading. A few experimental studies regarding the buckling of flat composite panels under biaxial loading conditions (Singer et al. 2002) have been carried out, but most concern biaxial

compression-compression buckling (Romeo and Frulla 1994, Kim and Hoa 1995, Romeo and Frulla 1997, Romeo and Ferrero 2001).

Only one study was found that concerns the buckling behavior of composite panels subjected to in-plane biaxial compression-tension loading (Tuttle et al. 1999). The buckling responses of rectangular graphite-epoxy panels with three different aspect ratios and four stacking sequences subjected to several combinations of in-plane biaxial compression-tension loading were examined. The laminates were simply supported and the displacements were measured using dial gages and optically observed using the shadow moiré technique. The transverse tension load delayed the onset of buckling and the buckling mode shape depended on the aspect ratio. However, large discrepancies (±30% on average) between experimental and numerical results (obtained by the Galerkin solution) were reported, which were attributed to specimen imperfections, difficulties in achieving the simply supported boundary conditions, and/or non-uniform loading of the panels.

Extending the limited experimental database concerning FRP plates subjected to biaxial compression-tension buckling as well as developing a consistent technique for determining the buckling load are therefore crucial for the understanding and accurate modeling of shear buckling. In this part of Chapter 3, the results of an experimental investigation of the buckling and post-buckling behavior of GFRP plates subjected to in-plane biaxial compression-tension loading are presented. The determination of the buckling loads is based on the general form of the numerical fitting method proposed by Fok (1984). The influence of an increasing transverse tension load on the buckling and post-buckling behavior is investigated for plates with three different fiber architectures in order to also investigate the effect of different orthotropic stacking sequences.

3.2.2. Experimental program and set-up

GFRP plates of 350×350 mm^2 were prepared by hand lay-up and cured at 25°C for at least 30 days. Four layers of unidirectional E-glass fiber fabrics and polyester resin were used. Two types of plates were fabricated: the first type used unidirectional fabrics Tissa 851.0800.01 (0°: 800 g/m^2, from Tissa, Oberkulm, Switzerland) and the second Selcom UNIE1000 (0°: 960 g/m^2, 90°: 50 g/m^2, from Selcom Multiaxial Technology, Fregona, Italy). The same polyester resin (Nuvopol 80-06, from Walter Mäder AG, Killwangen, Switzerland) was used for both types of

specimens. Plates of the first type had a nominal thickness of 3.1 mm while that of the second type was 3.4 mm. Tensile experiments were performed on laminate strips according to ASTM D 3039/D 3039M-08; the main mechanical properties of both types are summarized in Table 3.1.

Table 3.1. Mechanical properties of glass-polyester laminates.

Laminates	Thickness [mm]	Fiber volume fraction [%]	Tensile E-Modulus [GPa]	Tensile strength [MPa]
Type 1	3.1	41.7	10.6±1.1	72.3±1.6
Type 2	3.4	43.8	20.5±0.3	344.8±11.0

Specimens with a stacking sequence of $[\pm 45]_S$ were cut from the plates of the first type by a CNC vertical mill in semi cruciform shape with an aspect ratio of 1, as shown in Figure 3.2(a). Specimens with the same dimensions, but stacking sequences of $[0/90]_S$ and $[90/0]_S$ were cut from the plates of the second type. To prevent interference from biaxial grip motions during loading and smoothen load introduction the corners were truncated. Nine linear strain gages, (1)-(9), were applied along the specimen axes to record the in-plane strains (see Figure 3.2(a)). Gages (1)-(5) and (7)-(9) were located on one side while gage (6) was on the opposite side of the specimen. For the plates with stacking sequence of $[\pm 45]_S$, four strain gages, (10)-(13), were added on the plate diagonals. The out-of-plane displacement was recorded using an LVDT transducer located on the rear side of the specimens at the center point (see Figure 3.2(a)).

An Instron planar biaxial cruciform testing system of 63-kN capacity in the direction of both axes was used, (see Figure 3.3(a)). Each edge of the plates was fully clamped in the steel grips using four bolts (see Figures 3.2(b) and 3.3(b)), which were prestressed by a torque of 29 Nm to transfer load by friction. Compression and tension loads were applied horizontally and vertically, respectively, see Figure 3.4. The resulting set-up corresponded to the loading and boundary conditions in a girder web, as shown in Figure 3.1, under the following preconditions, which were assumed to be fulfilled: 1) pre-buckling stage: the web is fully clamped, 2) post-buckling stage (according to Höglund 1997): a) the tension stress field is anchored in the flanges (no stiffeners), b) flanges and surrounding webs are rigid, c) the bending moment is smaller than the

moment capacity of the flanges (to enable anchoring of the tension stress field), and d) material orthotropy does not fundamentally change the rotated stress field theory.

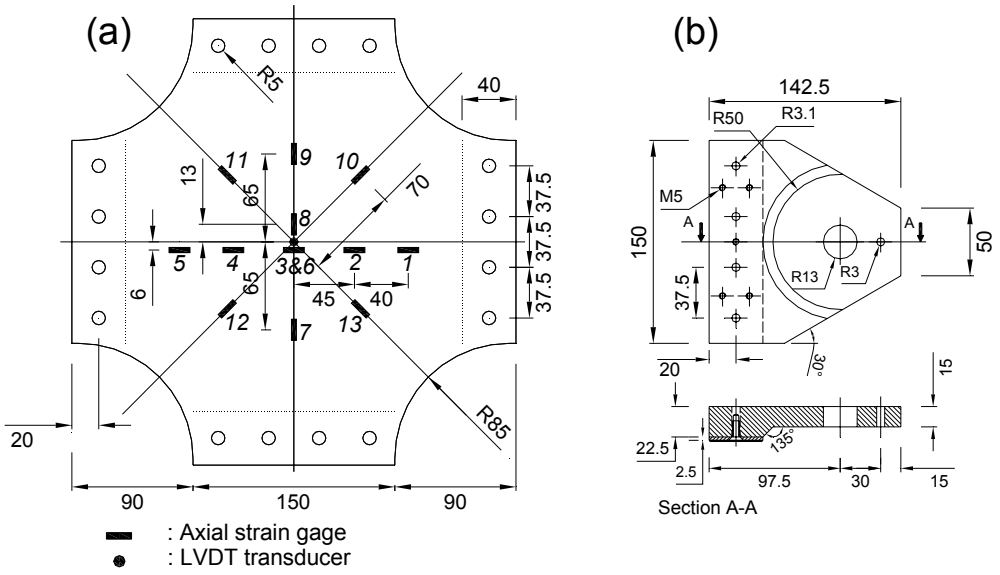

Figure 3.2. (a) Specimen geometry in [mm] and instrumentation; (b) grip configuration and dimensions.

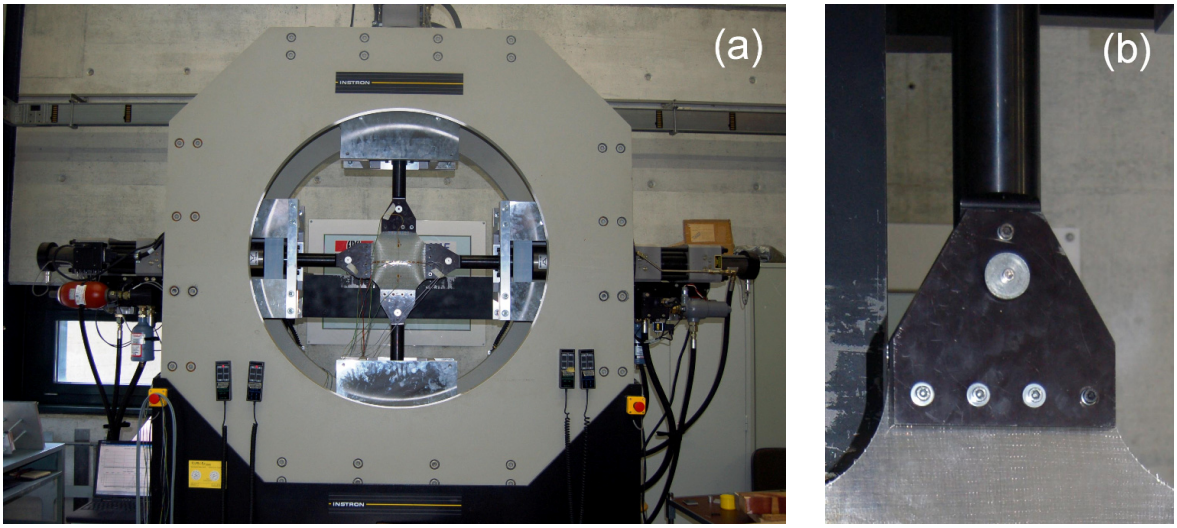

Figure 3.3. Instron planar biaxial cruciform testing systems: (a) test set-up; (b) detail of gripping system.

To simulate the post-buckling stage, the tension load was first applied at a loading rate of 0.3 kN/s and then kept constant throughout the test. Compression was then applied in displacement control at a rate of 0.017 mm/s up to specimen failure. Thanks to this loading method, a tension-dependent buckling and failure criterion could be obtained, wherein the tension-to-compression load or stress ratio is correlated to the angle, ϕ, shown in Figure 3.1. This angle changes as follows: in the pre-buckling stage, $\phi = 45°$ represents pure shear loading, V, while $\phi \neq 45°$ represents combined shear plus normal and bending stresses (either tension or compression) due to normal force, N, and/or bending moments M. In the post-buckling stage, ϕ changes further due to the redistribution of stresses. Tension loads were selected in 5-kN steps from 0 to 30 kN for $[0/90]_S$ and $[90/0]_S$ panels and up to 25 kN for $[\pm45]_S$. A minimum of two specimens were tested for $[0/90]_S$ laminates at each load level while only one specimen was used for $[90/0]_S$ and $[\pm45]_S$.

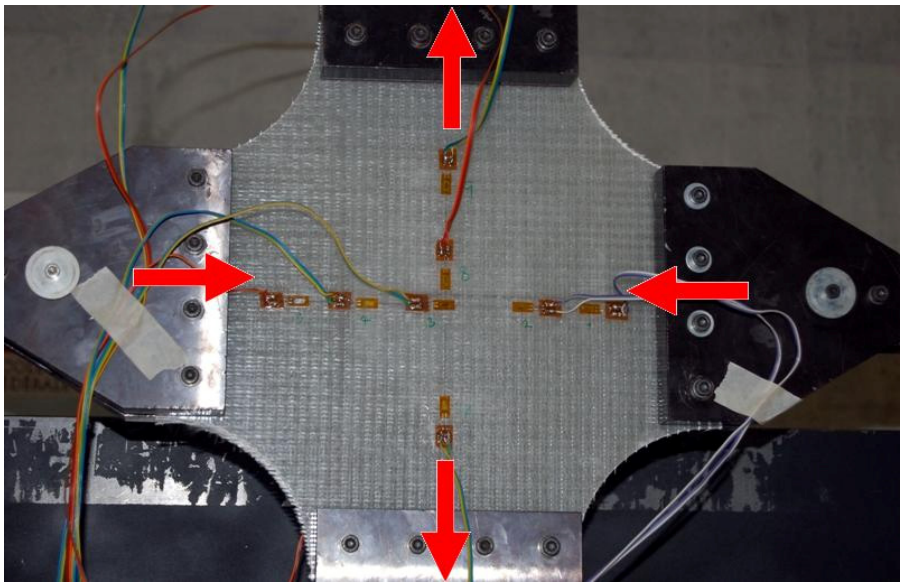

Figure 3.4. Biaxial compression-tension loading set-up for buckling GFRP plates.

Two specimens (one with $[0/90]_S$ and one with $[\pm45]_S$ stacking sequence, designated SCT) were loaded differently to compare and confirm the obtained results: both compression and tension loads were increased simultaneously, i.e. by alternating small steps of 0.5 kN in force control mode at a rate of 0.125 kN/s. For the $[\pm45]_S$ specimen, the tension load was kept constant

immediately after buckling (at 10 kN) and only compression was increased up to failure, while for the $[0/90]_S$ specimen, the tension and compression loads were simultaneously increased up to failure.

3.2.3. Experimental results

3.2.3.1. $[0/90]_S$ specimens

At low tension load, an almost half-sine wave buckling mode shape was observed for all $[0/90]_S$ plates, as shown in Figure 3.5. By increasing the tension load (as from 15 kN), in addition to the half-sine wave at the center, two small half-sine waves developed, one on either side, close to the grips. Typical strain responses at a tension load of 15 kN are presented in Figure 3.6 (plate 1 in Table 3.2). Gages (1) to (6) showed symmetric responses in accordance with the observed mode shape. Gages (3) and (6), on opposite sides, had the same compressive behavior up to the onset of buckling. Subsequently gage (3) changed to tension, while gage (6) continued measuring compressive strains. Gages (1) and (5) recorded compression due to the clamped edges. Gages (7)-(9) showed the prestressing effect induced by the tension load (at 0-kN compression) and later followed the trend of gages (2)-(4) according to the mode shape.

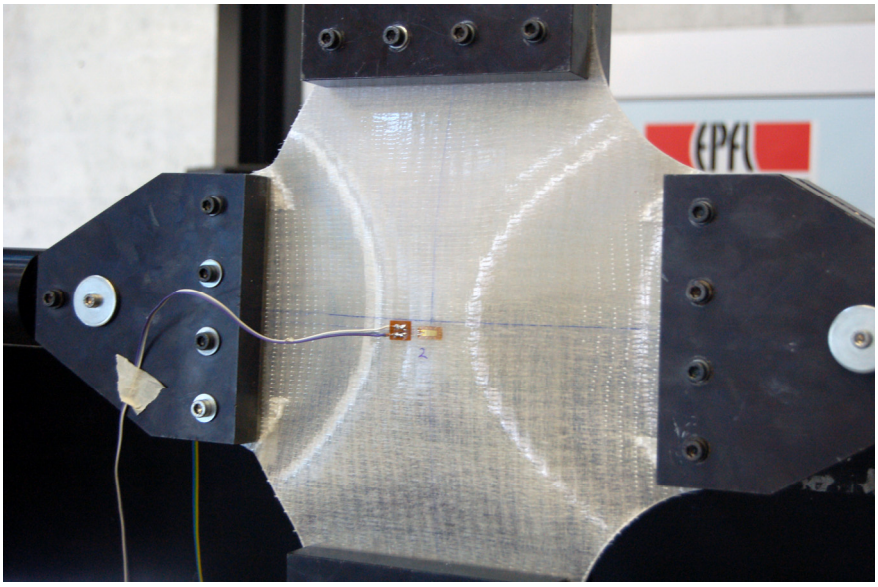

Figure 3.5. Buckling mode shape of $[0/90]_S$ specimens.

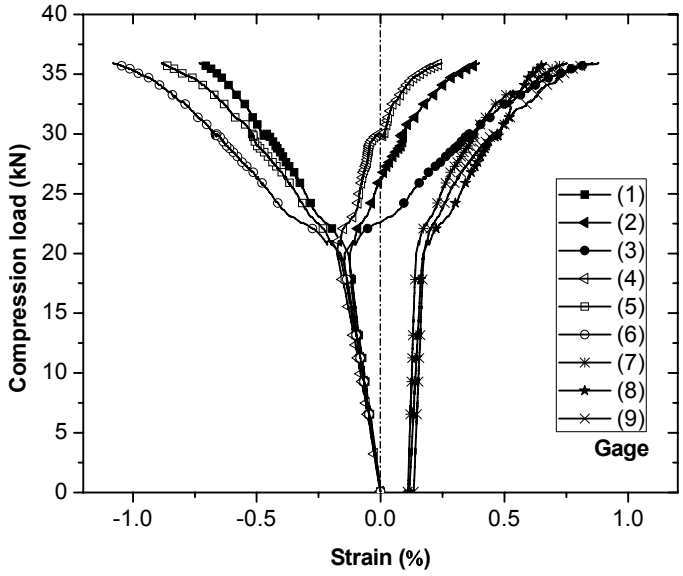

Figure 3.6. Compression load vs. strain responses of $[0/90]_S$ specimen at 15-kN tensile load.

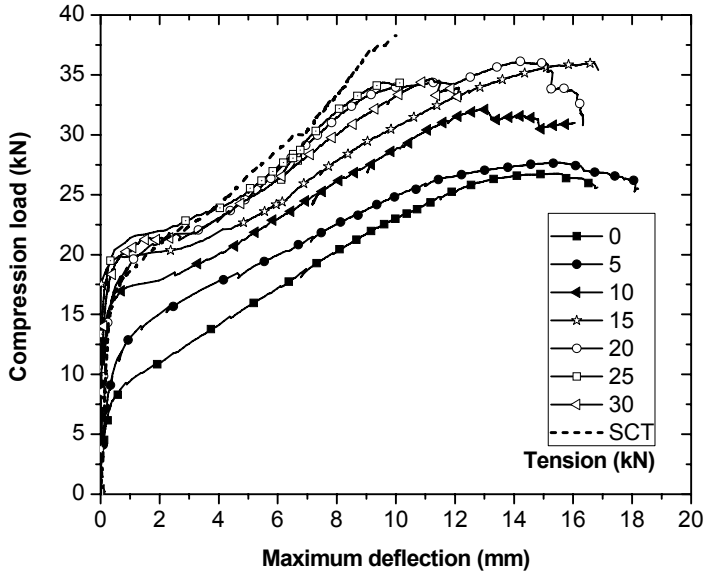

Figure 3.7. Compression load vs. maximum out-of-plane displacement responses of $[0/90]_S$ specimen at different tension loads.

The tension load level had no influence on the failure mode. For each specimen, at approximately 85% of the ultimate load, layer debonding, accompanied by matrix cracking and fiber crushing on the compressed panel side, started at the clamp edges where the compression load was applied,

as shown in Figure 3.8(a). This failure mode propagated diagonally with increasing load to the middle of the plate until the ultimate load was reached, see Figure 3.8(b).

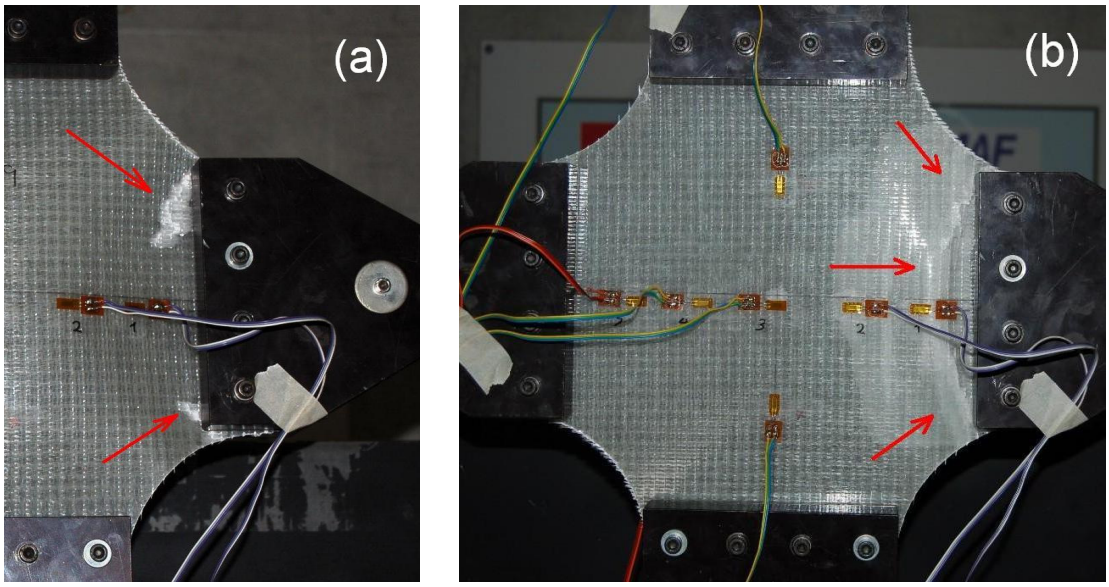

Figure 3.8. Failure mode of $[0/90]_S$ specimens: (a) debonding and fiber crushing initiation; (b) fully developed failure mode.

3.2.3.2. $[90/0]_S$ specimens

Two different buckling mode shapes were observed for the $[90/0]_S$ laminates. A half-sine wave buckling mode was recorded at 0-kN tensile load, similar to that shown in Figure 3.5. When tension loads were applied, the mode shape changed to a full-sine wave, as shown in Figure 3.9. Strain responses were again in accordance with the observed mode shape, as shown in Figure 3.10 for 20-kN tension load. Gages (2) and (4), located on the upper and lower apexes of the buckling mode shape, started recording tension and compression strains, respectively. The symmetry of the buckling mode shape was confirmed by the symmetric strain responses of gages (1)-(3) and gages (4)-(6).

Since the buckling mode was a full-sine wave, the LVDT transducer did not record any significant out-of-plane deflection at the midpoint, see experimental results presented in Section B.1.2 of Appendix B. The effect of transverse tension on the buckling load is therefore demonstrated by the gage (2) responses, see Figure 3.11. The reversal point of the strain curves, which is normally associated with the buckling load, moved upwards and the ultimate

compression load increased significantly when higher tension loads were applied. The failure mode was similar to that of the $[0/90]_S$ plates: layer debonding together with matrix cracking and fiber crushing. The debonding at the clamp edges of the specimens with tensile load, however, was more pronounced due to the much larger curvature caused by the full-sine wave, as shown in Figure 3.12.

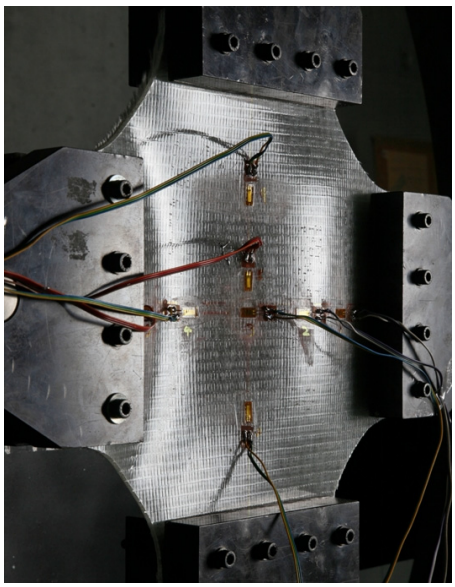

Figure 3.9. Buckling mode shape of $[90/0]_S$ specimens.

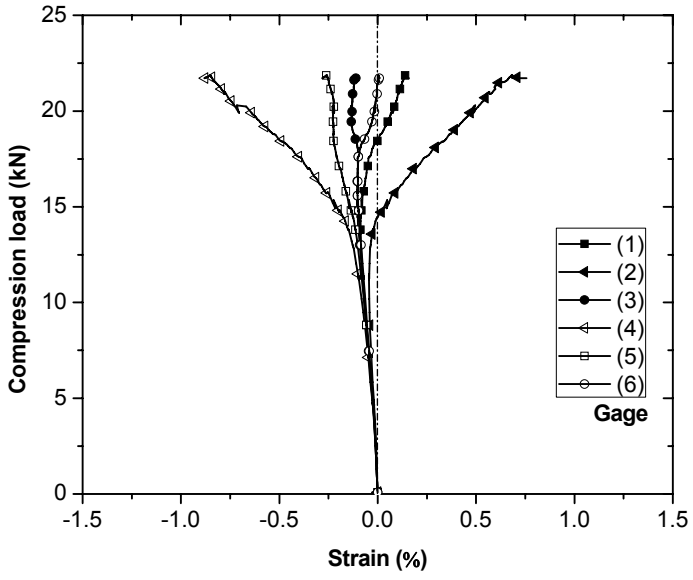

Figure 3.10. Compression load vs. strain responses of $[90/0]_S$ specimen at 20-kN tensile load.

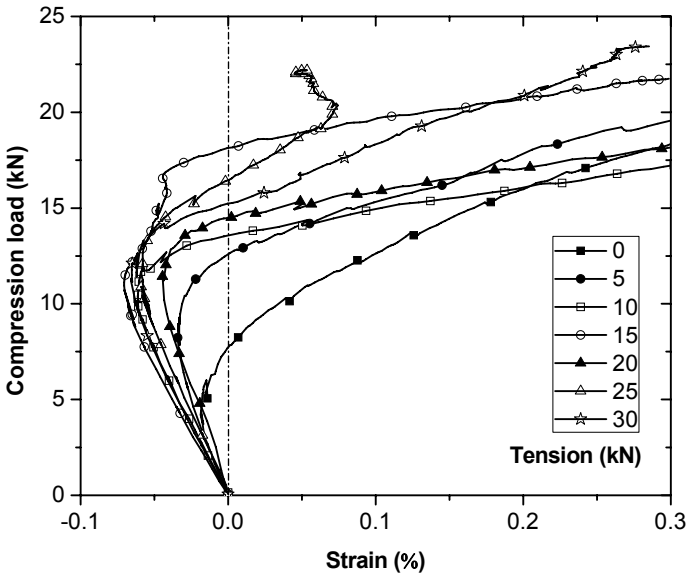

Figure 3.11. Comparison of gage (2) load-strain responses of $[90/0]_S$ panels at different tension loads.

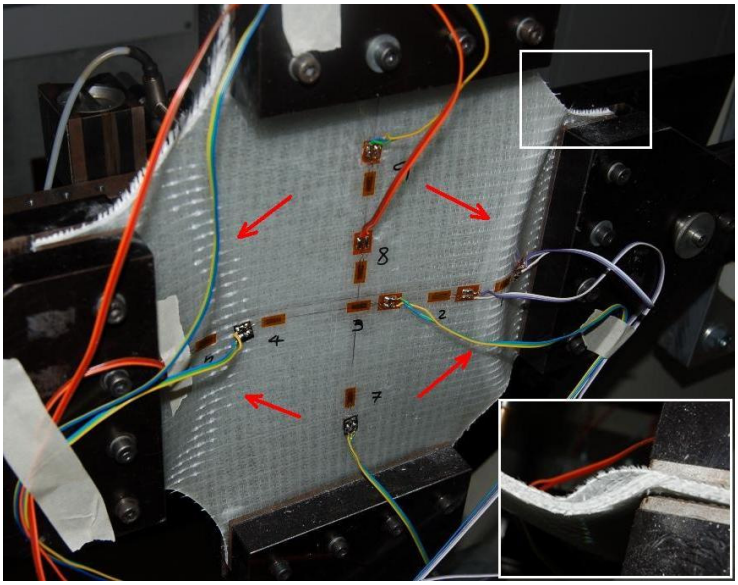

Figure 3.12. Failure mode of $[90/0]_S$ specimens.

3.2.3.3. $[\pm 45]_S$ specimens

All $[\pm 45]_S$ specimens exhibited a full-sine wave mode shape, which was not perpendicular to the compression loading axis however, but inclined at approximately 22.5° (half of the 45° fiber directions) relative to the tension loading axis, as shown in Figure 3.13. The shapes of the strain

responses of gages (1)-(6) were similar to those of the $[90/0]_S$ specimens (shown in Figure 3.10) and basically confirmed the full-sine wave mode. The inclination of the wave axis was traced by the lower strain values of gages (10) and (12) compared to the values of the symmetrically located gages (11) and (13), as shown in Figure 3.14.

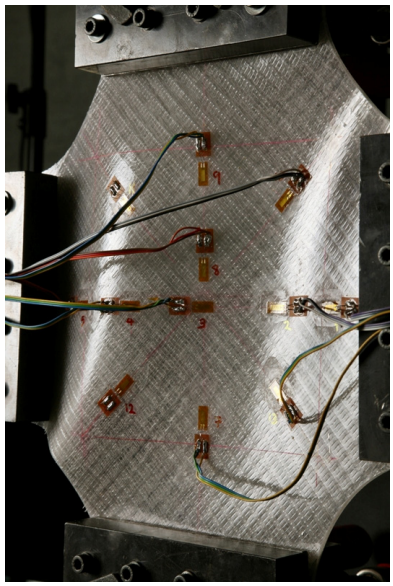

Figure 3.13. Buckling mode shape of $[\pm 45]_S$ specimens.

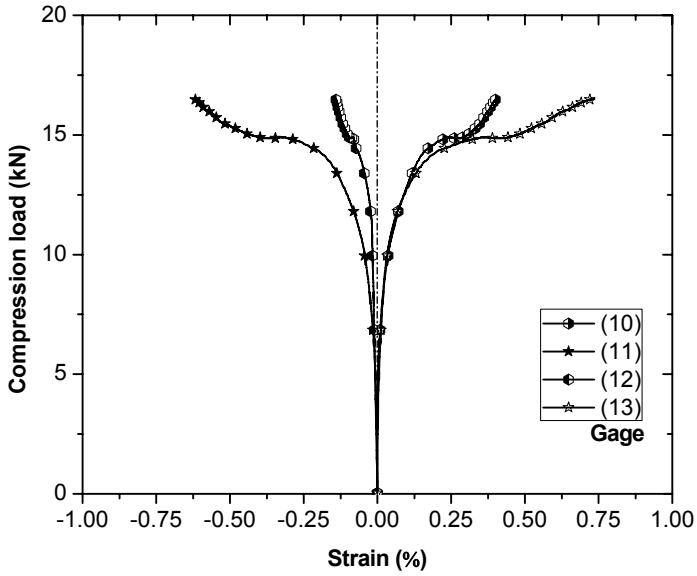

Figure 3.14. Compression load vs. strain responses of $[\pm 45]_S$ specimen at 5-kN tensile load.

Figure 3.15 shows the gage (2) responses at different tension loads and of the simultaneously loaded SCT specimen. Similar to the $[90/0]_S$ results (shown in Figure 3.11), the reversal point of the strain curves was shifted upwards and ultimate loads were increased by increasing the tension load. Failure initiation and propagation were similar to those of the other specimen types. Fiber crushing, however, was not observed; only debonding and matrix cracking occurred, which started from the clamp edges and then spread over the whole clamp width, as shown in Figure 3.16.

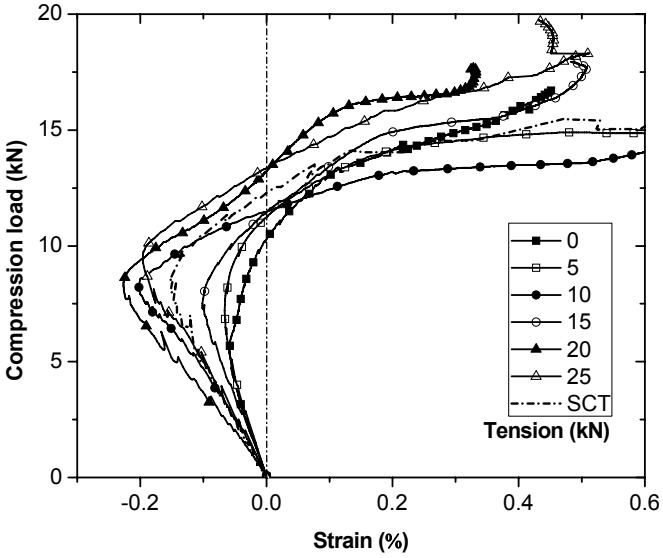

Figure 3.15. Comparison of gage (2) load-strain responses of $[\pm 45]_S$ specimens at different tension loads.

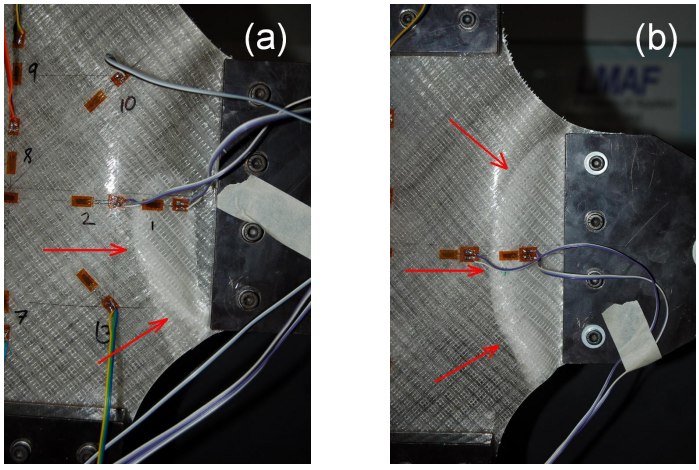

Figure 3.16. Failure mode of $[\pm 45]_S$ specimens: (a) debonding initiation; (b) fully developed failure mode.

3.2.4. Determination of buckling load

It is well known that determining the buckling load from measurements is difficult, since initial imperfections in specimen geometry and/or test conditions may merge the pre-buckling stage of the load-deflection curve with the post-buckling stage into one continuously increasing path, often making it impossible to obtain a clear bifurcation point. A number of simple and direct graphical derivation techniques have been proposed to estimate the buckling load, which are based on the axial load vs. out-of-plane mid-plate deflection curve or the axial load vs. axial strain curve, e.g. the "top-of-the-knee" and "strain-reversal" method (Singer et al. 1998). The accuracy of these techniques is limited in many cases however since it is actually difficult to avoid biased decisions when determining a linear portion of the post buckling stage in the case of biaxial plate buckling.

In addition to these direct methods, numerical indirect methods to determine the buckling load were developed, one of the most prominent being the Southwell plot method. This method was established for columns and was later used for plates (Timoshenko and Gere 1963, Singer et al. 1998). However, the stable nonlinear post-buckling response of plates is different from that of columns, which have a neutral post-buckling path, and this may lead to overestimation of the buckling loads (Spencer and Walker 1975). To overcome this problem, an energy method, known as the "modified Southwell for plates" or "Donnell method" was developed (Donnell 1938) and applied in a modified form in Abramovich (1990). Furthermore, Spencer & Walker (1975) proposed the so-called "Pivotal Plot" technique, which corrects the inherent zero error in the deflection by means of the pivot point. A general numerical approach by Fok (1984) uses the relationship between load, P, and total out-of-plane displacement, W_T, defined as the summation of initial imperfection, $W_\circ$, and measured maximum deflection, W, $W_T = W_\circ + W$ (according to Dawson and Walker 1972), for a plate which is in the post-buckling stage:

$$(W_T^2 - W_\circ^2)^{1/2} = B_1 \Psi + B_2 \Psi^3 \tag{3.1}$$

where $\Psi \equiv (P / P_{cr} - 1 + W_\circ / W_T)^{1/2}$. B_1 and B_2 are constants, dependent on the boundary conditions and plate geometry and P_{cr} denotes the buckling (critical) load. There are two approaches to solve Eq. (3.1). The first one supposes that parameter B_2 is one order of magnitude

smaller than B_1 and consequently the second term of Eq. (3.1) can be ignored. The simplification is acceptable when the specimen is loaded well into the post-buckling range and the initial imperfection not significant (Fok 1984). Solving the simplified form of Eq. (3.1) leads to Eq. (3.2) as follows:

$$P = P_{cr}\left(\frac{W}{W + W_\circ}\right) + \frac{P_{cr}}{{B_1}^2}(W^2 + 2WW_\circ) \tag{3.2}$$

which is identical to the modified Southwell method (Donnell 1938). The solution is reached through a non-linear least square fitting of Eq. (3.2) to the load vs. out-of-plane deflection experimental data with respect to $W_\circ$, P_{cr}, and B_1.

The second approach is to solve the general form of Eq. (3.1), which leads to:

$$P = P_{cr}\left(\frac{W}{W + W_\circ}\right) + P_{cr}\left(\frac{\varsigma}{6B_2} - \frac{2B_1}{\varsigma}\right)^2 \tag{3.3}$$

with

$$\varsigma = \left(\left(108\sqrt{W(W + 2W_\circ)} + 20.78\delta\right){B_2}^2\right)^{1/3} \tag{3.4-a}$$

and

$$\delta = \sqrt{\frac{4{B_1}^3}{B_2} + 27(W^2 + 2WW_\circ)} \tag{3.4-b}$$

Again, fitting Eq. (3.3) to the experimental data results in the specific values for $W_\circ$, P_{cr} and the two constants B_1 and B_2.

3.2.5. Modeling results and discussion

3.2.5.1. Buckling load determination

The numerical approach introduced by Fok (1984) was applied in its simplified form (Eq. (3.2)) and Eqs. (3.3)-(3.4) were derived from the general form in order to model the experimental results of the $[0/90]_S$ specimens shown in Figure 3.7. The initial imperfections, W_0, buckling load, P_{cr}, and the constants, B_1 and B_2, obtained from the fitting of Eqs. (3.2) and (3.3) to the

experimental results, are given in Table 3.2. For low tension loads (0 kN and 5 kN), significant differences in the resulting imperfections and corresponding buckling loads were obtained. Assuming parameter B_2 as being equal to zero led to an overestimation of both values, as shown in Figure 3.17 for the buckling load at 5-kN tension. The general solution, however, was accurate, particularly in the early post-buckling stage. The differences were reduced with increasing tension: both methods provided almost identical results at 30-kN tension, which compared perfectly to the experimental results, see Figure 3.18. The high-tension loads reduced the initial imperfections and thus increased the accuracy of the simplified method. Figure 3.19 demonstrates this effect of the tension load on the initial imperfections. The imperfections decreased with increasing tension load. At low tension, however, the imperfections are largely overestimated by the simplified method. Table 3.2 also shows the SCT results. Since buckling occurred at high tension loads (see Figure 3.7), the values of both methods are almost identical.

Table 3.2. Experimental and modeling results of $[0/90]_S$ specimens at different tension loads.

Tension load (kN)	Specimen No.	Simplified model – Eq. (3.2)			General model – Eq. (3.3)				Ultimate load (kN)
		W_0 (mm)	P_{cr} (kN)	B_1	W_0 (mm)	P_{cr} (kN)	B_1	B_2	
0	1	0.405	14.9	14.1	0.118	9.7	3.8	2.9	26.8
	2	0.544	17.9	15.9	0.122	10.5	2.8	3.2	29.8
5	1	0.427	20.1	22.1	0.168	13.2	2.3	8.6	27.7
	2	0.514	20.2	19.1	0.239	14.6	4.7	6.7	29.8
10	1	0.072	20.0	15.6	0.058	18.1	8.5	5.3	32.1
	2	0.078	18.9	15.2	0.061	17.1	7.6	5.5	32.1
15	1	0.013	20.5	9.5	0.010	19.2	2.9	11.4	35.9
	2	0.006	21.1	15.5	0.003	19.9	9.9	4.1	36.0
20	1	0.114	21.4	11.8	0.109	20.9	9.0	2.3	36.1
	2	0.201	21.7	13.2	0.163	20.1	7.7	4.8	33.1
25	1	0.018	21.3	11.6	0.017	20.8	8.7	2.4	34.4
	2	0.049	20.5	11.8	0.054	21.2	10.3	0.5	33.9
30	1	0.022	21.4	13.9	0.017	21.3	8.9	2.3	34.9
	2	0.115	21.0	11.2	0.115	21.0	9.0	1.6	33.6
	3	0.034	21.1	13.0	0.029	20.5	8.3	4.9	34.7
SCT	1	0.247	22.5	11.9	0.234	21.8	10.3	0.8	38.3

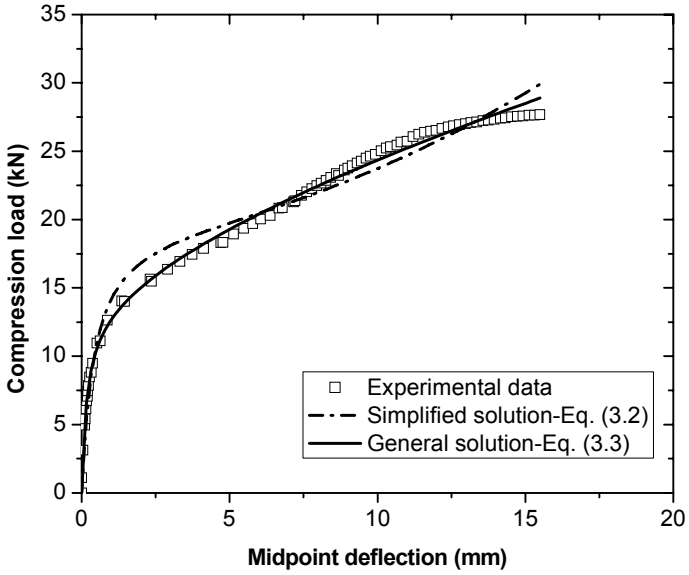

Figure 3.17. Comparison of load-deflection responses of $[0/90]_S$ specimen at 5-kN tensile load and fitting curves obtained from Eqs. (3.2) and (3.3).

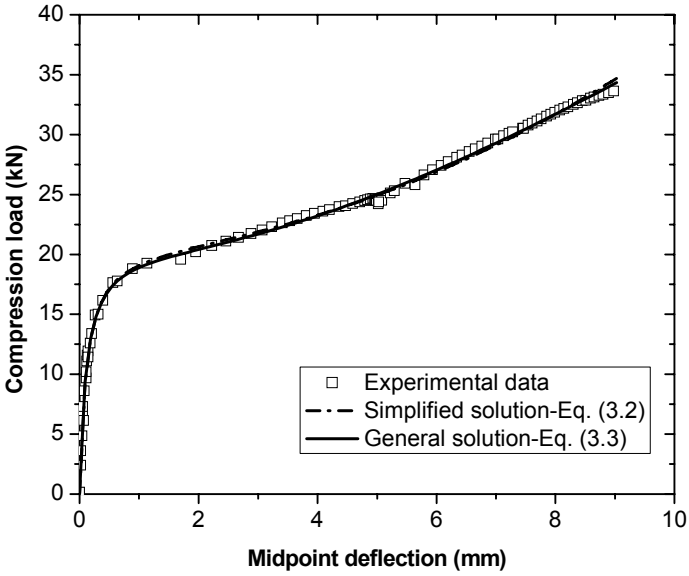

Figure 3.18. Comparison of load-deflection responses of $[0/90]_S$ specimen at 30-kN tensile load and fitting curves obtained from Eqs. (3.2) and (3.3).

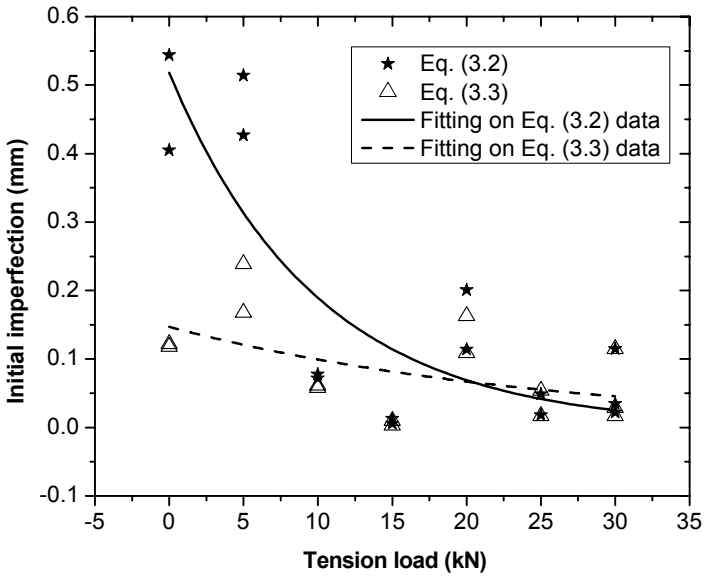

Figure 3.19. Initial imperfections obtained from Eqs. (3.2) and (3.3) vs. tension load.

Fok's numerical techniques were not applicable for $[90/0]_S$ and $[\pm 45]_S$ specimens as midpoint out-of-plane deflections were almost zero due to the full-sine wave mode shape. Hence, the strain reversal method (Singer et al. 1998) was used for determining the buckling loads. The method defines the buckling load as the load at which the maximum compression strain on the convex side of the buckling crest stops increasing and begins to decrease. The buckling loads were determined accordingly from Figures 3.11 and 3.15. Table 3.3 gives the resulting buckling and ultimate loads for $[90/0]_S$ and $[\pm 45]_S$ specimens at the different tension loads as well as for the SCT loading case.

Table 3.3. Buckling and ultimate loads of $[90/0]_S$ and $[\pm 45]_S$ specimens at different tension loads.

Tension load (kN)	$[90/0]_S$ specimen		$[\pm 45]_S$ specimen	
	Buckling load (kN)	Ultimate load (kN)	Buckling load (kN)	Ultimate load (kN)
0	4.5	20.5	5.5	16.7
5	8.0	21.7	7.3	16.6
10	10.3	20.9	8.2	15.5
15	11.0	21.7	8.0	17.9
20	11.5	21.9	8.4	17.7
25	12.2	22.2	9.5	19.8
30	12.2	23.4	-	-
SCT	-	-	8.0	16.5

3.2.5.2. Effect of transverse tension on buckling and post-buckling behavior

The resulting buckling loads as a function of the transverse tension loads are shown in Figure 3.20. Fitting curves were added to the experimental results. The buckling loads increased at lower tension loads and approached a plateau at higher tension loads. An average increase of 107% was observed for the $[0/90]_S$ specimens, 171% for the $[90/0]_S$ and 73% for the $[\pm45]_S$ specimens. Also shown in Figure 3.20 are the loading paths and buckling loads of the SCT specimens, the latter fitting well to the results.

The positive effect of the increasing transverse tension load on the ultimate compression loads was less pronounced in all three cases, see Figure 3.21. Nevertheless, the maximum increase in ultimate compression loads was 22% for $[0/90]_S$, 15% for $[90/0]_S$ and 18% for $[\pm45]_S$ specimens. Figure 3.21 also shows the loading paths of the SCT specimens. The ultimate loads again fit well to the results. The increase of both buckling and ultimate loads confirmed the significant stabilizing effect provided by the increasing transverse tension load.

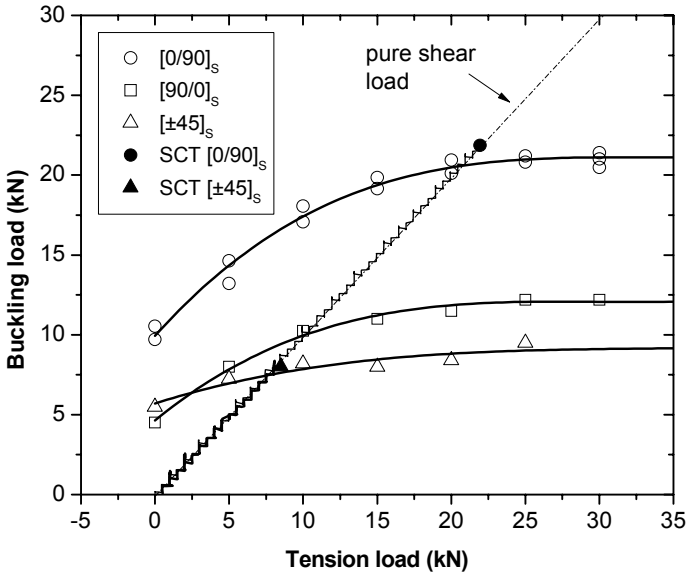

Figure 3.20. Buckling load vs. transverse tension load.

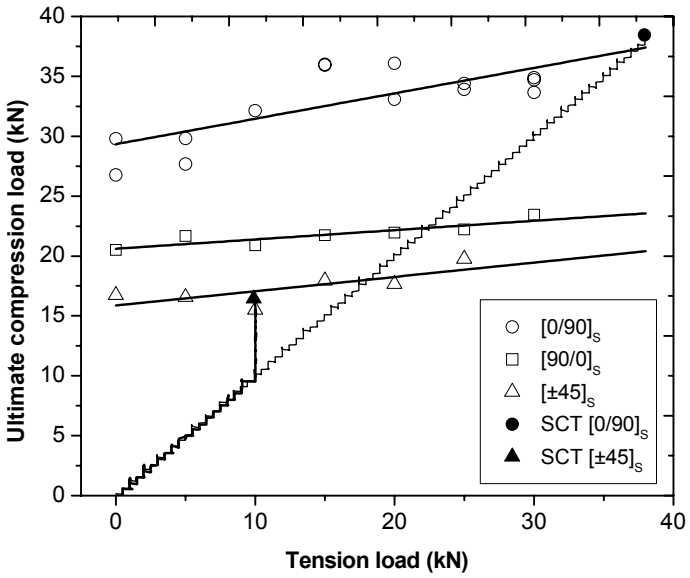

Figure 3.21. Ultimate compression load vs. transverse tension load.

3.2.5.3. Effects of fiber architecture on buckling and post-buckling behavior

Figures 3.20 and 3.21 demonstrate that the stacking sequence had a significant effect on the results. In the $[0/90]_S$ configuration, the fibers parallel to the compression axis were on the outer side in the cross section. Consequently, the bending stiffness along the compression axis was much higher in the $[0/90]_S$ configuration than in the $[90/0]_S$ and $[\pm45]_S$ configurations, which explains the much higher buckling and ultimate compression loads of this configuration.

Similar effects of the fiber architecture were observed on the buckling mode shape. The $[90/0]_S$ configuration had the highest bending stiffness in the tension direction. Furthermore applying stabilizing tension loads prevented out-of-plane deformations of the tension axis and changed the buckling mode from a half-sine wave (at zero tension) to a full-sine wave.

3.2.6. Concluding remarks

An extensive experimental study was performed on the biaxial compression-tension buckling behavior of symmetric GFRP plates with different stacking sequences. This biaxial loading simulates the shear loading in webs of plate girders. The following conclusions were drawn:

1) An increasing transverse tension load significantly increased the buckling loads (73-171%) and ultimate loads (15-22%). The transverse tension decreased the initial

imperfections and thus delayed the onset of buckling. The beneficial effects were significant up to the pure shear load (equal compression and tension) and then leveled off at tension loads higher than compression loads (combined shear and tension loading). The increasing post-buckling tension stresses further increased the ultimate loads.

2) The fiber architecture, i.e. stacking sequence, greatly influenced buckling and post-buckling behavior. Higher bending stiffness in the compression direction increased the buckling and ultimate loads, while higher bending stiffness in the tension direction changed the buckling mode shape.

3) The general solution of the Fok model was able to accurately model the experimental results while the simplified solution (modified Southwell method) provided accurate results only at higher tension loads, i.e. for cases of small imperfections.

3.3. Biaxial wrinkling of GFRP sandwiches

3.3.1. Introduction and objectives

As shown in Figure 3.1, in the case of web wrinkling which is a local buckling failure in the sandwich webs due to shear, normal and bending loads, the laminate is not only subjected to uniaxial compression (σ_1), but also to transverse tension (σ_2), similar to the shear buckling of plate girders (Höglund 1997), described in Section 3.2.1. Shear wrinkling can thus be considered as an in-plane biaxial compression-tension wrinkling problem and consists of interaction between the compression and transverse tension stress fields. Based on this approach, this study aims to establish a comprehensive experimental database concerning GFRP-foam sandwiches subjected to in-plane biaxial compression-tension wrinkling. The influence of an increasing transverse tension load on the wrinkling load is investigated for sandwich panels with two different fiber architectures in order to also investigate the effect of different orthotropic stacking sequences. The experimental results are compared with linear and nonlinear finite element analyses performed according to Euler and large displacement theories.

3.3.2. Experimental program and set-up

GFRP sandwich panels of 400×400-mm^2 length and width consisted of one thin face sheet corresponding to the web of the cell-core sandwich structure, stabilized by a 60-mm thick polyurethane (PU) foam. The face sheet of 1.1-mm thickness consisted of two almost unidirectional stitched E-glass fabrics (0°: 370 g/m^2, 90°: 20 g/m^2, from Tissa, Oberkulm, Switzerland) and polyester resin (Nuvopol 80-06, from Walter Mäder AG, Killwangen, Switzerland). In order to simulate an infinite core thickness, the foam thickness was estimated according to Ley et al. (1999):

$$\left(\frac{t_f}{t_c}\right)\left(\frac{E_f}{E_c}\right)^{1/3} < 0.2 \tag{3.5}$$

where E_c and E_f are the elastic modulus of foam and face sheets (given in Table 3.4), and t_c and t_f are the thicknesses of the foam and face sheets, respectively. The PU core had a density of 60 kg/m^3. The panels were prepared by hand lay-up and cured at 25°C for at least 30 days.

Table 3.4. Mechanical properties of sandwich components.

Properties	PU-60*	UD GFRP laminates
Longitudinal elastic modulus (MPa)	17.5	25700±689
Transverse elastic modulus (MPa)	17.5	4775±221
Shear modulus (MPa)	6.5	2250±173
Longitudinal tensile strength (MPa)	0.45	497.5±34.4
Transverse tensile strength (MPa)	0.45	24.5±1.9
Shear strength (MPa)	0.25	20.1±0.8

* Values according to Keller et al. (2008)

The tensile strength and elastic modulus of the GFRP laminates were determined according to ASTM D 3039/D 3039M-08. The shear strength and modulus were obtained from 45° off-axis tensile tests according to Dickson et al. (1995) and Ganesh and Naik (1997). Specimens were cut from four-layer-laminates of 2-mm thickness in the longitudinal (0°), and off-axes (90°) and (45°) directions. An MTS clip gage (model: 634.11F-25) with 25-mm gage length was used to measure

specimen deformations; one biaxial strain gage was used for off-axis (45°) tests. Fiber failure occurred for 0° and matrix failure for 90° and 45° specimens. The main mechanical properties of the sandwich components are summarized in Table 3.4.

Sandwich specimens with asymmetric stacking sequences of [90/0] (i.e.: foam - 90° in tension - 0° in compression) and [±45] were cut from the sandwich panels by a CNC vertical mill in semi-cruciform shape with an aspect ratio of 1, as shown in Figure 3.22. The corners were truncated in order to prevent the interference of grip motions during loading and to smoothen load introduction. To clamp the laminates into the steel grips, the foam was removed at the edges. A supporting frame, consisting of a 1.5-mm thick GFRP laminate, was bonded onto each specimen to avoid grip failure and force the wrinkling failure to occur in the part subjected to the transverse tension load, see Figures 3.22 and 3.23. In addition, an aluminum plate was placed behind the foam to prevent the out-of-plane displacement of the specimen. To prevent friction, the contact surface between the aluminum plate and the foam was covered with a rubbery Teflon tape. The same Instron planar biaxial cruciform testing system, as shown in Figure 3.3(a)-Section 3.2.2, with four advanced 63-kN servo-hydraulic actuators mounted in-plane and perpendicular to each other was used. Compression and tension loads were applied horizontally and vertically, respectively.

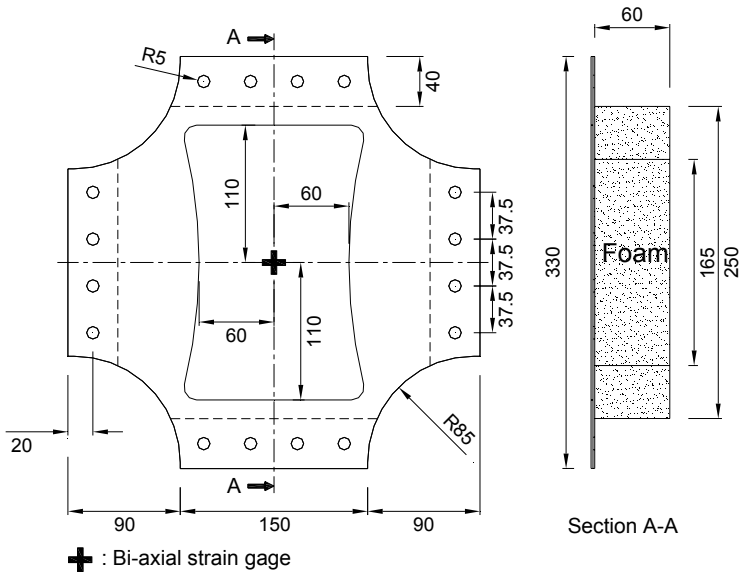

Figure 3.22. Specimen geometry in [mm] and instrumentation.

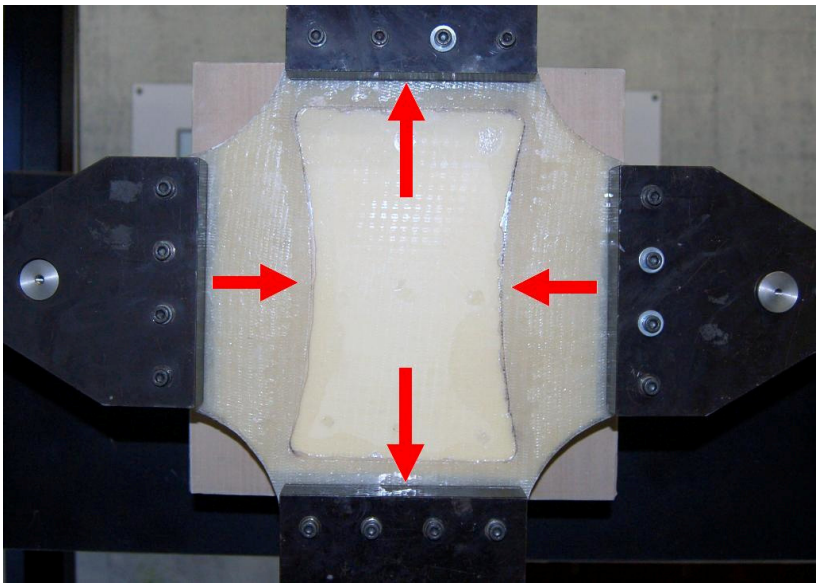

Figure 3.23. Biaxial compression-tension loading set-up for wrinkling of GFRP sandwiches.

Each edge was fully clamped in the steel grips using four bolts (see Figure 3.24), which were prestressed by a torque of 29 Nm to transfer load by friction. The resulting set-up corresponded to the loading and boundary conditions in a sandwich web, as shown in Figure 3.1, under the following preconditions based on the rotated stress field theory developed by Höglund (1997), which were assumed to be fulfilled: 1) the web is a thin-walled plate with insignificant bending stiffness, 2) the top and bottom face sheets (flanges), supported by the core, are sufficiently rigid to provide high rotation resistance, and 3) either the webs are supported by rigid transverse stiffeners or webs as is the case in cell-core sandwiches.

The tension load was first applied at a loading rate of 0.25 kN/s and then kept constant throughout the test. Compression was then applied in displacement control at a rate of 0.017 mm/s up to specimen failure. Thanks to this loading method, a tension-dependent wrinkling failure criterion could be obtained, in which the tension-to-compression load or stress ratio is correlated to the angle, ϕ, shown in Figure 3.1. Tension loads were selected in different steps from 0 to 20 kN for both [90/0] and [±45] sandwich panels. One specimen was examined at each load level, except a few cases for which two specimens were used (specimens were designated CT).

The specimens at 20-kN tension load were equipped with one biaxial strain gage located at the center point, as shown in Figure 3.22.

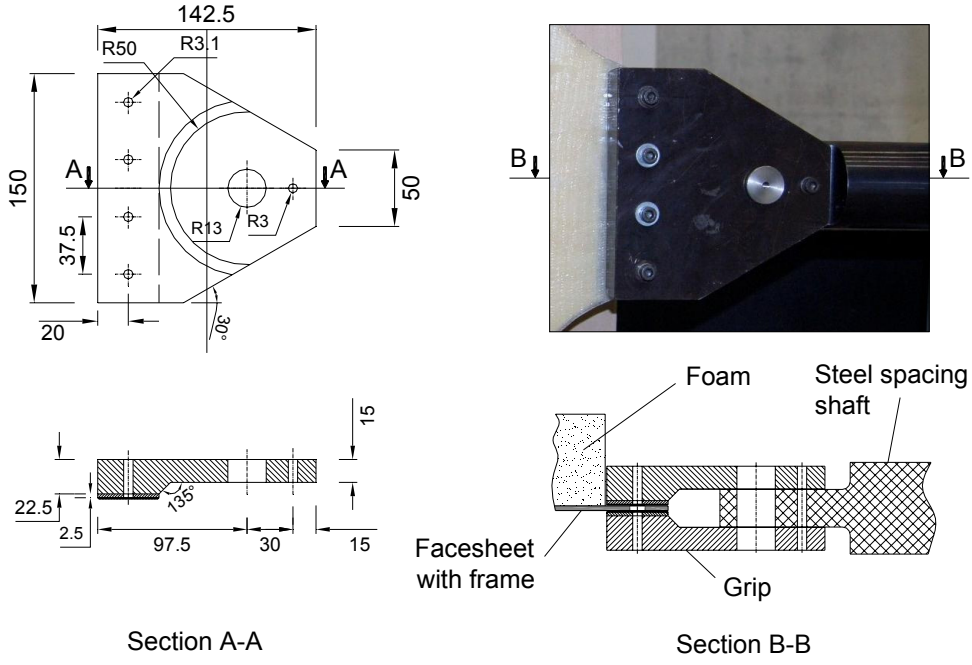

Figure 3.24. Grip configuration and dimensions.

In addition, five specimens (two with [90/0] and three with [±45] stacking sequence, designated SCT) were loaded differently to compare and confirm the obtained results: both compression and tension loads were increased simultaneously up to failure, i.e. by alternating small steps in force control mode at a rate of 0.125 kN/s. The load ratio tension/compression was selected to simulate different angles, ϕ, of 30°, 45° and 60°.

3.3.3. Experimental results

3.3.3.1. [90/0] specimens

Figure 3.25 shows the biaxial strain responses recorded at the center of the [90/0] specimen while applying the tension load up to 20 kN (still without any compression). The results demonstrate that applying a tension load in the vertical direction resulted in compressive strains in the

horizontal direction (almost 49% of the tensile strains) which represent the lateral contraction behavior due to the Poisson's effect.

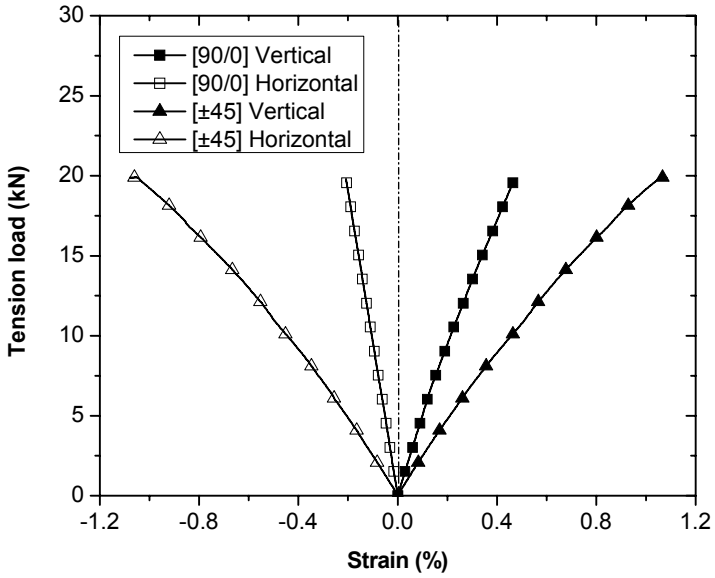

Figure 3.25. Tension load vs. biaxial strain responses of [90/0] and [±45] specimens tested at 20-kN tension load.

Subsequently applying compression up to failure led to two different wrinkling failure modes, as shown in Figure 3.26. The wrinkling wave, which appeared close to the support frame, either went inside the foam (Figure 3.26(a)) or came out of the foam (Figure 3.26(b)). In the latter case, failure occurred in the foam (and not in the interface). The mode type did not correlate with the tension load. The resulting wrinkling loads of the CT specimens, obtained as a function of the transverse tension loads, are shown in Figure 3.27 and the values are given in Table 3.5. A fitting curve was added to the experimental results. The average wrinkling load in the case without any tension load was 20.5 kN while this value decreased by 24.5% in the case of a 20-kN tension load to 15.5 kN. Also shown in Figure 3.27 are the loading paths and wrinkling loads of the SCT specimens with ϕ = 45° and 30°, which represent pure shear loading and combined shear plus normal tensile loading, respectively. The SCT and CT results compare well.

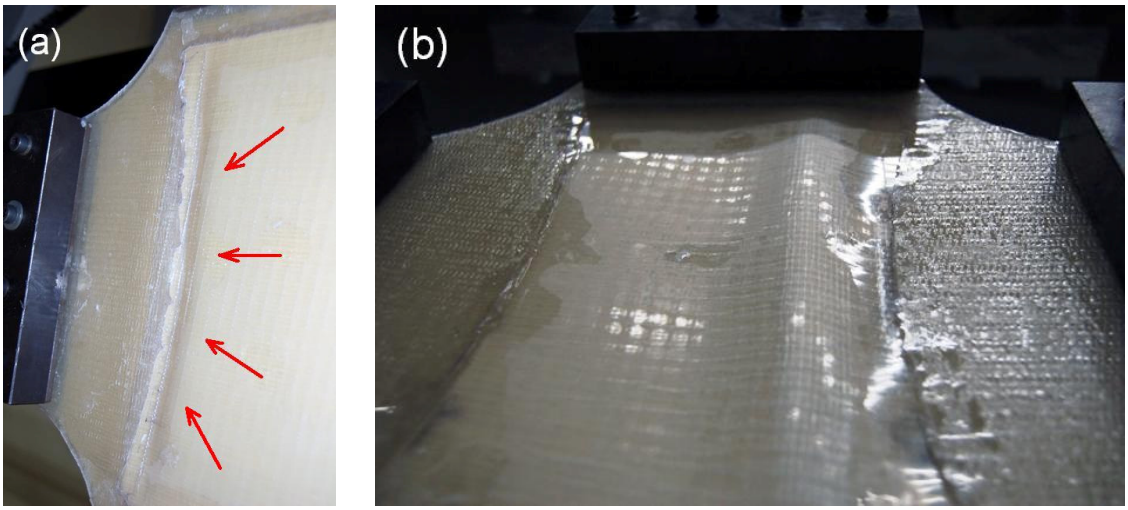

Figure 3.26. Wrinkling failure modes of [90/0] specimens: (a) wrinkling wave went inside foam; (b) wrinkling wave came out of foam.

Table 3.5. Wrinkling loads of [90/0] and [±45] specimens at different tension loads.

[90/0] specimen			[±45] specimen		
Test type	Tension load (kN)	Ultimate compression load (kN)	Test type	Tension load (kN)	Ultimate compression load (kN)
CT	0.0	19.9	CT	0.0	20.3
CT	0.0	21.0	CT	5.0	18.1
CT	3.0	19.2	CT	10.0	17.0
CT	5.0	17.1	CT	10.0	16.3
CT	10.0	15.8	CT	13.5	13.0
CT	11.3	15.9	CT	16.6	11.4
CT	17.7	15.3	CT	20.0	9.8
CT	19.8	14.9	SCT	$\phi = 30°$	16.6
CT	20.0	16.0	SCT	$\phi = 45°$	14.0
SCT	$\phi = 30°$	16.4	SCT	$\phi = 60°$	9.3
SCT	$\phi = 45°$	15.8			

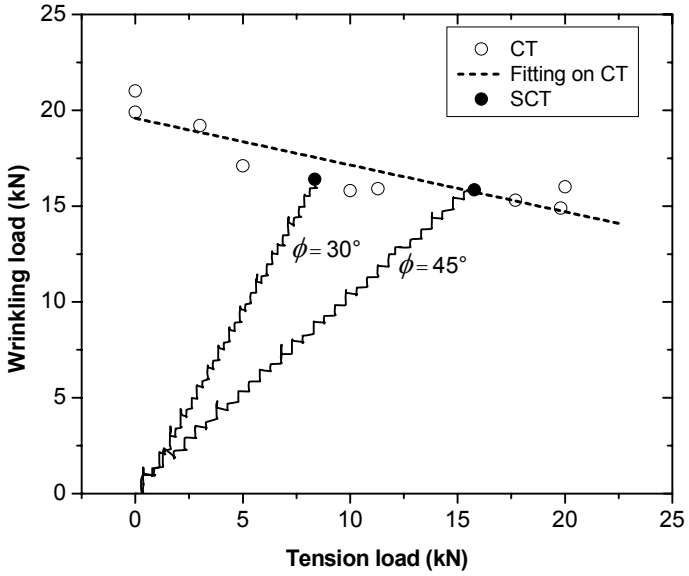

Figure 3.27. Wrinkling load of [90/0] specimens vs. transverse tension load.

3.3.3.2. [±45] specimens

The biaxial strain responses of the [±45] specimen during pure tension loading are shown in Figure 3.25. The compressive strains in the horizontal direction resulting from the vertical tension load were almost equal to the tensile strains in the vertical direction. The wrinkling failure modes captured for [±45] specimens are shown in Figure 3.28. Again, the wrinkling wave went inside the foam (at different positions, Figures 3.28(a),(b)&(c)) or came out of the foam (Figure 3.28(d)). Figure 3.29 and Table 3.5 show the resulting wrinkling loads vs. the transverse tension loads. Increasing the tension load up to 20 kN caused a decrease of 52% in the wrinkling load. Figure 3.29, moreover, shows the loading paths and wrinkling loads of the SCT specimens at ϕ = 30°, 45°, and 60°. Again, CT and SCT results compare well.

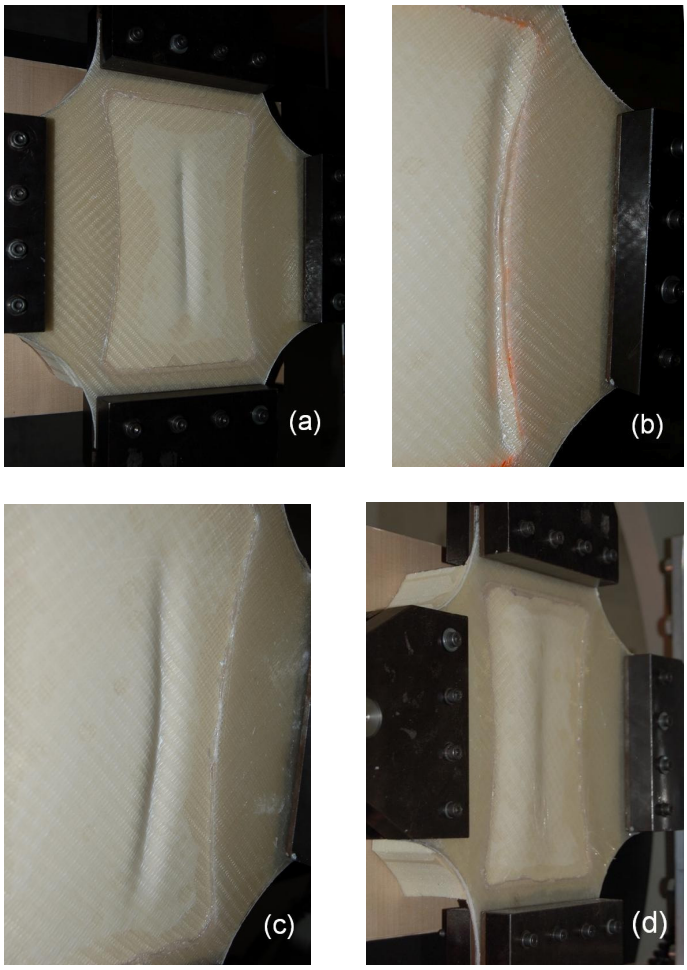

Figure 3.28. Wrinkling failure modes of [±45] specimens, (a), (b) and (c) wrinkling wave went inside foam, (d) wrinkling wave came out of foam.

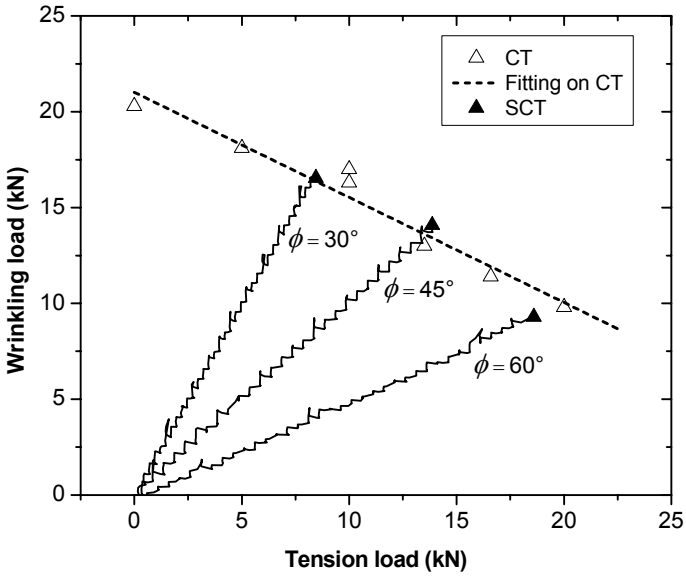

Figure 3.29. Wrinkling load of [±45] specimens vs. transverse tension load.

3.3.4. Discussion of results

Previous experimental investigations of the buckling of composite laminates subjected to biaxial compression-tension loading, e.g. Tuttle et al. (1999) and the results of Section 3.2, showed that the transverse tension load has a stabilizing effect and therefore increases the buckling and ultimate loads. Although wrinkling is a local buckling problem, it seems surprising that a significant decrease of the wrinkling load occurs as a result of increasing the transverse tension load, as demonstrated in Figures 3.27 and 3.29. Indeed, the buckling wave of a plate subjected to compression-tension loading can be represented as a surface with double curvature. Along the stretched direction, the tension stresses tend to push back the peak of the wave down to the median plane. Whereas, in the compressed direction, the compression stresses tend to bend the plate and therefore prevent it from returning to the median plane. Moreover, the lateral contraction due to the Poisson's effect, see Figure 3.25, also tends to increase the amplitude of the buckling waves. During stretching of the plate with a high number of waves, the lateral contraction effect of tension seemed more dominant than its stabilizing effect and therefore accelerated the second-order out-of-plane displacements and decreased the wrinkling loads with increasing transverse tension. This phenomenon has been addressed by studies on the buckling of very thin and flexible membranes under pure tension loading i.e. Friedl et al. (2000), Wong and Pellegrino (2006), and Lecieux and Bouzidi (2010). Thin flexible membranes, mainly used in spacecraft structures and incapable of bearing any compression, can buckle if subjected to pure tension due to the Poisson's effect.

The stacking sequence, i.e. the fiber orientation, had a significant effect on the results, as demonstrated in Figure 3.30. Although the in-plane stiffness of the [90/0] configuration in the compression loading direction was higher than that of the [±45] configuration, the wrinkling load of the latter at low tension loads was higher than that of the former, see fitting lines on experimental results in Figure 3.30. This is due to the coupling of in-plane and bending behavior in asymmetric laminates, which is more significant for [90/0] laminates than [±45] laminates. The coupling behavior caused additional out-of-plane displacements prior to wrinkling and reduced the wrinkling load. In addition, the decreasing slope of wrinkling loads vs. increasing transverse tension loads of [±45] specimens was significantly steeper than that for [90/0] specimens. This difference can be explained by the higher lateral contraction of the [±45]

configuration due to the Poisson's effect, as shown in Figure 3.25, which led to a greater reduction of the wrinkling loads.

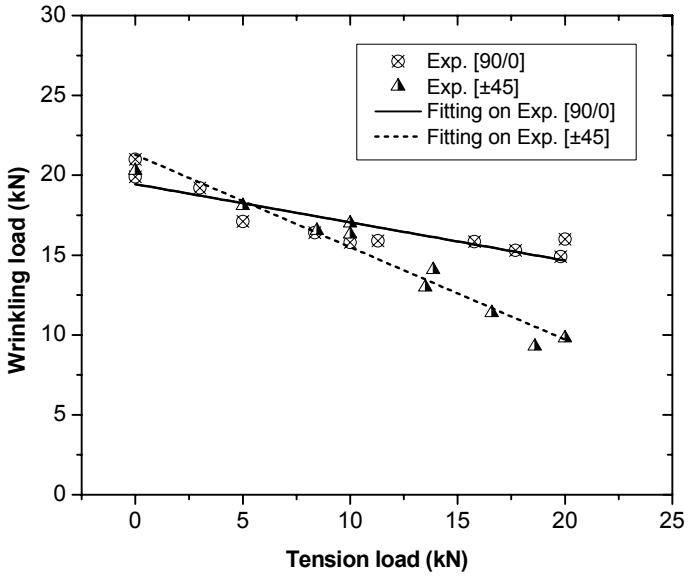

Figure 3.30. Comparison of experimental and numerical wrinkling loads at different transverse tension loads.

3.3.5. Concluding remarks

An exploratory study was performed on the biaxial compression-tension wrinkling behavior of GFRP sandwiches. This biaxial loading simulates the shear loading in the webs of cell-core sandwich structures. The following conclusions were drawn:

1) An increasing transverse tension load significantly decreased the wrinkling loads (up to 52%, according to experiments). The transverse tension increased the initial imperfections due to the Poisson's effect and thus accelerated the second-order bending of the face sheets, which finally led to a significant decrease in the wrinkling loads.

2) The fiber architecture, i.e. the fiber orientation, greatly influenced the wrinkling loads due to its effect on the Poisson's ratio. According to the results, at pure shear loading, a [90/0] fiber orientation in the webs of cell-core sandwiches seems more favorable than a [±45] configuration.

The results of this study have to be confirmed for other material systems and geometrical configurations. The development of an numerical and analytical model to predict wrinkling loads as a function of transverse tension loads and predict the ultimate resistance of wrinkled cell-core sandwich webs, anchored in the surrounding flanges and/or transverse stiffeners, constitute further stages of investigation.

4 Analysis of experiments and modeling

4.1. Overview

This chapter concerns the analytical and numerical modeling carried out to determine the in-plane stress field of the orthotropic plates and sandwich panels subjected to biaxial compression-tension loading according to the experimental set-up (see Chapter 3). A model for predicting the buckling and wrinkling behavior of composite plates and sandwich panels subjected to in-plane biaxial compression-tension loading is presented. Based on the resulting stress fields, the model is able to simulate the two counteracting effects of increasing transverse tension load on the buckling and wrinkling loads as observed from experiments. A stabilizing effect tends to push the plate back to the median plane and thereby delays the onset of buckling/wrinkling instability. In contrast, lateral contraction accelerates the bending of the plate, which leads to a significant decrease in the buckling/wrinkling loads. In composite plates, the first effect predominates and increases the buckling loads while in sandwich panels the second effect is dominant and decreases the wrinkling loads. A numerical study using FE modeling confirms the analytical results.

4.2. Lateral contraction of composite laminates subjected to partially uniform tension

4.2.1. Introduction and objectives

Applying non-uniform or partially uniform in-plane tension loads on plates leads to contraction in the direction transverse to the loading due to the stresses that occur between the opposite loading points, known as lateral contraction effect. This effect may cause wrinkling of thin films or membranes even under the application of pure tensile forces (Cerda et al. 2002, Lecieux and

Bouzidi 2010, Wong and Pellegrino 2006-a). These membrane structures are widely used in marine, space and terrestrial application i.e. for reflectors, solar arrays, sunshields, radars and inflatable antennas where the wrinkles can reduce the structural performance. The same effect might occur during the production of thin metal or plastic sheets and also during the process of forming large parts such as automobile panels that can lead to local buckling creating folds in the final products (Friedl et al. 2000, Tomita and Shindo 1988, Xu and Yu 1990). This is undesirable in final products as it decreases the component stiffness and affects appearance and assembly.

A similar problem occurs in composite plates and sandwich panels that are subjected to localized loading, such as design components that face a stiffener termination or the transition from a stiffened to a monolithic panel. In these cases, the lateral contraction effect can also influence the buckling or wrinkling failure of plates and sandwich panels subjected to biaxial compression-tension loading, see the results of Chapter 3. As shown in Section 3.3.3, an increasing transverse tension load intensified the initial imperfections due to the lateral contraction and thus led to a significant decrease in wrinkling loads.

In order to quantify the lateral contraction effect, it is first necessary to determine the stress field caused by the tensile forces, before addressing the buckling/wrinkling problem for plates and/or sandwich panels. Many experimental and numerical research efforts have been made to obtain the elastic stress field of non-uniform tension loads (Timoshenko and Goodier 1951, Yoshida 1974) and then based on this stress field, to predict the initiation and growth of local buckling (Tomita and Shindo 1988, Xu and Yu 1990, Segedin et al. 1988). However, all the above-mentioned studies were limited to isotropic materials. Recently, an analytical solution by Kassapoglou and Bauer (2010) has been dedicated to the stress field of an orthotropic rectangular composite plate under partially uniform load on one edge and uniform load on the opposite edge. The authors showed that their solution has a fair correlation with finite element results when the plate is long enough to satisfy the infinity assumptions. Nevertheless, the solution is not accurate for short plates that are loaded by partially uniform loads on both edges, which presents a more realistic case than the one analyzed in Kassapoglou and Bauer (2010).

This part of Chapter 4 aims to present the development of a new analytical approach to determine the in-plane stress field of orthotropic plates subjected to partially uniform tension

loading. In this context, based on the Green function hypothesis, an analytical model for an orthotropic half-plane subjected to partially uniform edge load is presented. The analytical model is then combined with a modification performed on an approach proposed by Xu and Yu (1990) in order to determine the stress field of an orthotropic rectangular plate subjected to partially distributed load on both edges. The effect of the laminate stacking sequence on lateral contraction is also investigated as three different fiber architectures are considered. The analytical solutions obtained for GFRP plates are compared to finite element solutions and experimental results for validation.

4.2.2. Analytical approach

4.2.2.1. Basic equations and assumptions

For thin plates, a state of generalized plane stress is assumed in which all three out of plane stress components are negligible. Then, the relationships between the mean stresses and strains in the (x, y) plane with reference to Figure 4.1 are

$$\begin{cases} \varepsilon_x = s_{11}\sigma_x + s_{12}\sigma_y + s_{16}\sigma_{xy} \\ \varepsilon_y = s_{12}\sigma_x + s_{22}\sigma_y + s_{26}\sigma_{xy} \\ \varepsilon_{xy} = s_{16}\sigma_x + s_{26}\sigma_y + s_{66}\sigma_{xy} \end{cases} \tag{4.1}$$

in which s_{mn} (m, n =1, 2, 6) are the elastic constants of composite laminates calculated by applying the classical laminate theory (CLT).

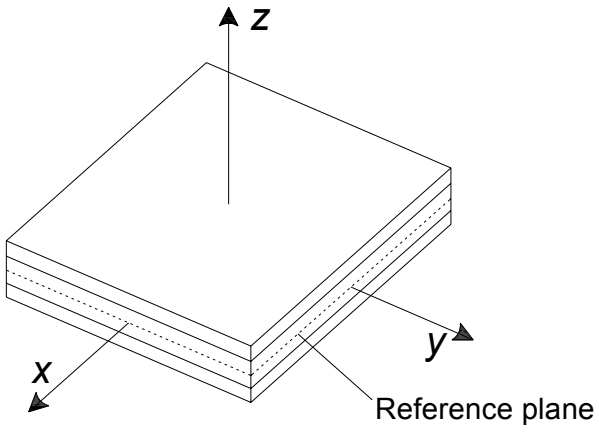

Figure 4.1. Coordinate system.

The mean stresses can be expressed in the form of

$$\sigma_x = \frac{\partial^2 \chi}{\partial y^2},\ \sigma_y = \frac{\partial^2 \chi}{\partial x^2}, \text{ and } \sigma_{xy} = \frac{\partial^2 \chi}{\partial x \partial y}, \tag{4.2}$$

where χ is a stress function. By inserting Eqs. (4.1) and (4.2) into the compatibility equation, Eq. (4.3):

$$\frac{\partial^2 \varepsilon_y}{\partial x^2} + \frac{\partial^2 \varepsilon_x}{\partial y^2} = \frac{\partial^2 \varepsilon_{xy}}{\partial x \partial y} \tag{4.3}$$

the following equation is obtained for χ

$$s_{22}\frac{\partial^4 \chi}{\partial x^4} - 2s_{26}\frac{\partial^4 \chi}{\partial x^3 \partial y} + \left(2s_{12} + s_{66}\right)\frac{\partial^4 \chi}{\partial x^2 \partial y^2} - 2s_{16}\frac{\partial^4 \chi}{\partial x \partial y^3} + s_{11}\frac{\partial^4 \chi}{\partial y^4} = 0 \tag{4.4}$$

When the plate material has two symmetry directions at right angles in the (x, y) plane and these are assumed to be parallel to the directions of x and y, then s_{16}= s_{26}=0 and Eq. (4.4) becomes:

$$\left(\frac{\partial^2}{\partial x^2} + \alpha_1 \frac{\partial^2}{\partial y^2}\right)\left(\frac{\partial^2}{\partial x^2} + \alpha_2 \frac{\partial^2}{\partial y^2}\right)\chi = 0 \tag{4.5}$$

where $\alpha_1 \alpha_2 = s_{11}/s_{22}$ and $\alpha_1 + \alpha_2 = \left(2s_{12} + s_{66}\right)/s_{22}$. The constants α_1 and α_2 may have real or imaginary values.

4.2.2.2. Stress field of an orthotropic half-plane subjected to partially uniform load

Considering a load p applied perpendicular to the edge of an orthographic half-plane, as shown in Figure 4.2(a), Green (1939) has given the stress components for generalized plane stress as

$$\begin{cases} \sigma_r = \dfrac{2p\alpha_1^{1/2}\alpha_2^{1/2}\sin(\theta)}{r\pi\left(\alpha_1^{1/2} - \alpha_2^{1/2}\right)}\left(\dfrac{\alpha_2 - 1}{\alpha_2 + 1 + \left(1 - \alpha_2\right)\cos(2\theta)} - \dfrac{\alpha_1 - 1}{\alpha_1 + 1 + \left(1 - \alpha_1\right)\cos(2\theta)}\right) \\ \sigma_{r\theta} = \sigma_\theta = 0 \end{cases} \tag{4.6}$$

where r is the polar radius and θ is the polar angle for the given position. The normal radial stress component is denoted by σ_r, the normal circumferential stress component by σ_θ, and the shear stress component by $\sigma_{r\theta}$, each symbol representing stress at point (r, θ). The stress components in the (x, y) coordinate system in terms of σ_r, σ_θ and $\sigma_{r\theta}$ are (Timoshenko and Goodier, 1951):

$$\begin{cases} \sigma_x = \sigma_r \cos^2\theta + \sigma_\theta \sin^2\theta - 2\sigma_{r\theta}\sin\theta\cos\theta \\ \sigma_y = \sigma_r \sin^2\theta + \sigma_\theta \cos^2\theta + 2\sigma_{r\theta}\sin\theta\cos\theta \\ \sigma_{xy} = (\sigma_r - \sigma_\theta)\sin\theta\cos\theta + \sigma_{r\theta}(\cos^2\theta - \sin^2\theta) \end{cases} \tag{4.7}$$

Considering the relationship between coordinate systems as:

$$r^2 = x^2 + (b-y)^2, \text{ and } \theta = \arctan\frac{b-y}{x}, \tag{4.8}$$

the stress components of an orthotropic half-plane subjected to an edge concentrated load p in the (x, y) coordinate system can be derived by incorporating Eq. (4.6) into Eq. (4.7). By integrating these stress components from $x–c$ to $x+c$, where the uniform load q' is applied perpendicular to the edge (see Figure 4.2(b)), the stress field of an orthotropic half-plane subjected to a partially uniform load is obtained as:

$$\begin{aligned} \sigma_{x,I} = Q\Bigg\{ & \sqrt{\alpha_1}\left(\arctan\left(\frac{x+c}{(b-y)\sqrt{\alpha_1}}\right) - \arctan\left(\frac{x-c}{(b-y)\sqrt{\alpha_1}}\right)\right) \\ & -\sqrt{\alpha_2}\left(\arctan\left(\frac{x+c}{(b-y)\sqrt{\alpha_2}}\right) - \arctan\left(\frac{x-c}{(b-y)\sqrt{\alpha_2}}\right)\right)\Bigg\} \end{aligned} \tag{4.9-a}$$

$$\begin{aligned} \sigma_{y,I} = Q\Bigg\{ & \frac{\sqrt{\alpha_1}}{\alpha_1}\left(\arctan\left(\frac{x+c}{(b-y)\sqrt{\alpha_1}}\right) - \arctan\left(\frac{x-c}{(b-y)\sqrt{\alpha_1}}\right)\right) \\ & -\frac{\sqrt{\alpha_2}}{\alpha_2}\left(\arctan\left(\frac{x+c}{(b-y)\sqrt{\alpha_2}}\right) - \arctan\left(\frac{x-c}{(b-y)\sqrt{\alpha_2}}\right)\right)\Bigg\} \end{aligned} \tag{4.9-b}$$

$$\begin{aligned} \sigma_{xy,I} = \frac{Q}{2}\Big\{ & Ln\left(\alpha_1(b-y)^2 + (x+c)^2\right) - Ln\left(\alpha_1(b-y)^2 + (x-c)^2\right) \\ & + Ln\left(\alpha_2(b-y)^2 + (x-c)^2\right) - Ln\left(\alpha_2(b-y)^2 + (x+c)^2\right)\Big\} \end{aligned} \tag{4.9-c}$$

in which $Q = \dfrac{q'\alpha_1^{1/2}\alpha_2^{1/2}}{\pi\left(\alpha_1^{1/2} - \alpha_2^{1/2}\right)}$.

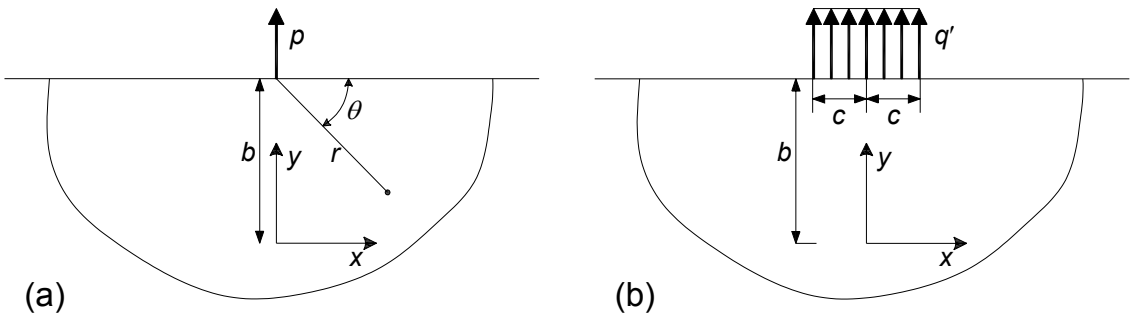

Figure 4.2. Loading conditions on half-plane: (a) concentrated load; (b) partially uniform load.

4.2.2.3. Stress field of an orthotropic rectangular plate subjected to partially uniform load

Considering a partially uniform load q' applied perpendicular to the two opposite edges of an orthotropic rectangular plate as shown in Figure 4.3, boundary conditions are defined as

$$x = \pm a \rightarrow \sigma_x = \sigma_{xy} = 0$$
$$y = \pm b \rightarrow \sigma_{xy} = 0, \begin{cases} |x| \le c : \sigma_y = q' \\ |x| > c : \sigma_y = 0 \end{cases} \tag{4.10}$$

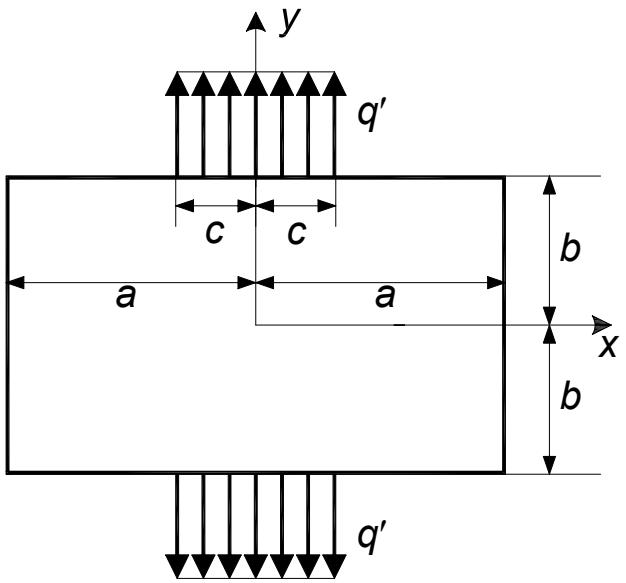

Figure 4.3. Orthotropic rectangular plate subjected to partially uniform tension.

The difficulty in solving the stress field concerns the discontinuity in the boundary conditions at $x=\pm c$. Xu and Yu (1990) overcame this difficulty by separating the problem into three elastic problems. The elastic problem I is the half-plane problem shown in Figure 4.4(a) and thus the stress components can be acquired by Eqs. 4.9(a)-(c). Similarly, the stress components for problem II (see Figure 4.4(b)) are expressed as follows:

$$\sigma_{x,II} = Q\left\{\sqrt{\alpha_1}\left(\arctan\left(\frac{x-c}{(b+y)\sqrt{\alpha_1}}\right)-\arctan\left(\frac{x+c}{(b+y)\sqrt{\alpha_1}}\right)\right)\right. \\ \left.-\sqrt{\alpha_2}\left(\arctan\left(\frac{x-c}{(b+y)\sqrt{\alpha_2}}\right)-\arctan\left(\frac{x+c}{(b+y)\sqrt{\alpha_2}}\right)\right)\right\} \tag{4.11-a}$$

$$\sigma_{y,II} = Q\left\{\frac{\sqrt{\alpha_1}}{\alpha_1}\left(\arctan\left(\frac{x-c}{(b+y)\sqrt{\alpha_1}}\right)-\arctan\left(\frac{x+c}{(b+y)\sqrt{\alpha_1}}\right)\right)\right. \\ \left.-\frac{\sqrt{\alpha_2}}{\alpha_2}\left(\arctan\left(\frac{x-c}{(b+y)\sqrt{\alpha_2}}\right)-\arctan\left(\frac{x+c}{(b+y)\sqrt{\alpha_2}}\right)\right)\right\} \tag{4.11-b}$$

$$\sigma_{xy,II} = \frac{Q}{2}\left\{Ln\left(\alpha_1\left(b+y\right)^2+\left(x-c\right)^2\right)-Ln\left(\alpha_1\left(b+y\right)^2+\left(x+c\right)^2\right)\right. \\ \left.+Ln\left(\alpha_2\left(b+y\right)^2+\left(x+c\right)^2\right)-Ln\left(\alpha_2\left(b+y\right)^2+\left(x-c\right)^2\right)\right\} \tag{4.11-c}$$

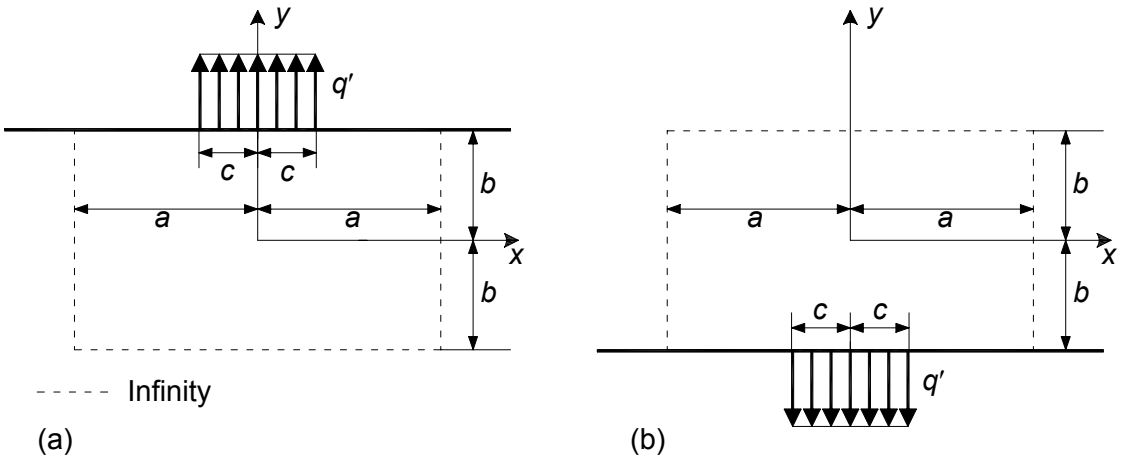

Figure 4.4. Boundary conditions of (a) elastic problem I; (b) elastic problem II.

By superposing problems I and II, the problem III is defined to satisfy the general boundary conditions given by Eq. (4.10) where

$$\begin{aligned} &x = \pm a \rightarrow \sigma_{x,III} = -(\sigma_{x,I} + \sigma_{x,II}),\ \sigma_{xy,III} = -(\sigma_{xy,I} + \sigma_{xy,II}) \\ &y = +b \rightarrow \sigma_{y,III} = -\sigma_{y,II},\ \sigma_{xy,III} = -\sigma_{xy,II} \\ &y = -b \rightarrow \sigma_{y,III} = -\sigma_{y,I},\ \sigma_{xy,III} = -\sigma_{xy,I} \end{aligned} \tag{4.12}$$

Accordingly, the stress field for an orthotropic rectangular plate subjected to partially uniform loading can be obtained by the summation of the stress components of problems I, II and III, i.e.

$$\begin{aligned} \sigma_x &= \sigma_{x,I} + \sigma_{x,II} + \sigma_{x,III} \\ \sigma_y &= \sigma_{y,I} + \sigma_{y,II} + \sigma_{y,III} \\ \sigma_{xy} &= \sigma_{xy,I} + \sigma_{xy,II} + \sigma_{xy,III} \end{aligned} \tag{4.13}$$

In order to solve problem III, a new stress function $\Phi(x, y)$, is introduced as

$$\sigma_{x,III} = \frac{\partial^2 \Phi}{\partial y^2},\ \sigma_{y,III} = \frac{\partial^2 \Phi}{\partial x^2}, \text{ and } \sigma_{xy,III} = -\frac{\partial^2 \Phi}{\partial x \partial y}. \tag{4.14}$$

Combining Eq. (4.14) and Eqs. (4.1) and (4.3), and also considering s_{16}= s_{26}=0, result in a similar expression to Eq. (4.5):

$$\left(\frac{\partial^2}{\partial x^2} + \alpha_1 \frac{\partial^2}{\partial y^2}\right)\left(\frac{\partial^2}{\partial x^2} + \alpha_2 \frac{\partial^2}{\partial y^2}\right)\Phi = 0 \tag{4.15}$$

The solution is assumed as being:

$$\Phi = \phi_\circ + \beta_1\phi_1 + \beta_2\phi_2 + \beta_3\phi_3 + \beta_4\phi_4 \tag{4.16}$$

where

$$\begin{aligned} \phi_1 &= \left(x^2 - a^2\right)^2 \left(y^2 - b^2\right)^2 \\ \phi_2 &= \left(x^2 - a^2\right)^2 \left(y^2 - b^2\right)^2 x^2 \\ \phi_3 &= \left(x^2 - a^2\right)^2 \left(y^2 - b^2\right)^2 y^2 \\ \phi_4 &= \left(x^2 - a^2\right)^2 \left(y^2 - b^2\right)^2 x^2 y^2 \end{aligned} \tag{4.17}$$

and $\phi_\circ$ satisfies all the boundary conditions given by Eq. (4.12). The suitable analytical form for $\phi_\circ$ is:

$$\phi_\circ = \phi'_\circ + \phi''_\circ \tag{4.18}$$

see Appendix A, where

$$\begin{cases} \phi_{\circ}' = \iint F'(x)dxdx + \iint G'(y)dydy \\ \phi_{\circ}'' = \dfrac{(x^2-a^2)}{2a}\displaystyle\int_b^y \left(-G''(y)+\frac{y}{2b}G''(b)\right)dy + \frac{(y^2-b^2)}{2b}\int_a^x \left(-F''(x)+\frac{x}{2a}F''(a)\right)dx \\ \begin{cases} F'(x) = -(\sigma_{x,I}+\sigma_{x,II})\big|_{x=+a} \\ G'(x) = -\sigma_{y,II}\big|_{y=+b} \end{cases} \\ \begin{cases} F''(x) = -(\sigma_{xy,I}+\sigma_{xy,II})\big|_{x=+a} \\ G''(x) = -\sigma_{xy,II}\big|_{y=+b} \end{cases} \end{cases} \tag{4.19}$$

Since $\Phi(x, y)$, expressed by Eqs. (4.16) and (4.17), satisfies all boundary conditions, Eq. (4.15) suffices to determine the β_m (m=1, 2, 3 and 4). Employing the Galerkin method leads to

$$\iint_{\Omega}\left\{\left(\frac{\partial^2}{\partial x^2}+\alpha_1\frac{\partial^2}{\partial y^2}\right)\left(\frac{\partial^2}{\partial x^2}+\alpha_2\frac{\partial^2}{\partial y^2}\right)\Phi\right\}\Phi_m\,dx\,dy = 0 \tag{4.20}$$

where the integral region is Ω=[$-a$, $+a$; $-b$, $+b$]. Eq. (4.20) will result in a system of linear equations for β_m. As long as β_m are determined, the stress field for problem III can be derived from Eqs. (4.14), (4.16) and (4.17). Thus, according to Eq. (4.13), the stress field for a rectangular plate subjected to partially uniform tension is found.

4.2.3. Bases for validation of analytical approach

The validation of the analytical approach has been performed in two stages. Firstly, the analytical solution was compared to the numerical results of a finite element analysis of the orthotropic half-plane. Secondly, the analytical solution for orthotropic rectangular plates was validated by experimental results presented in Section 3.2 for GFRP plates and corresponding finite element analyses.

4.2.3.1. Orthotropic half-plane subjected to partially uniform tension

A finite element model created using ANSYS v-10 software was used to model a plate with dimensions of 120 cm×120 cm, which was subjected to a uniform load of 1 MPa acting in-plane over a discrete edge length of 4 cm (see Figure 4.5). 4-node shell elements, SHELL181, with six degrees of freedom were used. The finite element model was created using a very fine mesh in the

load application area in order to accurately simulate the stress field in the high gradient regions. A transition from a refined mesh near the load application to a coarse density mesh near the far-field edges was carried out by using element edge lengths of 1 to 8 mm. This generated 29,653 elements and 180,102 degrees of freedom in total. The model was solved for the two cases of $[0/90]_S$ and $[\pm 45]_S$ laminates with a thickness of 3.1 mm each.

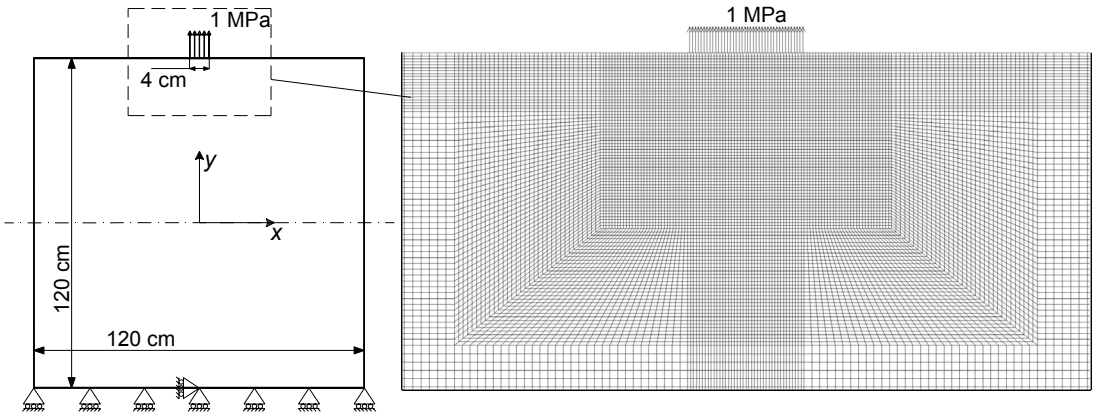

Figure 4.5. Half-plane model validation: geometry, finite element model, applied load and boundary conditions.

The symmetric laminates were simulated by one orthotropic lamina with effective in-plane properties determined by employing the classical laminate theory (CLT) and the properties of the unidirectional (UD) GFRP lamina (type I) given in Table 4.1. The displacement boundary conditions are shown in Figure 4.5. The plate was uniformly constrained in the load direction, but was free to move transversely to the load to allow the lateral contraction caused by the Poisson's effect. A linear static solution was applied. Contour plots and isolines of the resulting stress distribution are shown in Figures 4.6 and 4.7, which illustrate the differences between $[0/90]_S$ and $[\pm 45]_S$ lay-ups. Along the *y*-direction, the axial stresses dissipate deeper in the case of $[0/90]_S$ than $[\pm 45]_S$ while the area over which the transverse stress is distributed is larger for $[\pm 45]_S$ than $[0/90]_S$. However, at the far field, the stresses obtained for both laminates approach the values of those of the uniform stresses at the edges.

Table 4.1. Properties of UD GFRP lamina.

Properties	Type I	Type II
Longitudinal elastic modulus [GPa]	25.7	23.5
Transverse elastic modulus [GPa]	4.7	3.8
Shear modulus [GPa]	2.25	1.80
Thickness [mm]	0.78	0.85

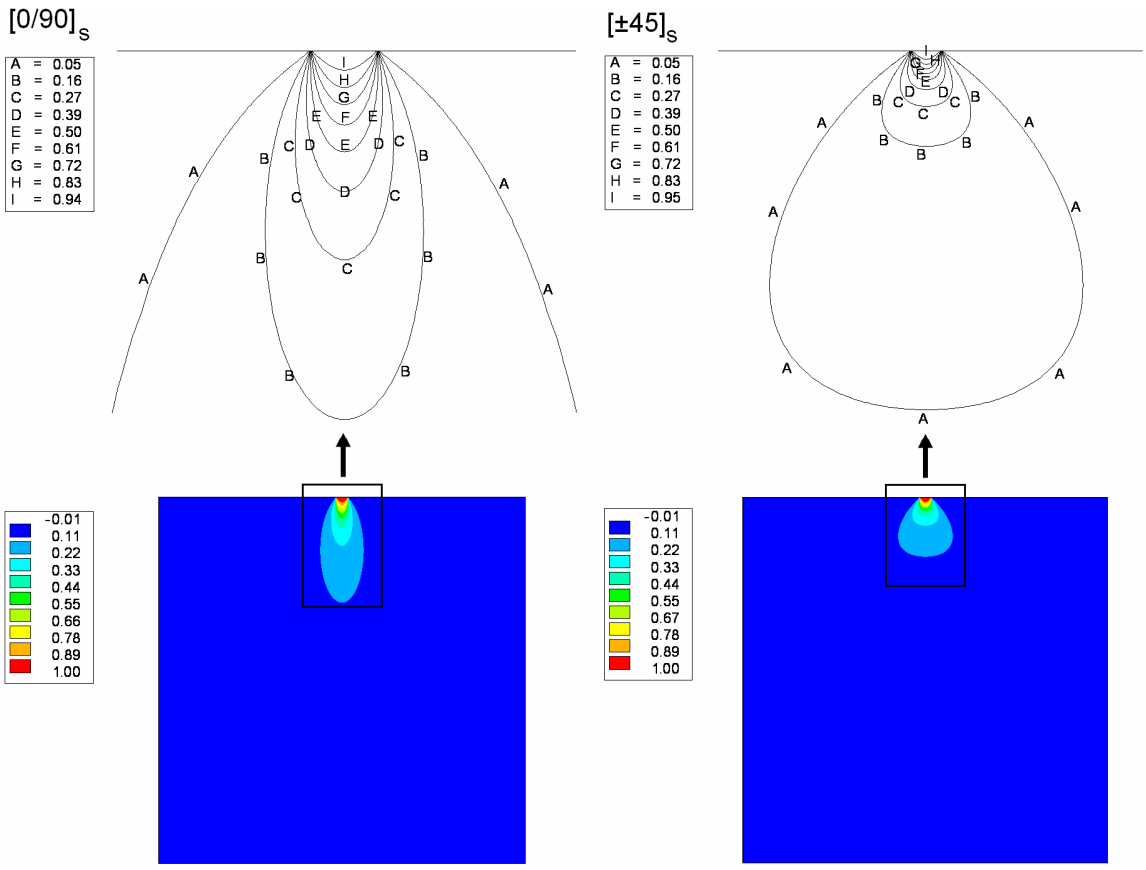

Figure 4.6. Half-plane model validation: axial y-direction stresses, σ_y, in [MPa] obtained by FE solution for $[0/90]_S$ and $[\pm 45]_S$ laminates.

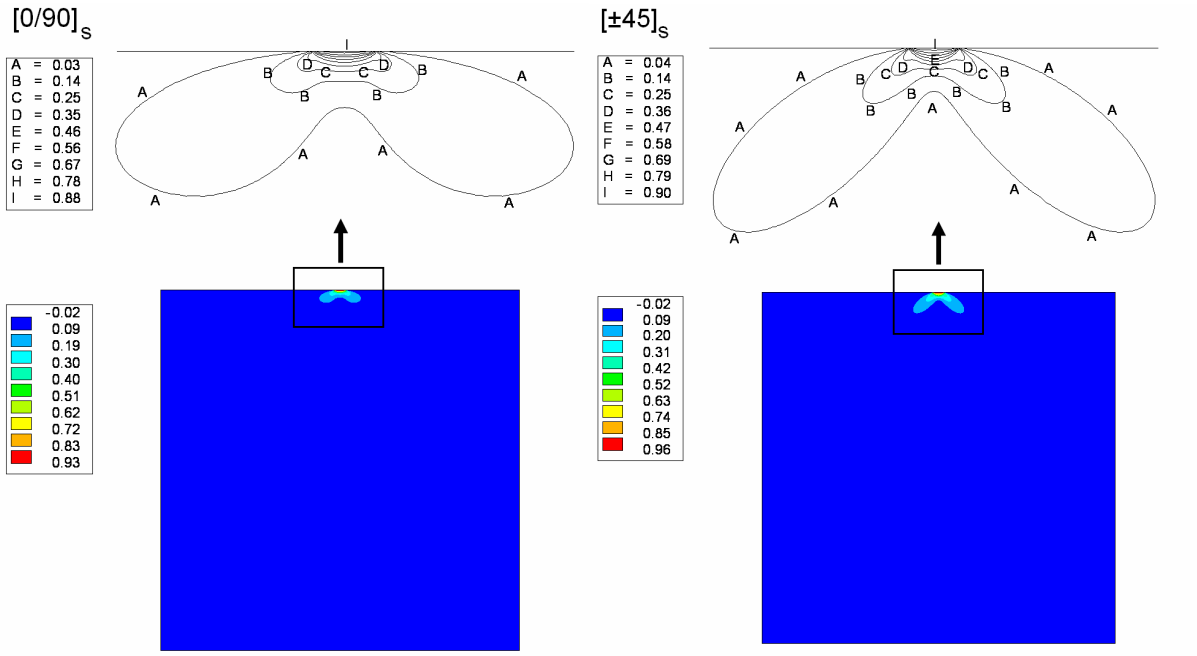

Figure 4.7. Half-plane model validation: transverse x-direction stresses, σ_x, in [MPa] obtained by FE solution for $[0/90]_S$ and $[\pm 45]_S$ laminates.

4.2.3.2. Orthotropic rectangular plate subjected to partially uniform tension

Experimental results from the study of the buckling of GFRP plates subjected to biaxial compression-tension loading elaborated in Section 3.2 were also used for validation of the analytical solution. GFRP plates consisting of four layers of two types of UD E-glass fiber fabrics and polyester resin were fabricated using the hand lay-up technique. The properties of the two lamina types are summarized in Table 4.1. Specimens with stacking sequences of $[\pm 45]_S$ were cut from type (I) and $[0/90]_S$ and $[90/0]_S$ from type (II) in semi cruciform shape with an aspect ratio of 1, as shown in Figure 3.2. Several strain gages, (1)-(13), were applied along the specimen axes to record the in-plane strains on both sides of the specimen, see Figure 3.2. Compression and tension loads were applied horizontally and vertically, respectively, over the four 150-mm edge lengths of the plate, which was fully clamped in steel grips (see Figure 3.4). As the tension load was applied over a discrete 150-mm edge length and not over the whole edge length of 250 mm, the set-up represented an orthotropic rectangular plate subjected to a partially uniform load according to Figure 4.3. Thus, the strain results recorded during the first stage of the experiments, when only the tension load was applied, could be compared to the results obtained from the analytical solution.

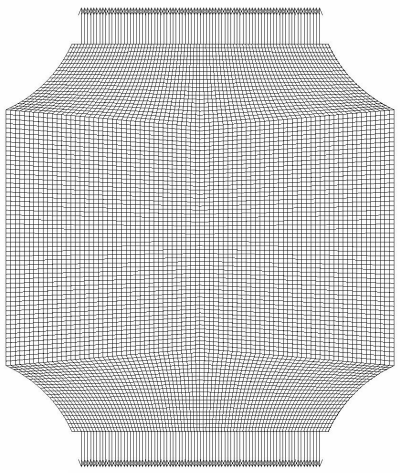

Figure 4.8. Rectangular plate model validation: FE model and loading configuration.

A finite element model was also created using ANSYS v-10 software to simulate these experiments. The specimens were modeled using 4-node layered shell elements, SHELL181. Figure 4.8 shows the mesh; 8,232 elements were used with 50,490 degrees of freedom. Linear elastic analyses were performed for all three lay-ups. The isoline plot of the transverse stress distribution, σ_x, within the $[\pm 45]_S$ plate is shown in Figure 4.9. The results demonstrate the lateral contraction effect produced by the tension load. Detailed comparisons of the finite element results and experiments with the analytical solutions are presented in the following section.

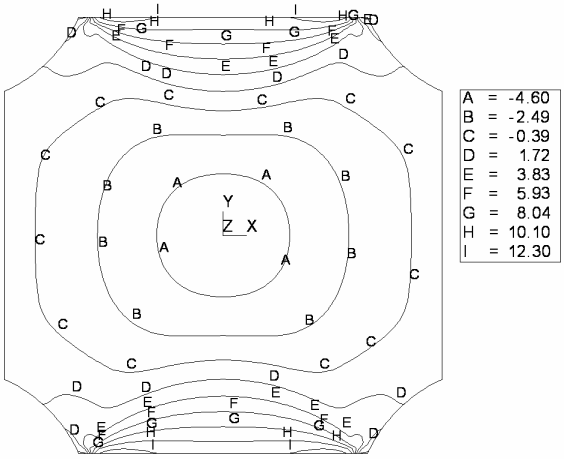

Figure 4.9. Rectangular plate model validation: transverse *x*-direction stress, σ_x, in [MPa] obtained by FE solution for $[\pm 45]_S$ at 10-kN tension load.

4.2.4. Validation and discussion

4.2.4.1. Orthotropic half-plane

The axial stresses σ_y along y at the center of the panel, resulting from Eqs. (4.9), are compared to the finite element results obtained for stacking sequences of $[0/90]_S$ and $[\pm45]_S$ in Figure 4.10. A good agreement is observed. The peak stress represents the applied load; as y increases however, the rate at which the stresses decrease depends strongly on the fiber architecture. The $[\pm45]_S$ has a faster rate of decay than the $[0/90]_S$. At the far field, both approach the value of the uniform stress at the opposite edge of the panel. Figures 4.11-4.13 show the transverse σ_x, axial σ_y and shear σ_{xy} stresses as a function of x at y = 54 cm, from x = –50 mm to x = 50 mm. The $[\pm45]_S$ lay-up exhibits transverse stresses of almost double those of $[0/90]_S$ at x = ±50 mm, see Figure 4.11. This difference can be explained by the fibers oriented at 45° that produce a greater Poisson's effect for $[\pm45]_S$ than $[0/90]_S$. However, in the case of axial stresses, see Figure 4.12, the $[0/90]_S$ results in a peak that is almost twice as high as that obtained for $[\pm45]_S$. This is because $[0/90]_S$ has a higher axial stiffness than $[\pm45]_S$. Figure 4.13 shows slightly higher shear stresses for $[\pm45]_S$ than $[0/90]_S$ laminates, which is also due to the greater Poisson's effect of the $[\pm45]_S$ lay-up. Again, a good agreement between analytical and numerical results is found.

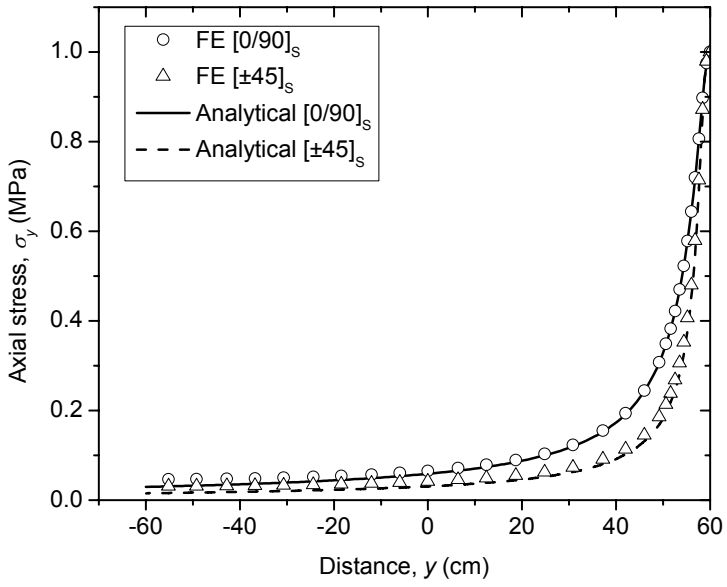

Figure 4.10. Half-plane model validation: numerical and analytical solutions of axial stresses, σ_y, along y at center of $[0/90]_S$ and $[\pm45]_S$ panels.

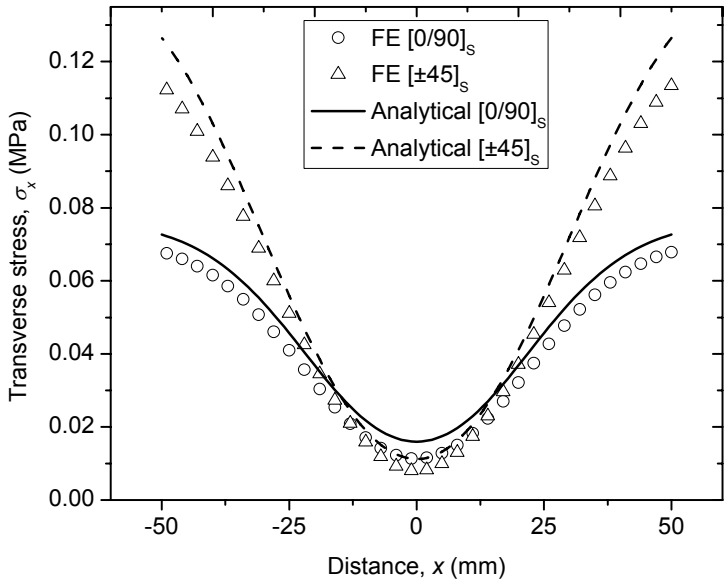

Figure 4.11. Half-plane model validation: numerical and analytical solutions of transverse stresses, σ_x, as function of x at y = 54 cm of $[0/90]_S$ and $[\pm 45]_S$ panels.

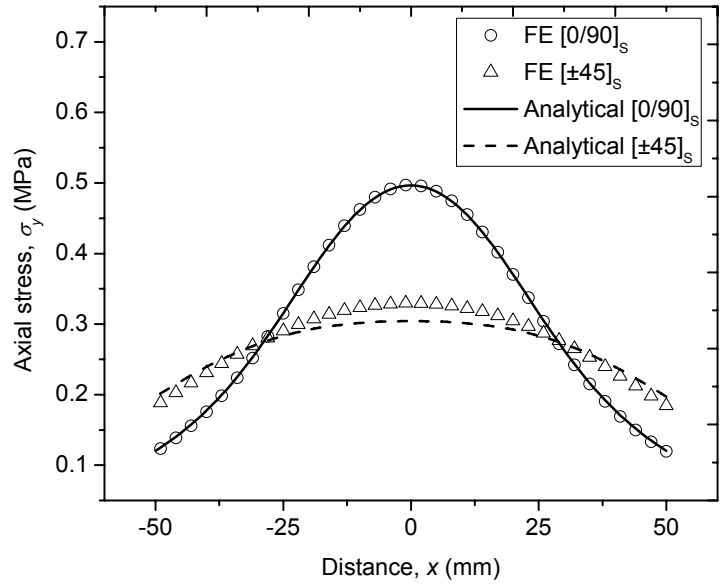

Figure 4.12. Half-plane model validation: numerical and analytical solutions of axial stress, σ_y, as function of x at y = 54 cm of $[0/90]_S$ and $[\pm 45]_S$ panels.

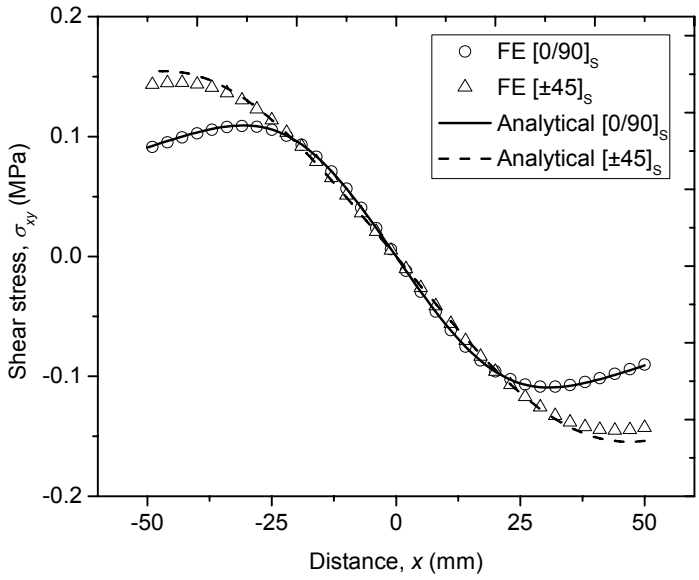

Figure 4.13. Half-plane model validation: numerical and analytical solutions of shear stress, σ_{xy}, as function of x at y = 54 cm of $[0/90]_S$ and $[\pm45]_S$ panels.

4.2.4.2. Orthotropic rectangular plate

Figure 4.14 presents the normalized transverse stress, σ_x, over the applied tensile stress, as calculated by the finite element analysis and the analytical solution for the rectangular composite plate. The stresses along x at the center (y = 0) of the panels with $[0/90]_S$, $[90/0]_S$ and $[\pm45]_S$ lay-ups are shown. The maximum transverse stress is 27% of the applied tension stress for $[\pm45]_S$ and more than 10% in the case of $[0/90]_S$ and $[90/0]_S$ laminates. The $[\pm45]_S$ lay-up shows a peak that is more than twice as high as for $[0/90]_S$ and/or $[90/0]_S$. This is again explained by the greater Poisson's effect of $[\pm45]_S$ lay-up due to the fibers oriented at 45°. In Figure 4.14, similar transverse stresses for $[0/90]_S$ and $[90/0]_S$ lay-ups are observed, as expected according to their similar in-plane effective stiffness.

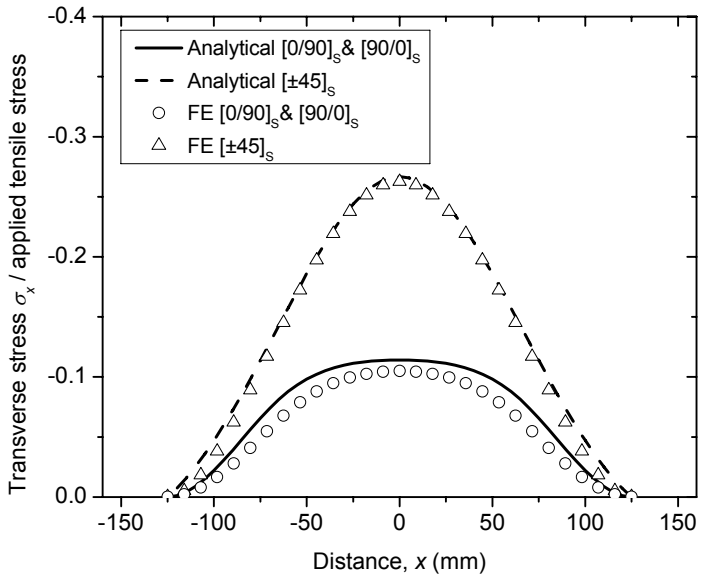

Figure 4.14. Rectangular plate model validation: normalized transverse stresses, σ_x/applied tensile stress, along x at center (y = 0) of $[0/90]_S$, $[90/0]_S$ and $[\pm45]_S$ panels.

Only small differences are noticed between the numerical and analytical solutions. One of the reasons for these differences may be the discrepancies observed between numerical and analytical solutions for the stress distribution of the orthotropic half-plane, see Figures 4.11-4.13, which form the basis of the solution for the orthotropic rectangular plates (Eqs. 4.9 and 4.11). Another reason may be any errors that might have occurred due to the polynomial stress function assumed in Eqs. (4.16) and (4.17) to satisfy the boundary conditions given by Eq. (4.10).

Furthermore, Figures 4.15 and 4.16 compare selected lateral contraction strain results calculated by analytical and numerical solutions with the experimental strains recorded by the strain gages. Figure 4.15 shows the transverse strains captured by gage (3) at the center of $[0/90]_S$, $[90/0]_S$ and $[\pm45]_S$ laminates, see Figure 3.4, as the tension load increased. Figure 4.16 compares the transverse strains resulting from the numerical and analytical solutions along x at y = –6 mm with the experimental strains recorded by gages (1)-(5) at 10-kN tension load. Both comparisons show good agreement.

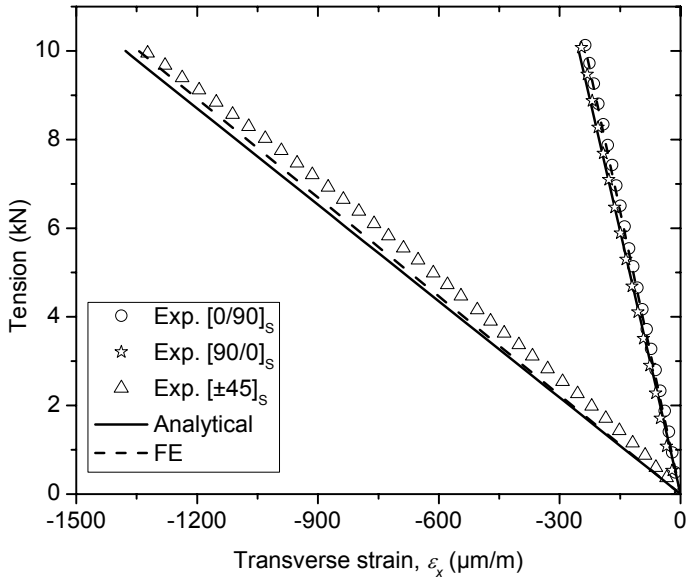

Figure 4.15. Rectangular plate model validation: transverse strain, ε_x, as function of tension load at $x = 0$ and $y = -6$ mm (position of gage (3)) of $[0/90]_S$, $[90/0]_S$ and $[\pm 45]_S$ panels.

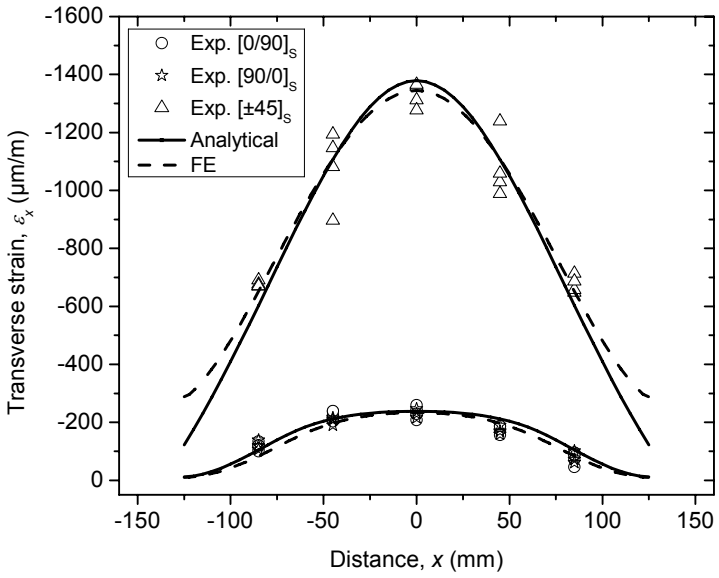

Figure 4.16. Rectangular plate model validation: transverse strain, ε_x, as function of distance x at $y = -6$ mm of $[0/90]_S$, $[90/0]_S$ and $[\pm 45]_S$ panels and tension of 10-kN.

4.2.5. Concluding remarks

An analytical approach to determine the in-plane stress field and thereby the lateral contraction of orthotropic rectangular plates subjected to partially uniform tension was developed. The

theoretical predictions for different composite laminate fiber architectures were compared to finite element simulations and experimental results.

Due to the difficulty of the discontinuity of the boundary conditions, the approach split the problem into three elastic problems: two orthotropic half-planes subjected to partially uniform load (problems I and II) and problem III to satisfy the general boundary conditions. The orthotropic half-plane problems were solved by employing the Green function hypothesis. Problem III was solved by introducing a polynomial stress function and solving it using the Galerkin method. Finally, the stress field was obtained by the summation of stress components of problems I, II and III.

The results showed significant lateral contraction effects for GFRP plates subjected to partially uniform tension. The maximum transverse compression stress was recorded as being 27% of the applied tension stress for $[\pm 45]_S$ and 11% for $[0/90]_S$ and $[90/0]_S$ laminates. These results also proved that the fiber architecture, i.e. the laminate stacking sequence, greatly influences the lateral contraction results due to the changes in the Poisson's effect.

The agreement between the analytical solution, finite element simulation and experimental results was good. The analytical approach has advantages in that it saves computing time compared with a pure numerical analysis and is able to study the geometry and material parameters independently. Moreover, the treatment of the discontinuity of the boundary conditions adopted in the present analysis is generally applicable and can therefore be used for other problems involving different discontinuities. The approach can also be used for investigation of the in-plane biaxial compression-tension buckling and wrinkling behavior of composite plates and sandwich panels respectively, where the lateral contraction induced by non-uniform tension loading accelerates the onset of instability, thereby significantly decreasing the failure load.

The proposed approach can be easily extended for use with composite plates without any symmetry in the (x, y) plane and for thick composite plates and sandwich panels under plane strain conditions.

4.3. Buckling and wrinkling behavior in GFRP plates and sandwiches subjected to biaxial compression–tension loading

4.3.1. Introduction

Experimental and numerical investigations by Tuttle et al. (1999) and the current research (see Section 3.2) have shown that for composite laminates subjected to biaxial compression-tension loading, the transverse tension load has a stabilizing effect and therefore increases the buckling and ultimate loads. In contrast, for sandwich panels, despite the fact that wrinkling is a local buckling problem and is of the same nature as the buckling phenomena, a significant decrease of the wrinkling load was observed as a result of increasing the transverse tension load (see Section 3.3). The decrease was attributed to the lateral contraction induced by the Poisson's effect, which increased the imperfections. It can be concluded from these experimental investigations that increasing the transverse tension load has two simultaneous counteracting effects: (1) a positive stabilizing effect which increases the buckling/wrinkling loads and (2) a negative lateral contraction effect that accelerates the onset of buckling/wrinkling instability. These effects are functions of the geometry and material properties as well as the boundary conditions.

In order to take into account the numerous parameter combinations, an analytical model for the simulation of the buckling and wrinkling behavior of orthotropic FRP plates stabilized by a thick foam and subjected to biaxial compression-tension in-plane loading is presented in this section. The model is based on the exact analytical solution proposed by Veres and Kollár (2001) for the buckling of orthotropic plates under biaxial loading conditions. This model is modified by adding the foam core and the interaction between the foam core and the plate. The applicability of the model is examined by comparisons with experimental data for the buckling of composite plates (see Section 3.2) and the wrinkling of composite sandwich panels (see Section 3.3) subjected to in-plane biaxial compression-tension loading. The positive and negative effects of increasing the transverse tension load on buckling and wrinkling loads are assessed in detail. The model is used to demonstrate the effect of the relative stiffness between plate and foam core on the critical buckling and wrinkling loads. A transition from buckling to wrinkling is simulated by increasing the foam density.

4.3.2. Analytical model

A thin rectangular orthotropic plate with length L_x, width L_y, and thickness t, as shown in Figure 4.17, stabilized by an isotropic core that is assumed to be infinitely thick, is considered. The plate is either simply supported or clamped and in-plane compression and tension loads, F_{x0} and F_{y0}, act along the edges with different patterns which may cause uniform or non-uniform internal plane stress fields. The edge loads are proportionally increased by a load factor λ to λF_{x0} and λF_{y0}, until buckling or wrinkling occurs, where $\lambda=\lambda_{cr}$. The critical load factor, λ_{cr}, can be calculated by the Ritz method after minimization of the potential energy, Π_p, which is composed of:

$$\Pi_p = U_f + U_C + \Omega \tag{4.21}$$

where U_f is the bending strain energy of the plate, U_c is the strain energy of the core, which is a summation of the shear and normal transverse strain energy of the core, while Ω is the work performed by the external forces.

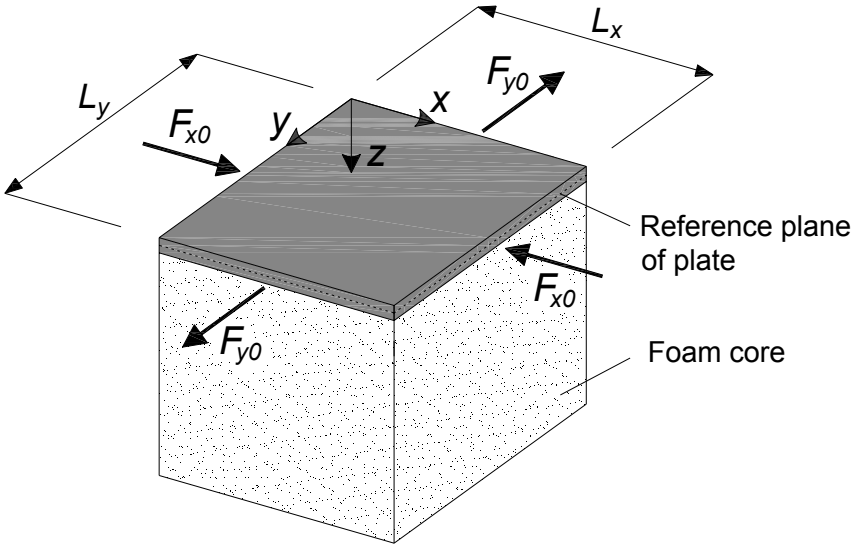

Figure 4.17. Rectangular plate with foam core subjected to biaxial compression-tension edge loads.

The bending strain energy of the orthotropic plate with symmetric lay-up is expressed as follows:

$$U_f = \frac{1}{2}\int_0^{L_x}\int_0^{L_y}\left(D_{11}\left(\frac{\partial^2 w}{\partial x^2}\right)^2 + D_{22}\left(\frac{\partial^2 w}{\partial y^2}\right)^2 + D_{66}\left(2\frac{\partial^2 w}{\partial x \partial y}\right)^2 + 2D_{12}\left(\frac{\partial^2 w}{\partial x^2}\right)\left(\frac{\partial^2 w}{\partial y^2}\right)\right) dx\, dy \tag{4.22}$$

in which D_{11} and D_{22} denote flexural stiffness components, D_{12} is the Poisson coupling stiffness, D_{66} is the twisting stiffness, and w is the deflection of the midplane, which represents the buckling wave form of the plate. If the lay-up of the plate is asymmetric, the strain energy terms resulting from the in-plane/out-of-plane coupling need to be added.

The strain energy in the core can be described by

$$U_C = \frac{1}{2}\int_0^{L_x}\int_0^{L_y}\int_0^{t_c}\left(\frac{{\sigma_{cz}}^2}{E_c}+\frac{{\sigma_{cxz}}^2+{\sigma_{cyz}}^2}{G_c}\right)dx\,dy\,dz \tag{4.23}$$

where t_c is the thickness of the core which is assumed to be infinite, σ_{cz}, σ_{cxz} and σ_{cyz} are the stresses in the isotropic core and are given by

$$\sigma_{cz} = E_c\frac{\partial w_c}{\partial z},\ \sigma_{cxz} = G_c\frac{\partial w_c}{\partial x},\ \text{and}\ \sigma_{cyz} = G_c\frac{\partial w_c}{\partial y} \tag{4.24}$$

in which E_c and G_c are the Young's and shear moduli of the core, w_c is the transverse deformation in the core corresponding to the buckling waves of the plate, as follows:

$$w_c(x,y,z) = w(x,y)\,Z(z) \tag{4.25}$$

where $Z(z)$ is the deflection function in z-direction that is taken from the model proposed by Plantema (1966). The model is based on the assumption that the plate deformation causes local deflection in the core, which decays in z-direction exponentially with the distance from the plate. Therefore, the deflection function $Z(z)$ is expressed as

$$Z(z) = e^{-Kz} \tag{4.26}$$

where K is an unknown model parameter.

The work of the applied stresses is given by

$$\Omega = \frac{\lambda t}{2}\int_0^{L_x}\int_0^{L_y}\left(\sigma_x\left(\frac{\partial w}{\partial x}\right)^2+\sigma_y\left(\frac{\partial w}{\partial y}\right)^2+\sigma_{xy}\left(\frac{\partial w}{\partial x}\right)\left(\frac{\partial w}{\partial y}\right)\right)dx\,dy \tag{4.27}$$

in which σ_x, σ_y and σ_{xy} are the internal in-plane stress values due to the external loads F_{x0} and F_{y0}.

In order to apply the Ritz method, it is necessary to assume a function for the deflection of the plate, w, which is assumed to take the following form:

$$w(x, y) = A X_i(x) Y_j(y) \tag{4.28}$$

where A is the deflection amplitude, $X_i(x)$ and $Y_j(y)$ are deflection functions that are defined according to the different boundary conditions and represent the buckling wave form of the plate in x- and y -directions, and i and j represent the number of buckling waves.

For different boundary conditions at the two edges along the x-axis of the plate, the deflection functions $X_i(x)$ is adopted by Veres and Kollár (2001) as follows, where $\xi = x/L_x$:

a) If the plate is simply supported at these two edges then $X_i(x)$ is defined by:

$$X_i(x) = \sin(i\pi\xi) \tag{4.29}$$

b) If the plate is clamped at one of these two edges, then $X_i(x)$ is as follows:

$$X_i(x) = \gamma_i \cos(\mu_i\xi) - \gamma_i \cosh(\mu_i\xi) + \sin(\mu_i\xi) - \gamma_i \sinh(\mu_i\xi) \tag{4.30}$$

in which μ_i and γ_i are described by the boundary condition at the other edge.

If the latter is simply supported:

$$\begin{cases} \mu_i \approx (i + 0.25)\pi \\ \gamma_i = \dfrac{\sin(\mu_i) - \sinh(\mu_i)}{\cosh(\mu_i) - \cos(\mu_i)} \end{cases} \tag{4.31}$$

If the latter is clamped, then μ_i and γ_i will be:

$$\begin{cases} \mu_i \approx (i + 0.5)\pi \\ \gamma_i = \dfrac{\cos(\mu_i) - \cosh(\mu_i)}{\sin(\mu_i) + \sinh(\mu_i)} \end{cases} \tag{4.32}$$

For $Y_j(y)$ the same formulae apply with ξ, x, L_x, i being replaced by η, y, L_y, j, respectively.

By choosing the deflection functions $X_i(x)$ and $Y_j(y)$ from Eqs. (4.29)-(4.32) according to the boundary conditions and substituting them into Eq. (4.28), the deflection of the plate and then, using Eq. (4.25), the deflection of the core are derived. Subsequently, by implementing the derived expressions for the deflections into Eqs. (4.22), (4.23) and (4.27), the bending strain energy of the plate, the strain energy of the core, and the work of the applied stresses are

obtained. By combining the results with Eq. (4.1) the total potential energy is obtained. The principle of minimum potential energy is then satisfied by

$$\frac{\partial \Pi_p}{\partial A} = 0 \tag{4.33}$$

Applying Eq. (4.33) leads to

$$\lambda_{i,j} = \frac{\dfrac{\alpha_1'^4 D_{11}}{L_x^4} + \dfrac{2\alpha_3'^2\alpha_4'^2(2D_{66}+D_{12})}{L_x^2 L_y^2} + \dfrac{\alpha_2'^4 D_{22}}{L_y^4} + \dfrac{1}{2}\left(E_c K + \dfrac{G_c}{K}\left(\dfrac{\alpha_3'}{L_x^2} + \dfrac{\alpha_4'}{L_y^2}\right)\right)}{t\left(\dfrac{\alpha_5'}{L_x^2} + \dfrac{\alpha_6'}{L_y^2} + \dfrac{\alpha_7'}{L_x L_y}\right)} \tag{4.34}$$

where:

$$\alpha_1' \equiv \sqrt[4]{\frac{1}{c_x^2}\int_0^1 \left(\frac{\partial^2 X_i}{\partial \xi^2}\right)^2 d\xi}\ ,\ \alpha_2' \equiv \sqrt[4]{\frac{1}{c_y^2}\int_0^1 \left(\frac{\partial^2 Y_j}{\partial \eta^2}\right)^2 d\eta} \tag{4.35-a}$$

$$\alpha_3' \equiv \frac{1}{c_x^2}\int_0^1 \left(\frac{\partial X_i}{\partial \xi}\right)^2 d\xi\,,\ \alpha_4' \equiv \frac{1}{c_y^2}\int_0^1 \left(\frac{\partial Y_j}{\partial \eta}\right)^2 d\eta \tag{4.35-b}$$

$$\alpha_5' \equiv \frac{1}{c_x^2 c_y^2}\int_0^1\int_0^1 \sigma_x Y_j \left(\frac{\partial X_i}{\partial \xi}\right)^2 d\xi\, d\eta \tag{4.35-c}$$

$$\alpha_6' \equiv \frac{1}{c_x^2 c_y^2}\int_0^1\int_0^1 \sigma_y X_i \left(\frac{\partial Y_j}{\partial \eta}\right)^2 d\xi\, d\eta \tag{4.35-d}$$

$$\alpha_7' \equiv \frac{1}{c_x^2 c_y^2}\int_0^1\int_0^1 2\sigma_{xy} \left(\frac{\partial X_i}{\partial \xi}\right)\left(\frac{\partial Y_j}{\partial \eta}\right) d\xi\, d\eta \tag{4.35-e}$$

$$c_x \equiv \sqrt{\int_0^1 X_i^2 d\xi}\ ,\ c_y \equiv \sqrt{\int_0^1 Y_j^2 d\eta} \tag{4.35-f}$$

The minimization of $\lambda_{i,j}$ in Eq. (4.34) with respect to parameter K results in

$$K = \sqrt{\frac{G_c}{E_c}\left(\frac{\alpha_3'}{L_x^2} + \frac{\alpha_4'}{L_y^2}\right)} \tag{4.36}$$

Substituting K according to Eq. (4.36) into Eq. (4.34) gives:

$$(\lambda_{cr})_{i,j} = \frac{\frac{\alpha_1'^4 D_{11}}{L_x^4} + \frac{2\alpha_3'^2\alpha_4'^2(2D_{66}+D_{12})}{L_x^2 L_y^2} + \frac{\alpha_2'^4 D_{22}}{L_y^4} + \frac{1}{2}E_c^{0.5}\left(1+G_c^{0.5}\right)\left(\frac{\alpha_3'}{L_x^2}+\frac{\alpha_4'}{L_y^2}\right)^{0.5}}{t\left(\frac{\alpha_5'}{L_x^2}+\frac{\alpha_6'}{L_y^2}+\frac{\alpha_7'}{L_x L_y}\right)} \quad (4.37)$$

The minimum value of the load factor λ is obtained by the iterative solution of Eq. (4.37) with respect to i and j and corresponds to the instability load, λ_{cr}, of the orthotropic plate stabilized by an isotropic foam core. The corresponding i and j represent the number of buckling waves.

When the foam is stiff, the instability load is obtained at a high number of waves (i and/or j) corresponding to the wrinkling load of a composite sandwich panel. However, when the foam core is extremely soft, which means the core stiffnesses, E_c and G_c, can be considered zero, the instability load represents the buckling load of composite plates. The transition from buckling to wrinkling failure mode can therefore be simulated with the model by increasing the foam density. This demonstrates the applicability of the model to the study of the buckling and wrinkling behaviors of the examined FRP structural components with regard to boundary conditions, material properties and geometrical characteristics.

The above-explained model is based on the classic linear buckling (bifurcation) solution, where the structure has no, or at least very few, imperfections so that the deformations prior to buckling are often considered negligible. For non-negligible imperfections, which are normally the case for composite structures, the prebuckling deformations lead to a nonlinear problem. The nonlinear solution is based on assuming an initial imperfection and loading the structure in increments. A conservative approach was selected in this model by setting the imperfection shape as the shape of the natural buckling pattern with an initial amplitude of A_0 as follows:

$$w_0(x,y) = A_0 X_i(x) Y_j(y) \quad (4.38)$$

The new total deformation, w_t, is based on the following linear equation:

$$w_t = \frac{w_0}{1-\left(F/F_{cr}\right)} \quad (4.39)$$

where F is the applied in-plane load and F_{cr} is the bifurcation load, which is obtained by:

$$F_{cr} = \lambda_{cr} F_{x0} \quad (4.40)$$

Eq. (4.39) was derived by Timoshenko and Gere (1951) for a strut or plate with an initial imperfection and is valid for plates on an elastic foundation (Allen 1969, Fagerberg and Zenkert 2005-b). Substituting Eqs. (4.28) and (4.38)-(4.40) into the w=wt–w_0 relationship results in:

$$A = \frac{A_0}{1-\left(F / F_{cr}\right)} - A_0 = \frac{F}{\lambda_{cr} F_{x0} - F} A_0 \tag{4.41}$$

Using Eq. (4.41), the nonlinear curves for the imperfect plate can be plotted in the F/F_{cr} – A plane for different initial imperfection amplitudes, A_0, as shown in Figure 4.18. Buckling can then be defined by the intersection point of the straight lines fitted to the small and large out-of-plane displacement parts of the curve.

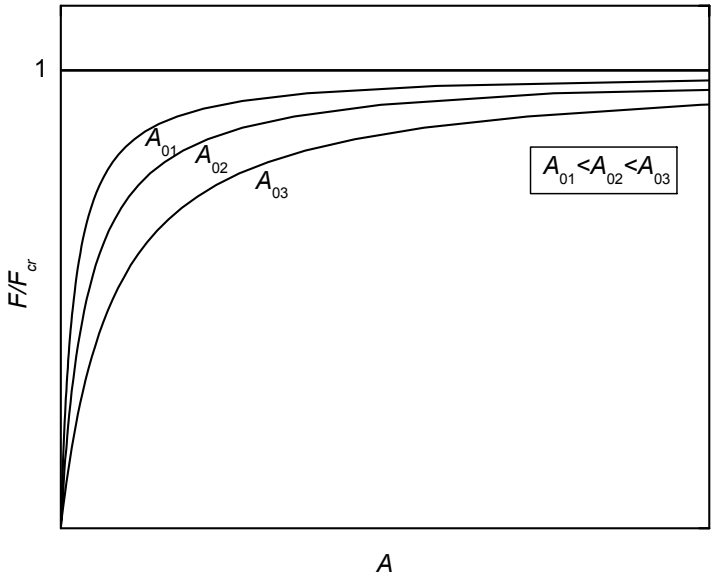

Figure 4.18. F/F_{cr} – Plane for different initial imperfection amplitudes.

4.3.3. Bases for validation of analytical model

The developed model was applied for the prediction of the buckling behavior of the examined GFRP plates and wrinkling behavior of GFRP sandwich panels presented in Sections 3.2 and 3.3. As described in these sections, the GFRP plates, with and without polyurethane (PU) foam support, consisting of unidirectional (UD) E-glass fiber fabrics and polyester resin, were fabricated using the hand lay-up technique. Compression and tension loads were applied

horizontally and vertically, respectively, over the four 150-mm edge lengths of the plates, which were fully clamped in the steel grips using four bolts (see Figures 3.4 and 3.23). The experiments were carried out for numerous specimens with different stacking sequences. Selected results of these studies are assessed by the presented analytical model in the following. For the buckling case, specimens with stacking sequences of $[0/90]_S$ and nominal thickness of 3.4 mm were selected, which consisted of four layers of almost unidirectional stitched E-glass fiber fabrics (0°: 960 g/m^2, 90°: 50 g/m^2) and polyester resin. For wrinkling, sandwich specimens with stacking sequences of [90/0] (i.e.: foam, 90° in tension, 0° in compression) and [±45] were chosen that consisted of two almost unidirectional stitched E-glass fabrics (0°: 370 g/m^2, 90°: 20 g/m^2) and polyester resin. The main mechanical properties of the UD lamina and sandwich components are summarized in Table 4.2.

Table 4.2. Properties of UD GFRP laminate and polyurethane foam.

Properties	PU-60	UD GFRP laminate	
		E-glass fabrics (0°: 960 g/m^2, 90°: 50 g/m^2) and polyester resin	E-glass fabrics (0°: 370 g/m^2, 90°: 20 g/m^2) and polyester resin
Longitudinal elastic modulus [MPa]	17.5	23500	25700
Transverse elastic modulus [MPa]	17.5	3800	4700
Shear modulus [MPa]	6.5	1800	2250

4.3.4. Modeling of in-plane stress field

The first step of the analytical solution is to obtain the internal plane stress field corresponding to the externally applied loads. According to the experimental set-up (see Figures 3.4 and 3.23), the external compression and tension loads were applied over a discrete 150- mm length of the 250-mm edge length. The set-up therefore represents an orthotropic rectangular plate subjected to partially uniform loads, as shown in Figure 4.19. An analytical approach to determine the in-plane stress field of composite rectangular plates subjected to partially uniform tension in one direction has been derived in Section 4.2.

Considering a partially distributed tension $q'=F_{y0}/2ct$ perpendicular to the two opposite edges of an orthotropic rectangular plate with dimensions of $L_x \times L_y$ and thickness t (according to Figure 4.3), the boundary conditions are defined as:

$$\begin{aligned} &x = \pm L_x/2 \rightarrow \sigma'_x = \sigma'_{xy} = 0 \\ &y = \pm L_y/2 \rightarrow \sigma'_{xy} = 0, \begin{cases} |x| \le c : \sigma'_y = q' \\ |x| > c : \sigma'_y = 0 \end{cases} \end{aligned} \tag{4.42}$$

where σ'_x, σ'_y and σ'_{xy} are the stress components induced by the partially distributed tension applied perpendicular to the two opposite edges of the plate in y-direction, see Figure 4.3.

The approach was based on the Green function hypothesis (Green 1939) combined with a modification performed on the solution proposed by Xu and Yu (1990). The difficulty in solving the stress field is based on the discontinuity in the boundary conditions at $x=\pm c$. To overcome this the problem was separated into three elastic problems (see Section 4.2.2.3). The elastic problems I and II are the half plane problems shown in Figure 4.4-(a) and (b). Their solution is obtained by the Galerkin function hypothesis. By superposing problems I and II, problem III is defined in order to satisfy the general boundary conditions given by Eq. (4.42). Problem III can be solved by introducing a polynomial stress function and using the Galerkin method to determine the constants of the polynomial function. Finally, similarly to Eq. 4.13, the stress field is obtained by the summation of the stress components of problems I, II and III, i.e.

$$\sigma'_x = \sigma'_{x,I} + \sigma'_{x,II} + \sigma'_{x,III} \tag{4.43-a}$$

$$\sigma'_y = \sigma'_{y,I} + \sigma'_{y,II} + \sigma'_{y,III} \tag{4.43-b}$$

$$\sigma'_{xy} = \sigma'_{xy,I} + \sigma'_{xy,II} + \sigma'_{xy,III} \tag{4.43-c}$$

where $\sigma'_{x,n}$, $\sigma'_{y,n}$, $\sigma'_{xy,n}$ ($n=I, II, III$) are the stress components in the (x, y) plane obtained by solving problems I, II and III. Similarly, the stress components σ''_x, σ''_y and σ''_{xy} are obtained for the partially distributed compression $q''=F_{x0}/2ct$ perpendicular to the two opposite edges of the plate in x-direction. By superposing the two solutions, the stress distribution of the orthotropic rectangular plate subjected to biaxial compression-tension, q'' and q', as shown in Figure 4.19, is obtained by:

$$\sigma_x = \sigma'_x + \sigma''_x \tag{4.44-a}$$

$$\sigma_y = \sigma'_y + \sigma''_y \tag{4.44-b}$$

$$\sigma_{xy} = \sigma'_{xy} + \sigma''_{xy} \tag{4.44-c}$$

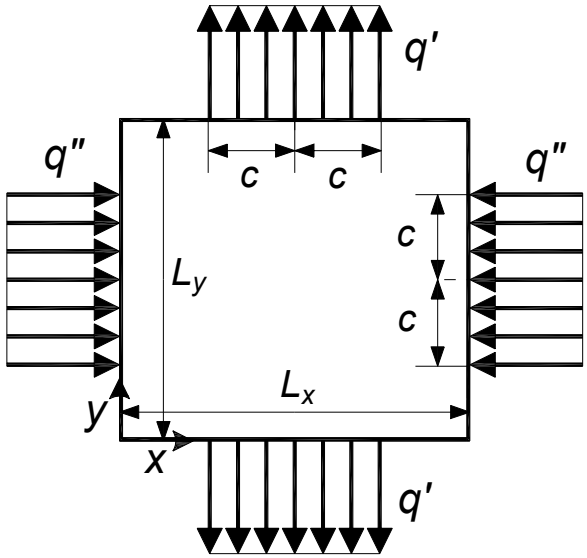

Figure 4.19. Orthotropic rectangular plate subjected to partially uniform loads.

4.3.4.1. Stress field in GFRP plates

The in-plane stress field in the GFRP plate specimens with stacking sequence of $[0/90]_S$, described in Section 3.2.2, was derived from Eqs. (4.44). To avoid computational complexity caused by introducing the exact solution of Eqs. (4.44) into the analytical solution described in Section 4.3.2, the derivations were simplified. The resulting simplified in-plane stress fields obtained from Eqs. (4.44) are as follows:

$$\sigma_x(x,y) = \left(\frac{F_{x0}}{L_x t} + \left(\sigma'_{centre}\right)\Big|_{F_{y0}} \times \sin\left(\frac{\pi x}{L_x}\right) \right) \times \sin\left(\frac{\pi y}{L_y}\right) \tag{4.45}$$

$$\sigma_y(x,y) = \left(\frac{\beta F_{x0}}{L_y t} + \frac{\left(\sigma'_{centre}\right)\Big|_{F_{y0}}}{\beta} \times \sin\left(\frac{\pi y}{L_y}\right) \right) \times \sin\left(\frac{\pi x}{L_x}\right) \tag{4.46}$$

where $\beta=F_{y0}/F_{x0}$, $\left(\sigma'_{centre}\right)\Big|_{F_{y0}}$ is the compressive stress in x-direction (according to Eq. (4.43-a)), at the centre of the plate due to the partially distributed tension of $F_{y0}/2ct$. In fact, the term $\left(\sigma'_{centre}\right)\Big|_{F_{y0}} \times \sin(\pi x/L_x) \times \sin(\pi y/L_y)$ in Eq. (4.45) represents the lateral contraction distribution in the (x, y) plane which is induced by the tension load.

The stress results in x-direction, i.e. the solution of Eq. (4.43-a), obtained for $[90/0]_s$ plates subjected to the partially distributed tension load in only one direction, showed that the compression stress at the centre of the plate is as follows:

$$\left(\sigma'_{centre}\right)\Big|_{F_{y0}} = -0.12 \times \frac{F_{y0}}{2ct} \tag{4.47}$$

The in-plane shear stress is negligible compared to σ_x and σ_y, therefore, $\sigma_{xy}(x, y) = 0$. The validation of the simplified Eqs. (4.45) and (4.46) was performed by comparing the stress field results obtained for the $[0/90]_S$ lay-up with the results from the exact solutions obtained from Eqs. (4.44). Figure 4.20 shows the stress components σ_x and σ_y along the x-axis at the center ($y = L_y/2$) for β=-2. The comparison shows that Eqs. (4.45) and (4.46) appropriately represent the exact solution given by Eqs. (4.44). Furthermore, Figure 4.21 compares the analytical (Eqs. (4.45) and (4.46)) and experimental transverse strain results, ε_x, of $[0/90]_S$ as a function of the distance x at y = 119 mm (position of strain gages (1) to (5)) and at different combinations of tension and compression loads. A good agreement between the results was found.

4.3.4.2. Stress field in GFRP sandwich panels

An approach similar to that adopted in Section 4.3.4.1 can be applied to obtain the in-plane stress field in GFRP plates supported by foam. Since the stiffness of the foam is significantly lower than the stiffness of the GFRP plate it can be assumed that the out-of-plane stress components of the foam are negligible. Therefore, the classic laminate theory (CLT) can be used for calculation of the in-plane elastic constants considering the foam as one single layer.

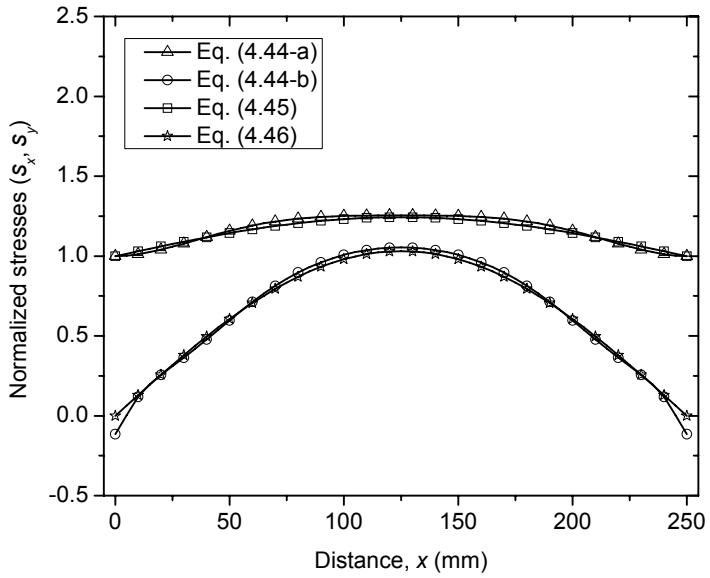

Figure 4.20. Biaxial compression-tension buckling: Normalized stresses, $S_m=\sigma_m$/applied stresses in m-direction (m= x, y), along x at center (y = $L_y/2$) of $[0/90]_S$ plate.

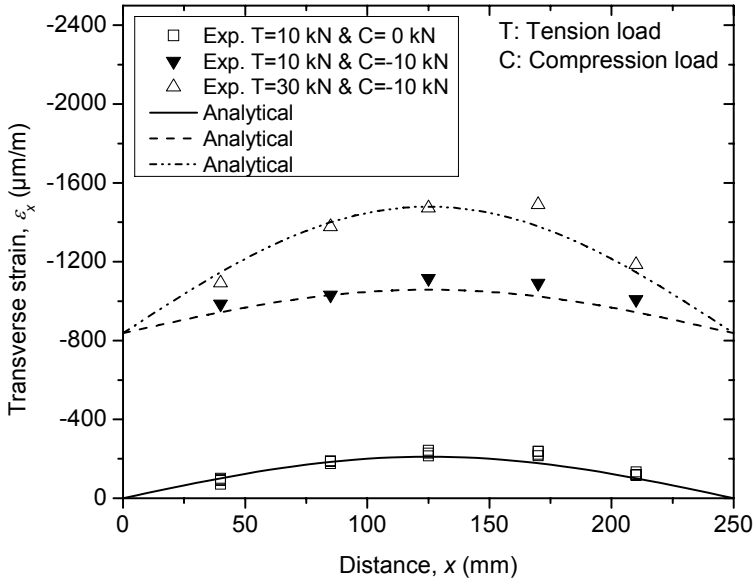

Figure 4.21. Biaxial compression-tension buckling: comparison of experimental and analytical transverse strain results, ε_x, of $[0/90]_S$ as function of distance x at y = 119 mm (position of gages (1) to (5)) at different combinations of tension and compression loads.

Due to the supporting frame, see Figures 3.22 and 3.23, the compressive stress in x-direction is uniformly distributed over the height of the area without the supporting frame. Moreover, the

supported part of the sandwich panel, which is stiffer than the unsupported part, contributes more to transferring the tension load along the *y*-direction, thereby causing more compressive deformation to the unsupported area along *x*-direction.

To take these effects into account, the expressions for the stress field represented by Eqs. (4.45) and (4.46) were slightly modified as follows:

$$\sigma_x(x,y)=\left(\left(\sigma'_{centre}\right)\Big|_{F_{y0}}\times F_C\times\sin\left(\pi\left(0.48\frac{x}{L_x}+0.26\right)\right)+\frac{F_{x0}}{L'_x t}\right) \tag{4.48}$$

$$\sigma_y(x,y)=\left(\frac{\left(\sigma'_{centre}\right)\Big|_{F_{y0}}}{\beta}+\frac{\beta F_{x0}}{L'_y t F_C}\right)\times\sin\left(\pi\left(0.48\frac{x}{L_x}+0.26\right)\right) \tag{4.49}$$

where L'_x and L'_y are total specimen width and height (250 mm × 250 mm) and L_x, L_y and t are the width, height and thickness of the un-supported area. Again, the in-plane shear stress, $\sigma_{xy}(x,y)$, is negligible compared to σ_x and σ_y, and can be assumed as being equal to zero. F_C is the correction factor for the extra lateral contraction induced by the supporting frame. This factor was determined as being 1.22 by fitting the mathematical model to the FE solution. Again, $\left(\sigma'_{centre}\right)\Big|_{F_{y0}}$ is the compressive stress in *x*-direction (according to Eq. (4.43-a)), at the center of the plate due to the partially distributed tension of $F_{y0}/2ct$, in the case without the supporting frame. The stress results in *x*-direction (acc. to Eq. (4.43-a)), obtained for [90/0] and [±45] laminates subjected to the partially distributed tension load in only one direction showed that the compression stresses at the center of the plate, $\left(\sigma'_{centre}\right)\Big|_{F_{y0}}$, are as follows:

$$\text{[90/0]: } \left(\sigma'_{centre}\right)\Big|_{F_{y0}}=-0.21\times\frac{F_{y0}}{2ct} \tag{4.50}$$

$$\text{[±45]: } \left(\sigma'_{centre}\right)\Big|_{F_{y0}}=-0.31\times\frac{F_{y0}}{2ct} \tag{4.51}$$

The modeling Eqs. (4.48)-(4.49) and the correction factor applied for the stress field formulation are validated by comparing the analytical and experimental strain results (see Section 3.3) (both horizontal and vertical) obtained at the center of the plate as the tension load was increased up to 20 kN, see Figure 4.22. Furthermore, Figure 4.23 shows the strain results at the

same position as the compression load was increased up to 4.5 kN while the tension load was kept constant at 20 kN. In both cases, good agreement between the analytical and experimental results was found.

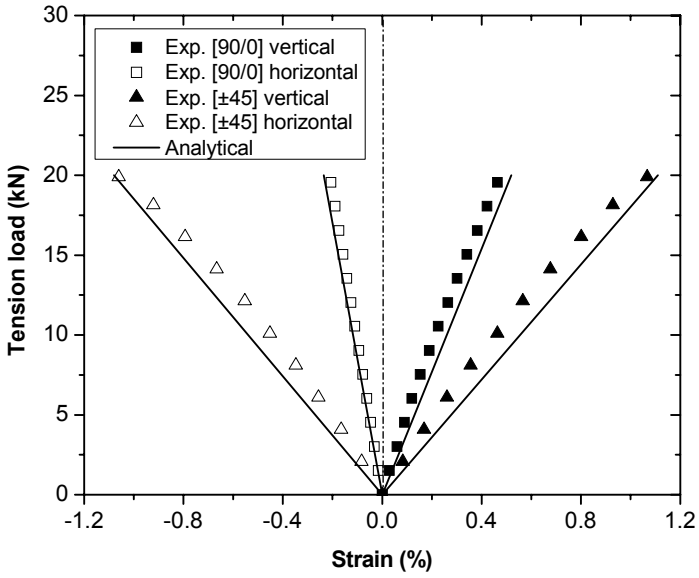

Figure 4.22. Biaxial compression-tension wrinkling: comparison of experimental and analytical strain results at different transverse tension loads for [90/0] and [±45] sandwiches.

The modeling Eqs. (4.48)-(4.49) and the correction factor applied to the stress field formulation are validated by comparing the analytical and experimental strain results (see Section 3.3) (both horizontal and vertical) obtained at the center of the plate as the tension load was increased up to 20 kN, see Figure 4.22. Furthermore, Figure 4.23 shows the strain results at the same position as the compression load was increased up to 4.5 kN while the tension load was kept constant at 20 kN. In both cases, good agreement between the analytical and experimental results was found.

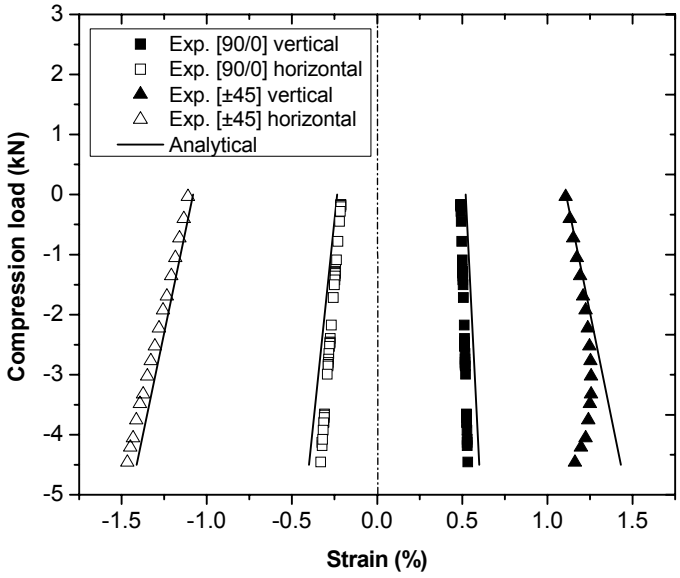

Figure 4.23. Biaxial compression-tension wrinkling: comparison of experimental and analytical strain results at 20-kN tension load and different compression loads for [90/0] and [±45] sandwiches.

4.3.5. Validation and discussion

4.3.5.1. Buckling of GFRP plates

The new model was applied for the estimation of the buckling loads of the examined GFRP plates. Eq. (4.37) was iteratively solved for different values of i, considering j = 1 since one buckling wave was expected in the y-direction where the specimen was under tension. The minimum λ, resulting from this process, λ_{cr}, represented the linear buckling (bifurcation) load for the $[0/90]_s$ specimens (without taking initial imperfections into account) and was calculated with and without the effect of lateral contraction, i.e. for $\left(\sigma'_{centre}\right)\Big|_{F_{y0}} \neq 0$ and $=0$. The theoretical results are shown in Figure 4.24 together with the corresponding experimental results as a function of the applied tension load.

For a 0-kN tension load, the mode shape (i=1) and buckling load (12.9 kN) of both theoretical solutions coincided. The stabilizing effect was obvious when the tension load was applied on the GFRP plate. As from a tension load of 5.5 kN the buckling load could be increased by 47% to 19 kN when the lateral contraction effect was not considered. Lateral

contraction reduced this increase to 39%, indicating an 8% negative effect owing to the lateral contraction of the transverse tension.

The lateral contraction effect became more significant as the mode shape changed from one to two between 5-kN and 10-kN tension. At 30 kN, the buckling load, without taking the lateral contraction effect into account, increased by 98% to 25.6 kN. The solution with the lateral contraction effect showed a 26% reduction of the buckling to 22.2 kN. Simultaneous increments due to the lateral contraction effect and decrements due to the stabilizing effect caused by increasing the number of buckling waves at higher tension loads made the buckling load approach a plateau at high tension loads, as shown in Figure 4.24.

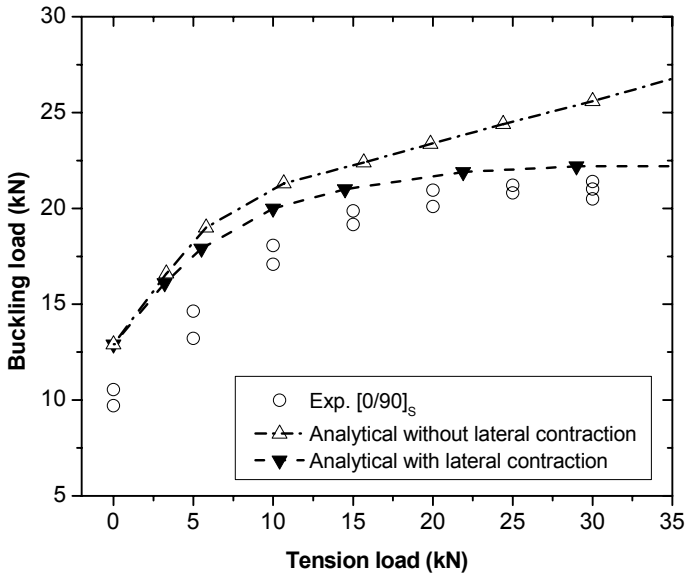

Figure 4.24. Biaxial compression-tension buckling: comparison of experimental and analytical buckling loads at different transverse tension loads for $[0/90]_S$ laminates.

The above results correspond to the linear buckling solution, without taking into account any imperfections, and therefore overestimated the buckling loads. As demonstrated in Section 3.2.5, applying tension exponentially reduced initial imperfections from 0.15 mm to 0.03 mm by increasing the tension load from 0 to 30 kN. Using these initial imperfections (which vary according to the tension load) and plotting the $F/F_{cr} - A$ plane for different imperfection amplitudes (see Figure 4.18), the buckling loads were determined as the intersection points of the

straight lines fitted to the small and large out-of-plane displacement parts of the curves. Considering initial imperfections significantly improved the theoretical predictions, as shown in Figure 4.25 (curves take the lateral contraction effect into account).

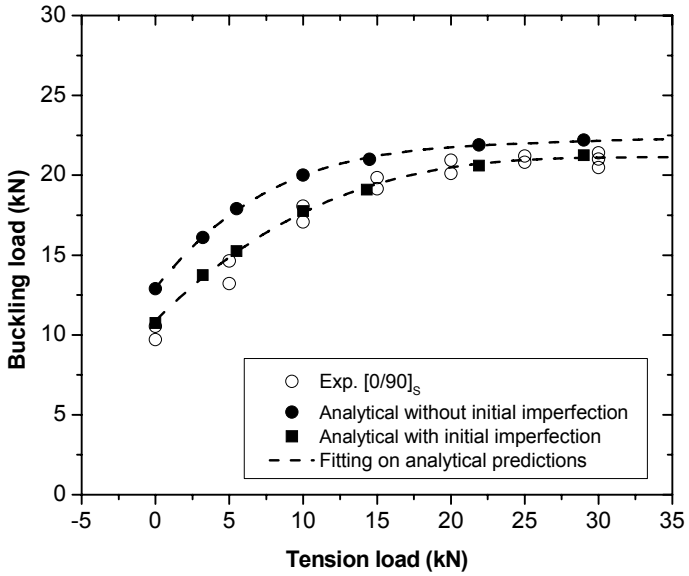

Figure 4.25. Biaxial compression-tension buckling: comparison of experimental and analytical results (with /without initial imperfection) at different transverse tension loads for $[0/90]_S$ laminates.

4.3.5.2. Wrinkling of sandwich panels

The supporting frame obliged the wrinkling failure to occur in the unsupported area, whereas the relatively high stiffness of the supported part satisfied the assumed clamped boundary conditions for the unsupported area. Therefore, for the model application, L_x, L_y and thickness t were defined by the dimensions of the unsupported area, which in [mm] were 120, 220 and 1.1, respectively. Since the sandwich plate was subjected to tension in y-direction, one buckling wave was expected in this direction (j = 1). The minimization of λ_{cr} from Eq. (4.37) with respect to i resulted in the wrinkling loads of the sandwich panels, which are shown in Figure 4.26 for sandwiches with stacking sequences of [90/0] and [±45]. The analytical results are shown as a function of the applied tension load with and without the lateral contraction effect, together with the experimental data; initial imperfections had not yet been considered.

For 0-kN tension, the analytical solutions with and without lateral contraction converged to the same wrinkling loads, 22.2 kN and 20.1 kN for [90/0] and [±45], respectively. For both cases, the minimum λ_{cr} was calculated for i = 7. For this mode shape, with a high number of waves, the stabilizing effect of the tension was very low, increasing the wrinkling loads by less than 1%. On the other hand, because of the high number of waves, the negative effect of the lateral contraction became significant; the wrinkling loads were decreased by 21% for [90/0] and 38% for [±45] specimens. Superposition of the two effects of tension resulted in a decrease of the wrinkling loads, as was also proved by the experimental results.

As for the buckling case, the theoretical results overestimated the wrinkling loads when no initial imperfections were taken into account and, in addition, the asymmetry of the face sheets was disregarded. Since the face sheets were laid up on the smooth foam surface, an initial imperfection of 0.03 mm was considered, according to the experimental results presented in Section 3.2.5 where similar GFRP plates were also fabricated by hand lay-up. An additional imperfection was introduced to compensate for the asymmetry. This imperfection was assumed as being a linear function of the tension load. The maximum values for [90/0] and [±45] at 20-kN tension were determined as being 0.035 mm and 0.029 mm according to the FE analyses performed (described in the following sections). The theoretical results, considering the initial imperfection and lateral contraction effect, are also compared to the experimental results in Figure 4.26. The predictions were significantly improved compared to those for the linear buckling solution.

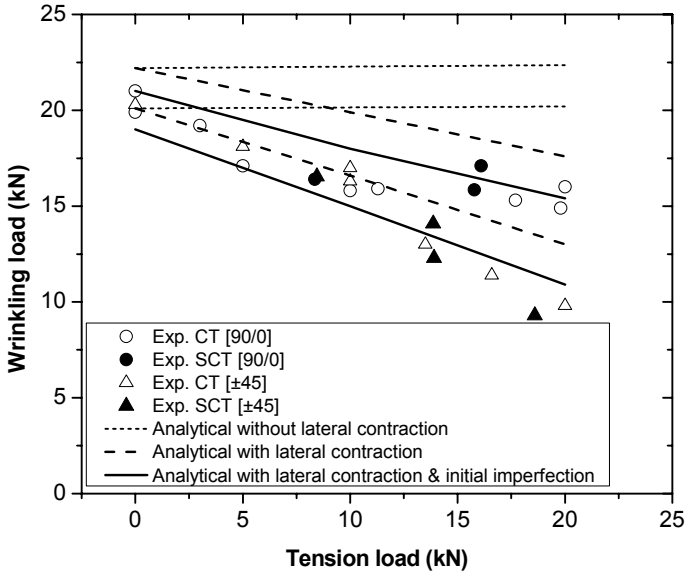

Figure 4.26. Biaxial compression-tension wrinkling: comparison of experimental and analytical wrinkling loads for [90/0] and [±45] laminates at different transverse tension loads for [90/0] and [±45] sandwiches.

4.3.6. Influence of relative plate and foam core stiffness on buckling and wrinkling loads

A case study is presented in this section to demonstrate how the relative stiffness of the GFRP plates and foam core influence the effect of transverse tension on the buckling and wrinkling loads. The new model allows the transition from biaxial compression-tension plate buckling to biaxial compression-tension sandwich wrinkling to be easily demonstrated.

In this context, an orthotropic GFRP plate of 250-mm length by 250-mm width and 6- mm thickness consisting of eight layers of unidirectional stitched E-glass fabrics (0°: 370 g/m^2, 90°: 20 g/m^2) and polyester resin with stacking sequence of $[0/90]_{2S}$ is modeled. The properties used for the UD lamina are those shown in Table 4.2. The GFRP plates are assumed as being ideal with no initial imperfections; the plates are stabilized by an isotropic foam core assumed to be infinitely thick. Each edge of the plate is assumed to be clamped and in-plane compression and tension loads, F_{x0} and F_{y0}, are applied along the edges in a partially uniform pattern, over 150-mm lengths, similar to Figure 4.19. The biaxial loading causes a non-uniform internal plane stress field, as described by Eqs. (4.45) and (4.46). Analytical results for two load cases are derived: for

0-kN tension load, for which the corresponding critical buckling load is designated as $\lambda_{cr,\beta=0}$, and equal compression-tension loading, i.e. $\lambda_{cr,\beta=-1}$. In both solutions, the buckling mode shape in *y*-direction (tension direction) is assumed as being one, $j = 1$. The dimensionless increment of the buckling load due to the transverse tension is defined by:

$$\Delta_{Inc} = \frac{\lambda_{cr,\beta=-1} - \lambda_{cr,\beta=0}}{\lambda_{cr,\beta=0}} \times 100 \tag{4.52}$$

Δ_{Inc} is calculated for a range of compressive/tensile foam stiffnesses varying from 0 (no foam) to 250 MPa, which is selected based on commercially available high density foams, e.g. AIREX T90-3A (160-220 MPa) with a density of 320 kg/m^3. The calculations are carried out for two cases: (I) without the lateral contraction effect of tension, which means that $\left(\sigma'_{centre}\right)\Big|_{F_{y0}} = 0$ in Eqs. (4.45) and (4.46), and (II) with the lateral contraction effect in which $\left(\sigma'_{centre}\right)\Big|_{F_{y0}}$ for $[0/90]_{2S}$ is determined using Eq. (4.43-a) as follows:

$$\left(\sigma'_{centre}\right)\Big|_{F_{y0}} = 0.15 \times \frac{F_{y0}}{2ct} \tag{4.53}$$

Figure 4.27 shows the resulting Δ_{Inc} as a function of the foam stiffness, E_c. The positive effect of transverse tension on the buckling load descends exponentially with the increase of the stiffness of the foam. The reduction is discrete and each step corresponds to a specific number of buckling waves in *x*-direction, *i*. The number of the buckling waves increases with the foam stiffness. When the lateral contraction is taken into account, its negative effect together with the decreased stabilizing effect can derive negative Δ_{Inc} values for high core stiffness. These results are compatible with the buckling and wrinkling behavior observed in Sections 4.3.5.1 and 4.3.5.2.

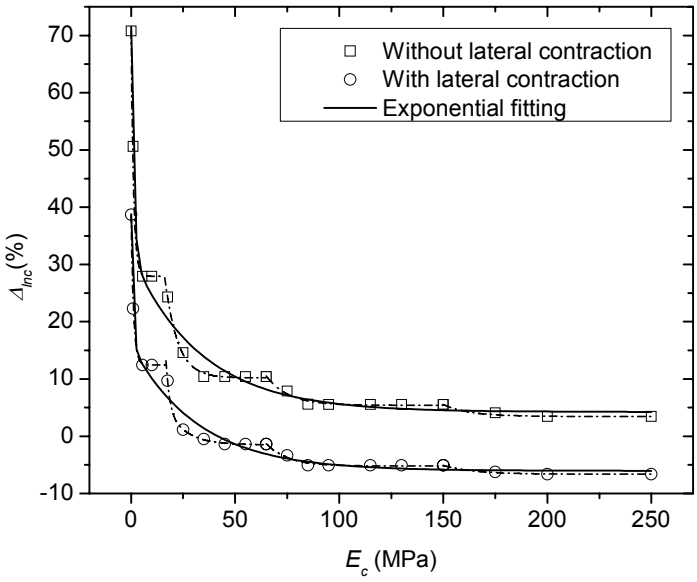

Figure 4.27. Dimensionless increment of buckling load due to transverse tension, Δ_{Inc}, as a function of foam stiffness, E_c.

The effect of various plate thicknesses (3, 6 and 8 mm) on Δ_{Inc} is shown in Figure 4.28 for the case without lateral contraction effect. The effect of transverse tension on buckling load is influenced not only by the foam core stiffness but also by the plate thickness and plate stiffness. Therefore the decrease of Δ_{Inc} is less pronounced for thicker plates with lower foam stiffness. Indeed, the relative foam to plate stiffness is the key parameter. Figure 4.29 shows the obtained Δ_{Inc} for different plate thicknesses as a function of E_c/D_{11}, where D_{11} is the bending stiffness of the plate in x-direction (compression direction). The results demonstrate that Δ_{Inc} can be appropriately predicted as an exponential function of E_c/D_{11}. The exponential behavior demonstrates that the effect of tension approaches zero at relatively high core stiffness or very low plate bending stiffness. For this case this means that the loads obtained from the uniaxial buckling/wrinkling solution can be considered as a conservative solution of the biaxial compression-tension problem. Knowing the ratio between the core stiffness and the plate bending stiffness, the prediction can furthermore help to extract the effect of tension from the biaxial compression-tension buckling/wrinkling problem and transform the problem into a uniaxial compression problem of considerably less complexity. This approach can be used for the prediction of the shear wrinkling loads of sandwich panels, since shear wrinkling can be

considered as an in-plane biaxial compression-tension wrinkling problem, consisting of the interaction between the compression and transverse tension stress fields.

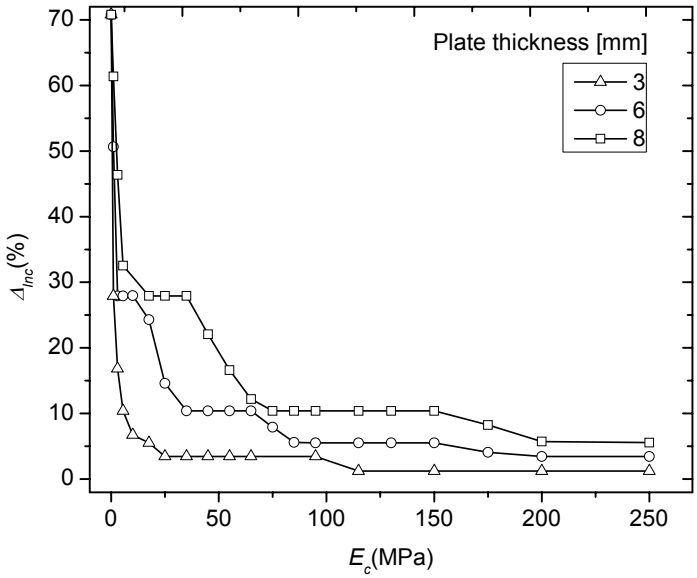

Figure 4.28. Dimensionless increment of buckling load due to transverse tension, Δ_{Inc}, for various plate thicknesses as function of foam stiffness, E_c.

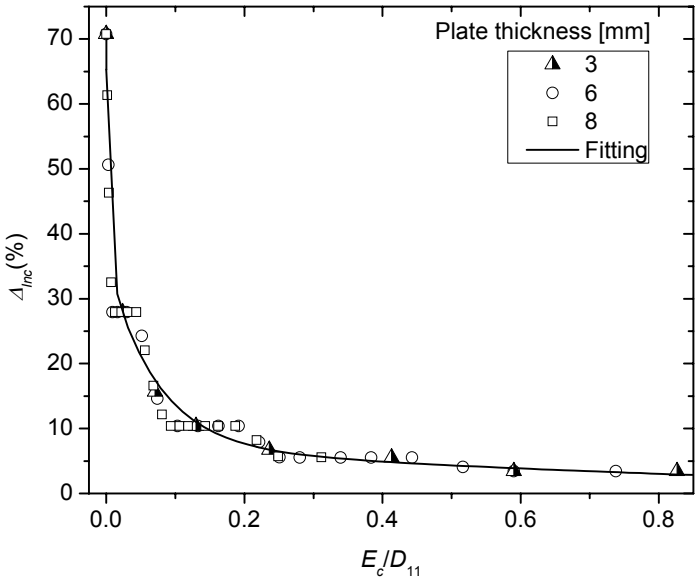

Figure 4.29. Dimensionless increment of buckling load due to transverse tension, Δ_{Inc}, for various plate thicknesses as function of relative foam stiffness and plate bending stiffness, E_c/D_{11}.

4.3.7. Concluding remarks

An analytical study was performed of the buckling/wrinkling behavior of composite plates and sandwich panels subjected to in-plane biaxial compression-tension loading. A model was developed based on adding the interaction between the foam core and plate to the analytical solution proposed by Veres and Kollár (2001) for the buckling of clamped and/or simply supported orthotropic plates under biaxial loading conditions. The model is able to simulate the buckling and wrinkling behavior of the examined FRP structural components with regard to boundary conditions, material properties and geometrical characteristics. The following conclusions were drawn:

1) For both experimental investigations carried out in the present work (see Sections 3.2 and 3.3), analytical solutions proved that transverse tension induced two simultaneous counteracting effects: stabilizing effect and lateral contraction. The stabilizing effect tends to push the plate back to the median plane and thereby delays the onset of buckling/wrinkling instability. In contrast, the lateral contraction accelerates the bending of the plate, leading to a significant decrease in the buckling/wrinkling loads.

2) In the biaxial compression-tension buckling behavior of symmetric GFRP plates, at low transverse tension loads, where the number of buckling wave was low, the stabilizing effect was much greater than the lateral contraction effect. Changing the buckling mode shape to higher wave numbers started to reduce the stabilizing effect and increase the lateral contraction effect. Therefore, the buckling loads approached a plateau at higher tension loads.

3) In the biaxial compression-tension wrinkling behavior of GFRP sandwiches, the lateral contraction effect of transverse tension became more dominant than the stabilizing effect, since the number of waves was high due to the bonded foam. Consequently the wrinkling loads decreased with increasing transverse tension.

4) The analytical model successfully modeled the stabilizing and lateral contraction effects and thus could predict the influence of an increasing transverse tension load on the buckling and wrinkling behavior of GFRP composite laminates and sandwich panels. The linear solution that did not consider the initial imperfections overestimated the

experimental results while the nonlinear solution, by taking into account the initial imperfections, improved the predictions.

5) A parametric study showed that the influence of transverse tension on biaxial compression-tension buckling/wrinkling loads could be predicted as a function of the relative stiffness of foam and plate. In order to develop a more general prediction model, other parameters such as aspect ratio or stacking sequences need to be integrated.

4.4. Finite element modeling of wrinkling behavior in sandwich panels

4.4.1. Linear buckling analysis

Linear elastic finite element (FE) buckling analysis was performed using ANSYS v-10 software (which does not differentiate between buckling and wrinkling in the eigen-value solution). The specimens were modeled in 3D using 8-node layered shell elements (Shell-91) for the face sheets and 20-node structural solid elements (Solid-95) for the foam. Figure 4.30 shows the mesh; 14776 elements were used in total. According to the recommendations made by Fagerberg (2003), the element length inside the support frame (where wrinkling occurred) was selected as being shorter than one quarter of the wrinkling wavelength. Also, the core was modeled with six layers through the thickness. The material properties given in Table 4.2 were used. To simulate the experimental boundary conditions, the areas where the specimen was clamped by the grips (see Figure 3.24) were restrained against rotation and out-of-plane displacement as well as in-plane displacement in the direction orthogonal to the grip movement. The wrinkling loads were determined as the Euler buckling loads by performing the eigen-value buckling analysis according to the Lanczos method (which is implemented in ANSYS). The first resulting buckling modes obtained for [90/0] and [±45] specimens are shown in Figure 4.31. The buckling modes consisted of several parallel waves. During the experiments, only one of these local waves grew rapidly up to ultimate failure; the other waves could not be detected. Figure 4.32 shows the resulting wrinkling loads as a function of the applied tension loads, together with the experimental data. The results confirm the negative effect of the increasing transverse tension on the wrinkling loads; however, they considerably overestimate the experimental results, as

commonly occurs in the case of plate buckling where the Euler buckling load represents an upper limit of the ultimate load.

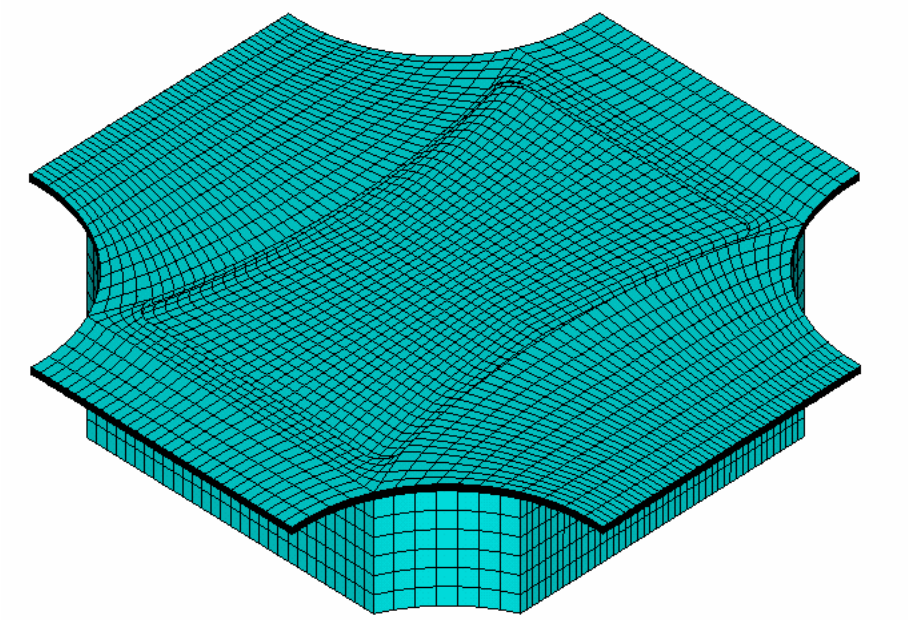

Figure 4.30. Finite element model of sandwich specimen.

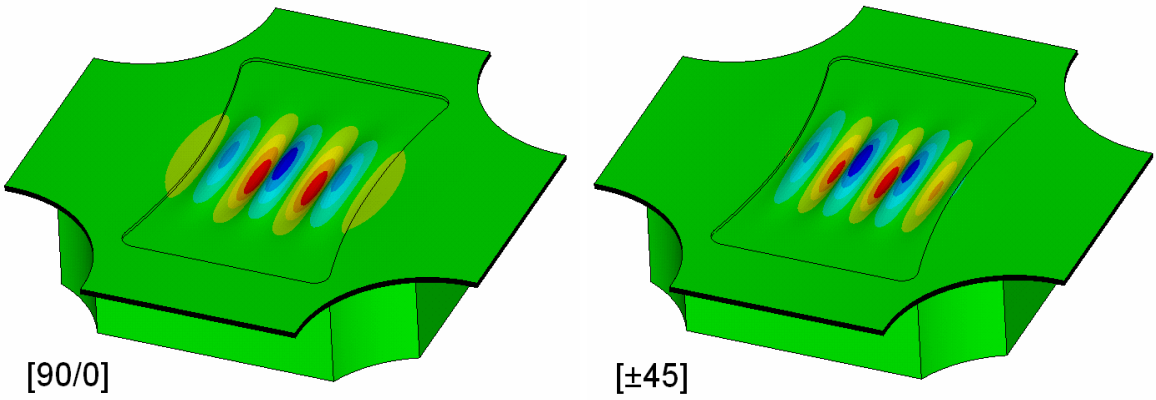

Figure 4.31. First "buckling" mode of [90/0] and [±45] specimens.

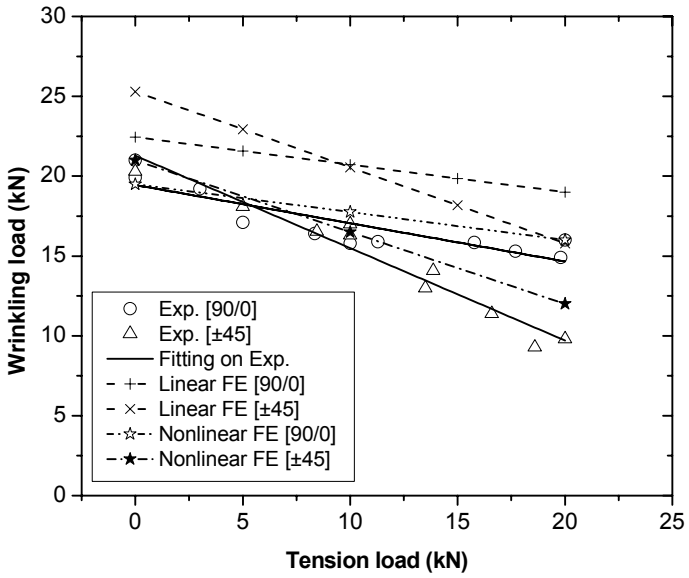

Figure 4.32. Comparison of experimental and numerical wrinkling loads at different transverse tension loads.

4.4.2. Nonlinear static analysis

Like every structural component in real applications, the specimens - and the face sheets in particular - exhibited out-of-plane imperfections that evidently changed the ideal Euler bifurcation behavior to a higher order bending behavior. Nonlinear static analysis was therefore performed by assuming an initial imperfection and loading the structure in increments. By activating the large displacement feature, the stiffness of the structure was automatically updated between loading increments to incorporate deformation, which affects the bending behavior. A conservative approach was selected by considering the imperfection shape as being equal to the eigen-mode shape of the specimen (obtained from the linear buckling analysis). The maximum amplitude was set to 0.03 mm, i.e. 2.5% of the thickness of the face sheet, according to the results given in Section 3.2.5 where similar GFRP laminates, also fabricated by hand lay-up, were used. The same loading sequence was used as in the CT experiments, see Section 3.3.3: tension was applied in the first time step (without any substep) and kept constant; in the second time step compression was then applied in 20 substeps up to the point where the specimen clearly moved into the post-buckling range. Throughout the solution, "automatic time step" was defined as being "off" in order to not apply any linear or nonlinear step search methods (such as the Newton-Raphson or Arc-Length methods). Convergence criteria were set to 0.1% for force and moment. The resulting maximum out-of-plane displacement responses obtained for [90/0] and

[±45] specimens by increasing the compression load at different tension load levels are shown in Figure 4.33. The results show a stiff and linear behavior at low compression. At higher compression, the behavior changed to nonlinear, exhibiting the well-known post-buckling behavior that occurs in the case of large out-of-plane displacements. Similar to buckling, the wrinkling load (reached at the end of the linear part) should be differentiated from the higher ultimate load, see Section 3.2.3. In reality, however, the local displacement increase at the wrinkling load level causes local foam failure and subsequent fiber failure (as observed in the experiments), both linked to a drop in the load before the post-wrinkling stage was reached. Wrinkling and ultimate loads therefore coincide. The sensitivity of the above results to the initial imperfection selection was checked by doubling the amplitude to 0.06 mm; however, less than 10% deviation in the results was observed.

Straight lines were fitted to the pre- and post-wrinkling branches of the load-out-of-plane displacement curves to determine the wrinkling loads at the intersection points; the results are shown in Figure 4.32. The nonlinear analysis again confirms the negative effect of the increasing transverse tension load on the wrinkling loads, which were also 15% (on average) lower than those of the eigen-value solution and agreed much better with the experimental results.

The typical six half wave out-of-plane displacement responses along the horizontal symmetry axis of the [±45] specimens, in the part without supporting frame according to Figure 4.31 (right), are shown in Figure 4.34 for different tension-compression load combinations. The initial imperfections, shown by the curve without any load (0, 0), were increased by 60% by applying a 20-kN tension load (curve (20, 0)). A nonlinear increase in the amplitudes is observed after the application of the increasing compression loads. The maximum amplitude, shown in the 3rd half wave from the left, increased from 0.08 mm in the (20, 6) case to 0.45 mm in the (20, 15) case.

4.4.3. Discussion and conclusions

As demonstrated by comparing the (0, 0) and (20, 0) curves in Figure 4.34, during stretching of the plate with a high number of waves, the lateral contraction effect of tension seemed more dominant than its stabilizing effect and therefore accelerated the second-order out-of-plane displacements and decreased the wrinkling loads with increasing transverse tension, as observed in the experiments and proven by the FE analyses (see Figure 4.32). Both linear and nonlinear FE

results confirmed the negative effect of the increasing transverse tension on the wrinkling loads. The linear solution considerably overestimated the experimental results while the nonlinear FE solution, by taking into account the initial imperfections, improved the predictions, particularly at lower tension loads.

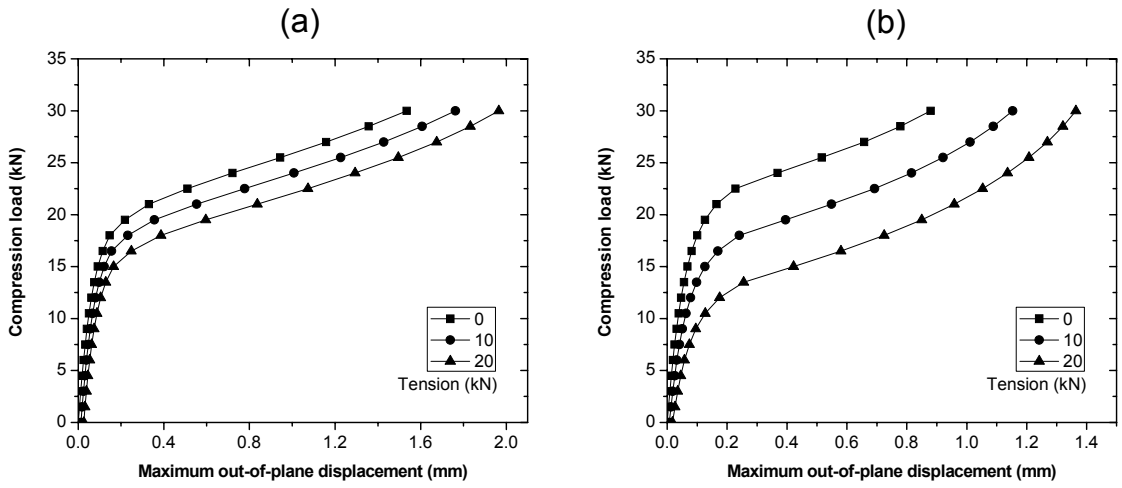

Figure 4.33. Compression load vs. out-of-plane displacement responses of wave with maximum peak at different transverse tension loads for [90/0] specimens

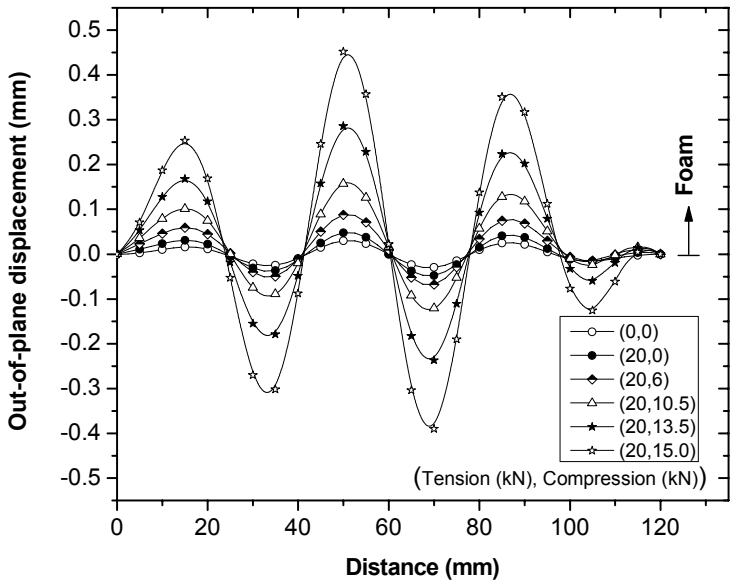

Figure 4.34. Out-of-plane displacement of [±45] specimens along horizontal symmetry axis at different load combinations.

5 Instability of cell-core sandwich webs

5.1. Introduction and objectives

One of the composite sandwich structures commonly used in civil applications is the FRP cell-core sandwich which is composed of outer FRP face sheets, a foam core and a grid of FRP webs integrated into the core (see Figure 2.6). This structural concept, together with some corresponding examples, was introduced in Section 2.2. The thin webs of the FRP cell-core sandwich, the so-called web-core panels, are relatively long panels that are sensitive to global and local instabilities due to in-plane shear and bending stresses. The buckling/wrinkling behavior of web-core panels is modeled by treating the webs as plates stabilized by an elastic core material, e.g. foam, and subjected to combined shear and bending stresses, as shown in Figure 5.1. The buckling behavior of isotropic and anisotropic plates without any foam support and subjected to pure shear or combined shear and bending stresses has been extensively investigated (Johns 1971, Leissa 1985, Nemeth 1997, Featherston and Ruiz 1998). The interaction between the webs and the core material, however, can have a substantial impact on web buckling/wrinkling strength and is a key element in lightweight structural design.

The only studies to date that have considered the effect of an elastic core foundation are those carried out by Davis and Fragos (2003) and Briscoe et al. (2010) who studied the buckling of isotropic webs under pure shear stresses. Davis and Fragos (2003) investigated the buckling of metallic open-C-channel sections filled with foam. They used a combination of physical testing and finite element modeling to develop an empirical design equation for sections attached to foam. However, their empirical results are not generally applicable to web-core design. Later on, Briscoe et al. (2010) introduced an analytical model for the buckling of isotropic webs in foam-filled sandwich panels under distributed transverse loading. The web was modeled as a simply

supported plate resting on a Pasternak elastic foundation under pure shear stresses. However, the model was not accurate compared to finite element modeling for two main reasons: in cell-core sandwich beams, the face sheets provide some rotational resistances to the webs, which depend on material properties and geometric parameters such as web spacing and face sheet thickness. Therefore, assuming simply supported boundary conditions for the web at the junction of the web and face sheets may lead to considerably conservative results. Moreover, in a more realistic case, a web-core panel is subjected not only to shear stresses but also to in-plane bending stresses and the bending stresses may be significant assuming that the face sheet thickness is of the same order as the web thickness, as did Briscoe et al. (2010).

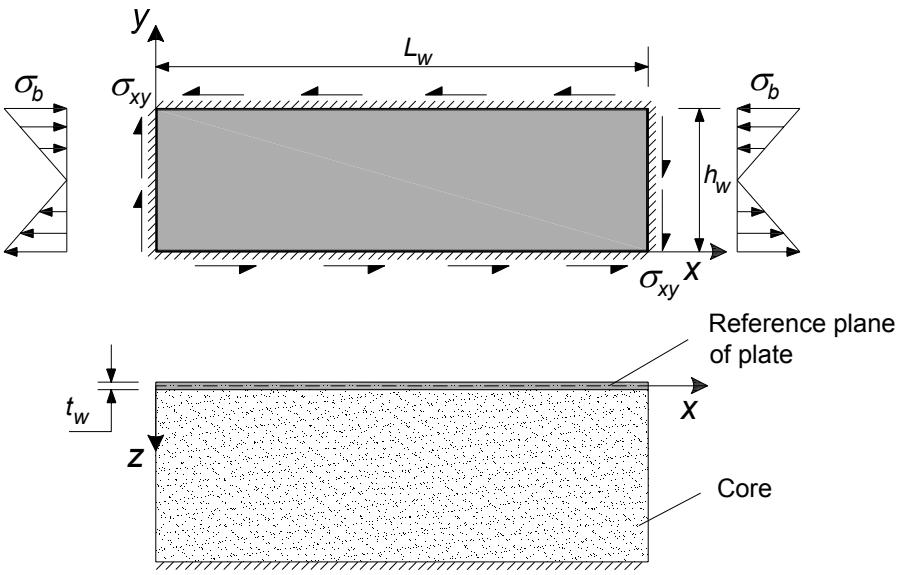

Figure 5.1. Rectangular plate with foam core subjected to shear and bending loads.

In this context, this chapter aims to predict the wrinkling behavior of orthotropic web-core panels using two approaches. The first approach is to predict the buckling of webs subjected to combined shear and bending loads using a mixed-mode interaction formula. In this regard, two new models are developed to simulate the buckling of orthotropic webs under pure shear and bending loads, independently. Subsequently, an interaction formula presented by Weaver and Nemeth (2008) for orthotropic plates was extended in order to predict the buckling of webs under combined shear and bending loads. The validity of this approach is examined via comparison with FE solutions. In the second approach, the wrinkling behavior of web-core

panels is treated as a biaxial compression-tension local buckling problem and the analytical model presented in Section 4.3.2 for the biaxial compression-tension buckling and wrinkling of GFRP plates and sandwiches is applied.

In both approaches, the web-core panels are modeled as long orthotropic plates stabilized by a relatively thick elastic core, see Figure 5.1. The boundary condition of the plate is defined according to the interaction between the webs and face sheets in the presence of the core material and this is done by applying a series of numerical analyses using three-dimensional finite element modeling.

In the last part of this chapter, the developed approaches are applied to predict the wrinkling loads of thin-walled webs in GFRP cell-core sandwich beams designed and tested by Keller et al. 2008 for the GFRP cell-core sandwich roof of the Novartis Campus Main Gate Building.

5.2. Definition of boundary conditions

In a cell-core sandwich structure, the web-core panels are elastically restrained at the junction between the webs and face sheets. The degree of elastic restraint depends on the material properties and many geometric parameters i.e. web spacing and web aspect ratio as well as the ratio of face sheet and web thicknesses. A similar issue has been addressed by Lee et al. (1996) and Estrada et al. (2008) for determining the shear buckling coefficients of web panels in steel plate girders. Historically, elastic shear buckling in steel plate girders was determined by assuming that web panels are simply supported at the web-flange junctions, and based on this conservative assumption, the design expressions to determine the shear buckling strength included in the current AISC (1989) and AASHTO (1992) codes and Eurocode 3, Part 1-4 (1996), were developed.

Cell-core sandwiches have, however, two main differences compared to plate girders. First, the face sheets of cell-core sandwiches are connected on both sides to webs, while flanges are free on one side. Second, in cell-core sandwiches the webs and upper and lower face sheets are bonded to foam cores. As a result of these two important differences, the face sheets provide more rotational resistances to the webs. It is therefore the aim of this section to perform a numerical investigation via finite element analysis of the effects of foam core rigidity and the ratio between

face sheet and web thickness on the boundary conditions at the web-face sheet junction for long web-core panels (when the ratio between the length and the height of web is equal or higher than 3).

5.2.1. Finite element modeling

A segment of a typical cell-core sandwich structure, e.g. the roof structure presented by Keller et al. 2008, was chosen, as shown in Figure 5.2. The segment was a beam consisting of one longitudinal web, nine transverse webs and the upper and lower face sheets. The face sheets and longitudinal webs next to the selected segment are modeled by applying symmetry boundary conditions on two sides of the segment. Cells, surrounded by orthogonal webs (longitudinal and transverse) and top and bottom face sheets, are filled with foam core materials. The beam was assumed to be under four-point bending. The dimensions and materials of the face sheets and webs were selected as being identical to the beams tested for the validation of the roof structure design (Keller et al. 2008). The beam length was 7.2 m, the width 0.9 m and the height 0.3 m, see Figure 5.2. The face sheets and webs consist of several layers of GFRP fabrics and mats and polyester resin. The reinforcements used for the laminates with their properties are listed in Table 5.1. The resulting laminate stacking sequences of the upper and lower face sheets and webs are given in Table 5.2. The core material properties (Young's modulus E_c=1 MPa and shear modulus G_c=0.40 MPa) were chosen based on the use of low-density (10 kg/m^3) rigid polyurethane foam. The foam properties were determined based on the extrapolation of test data provided by the foam manufacturer.

Linear elastic finite element (FE) buckling analysis was carried out using ANSYS v-10 software. The face sheets and webs were modeled using SHELL181 elements, and the core material was modeled using SOLID185 elements. Perfect bonding was assumed between the shell elements and the core. The model is shown in Figure 5.3. Due to symmetry, only half of the beam length is modeled; symmetry boundary conditions are applied at the surfaces corresponding to x=3.6 m. As mentioned above, symmetry boundary conditions were also applied at the surfaces corresponding to z=±0.45 m to simulate the face sheets and longitudinal webs next to the selected segment. In order to assess the mesh refinement required, a convergence study was carried out resulting in a total number of 51,680 elements (7,520 shell elements and 44,160 solid elements).

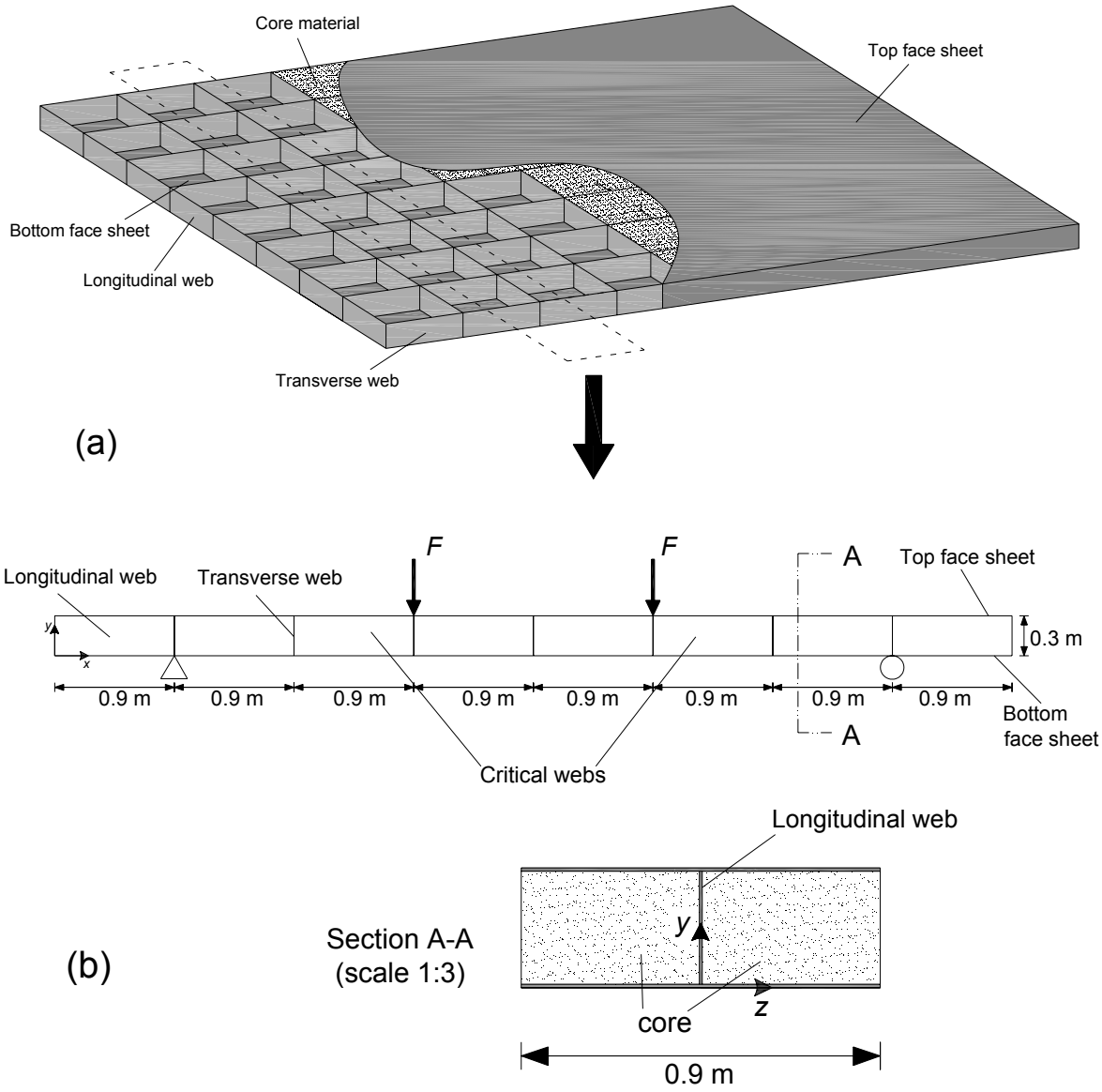

Figure 5.2. (a) Cell-core sandwich concept (for clarity, top face sheets and core material are only partially displayed); (b) segment of cell-core sandwich under four-point bending test.

Buckling analysis was performed on the model for three cases. In the first case (which is the real case) the bond between the face sheets and webs was modeled by imposing equal displacements on the face sheets and the web at their interface. In the second case, clamped boundary conditions were applied at the junction between the face sheets and the critical webs as well as between the critical webs and transverse webs. The critical webs are the web segments that are subjected to maximum combined bending and shear stresses, as illustrated in Figure 5.2. In the last case, the boundary conditions at the junction between the face sheets and web were simply supported. In

order to produce simply supported boundary conditions, the SHELL181 elements used for the face sheets were replaced by three-dimensional beam elements (BEAM4) that had an equivalent moment of inertia in bending and zero torsional moment of inertia. Accordingly, the web was not subjected to any rotational resistance from the face sheets.

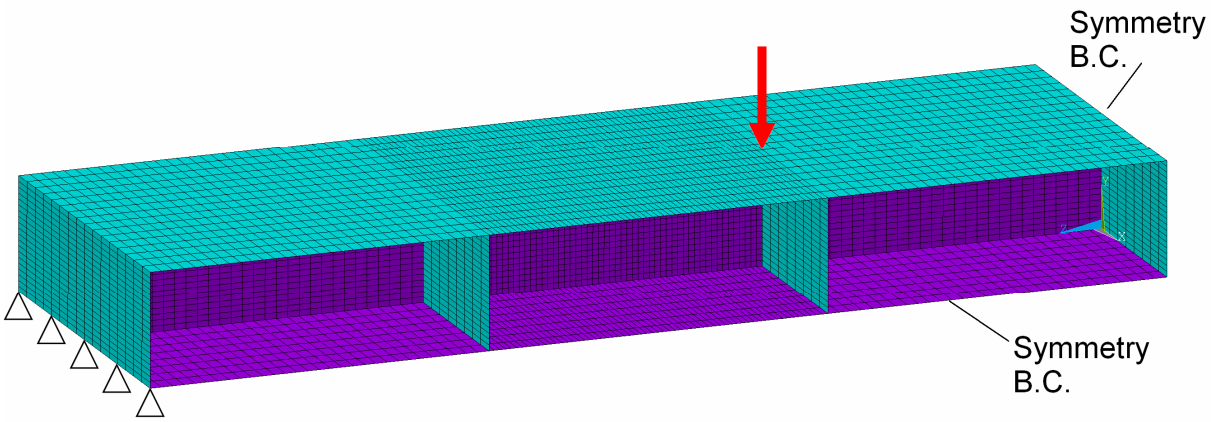

Figure 5.3. Finite element model (core elements are not displayed for clarity), applied load and boundary conditions.

Table 5.1. E-glass fiber reinforcement and polyurethane foam properties.

Reinforcement	Chopped Strand Mat	Woven roving fabric 0°/90°	Binding-warp fabric (UD)	Polyurethane foam-60 kg/m^3	Polyurethane foam-10 kg/m^3
Weight [g/m^2]	225	460 (0°) 460 (90°)	800	-	
Thickness of laminate [mm]	0.5	1.0	1.0	-	
Longitudinal elastic modulus [MPa]	7800	13000	37000	17.5	1.0
Transverse elastic modulus [MPa]	7800	13000	4960	17.5	1.0
Shear modulus [MPa]	2750	3050	2470	6.5	0.4
Denomination	M	F	UD0 or UD90	PU-60	PU-10

Table 5.2. Composition of face sheets and webs.

Sandwich component	Stacking sequence	Total thickness [mm]

Lower face sheet	$[(F/M)_2/$ UD0/M/UD90/M]	6
Upper face sheet	$[(F/M)_2/$ UD0/M/UD90/M]	6
Single webs	$[F/M]_2$	3

5.2.2. Analysis of results

Several numerical analyses were carried out on a number of combinations of two key parameters, the ratios between face sheet and web thickness (t_f/t_w) and foam stiffness (E_c), in order to determine their influence on the boundary conditions between the webs and face sheets. Figure 5.4 shows different values of the critical load, corresponding to web buckling obtained at different t_f/t_w ratios. The changes in the t_f/t_w ratio were implemented by changing the thickness of the face sheet while a 3-mm web thickness was maintained. The total thickness of the face sheet was changed by scaling up and down the thickness of the reinforcements used for the laminates. The results in Figure 5.4 show that the actual support condition at the face sheet and web junction depends primarily on the ratio t_f/t_w. If t_f/t_w is much less than 1, the actual support condition is close to a simple support, while for cases with t_f/t_w larger than 2, the actual support condition is closer to a clamped support. Figure 5.5 shows the ratio of $F_{cr,a}/F_{cr,cc}$ versus different foam core stiffnesses for two ratios of t_f/t_w that are equal to 1 and 0.25. $F_{cr,a}$ is the critical load obtained for the actual condition and $F_{cr,cc}$ is the critical load obtained when the clamped boundary conditions were applied. The results show that increasing the foam stiffness increases the degree of rotational restraint of the web. For $t_f > t_w$ and high foam stiffnesses the clamped condition is approached.

The ratio of the face sheet to the web thickness is larger than 1 for commonly used GFRP cell-core sandwiches and the foam core used in these structures has stiffnesses higher than 45 kg/m^3. According to the results, it is concluded that assuming simply supported boundary conditions for the web-core panel at the face sheet-web junction is an overly conservative assumption, particularly in GFRP cell-core sandwich structures with long web-core panels for which the length-to-width ratio is larger than 3. It therefore can be assumed that the web-core panel for commonly used GFRP cell-core sandwiches is clamped along the face sheet-web junction.

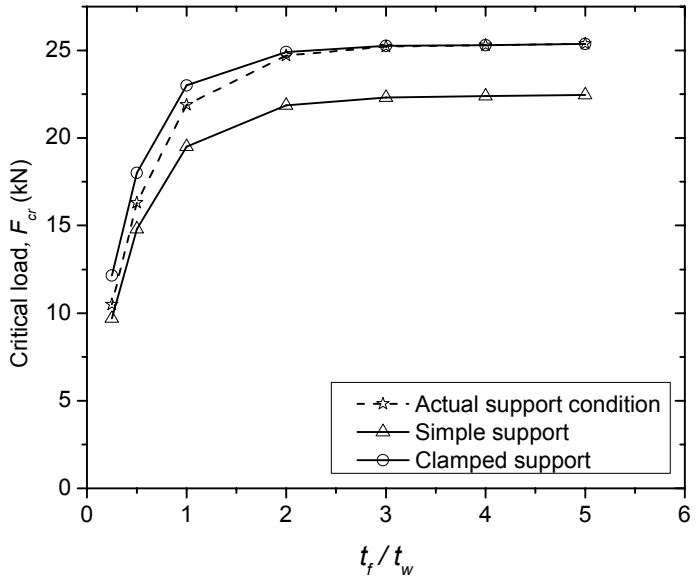

Figure 5.4. Critical loads corresponding to web buckling for different face sheet-web thickness ratios.

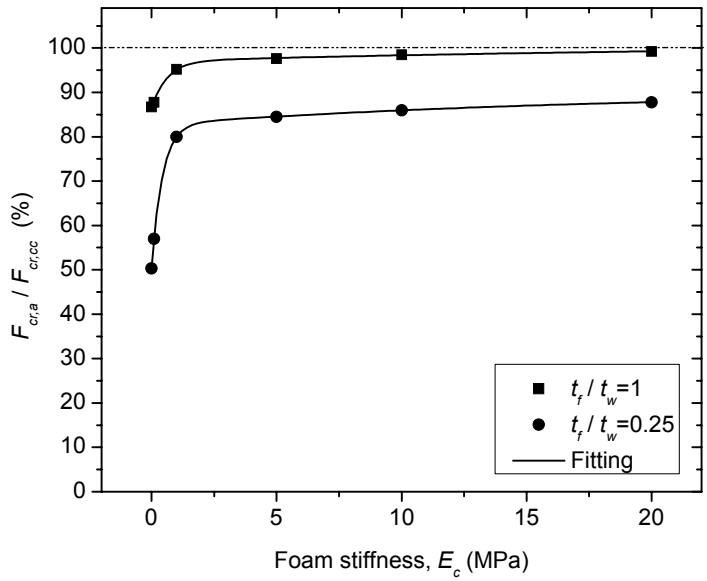

Figure 5.5. Ratio of $F_{cr,a}/F_{cr,cc}$ versus foam core stiffness for ratios t_f/t_w equal to 1 and 0.25.

5.3. Buckling load prediction using mixed-mode formula

A thin rectangular orthotropic long plate is considered whose lay-up is symmetric with length L_w, width h_w (L_w/ h_w >3), and thickness t_w as shown in Figure 5.1, stabilized by an isotropic foam that

is assumed to be infinitely thick. The plate is clamped on its four edges and subjected to combined shear and bending stresses. Timoshenko (1935) presented buckling data for long isotropic plates subjected to combined bending and shear loads with an interaction formula as follows:

$$\left(\frac{\sigma_{xy}}{\sigma_{xy,cr}}\right)^2+\left(\frac{\sigma_b}{\sigma_{b,cr}}\right)^2\le 1 \tag{5.1}$$

where σ_{xy} is the shear stress, σ_b is the maximum compressive in-plane stress due to bending, and $\sigma_{xy,cr}$ and $\sigma_{b,cr}$ are the critical buckling stresses when the shear and bending stresses act independently on the plates. Recently, Weaver and Nemeth (2008) demonstrated that Eq. (5.1) may be up to 25% too conservative. Hence, they presented an improved buckling formula for long orthotropic plates with clamped edge conditions as follows:

$$\left(\frac{\sigma_{xy}}{\sigma_{xy,cr}}\right)^{\frac{12+\Upsilon}{6}}+\left(\frac{\sigma_b}{\sigma_{b,cr}}\right)^{\frac{13.8+\Upsilon}{6}}\le 1 \tag{5.2}$$

where Υ is a non-dimensional parameter given by

$$\Upsilon=\frac{\left(D_{12}+2D_{66}\right)}{\sqrt{D_{11}D_{22}}} \tag{5.3}$$

where D_{11} and D_{22} denote flexural stiffness components, D_{12} is the Poisson coupling stiffness and D_{66} is the twisting stiffness.

5.3.1. Solution method

To estimate the critical buckling stresses of the plate under shear and bending loads independently, $\sigma_{xy,cr}$ and $\sigma_{b,cr}$, the energy method is applied. The approximate solution is similar to the one presented in Section 4.3.2. The total potential energy, Π_p, of a thin rectangular orthotropic long plate supported by an isotropic foam, as shown in Figure 5.1, is given by:

$$\Pi_p=U_f+U_c+\Omega \tag{5.4}$$

where U_f is the bending strain energy of the plate, U_c is the strain energy of the core (which is a summation of the shear and normal transverse strain energy of the core), while Ω is the work

performed by the external forces. The bending strain energy of the orthotropic plate with symmetric lay-up is expressed as follows:

$$U_f = \frac{1}{2}\int_0^l \int_0^{h_w} \left(D_{11}\left(\frac{\partial^2 w}{\partial x^2}\right)^2 + D_{22}\left(\frac{\partial^2 w}{\partial y^2}\right)^2 + D_{66}\left(2\frac{\partial^2 w}{\partial x \partial y}\right)^2 + 2D_{12}\left(\frac{\partial^2 w}{\partial x^2}\right)\left(\frac{\partial^2 w}{\partial y^2}\right)\right) dx\, dy \qquad (5.5)$$

where l is the buckling wavelength and w is the deflection of the mid-plane which presents the buckling wave form of the plate. When the plate is asymmetric, the strain energy terms due to in-plane/out-of-plane coupling will be added.

The strain energy in the core is described by:

$$U_c = \frac{1}{2}\int_0^l \int_0^{h_w} \int_0^{t_c} \left(\frac{\sigma_{cz}{}^2}{E_c} + \frac{\sigma_{cxz}{}^2 + \sigma_{cyz}{}^2}{G_c} \right) dx\, dy\, dz \qquad (5.6)$$

where t_c is the thickness of the core which is assumed to be infinite. σ_{cz}, σ_{cxz} and σ_{cyz} are the stresses in the isotropic core and are given by:

$$\sigma_{cz} = E_c \frac{\partial w_c}{\partial z},\ \sigma_{cxz} = G_c \frac{\partial w_c}{\partial x},\ \sigma_{cyz} = G_c \frac{\partial w_c}{\partial y} \qquad (5.7)$$

in which E_c and G_c are the Young's and shear moduli of the core, respectively and w_c is the transverse deformation in the core corresponding to the buckling waves of the plate, thus:

$$w_c(x, y, z) = w(x, y)Z(z) \qquad (5.8)$$

$Z(z)$ is the deflection function in z-direction that is taken from the model proposed by Plantema (1966). The model is based on the assumption that the plate deformation causes local deflection in the core, which decays in z-direction exponentially with the distance from the plate. Therefore, the deflection function $Z(z)$ is written as:

$$Z(z) = e^{-Kz} \qquad (5.9)$$

where K is an unknown model parameter. The work of applied stresses is given by

$$\Omega = \frac{t}{2}\int_0^l \int_0^{h_w} \left(\sigma_x \left(\frac{\partial w}{\partial x}\right)^2 + \sigma_y \left(\frac{\partial w}{\partial y}\right)^2 + \sigma_{xy}\left(\frac{\partial w}{\partial x}\right)\left(\frac{\partial w}{\partial y}\right)\right) dx\, dy \qquad (5.10)$$

in which σ_x, σ_y and σ_{xy} are the internal in-plane stress values due to the external loads.

Based on the principle of minimum total potential energy, the Ritz method requires that the total potential energy should be at a stationary position and this occurs when an infinitesimal variation of the deflection of the plate, *w,* involves no change in energy, hence:

$$\delta\Pi_p = \delta\left(U_f + U_c + \Omega\right) = 0 \tag{5.11}$$

In order to be able to solve Eq. (5.11), it is necessary to assume a function for the deflection of the plate, *w*. The deflection function *w* is defined according to the different loading conditions. In the following sections, deflection functions assumed for the plates subjected to pure shear and pure bending loading are presented as well as the buckling solutions obtained for the corresponding loading conditions.

5.3.2. Pure shear load

In the pure shear loading case, when σ_x and σ_y are zero, the deflection of the plate is assumed in the form of:

$$w(x,y) = A\left(1-\cos\left(\frac{2\pi y}{h_w}\right)\right)\sin\left(\frac{\pi}{l}\left(x-\varepsilon y\right)\right) \tag{5.12}$$

where *A* is the amplitude of deflection. This function represents the surface of inclined waves (see Figure 5.6) the length of which in *x*-direction is *l* with an angle of inclination ψ from the *y*-axis, the tangent of which is equal to ε. Eq. (5.12) was originally formulated by Timoshenko and Gere (1963) for isotropic plates and used by Thielemann (1950) for orthotropic plates. In this thesis, however, this function is used for an orthotropic plate stabilized by thick foam. Substituting the term *w* in Eqs. (5.5) and (5.10) by Eq. (5.12) and integrating with respect to *x* and *y* give the expressions for the bending strain energy of the plate, U_f, as well as the work performed by the external forces, Ω. Furthermore, the transverse deformation in the core, w_c, obtained by substituting *w* in Eq. (5.8) with Eq. (5.12), is combined with Eqs. (5.6) and (5.7) to obtain the expression for the strain energy of the core, U_c. The combination of U_f, U_c and Ω in Eq. (5.4) results in the total potential energy. The variation of the deflection of the plate, *w*, is imposed by the variation of the amplitude of the deflection function, *A*. Therefore, the principle of minimum total potential energy states that:

$$\frac{\partial \Pi_p}{\partial A} = 0 \tag{5.13}$$

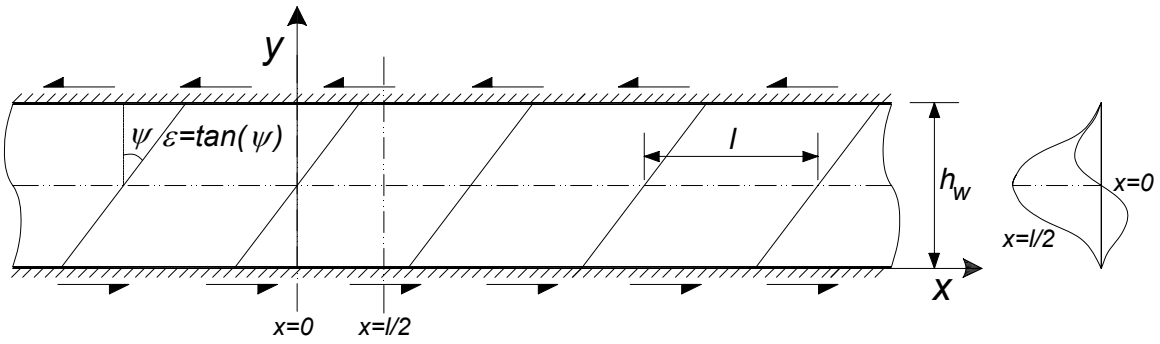

Figure 5.6. Approximate assumptions for buckling surface of thin rectangular orthotropic long plate with clamped plate edges subjected to pure shear loading.

Solving Eq. (5.13) gives the shear buckling stress as follows:

$$\sigma_{xy} = \frac{1}{12\pi^2 t_w h_w^{\,4} l^2 \varepsilon}\left(\gamma_1 + \gamma_2 K + \frac{\gamma_3}{K}\right) \tag{5.14}$$

where

$$\begin{aligned}
\gamma_1 &= \pi^4\left(6\left(D_{11} + 2\varepsilon^2 D'_{12} + D_{22}\varepsilon^4\right)h_w^{\,4} + 16\left(D'_{12} + 3D_{22}\varepsilon^2\right)l^2 h_w^{\,2} + 32\left(D_{22}\right)l^4\right)\\
\gamma_2 &= 3h_w^{\,4} l^4 E_c\\
\gamma_3 &= \pi^2\left(3\left(\varepsilon^2+1\right)h_w^{\,2} + 4l^2\right)h_w^{\,2} l^2 G_c\\
D'_{12} &= D_{12} + 2D_{66}
\end{aligned} \tag{5.15}$$

The minimum value of the shear buckling stress, $\sigma_{xy,cr}$, as a function of three undetermined variables, l, ε and K, is obtained by solving the following system of equations:

$$\begin{cases}
\dfrac{\partial \sigma_{xy}}{\partial l} = 0\\
\dfrac{\partial \sigma_{xy}}{\partial \varepsilon} = 0\\
\dfrac{\partial \sigma_{xy}}{\partial K} = 0
\end{cases} \tag{5.16}$$

5.3.3. Pure bending load

A linearly varying in-plane stress is considered as the result of an in-plane bending moment (see Figure 5.7). The in-plane bending stress variation is expressed as:

$$\sigma_x = \sigma_b \left(1 - \alpha \frac{y}{h_w} \right) \tag{5.17}$$

where σ_b is the maximum compressive stress due to the bending moment. α is a coefficient that represents the position of the neutral axis at which the in-plane stress of σ_x is zero. The linearly varying in-plane stresses, Eq. (5.17), can be considered as a superposition of constant in-plane stresses due to a tension or compression force and linearly varying stresses which arise from an in-plane bending moment. When the neutral axis is at $y = h_w/2$ and α=2, the compressive stress ($-\sigma_b$) at $y=h_w$ is of the same magnitude as the tensile stress ($+\sigma_b$) at $y = 0$, which is the case for pure in-plane bending.

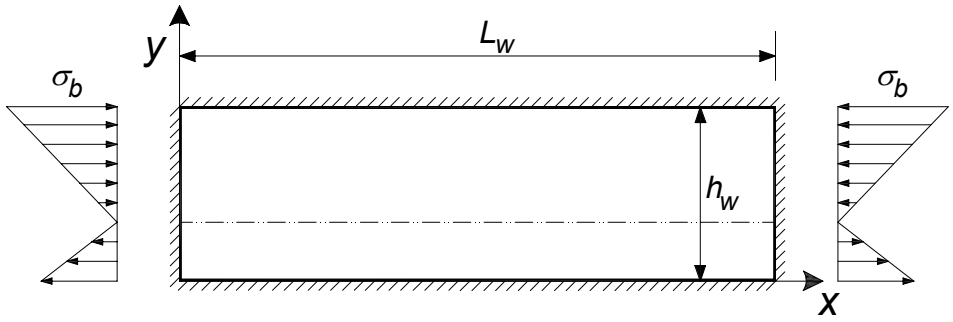

Figure 5.7. Clamped plate with linearly varying in-plane stresses.

In the bending loading case, the deflection of the plate is assumed in the form of:

$$w(x, y) = \left(A_1 Y_1(y) + A_2 Y_2(y) \right) \sin\left(\frac{\pi x}{l} \right) \tag{5.18}$$

where A_1 and A_2 are two amplitude coefficients. A two-term deflection function was defined in y-direction in order to obtain a satisfactorily accurate approximation (Leissa 1985, Lekhnitskii 1968). $Y_j(y)$ (j=1, 2) are deflection functions defined according to the clamped boundary conditions in y-direction as:

$$
\begin{aligned}
&Y_j(\eta) = \gamma_j \cos(\mu_j \eta) - \gamma_j \cosh(\mu_j \eta) + \sin(\mu_j \eta) - \gamma_j \sinh(\mu_j \eta) \\
&\eta = y / h_w \\
&\begin{cases} \mu_j \approx (j + 0.5)\pi \\ \gamma_j = \dfrac{\cos(\mu_j) - \cosh(\mu_j)}{\sin(\mu_j) + \sinh(\mu_j)} \end{cases}
\end{aligned}
\tag{5.19}
$$

Substituting the term w in Eq. (5.5) by Eq. (5.18) and integrating with respect to x and y give the expressions for the bending strain energy of the plate, U_f. Similarly, combining the deflection function of Eq. (5.18) and the in-plane pure bending stress of Eq. (5.17) (with α=2) into Eq. (5.10) (while σ_y and σ_{xy} are zero) results in the work performed by the external forces, Ω. Furthermore, the transverse deformation in the core, w_c, is obtained by substituting w in Eq. (5.8) with Eq. (5.18). Subsequently, the strain energy of the core, U_c, is derived by incorporating w_c into Eqs. (5.6) and (5.7). Then, the summation of U_f, U_c and Ω gives the total potential energy, see Eq. (5.4).

According to the Ritz method, the total potential energy of the system is stationary when:

$$
\frac{\partial \Pi_p}{\partial A_i} = 0 \quad (i = 1,2) \tag{5.20}
$$

Eq. (5.20) results in two simultaneous equations:

$$
\begin{cases} c_1 A_1 + c_2 A_2 = 0 \\ c_3 A_1 + c_4 A_2 = 0 \end{cases} \tag{5.21}
$$

where c_1 to c_4 are the coefficients of the equation system.

By equating the determinant of this system (Eq. (5.21)) to zero, an expression for σ_b as a function of two undetermined variables of l and K is obtained. The minimum value of the bending compressive stress, $\sigma_{b,cr}$, as a function of two undetermined variables of l and K is obtained by solving the following system of equations:

$$
\begin{cases} \dfrac{\partial \sigma_b}{\partial l} = 0 \\ \dfrac{\partial \sigma_b}{\partial K} = 0 \end{cases} \tag{5.22}
$$

5.3.4. Model validation

The validity of the analytical buckling models was studied by applying the models for the sandwich beam numerically analyzed in Section 5.2. The results were compared with the finite element results. The sandwich beam with relatively weak foam core (E_c=1 MPa) was subjected to four-point bending (see Figure 5.2). The maximum shear and bending stresses, appearing in the second web segment from the supports due to the bending load F, are obtained as follows:

$$\sigma_{xy} = \frac{F}{t_w h_w} \tag{5.23}$$

$$\sigma_b = \frac{12 L_w F}{t_w h_w^{\,2} + 6 d_w t_f h_w} \tag{5.24}$$

where d_w is the distance between the longitudinal webs of the cell-core sandwich shown in Figure 5.2. The critical buckling stresses, $\sigma_{xy,cr}$ and $\sigma_{b,cr}$, were calculated based on the developed approximate models described in Sections 5.3.2 and 5.3.3. Throughout the calculation, the strain energy of the core, U_c, was multiplied by two since the web was supported by foam on both sides. The obtained $\sigma_{xy,cr}$ and $\sigma_{b,cr}$ together with the stress expressions in Eqs. (5.23)-(5.24) were incorporated into Eq. (5.2) and solved with respect to the external load, F. The solution results in the critical external load, F_{cr}, at which global or local buckling occurs in the web of the beam. Figure 5.8 demonstrates the analytical results obtained at different face sheet and web thickness ratios (t_f/t_w) and compares these results with the FE results acquired with the clamped boundary condition at the junction of the face sheets. Similarly, Figure 5.9 compares the analytical and FE results obtained at a ratio of t_f/t_w =1 for a range of foam stiffnesses varying from 0 (no foam) to 20 MPa (the latter representing ~80 kg/m^3 polyurethane foams). Futhermore, the $\sigma_{xy,cr}$ and $\sigma_{b,cr}$ calculated for different foam stiffnesses along with values obtained for variables l, K, and ε are presented in Tables 5.3-5.4. In Figures 5.8 and 5.9, good agreement between the analytical and FE results is found. Figure 5.8, moreover, demonstrates the difference between the solutions of pure shear loading (without considering the bending stresses) and combined shear and bending stresses. The results confirm that at a low t_f/t_w ratio, the influence of bending stresses on the buckling load becomes very significant. In this context, a parametric study was performed on two key ratios t_f/t_w and d_w/h_w using the analytical model. Figure 5.10 shows the portion of bending

stresses in the web buckling formula (Eq. (5.2)) obtained for different values of these two ratios. The results confirm the high influence of bending at low t_f/t_w and d_w/h_w ratios, while its influence is drastically reduced by increasing the ratio values, in particular for d_w/h_w.

Table 5.3. Buckling results of plate under pure shear load at different foam stiffnesses.

Foam stiffness (MPa)	0	0.1	1	5	10	20
$\sigma_{xy,cr}$ (MPa)	8.8	11.7	27.3	67.5	103.4	160.5
l (mm)	238.1	204.0	131.6	83.6	67.5	54.2
K	-	14.3	21.3	33.2	41.0	51.0
ε	0.73	0.79	0.91	0.96	0.97	0.98

Table 5.4. Buckling results of plate under in-plane bending load at different foam stiffnesses.

Foam stiffness (MPa)	0	0.1	1	5	10	20
$\sigma_{b,cr}$ (MPa)	40.9	50.0	101.0	240.4	365.7	564.9
l (mm)	150.0	128.6	90.0	60.0	50.0	39.1
K	-	17.8	24.1	34.2	40.5	51.0

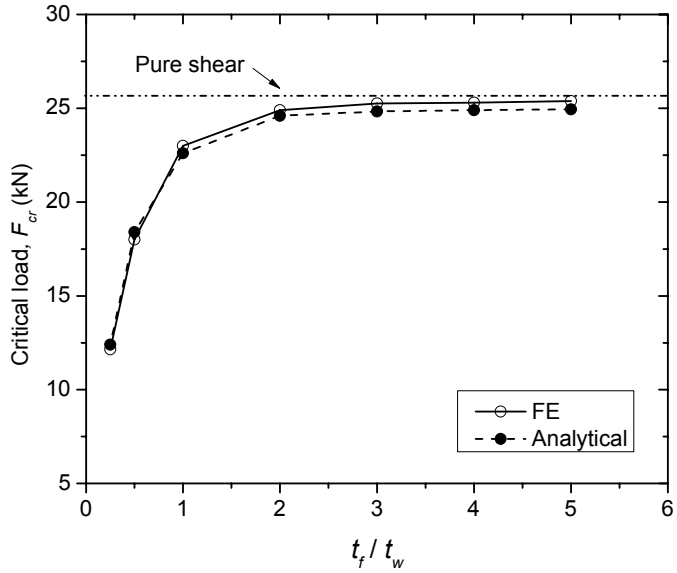

Figure 5.8. Comparison of numerical and analytical critical loads at different face sheet-web thickness ratios.

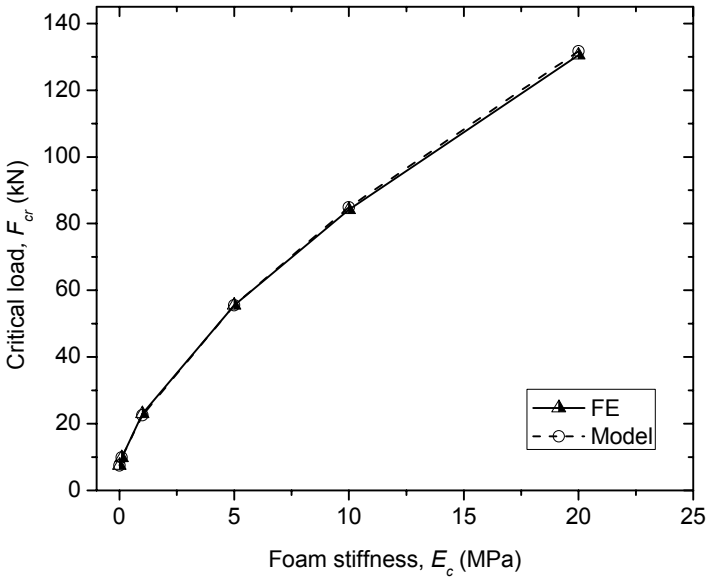

Figure 5.9. Comparison of numerical and analytical critical loads at t_f/t_w=1 for different foam stiffnesses.

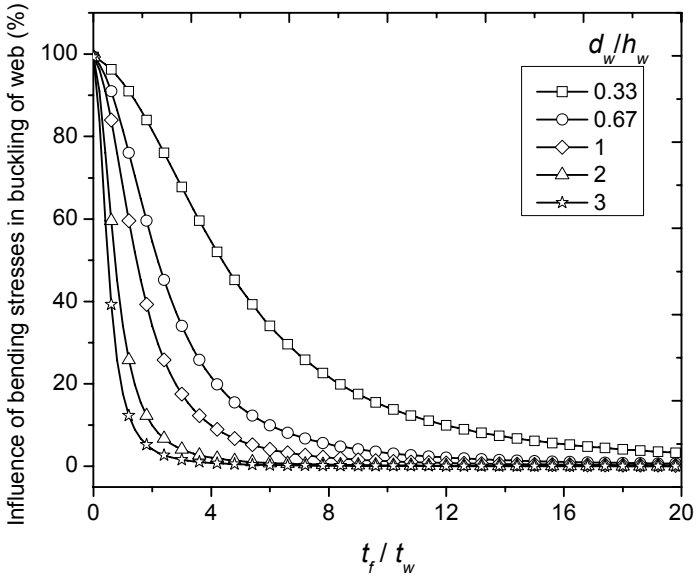

Figure 5.10. Bending influence in buckling of web at different t_f/t_w and d_w/h_w ratios.

5.4. Application to cell-core sandwich webs

Application of the previously developed buckling models (which are based on the mixed-mode interaction formula) and the model presented in Section 4.3.2 (which is based on the biaxial compression-tension buckling approach) to the analysis of web-core sandwich panels is presented

in the following. The analytical solutions together with the results of three-dimensional FE modeling are compared to the model used for the design of the Novartis GFRP sandwich roof structure (Keller et al. (2008)). Suggestions concerning optimization of the design are discussed.

5.4.1. Novartis GFRP cell-core sandwich roof

Keller et al. (2008) reported on the design and construction of the Main Gate of the Novartis Campus in Basel, Switzerland, constructed in 2006 and shown in Figure 2.5. The building is covered with a 21.6×18.5-m function-integrated GFRP sandwich roof structure that integrates load-bearing, building physical and architectural functions. The roof must be lightweight due to the limited load-bearing capacity of the glass walls and, at the same time, provide thermal insulation and waterproofing for the building. Consideration of the complex double-curved geometry led to the use of a GFRP sandwich structure of variable depth in which the core consisted of a polyurethane (PU) foam of three different densities and strengths. Since the shear load-bearing capacity of even the densest core type was not sufficient, the foam core had to be reinforced by an internal system of orthogonal GFRP webs. Figure 5.11 shows a plan view of the roof with the internal web grid and distribution of core densities. The base components of the roof are 0.9×0.9×d-m^3 foam blocks between the orthogonal webs (d = variable roof depth). 460 blocks, each with a different geometry, were cut; subsequently, four blocks at a time were assembled into a block-strip. First, the inserts and double webs were laminated into the blocks, and the adjacent sides between two blocks were overlaid with one laminate. The four blocks were pressed together and the upper and lower sides of the block-strips were then overlaid with two laminates. The block-strips were then assembled into four roof elements of 18.50×5.63/5.63/4.70/5.63 m. Adhesive bonding was used to connect the webs of the block-strips, thereby providing continuity of the longitudinal and transversal webs. The four roof elements were transported to Basel, Switzerland and assembled and adhesive bonding was used again to connect the webs.

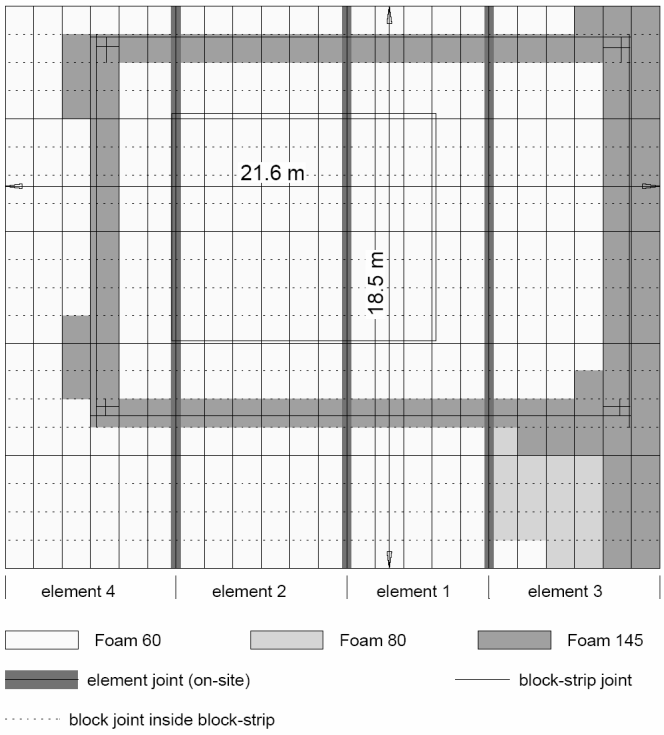

Figure 5.11. Plan view of sandwich roof structure of Novartis campus main gate building with internal web grid, core density distribution, block, block-strip and element arrangement (Keller et al. 2008).

Four full-scale beams, designated B1-B4 by Keller et al. (2008), were fabricated to experimentally validate the structural design of the roof structure and the applicability of the characteristic material properties obtained from small-scale experiments. The same calculation models were used for the beam design as for the roof design. Specific verifications (e.g. tensile strength of the face sheets, wrinkling strength of the face sheets and webs in compression, strength of the epoxy bonded joints, and sandwich stiffness) were carried out via four-point bending tests. The four beams were built up from eight 0.9×0.9×d'-m^3 foam blocks (d' = beam depth), as was planned for the roof. Two block-strips were fabricated and joined with epoxy adhesives to form the beams. Two types of foam block were used with the lowest and highest densities used in the roof (60 kg/m^3 for B1 and B3 and 145 kg/m^3 for B2 and B4). Beams B1 and B3, the beams most sensitive to face sheet or web wrinkling, were selected for assessment in the present work. Figure 5.12 shows side views of these two beam configurations and Figure 5.13 demonstrates the four-point bending set-up of beams. The beam length was 7.2 m, the width 0.9 m and the depth 0.3 m. The

adhesive joint of beam B1 was at mid-span (and therefore not shear loaded), while for beam B3, two joints were placed between the supports and loading jacks to also verify the shear strength of the adhesive joints. The upper and lower face sheets were laid-up over the whole beam length. The fiber architecture and materials of all beams were identical and corresponded exactly to those of the roof structure with the exception of the double webs over the supports, which were only half as thick as the roof webs due to the smaller support reactions. The reinforcements used for the laminates with their properties, the main mechanical properties of PU-60 kg/m^3 and the resulting laminate stacking sequences of each component are presented in Tables 5.1 and 5.2.

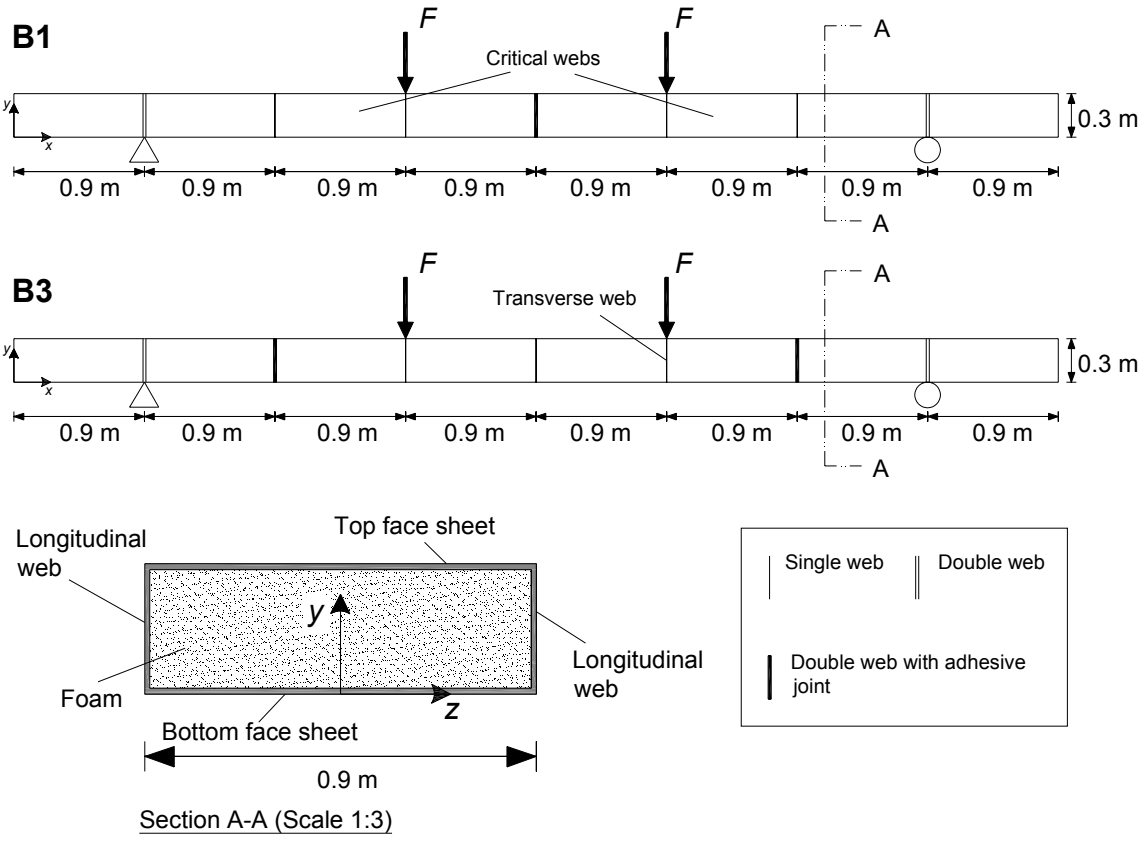

Figure 5.12. Configurations of sandwich beams B1 and B3.

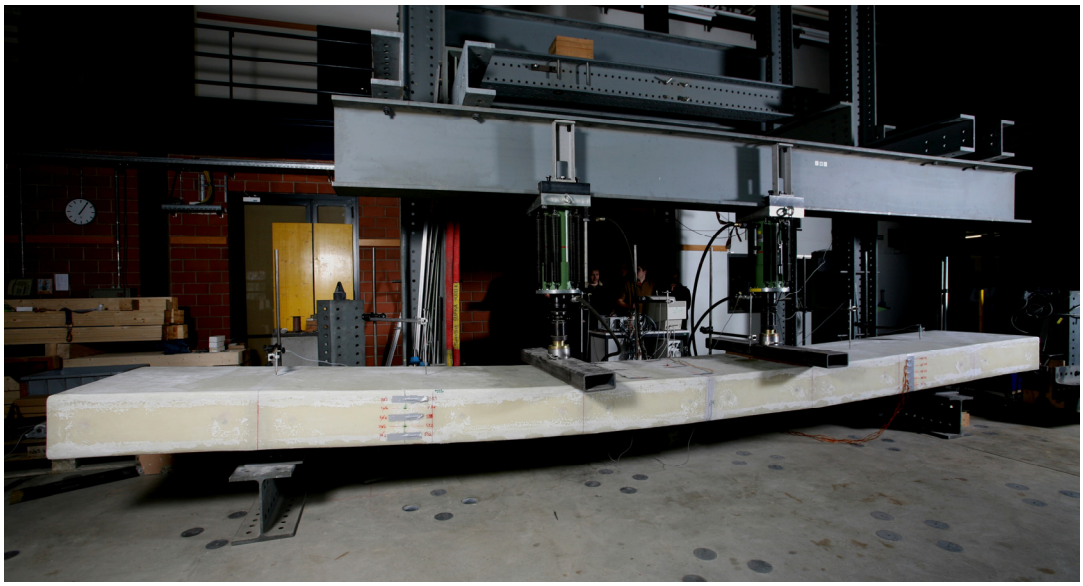

Figure 5.13. Four-point bending set-up, beam B1 (Keller et al. 2008).

5.4.2. Analytical and numerical modeling results

5.4.2.1. First approach: mixed-mode buckling problem

For beams B1 and B3, the maximum shear and bending stresses occurred at the second web segments from the supports, designated as critical webs (see Figure 5.12). The stresses are determined by Eqs. (5.23) and (5.24), in which t_w should be, however, substituted by $2\times t_w$, since there are two webs for beams B1 and B3. Based on the approximate models described in Sections 5.3.2 and 5.3.3 (Eqs. (5.16) and (5.22)), the critical buckling stresses, $\sigma_{xy,cr}$ and $\sigma_{b,cr}$, are obtained as being 94.1 MPa and 333.5 MPa, respectively. Incorporating the obtained $\sigma_{xy,cr}$ and $\sigma_{b,cr}$ together with the maximum stress expressions into Eq. (5.2) results in Eq. (5.25) as follows:

$$\left(\frac{555.55\times F}{94.1\times 10^6}\right)^{\frac{12+\Upsilon}{6}}+\left(\frac{1052\times F}{333.5\times 10^6}\right)^{\frac{13.8+\Upsilon}{6}}=1 \qquad (5.25)$$

where Υ = 0.768 based on Eq. (5.3) and the fiber architecture of the web. Solving Eq. (5.25) with respect to F results in the critical load, F_{cr}, equals 154.6 kN. In addition, a critical load of 169.3 kN is obtained providing that the bending stresses are disregarded. The comparison reveals an almost 10% influence of bending stresses on the wrinkling load of the web-core panels.

5.4.2.2. Second approach: biaxial compression-tension buckling problem

The wrinkling of web-core panels can be approximated as an in-plane biaxial compression-tension local buckling problem which consists of the interaction between the compression and transverse tension stress fields. The biaxial compression-tension buckling/wrinkling behavior of GFRP plates and sandwiches as well as the interaction between the compression and transverse tension stress fields are experimentally, analytically and numerically studied in Chapters 3 and 4.

To apply the biaxial compression-tension approach, the first step is to find the region of the web with the highest potential for local buckling, which corresponds to the region with the maximum compression stresses. This region for beams B1 and B3 can be located at the upper corner of the critical web (near the location where the external loads F were applied), where the maximum bending moment combined with maximum shear occurs, see Figure 5.14. At this position, along the height of the web (from the top face sheet down to the neutral line), the angle of principal stresses measured from y-direction varies from 23° to 45°. Therefore, local buckling waves with relatively short wavelength inclined by an angle of between 23° and 45° (from y-direction) and anchored between the transverse web and top face sheet are expected. This region of the web-core panel is divided into several strips as shown in Figure 5.14(b). It is assumed that the boundary conditions at the junctions of the web and face sheet and crossed webs are clamped (according to the investigation carried out in Section 5.2) and the buckling occurs at the mid-length of the strips. The angle of the principal stresses obtained at the middle of each strip is selected as the inclination of the buckling wave. Thus, the buckling solution for each strip, rotated according to the angle of principal stresses, is simulated by the buckling of a relatively long plate subjected to biaxial compression-tension stresses, as shown in Figure 5.14(c). The principal stresses (maximum compression and tension) at the mid-length of each strip are considered as constant stresses for solving the biaxial compression-tension buckling problem.

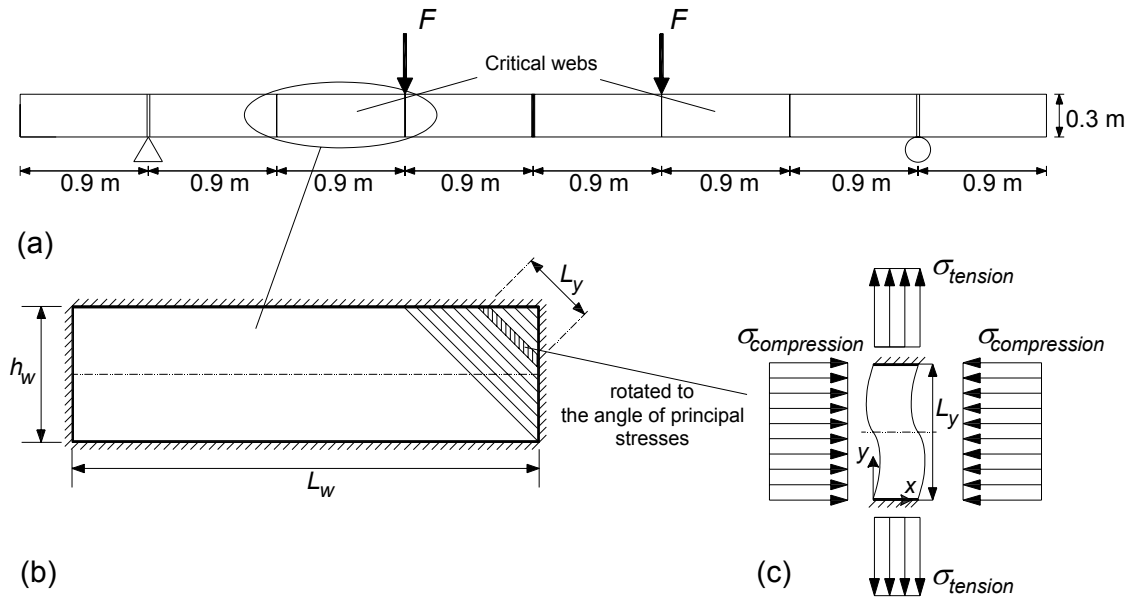

Figure 5.14. Biaxial compression-tension buckling approach for local buckling of web-core panels.

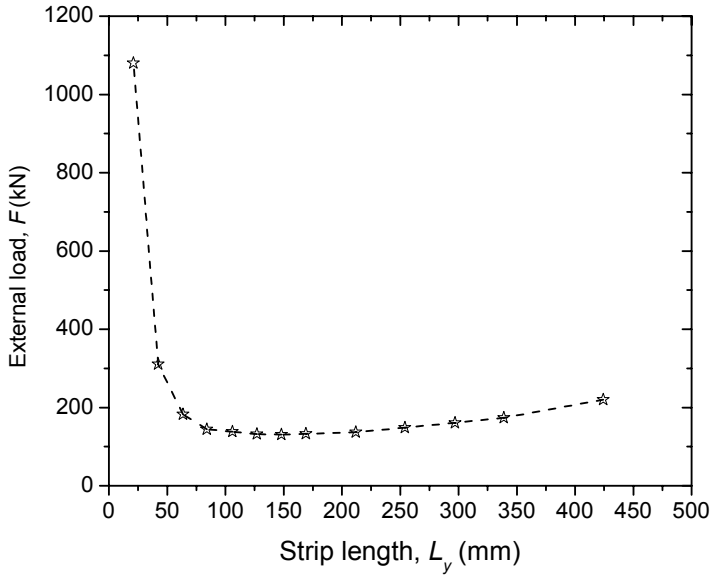

Figure 5.15. Results of biaxial compression-tension buckling approach for different strip lengths.

The length of the strips is considered as being the height of the plate, see Figure 5.14(c). The analytical solution presented in Section 4.3.2 for the biaxial compression-tension buckling problem is applied. Accordingly, the corresponding external load, *F*, for the buckling solutions for each strip is obtained. This solution is iterated for different strip lengths and Figure 5.15 shows the corresponding results. The minimum value of 131 kN is the critical external load, F_{cr},

when the local buckling wave occurs at an inclined angle of 30° in the strip with a length of 148 mm.

5.4.2.3. FE modeling

The sandwich beams, B1 and B3, were modeled using ANSYS v-10 software. The adhesive joints in both beams were assumed as being perfectly bonded; therefore one FE model was created for both beams. The two overhanging end parts of the beams were not modeled. Similarly to the FE modeling in Section 5.2.1, the face sheets and webs were modeled using SHELL181 elements, and the core material was modeled using SOLID185 elements. A perfect bond was assumed between the shell elements and the core. The model is shown in Figure 5.16. Due to symmetry, only half of the beam was modeled; symmetric boundary conditions were applied. A refined mesh for the second cell from the support position (where the buckling wave occurs) was used while for the rest of the model a coarse density mesh was applied in order to reduce computational time. This configuration generated 37,400 solid elements and 8,900 shell elements. A linear elastic finite element buckling analysis was performed and the critical bending load was obtained as being 153.5 kN. The resulting web buckling mode is shown in Figure 5.17.

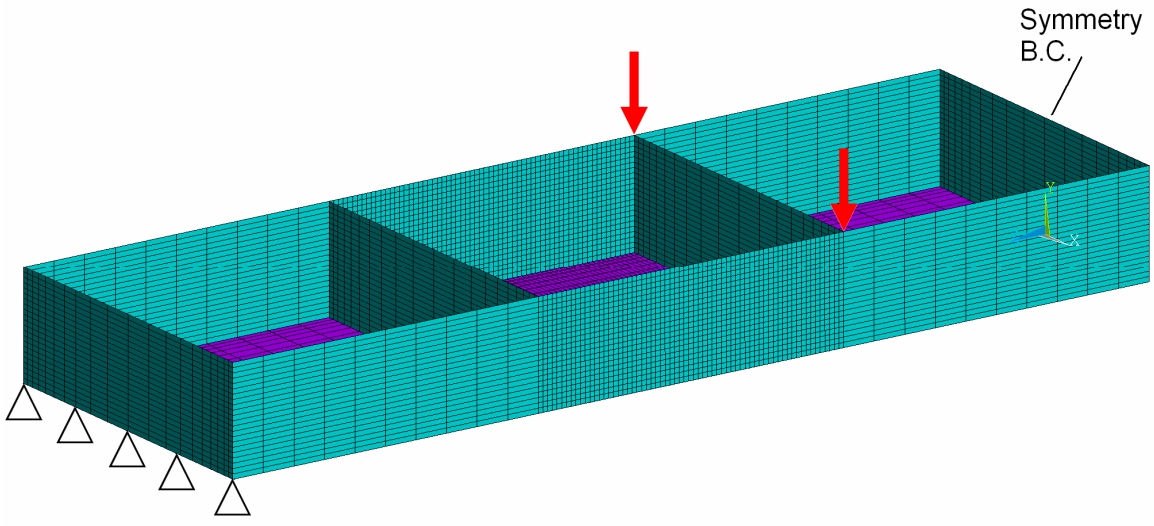

Figure 5.16. FE model of beams B1 and B3, applied load and boundary conditions (for clarity, the top face sheet and foam elements are not displayed).

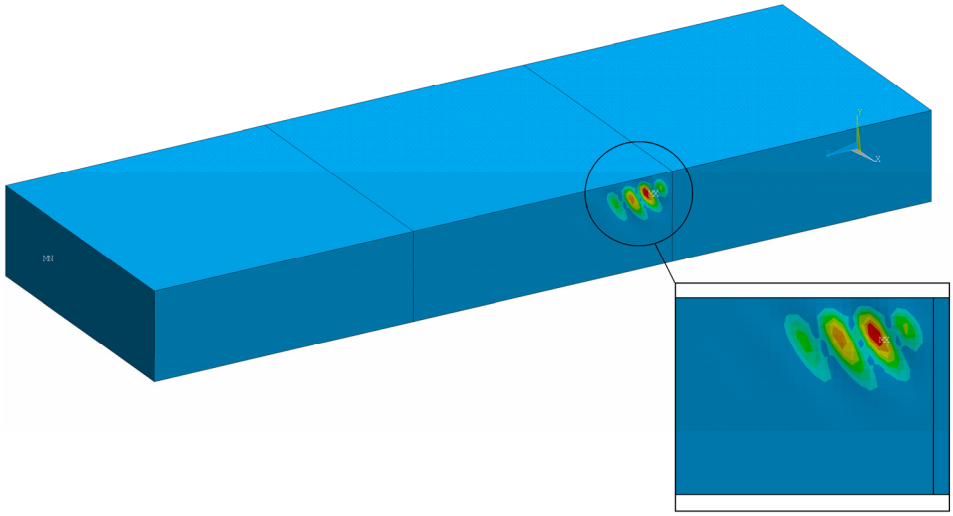

Figure 5.17. Web buckling mode of beams B1 and B3.

5.5. Comparison and discussion

Table 5.5 summarizes the results of the three presented solutions. As compared to the FE results, the accuracy of the first approach (based on the mixed-mode interaction formula) in predicting the web wrinkling load was confirmed. Furthermore, the approach, in which the wrinkling behavior of web-core panels was treated as a biaxial compression-tension local buckling problem, approximated the wrinkling load reasonably well with an underestimation of less than 15%. However, the strip position predicted for local buckling in this approach (length of 148 mm) and the inclination angle of the buckling wave (30°) were in good agreement with the FE buckling mode shown in Figure 5.17. The discrepancies compared to FE results can result from the assumptions that the buckling was considered to occur at the mid-length of the strips and that the principal stresses at the mid-length of each strip were applied as constant stresses for solving the biaxial compression-tension buckling problem. The principal stresses, however, are not constant but change linearly throughout the length of each strip. By improving the latter assumption, this approach can result in more accurate predictions.

Table 5.5 also comprises the values calculated in Keller et al. (2008) during the design of the Novartis sandwich roof structure. The calculation for the shear strength of the webs was based on the design model presented by Wiedemann (1996), which is as follows:

$$\tau_{wrk} = 0.5 \cdot f_{wrk} \tag{5.26}$$

where, τ_{wrk} is the shear wrinkling strength and f_{wrk} is the wrinkling strength of the laminates, f_{wrk} , subjected to uniaxial compression and estimated according to Wiedemann (1996), using the conservative Hoff's formula (Hoff and Mautner 1945):

$$f_{wrk} = 0.5 \cdot \left(E_c \cdot E_{FRP} \cdot G_c \right)^{1/3} \tag{5.27}$$

where E_{FRP} is the elastic modulus of laminates.

In addition, the critical load achieved by applying the model proposed by Fagerberg and Zenkert (2005-a) for the wrinkling of anisotropic sandwich panels subjected to multi-axial loading (see Section 2.4.2) is presented in Table 5.5. Comparison of the results reveals that although the model proposed by Wiedemann (1996), (Eqs. (5.26) and (5.27)), took only the pure shear stresses and not the bending stresses into account, it extremely underestimated the wrinkling strength of the web-core panels (64% in comparison with FE results). Similarly, Fagerberg and Zenkert's model gave a very conservative prediction since these sorts of models are based on the assumption that the face sheet is like an infinite plate (in comparison to the small length of wrinkles) and thus the wrinkling load is independent of the boundary conditions. This assumption is not applicable to web wrinkling, as wrinkles might occur close to the corners of the rectangular webs where the maximum stresses exist due to the combined shear and bending loading.

Throughout the experiments, instant failure occurred in the case of beam B3 (see Figure 5.18) at an ultimate load of 77 kN and based on the applied model's prediction at that time (Eqs. (5.26) and (5.27)), a web wrinkling failure was reported as the final failure. The new results now prove however that the failure mode was first compressive wrinkling on the top face sheet, followed by a shear failure of the webs. In fact, the ultimate load was significantly lower than the load predicted for web wrinkling.

For these specific beams, applying the first analytical approach (the mixed-mode interaction model) for increasing web heights from 0.3 m up to 0.5 m decreases the critical web winkling load by only 15%. It can be concluded that an optimum design is obtained by increasing web height in order to reduce the shear stresses in the web and also decrease the compressive stresses in the top face sheet. These changes enhance the ultimate failure loads while the total weight is kept constant.

Table 5.5. Summary of results for different solutions.

Results	Critical loads, F_{cr} (kN)
FE model	153.5
1st approach: Mixed-mode buckling model	154.6
2nd approach: Biaxial compression-tension buckling model	131.0
Model proposed by Wiedemann (1996)	55.1
Model proposed by Fagerberg and Zenkert (2005-a)	69.4

Figure 5.18. Failure at top face sheet and web of beam B3.

5.6. Concluding remarks

In this chapter, an extensive analytical and numerical study was performed of the buckling/wrinkling of web-core panels in cell-core sandwiches. Web-core panels were modeled as long orthotropic plates stabilized by a relatively thick elastic foam and subjected to combined bending and shear loads. A new approach was developed based on the mixed-mode interaction formula to predict the wrinkling load. The applicability of this approach together with the approach developed in Chapters 3 and 4, in which the wrinkling of web-core panels is treated as a biaxial compression-tension problem, were examined. The following conclusions were drawn:

1) The numerical studies carried out of the definition concerning the boundary conditions at the junction of web and face sheet in sandwich beams demonstrated that for t_f/t_w less than 1, the effective support condition is close to a simple support, while for t_f/t_w larger

than 2, it is closer to a clamped support. Likewise, increasing the foam stiffness increases the degree of rotational restraint of the web so that at high foam stiffnesses, webs behave rather more similarly to a clamped plate than a simply supported one at its junction to the face sheet.

2) For common GFRP cell-core sandwich structures with foam densities higher than 45 kg/m^3 and t_f/t_w larger than 1, simply supported boundary conditions for the web-core panel along the face sheet-web junction is a very conservative assumption, and the realistic support condition is close to a clamped support.

3) The agreement between the results of the new approach based on the mixed-mode interaction formula and finite element simulation was good. The analytical model has advantages in that it significantly saves computing time compared with pure numerical analysis and provides the possibility for extensive exploration of different design (geometry and material) parameters.

4) For the GFRP sandwich roof of the Novartis building, the results of the approach based on the mixed-mode interaction formula were again in good agreement with FE results. The solutions confirmed a 10% influence of bending stresses on the wrinkling loads of the web-core panel and proved the importance of taking the bending stresses into account.

5) The biaxial compression-tension approach approximated the wrinkling load reasonably well (with a 15% underestimation). The position and inclination angle of the local buckling waves, however, were well predicted.

6) Comparison of the results demonstrated the imprecision (enormous underestimation) of the models presented by Wiedemann (1996) and Fagerberg and Zenkert (2005-a) for the prediction of buckling loads in the webs of sandwich beams. However, the introduced approaches (using the biaxial compression-tension buckling model or mixed mode interaction formula) are sufficiently accurate to be used for the optimum design of these structures.

6 Conclusions and future research

This chapter contains the principal conclusions and recommendations for future work. The conclusions may be considered as "answers" to the question "How can a model be developed to accurately predict the wrinkling behavior of cell-core sandwich webs which are subjected to an in-plane biaxial compression-tension stress field?" posed in Section 1.1 and are linked with the objectives of this thesis (also summarized in Section 1.2).

6.1. Conclusions

6.1.1. Biaxial compression-tension buckling and wrinkling behavior

An extensive experimental, numerical and analytical study was performed to investigate the interaction between the compression and transverse tension stress fields during the buckling/wrinkling instability phase of GFRP plates and sandwich panels subjected to biaxial compression-tension loading.

The experiments eventually showed that the transverse tension in the biaxial compression-tension test set-ups induced two simultaneous counteracting effects: a stabilizing effect and lateral contraction. The stabilizing effect tends to push the plate back to the median plane and thereby delays the onset of buckling/wrinkling instability. In contrast, lateral contraction accelerates the bending of the plate, which leads to a significant decrease in the buckling/wrinkling loads. In composite plates, the first effect predominates and increases the buckling loads while in sandwich panels the second effect is dominant and decreases the wrinkling loads.

The analytical and numerical models proposed successfully simulated these two positive and negative effects of transverse tension and thus could predict the influence of an increasing transverse tension load on the buckling and wrinkling behavior of GFRP composite laminates

and sandwich panels. Additional analytical studies showed that the influence of transverse tension on biaxial compression-tension buckling/wrinkling loads can be predicted as a function of the relative stiffness of foam and plate.

6.1.2. Wrinkling of cell-core sandwich webs

Two new approaches were introduced and applied for the prediction of wrinkling instability behavior in the orthotropic webs of cell-core sandwich structures which were assumed to be under in-plane shear and bending stresses.

The first approach dealt with the wrinkling instability of web-core panels as a biaxial compression-tension local buckling problem, while the second approach used a mixed-mode interaction formula to predict the buckling/wrinkling stabilities of web-core panels.

In both approaches, the webs of cell-core sandwich structures were treated as a long plate stabilized by a relatively thick core foundation. The boundary condition of the plate was defined according to the interaction between the webs and face sheets in the presence of the core material. A series of numerical analyses via finite element modeling was performed in order to define the degree of elastic restraint that foam and face sheets exercised on the web at its connection to the face sheets. The results showed that for commonly used GFRP cell-core sandwich structures, the most realistic support condition is a clamped support while by assuming the unrealistic simply supported boundary condition, web design tends to be too conservative.

The application of both approaches to a real case study, the GFRP cell-core sandwich roof of the Novartis Campus Main Gate Building (Keller et al. 2008), proved that:

- The biaxial compression-tension buckling approach approximated reasonably well the buckling load as well as the position and inclination angle of the wrinkling waves. These results confirmed that this approach can indeed be used for prediction of the wrinkling behavior in the webs of sandwich structures since it can be considered as an in-plane biaxial compression-tension local buckling problem according to the rotated stress field theory.

- Although the second approach does not provide the designer with the precise location of wrinkling waves in the web, it can accurately predict the buckling/wrinkling instability load of cell-core sandwich webs.

6.1.3. Original contributions

The new findings contributing to the state –of –the art can be summarized as follows:

- The effects of transverse tension on the buckling behavior of structural components, e.g. thin-walled webs in FRP girders or cell-core sandwiches, were explored by experimental investigations on the buckling and wrinkling of GFRP plates and sandwich panels subjected to biaxial compression-tension loading.
- Based on the comprehensive experimental database, a new analytical model was developed for the prediction of the biaxial compression-tension buckling and wrinkling behavior of GFRP plates and sandwich panels. The new model allows the transition from biaxial compression-tension plate buckling to biaxial compression-tension sandwich wrinkling to be easily demonstrated and thus proves how certain key parameters such as the relative stiffness of the GFRP plates and foam core influence the effect of transverse tension on the buckling and wrinkling loads.
- In contrast to the existing model (Briscoe et al. 2010) for the wrinkling of webs in cell-core sandwich structures, which assumed simply supported boundary conditions for the web at the junction of the web and face sheets, in the present study, the boundary condition of the web-core panels was quantitatively evaluated according to the interaction between the webs and face sheets in the presence of the core material. The results showed that considering simply supported boundary conditions for the web-core panel at the face sheet-web junction is a conservative assumption in most cases, particularly in GFRP cell-core sandwich structures with long web-core panels for which the length-to-width ratio is larger than approximately three.
- Two new approaches were developed for the prediction of the wrinkling instability behavior in the orthotropic webs of cell-core sandwich structures based on (1) a biaxial

compression-tension local buckling model; (2) a mixed-mode interaction buckling model. In contrast to the former models (Fagerberg and Zenkert 2005-a, Birman and Bert 2004, Vonach and Rammerstorfer 2000-a&b, Sullins et al. 1969), which assumed the face sheet as being an infinite plate and whose solutions for wrinkling loads were thus independent of boundary conditions, the newly developed approaches do not have these limitations. They are proposed for webs with finite dimensions and defined boundary conditions. Furthermore, the introduced approaches predict the wrinkling instability behavior in orthotropic webs under combined shear and bending stresses and not just shear stresses as assumed by Briscoe et al. (2010). The results confirmed that the influence of bending stresses is significant and should be taken into account in the prediction of the wrinkling behavior of webs in cell-core sandwiches.

- The investigation proved that the two newly developed approaches are capable of accurately predicting the wrinkling of cell-core sandwich webs, which can contribute to the optimum design of cell-core sandwich structures, whereas using existing models, e.g. models presented by Wiedemann (1996) or Fagerberg and Zenkert (2005-a), results in too conservative predictions and subsequently too conservative structural designs. Compared to the frequently used numerical modeling, e.g. FE, the analytical models offer the advantages that they significantly save computing time and also allow designers to perform parametric studies on different design (geometry and material) parameters and/or utilize them in optimization procedures in order to find the optimum designs.

6.2. Future research

This section concerns research that should be carried out in the future. It involves the analytical, numerical and experimental investigation and further development stages of new models for predicting web wrinkling in cell-core sandwich structures.

6.2.1. Post-wrinkling in webs of cell-core sandwich structures

The design process for plate girder webs is frequently performed in two different ways: (1) allowable stress design based on elastic buckling as a limiting condition; (2) strength design based on ultimate strength that includes the post-buckling stage. Post-buckling behavior was first

discovered by Wilson (1886) and developed by Wagner (1931) for aircraft structures and since then numerous research efforts and models have been developed and some have been incorporated into the relevant standards.

One of these models is the rotated stress field theory, developed by Höglund (1997). According to this theory, for the shear buckling of steel and aluminum plate girders, substantial post-buckling strength is provided via the tension membrane stress field developed in the surrounding flanges and/or transverse stiffeners. If it is assumed that the web is only under a pure state of shear, the absolute values of the principal membrane stresses, tension and compression, are identical as long as no buckling occurs. After web buckling, stresses are redistributed and tension stresses increase significantly, while compression stresses increase much less.

Similar phenomena can occur after wrinkling in the webs of cell-core sandwich structures, known as "post-wrinkling". Similarly to steel girders, the strength design of cell-core sandwich webs can be improved to the ultimate strength, which includes the post-wrinkling stage. Post-wrinkling is, however, different from post-buckling behavior. This is because wrinkling is a local buckling instability which can occur in any part of the web, e.g. at the corner of the web (see Figure 5.17) or in the middle of web panels; therefore the redistribution of tension and compression stress fields after wrinkling can differ from that observed after buckling. Furthermore, all the theories or models presented up to now have been limited to isotropic web plates, while the fiber architecture of orthotropic plates can be a key parameter that greatly influences post-buckling/post-wrinkling behavior.

Thus, the post-wrinkling behaviors in FRP cell-core sandwiches with orthotropic webs as well as the applicability of existing theories, e.g. the rotated stress field theory, to orthotropic FRP material systems require further experimental, numerical and analytical investigation. In this context, the biaxial compression-tension test set-up can be an appropriate way of experimentally simulating the redistribution of the stress field after wrinkling instability and simulating post-wrinkling behavior in web-core panels.

6.2.2. Wrinkling in perforated cell-core sandwich webs

Openings are frequently found in the webs of plate girders, box girders as well as cell-core sandwich structures in order to accommodate large ducts and pipes used for air-conditioning

systems and also to create access for inspection and maintenance services. The depths of these openings are sometimes as great as 60% of the beam depth and their length is two or three times the depths of the opening. Openings of different shapes, i.e. circular and rectangular, are widely performed. When these structures are loaded, the presence of openings will cause changes in the stress distribution within the web panels and there will therefore be a change in the wrinkling characteristics of the webs as well as in the post-wrinkling and ultimate load capacity of the structures. In fact, the compression stress concentrations occurring around the opening are significantly intensified by the lateral contraction induced by the transverse tension field due to the presence of the opening. A considerable amount of research has been directed towards the study of the buckling and post-buckling behavior of perforated web girder plates. No investigation has been dedicated to the instability behavior in the perforated webs of cell-core sandwich structures however. Thus, an experimental and analytical study of the wrinkling and post-wrinkling of perforated cell-core sandwich webs seems crucial since the presence of openings in webs is usually necessary.

6.2.3. Failure map for FRP cell-core sandwiches

All the research concerning the prediction of failure modes of a particular structure will be portrayed in a failure map, which is a useful design tool for designers and manufacturers. In Section 2.3, common failure modes in sandwich constructions, such as face sheet compressive failure, adhesive bonding failure, core indentation, wrinkling, crimpling, dimpling and core shear failure, and their failure mechanisms are briefly described. Some research has attempted to develop failure maps for sandwich panels with different core materials (Triantafillou and Gibson 1987, Petras and Sutcliffe 1999). Thus, by combining the analyses for the wrinkling and post-wrinkling behavior of web-core panels with and without openings, the existing failure maps can be improved for use in the design of FRP cell-core sandwich structures. Experimental investigation of full-scale sandwich structures like the examined beams presented in Keller et al. (2008) would be useful for validating the suggested failure map.

7 Notations

Abbreviations

AASHTO	–	American Association for State Highway and Transportation Officials
AISC	–	American Institute of Steel Construction
ASSET	–	Advanced Structural Systems for Tomorrow's Infrastructure
ASTM	–	American Standard Test Method
CAB	–	Composite Army Bridge
CLT	–	Classical Laminate Theory
CNC	–	Computer Numerically Controlled
CT	–	Constant Tension test
FE	–	Finite Element
FRP	–	Fiber-Reinforced Polymer
GFRP	–	Glass Fiber-Reinforced Polymer
SCT	–	Simultaneously Compression-Tension loading test
UD	–	Unidirectional

Latin upper case letters

A	–	deflection amplitude
A_0	–	initial amplitude
A_1, A_2	–	amplitude coefficients
A', B', D'	–	material coefficients
B_1, B_2	–	constant parameters
$B^f_{()}$	–	face sheet stiffness parameters
C^m_{ij}	–	coefficients
D_{11}, D_{22}	–	flexural stiffness components
D_{12}	–	Poisson coupling stiffness
D_{66}	–	twisting stiffness
D'_{12}	–	$D_{11} + 2\ D_{66}$
D_f	–	bending stiffness of face sheet
$D_{\varphi 11}$	–	bending stiffness of face sheet at angle φ
E_c	–	Young's modulus of core
E_f	–	Young's modulus of face sheet
E_{FRP}	–	elastic modulus of laminates
F	–	applied load
F_C	–	correction factor

F_{cr} – critical load
$F_{cr,cc}$ – critical load for clamped support
$F_{cr,a}$ – critical load for actual support condition
F_x – compressive load acting on face sheet
F_{x0} , F_{y0} – in-plane compression and tension loads
$F_{Winkler}$ – critical compressive force of Winkler foundation model
F', G' – applied normal forces per unit length
F'', G'' – applied shear forces per unit length
G_c – shear modulus of core
K – model parameter
K_z – foundation modulus
L_x – length
L_y – width
L_w – web length
M – bending moment
N – normal force
N_x, N_y , N_{xy} – external compressive normal and shear forces per unit width
P – applied load
P_{cr} – critical load
P_x, P_y , P_{xy} – external compressive normal and shear forces per unit width
P_φ – applied load at angle φ
$P_{\varphi,cr}$ – critical compressive force at angle φ
$P_{Plantema}$ – critical compressive force of Plantema's model
$[P']$ – structure stiffness matrix
P_x^* – compressive force
Q – model parameter
$[Q']$ – stress stiffness matrix
S_m – normalized stress
U_f – face sheet strain energy
U_c – core strain energy
V – pure shear load
W_T – total out-of-plane displacement
$W_\circ$ – initial imperfection
W – measured maximum deflection
$X(x)$, $Y(y)$, $Z(z)$ – deflection function in x-, y- and z-directions

Latin lower case letters

a, b, c – geometry parameters
a' – model parameter
c_1, c_2, c_3, c_4 – coefficients
d – variable roof depth
d' – beam depth
d_w – webs distance

f_{wrk} – wrinkling strength of the laminates
f, g – sinusoidal or co-sinusoidal functions in x- and y-directions
h – depth of linear decay
h_w – web height
i, j – number of buckling waves in x- and y-directions
k – model parameter
l – wavelength
m, n – index parameter
p – applied singular load
q' – partially uniform tension in y-direction
q'' – partially uniform compression in x-direction
(r, θ, z) – polar coordinate system
(r, s, z) – polar coordinate system
s_{mn} – elastic constants of composite laminates
t – thickness
t_c – core thickness
t_f – Face sheet thickness
t_w – web thickness
u_c – displacement of core in x-direction
u_f – displacement of face sheet in x-direction
u, v, w – displacements in x-, y- and z-directions
v_c – Poisson ratio of core
v_f – Poisson ratio of face sheet
w – deflection of the midplane
w_0 – initial imperfection
w_c – transverse deformation in core
w_f – defection function of face sheet
w_t – total deformation
w^* – amplitude of the transverse displacement at interface
(x, y, z) – cartesian coordinate system

Greek letters

α – coefficient
α_1, α_2 – constant parameters
$\alpha'_{()}$ – model parameters
β – compression-tension load ratio
$\beta_1, \beta_2, \beta_3, \beta_4$ – coefficients
γ – model parameter
δ – model parameter
Δ_{Inc} – dimensionless increment of buckling load due to the transverse tension
ε – tangent of angle ψ
$\varepsilon_x, \varepsilon_y, \varepsilon_{xy}$ – strain components in (x, y) plane

ε_z – strain of core in z-direction
η – model parameter
λ – load factor
λ_{cr} – critical load factor
μ – model parameters
ξ – model parameter
Π – total potential energy
Π_p – total potential energy
σ_b – maximum compressive in-plane stress due to bending
$\sigma_{b,cr}$ – critical bending buckling stresses
σ_{cxz} – core shear stress in (x, z) plane
σ_{cyz} – core shear stress in (y, z) plane
σ_{cz} – stress of core in z-direction
σ_{Hoff} – critical compressive stress of Hoff and Mautner's model
$\sigma_{Plantema}$ – critical compressive stress of Plantema's model
$\sigma_{z=0}$ – normal core stress at z=0
$\sigma^{c}_{z,0}$ – stress amplitude
σ_r, σ_θ, $\sigma_{r\theta}$ – stress components in (r, θ) plane
σ_x, σ_y, σ_{xy} – stress components in (x, y) plane
$\sigma_{x,I}$, $\sigma_{y,I}$, $\sigma_{xy,I}$ – stress components for problem I
$\sigma_{x,II}$, $\sigma_{y,II}$, $\sigma_{xy,II}$ – stress components for problem II
$\sigma_{x,III}$, $\sigma_{y,III}$, $\sigma_{xy,III}$ – stress components for problem III
$\sigma_{xy,cr}$ – critical shear buckling stress
σ'_x, σ'_y , σ'_{xy} – stress components induced by partially distributed tension
σ''_x, σ''_y , σ''_{xy} – stress components induced by partially distributed compression
$\left(\sigma'_{centre}\right)\Big|_{F_{y0}}$ – compressive stress in x-direction, at the centre of the plate due to the partially distributed tension
σ_1, σ_2 – principal stresses
σ_{1cr} , σ_{2cr} – critical stresses in the directions of principal stresses
ς – model parameter
τ_{cxz} – shear stress of core in (x, z) plane
τ_{wrk} – shear wrinkling strength
Υ – non-dimensional parameter
φ – wrinkling wave angle
ϕ – principal stresses angle
ϕ_1, ϕ_2, ϕ_3, ϕ_4 – model parameters
$\phi'_\circ$, $\phi''_\circ$ – model parameters
Φ – stress function
χ – stress function
ψ – inclination angle
Ψ – model parameter
Ω – work by external forces

References

AASHTO (1992). *Standard specifications for highway bridges,* ASD and LFD, 15th Edn. American Association for State Highway and Transportation Officials, Washington, DC.

Abramovich, H., Weller, T., and Yaffe, R. (1990). Application of modified Donnell technique for the determination of critical loads of imperfect plates. *Comput Struct*, 37(4), 463-469.

AISC (1989). *Specification for the design, Fabrication and Erection of Structural Steel for Building*, ASD, 9th Edn. American Institute of Steel Construction, Chicago, IL.

Alampalli, S., O'Connor, J., and Yannotti, A.P. (2002). Fiber reinforced polymer composites for the superstructure of a short-span rural bridge. *Compos Struct*, 58 (1), 21-27.

Allen, H.G. (1969). *Analysis and design of structural sandwich panels*. Oxford: Pergamon Press.

Ashby, M.F., and Brechet, Y.J.M. (2003). Designing hybrid materials. *Acta Mater*, 51 (19), 5801-5821.

Bakis, C. E., et al. (2002). Fiber-reinforced polymer composites for construction—State–of–the–art review. *J Compos Constr*, 6(2), 73-87.

Barbero, E.J., and Raftoyiannis, I.G. (1993). Local buckling of FRP beams and columns. *J Mat Civil Eng*, 5(3), 339-355.

Benson, A.S., and Mayers, J. (1967). General instability and face wrinkling of sandwich plates–unified theory and applications. *AIAA J*, 5(4): 729-739.

Birman, V., and Bert, C.W. (2004). Wrinkling of composite-facing sandwich panels under biaxial loading. *J Sandw Struct Mater*, 6(3), 217-237.

Briscoe, C.R., Mantell, S.C., and Davidson J.H. (2010). Shear buckling of foam-filled web core sandwich panels using a Pasternak foundation model. *Thin Wall Struct*, 48(6), 460-468.

Cerda, E., Ravi-Chandar, K., and Mahadevan, L. (2002). Thin films: Wrinkling of an elastic sheet under tension. *Nature*, 419, 579-580.

Cox, H.L. and Riddell, J.R. (1945). *Sandwich construction and core materials III: Instability of sandwich struts and beams*, ARC Technical Report R&M 2125.

Daniel, I.M., Gdoutos, E.E., Wang, K.A., and Abot, J.L. (2002). Failure modes of composite sandwich beams. *Int J Damage Mech*, 11 (4), 309-334.

Davies, J.M., and Fragos, A.S. (2003). Shear strength of empty and infilled cassettes. *Thin Wall Struct*, 41, 109–25.

Dawson, R.G., and Walker, A.C. (1972). Post-buckling of geometrically imperfect plates. *J Struct Div-ASCE*, 98(ST1), 75-94.

Dickson, T., Munro, M., and Lee, S. (1995). Selection of an in-plane shear test method based on the shear sensitivity of laminate tensile modulus. *Composites*, 26(1), 17-24.

Donnell, L.H. (1938). *On the application of Southwell's method for the analysis of buckling tests*, Timoshenko 60th Anniv. Vol., McGraw-Hill, New York.

Ehlen, M.A. (1999). Life-cycle costs of fiber-reinforced-polymer bridge decks, *J Mater Civil Eng*, 11(3), 224-230.

Estrada, I., Real, E., and Mirambell, E. (2008). A new developed expression to determine more realistically the shear buckling stress in steel plate structures. *J Constr Steel Res*, 64 (7-8), 737-747.

European Committee for Standardisation (1996). ENV-1993-1-4. *Eurocode 3: Design of steel structures*. Part 1–4: General rules—Supplementary rules for stainless steel. Brussels.

Fagerberg, L. (2000). *Wrinkling of anisotropic sandwich panels subjected to multi-axial loading*. Report 2000-27, Sandwich Construction 5 – Proceedings of the 5th International Conference on Sandwich Construction, Ed. H.-R. Meyer-Piening and D. Zenkert, EMAS Publishers, London, 211-220.

Fagerberg, L. (2003). *Wrinkling of sandwich panels for marine applications*. PhD thesis, ISSN 1651-7660, KTH Aeronautical and Vehicle Engineering, Stockholm, Sweden.

Fagerberg, L., and Zenkert, D. (2005-a). Effects of anisotropy and multi-axial loading on the wrinkling of sandwich panels. *J Sandw Struct Mater,* 7(3), 177-194.

Fagerberg, L., and Zenkert, D. (2005-b), Imperfection-induced wrinkling material failure in sandwich panels. *J Sandw Struct Mater*, 7, 195-219.

Fam, A., and Sharaf, T. (2010). Flexural performance of sandwich panels comprising polyurethane core and GFRP skins and ribs of various configurations. *Comput Struct*, 92(12), 2927-2935.

Featherston, C.A., and Ruiz, C. (1998). Buckling of flat plates under bending and shear. *Proceedings of the Institution of Mechanical Engineers, Part C: J Mech Eng Sci*, 212 (4), 249-261.

Fok, W.C. (1984), Evaluation of experimental data of plate buckling. *J Eng. Mech-ASCE,* 110 (4), 577-588.

Friedl N., Rammerstorfer F.G., and Fischer, F.D. (2000). Buckling of stretched strips. *Comput Struct*, 78(1), 185-190.

Ganesh, V.K., and Naik, N.K. (1997). (±45) degree off-Axis tension test for shear characterization of plain weave fabric composites. *J Compos Tech Res*, 19(2), 77-85.

GangaRao, H.V.S., Thippeswamy, H.K., Shekar, V., and Craigo, C. (1999). Development of glass fiber reinforced polymer composite bridge deck, *SAMPE J*, 35(4), 12-24.

Gdoutos, E.E., Daniel, I.M., and Wang, I.M. (2003). Compression facing wrinkling of composite sandwich structures. *Mech Mater*, 35 (3), 511-522.

Goodier, J.N. (1931). Compression of rectangular blocks and the bending of beams by non-linear distributions of bending forces. *Appl Mech Div ASME*, APM-54-17, 173-183.

Gough, C.S., Elam, C.F., and deBruyne, N.A. (1940). The stabilization of a thin sheet by a continuous supporting medium. *J R Aeronaut Soc*, 44, 12-43.

Green, A.E. (1939). *Stress system in aeolotropic plates II*. Proceedings of Royal Society of London. Series A, Mathematical and Physical Sciences, 173(953), 173-192.

Gutierrez, A.J., and Webber, J.P.H. (1980). Flexural wrinkling of honeycomb sandwich beams with laminated faces. *Int J Solids Struct*, 16 (7), 645-651.

Hadi, B.K., and Matthews, F.L. (2000). Development of Benson-Mayers theory on the wrinkling of anisotropic sandwich panels. *Comput Struct*, 49(4), 425-434.

Hemp, W.S. (1948). *On a theory of sandwich construction*, ARC Technical Report R&M 2672.

Hoff, N. J., and Mautner, S. F., (1945). The buckling of sandwich-type panels. *J. Aeronaut. Sci.*, 12(3), 285–297.

Höglund, T. (1997). Shear buckling resistance of steel and aluminium plate girders. *Thin Wall Struct*, 29(1-4), 13-30.

Johns, D.J. (1971). *Shear buckling of isotropic and orthotropic plates: a review*. ARC R&M no. 3677.

Hutcheson, D., and Sheppard, M. (2003). Sandwich panel performance optimizing with 3D fiber reinforcing core architecture. *SAMPE J*, 39(6), 68-75.

Kassapoglou, C., Fantle, S.C., and Chou, J.C. (1995). Wrinkling of composite sandwich structures under compression. *J Compos Tech Res*, 17(4), 308-316.

Kassapoglou, C., and Bauer, G. (2010). Composite plates under concentrated load on one edge and uniform load on the opposite edge. *Mech Adv Mater Struct*, 17, 196-203.

Keller, T. (2003). *Use of fibre reinforced polymers in bridge construction*. International Association for Bridge and Structural Engineering (IABSE).

Keller, T., and Schollmayer, M. (2004). Plate bending behavior of a pultruded GFRP bridge deck system. *Compos Struct*, 64(3-4), 285–295.

Keller, T. (2006). *Emerging markets - FRP composites in bridge superstructures*. In: Eighth World pultrusion conference, Emerging markets: globalization of the pultrusion industry, Budapest, Hungary.

Keller, T., Haas, Ch., and Vallée, T. (2008). Structural concept, design and experimental verification of a GFRP sandwich roof structure. *J Compos Constr*, 12(4), 454-468.

Kim, Y.S., and Hoa, S.W. (1995). Bi-axial buckling behavior of composite rectangular plates. *Compos Struct*, 31(4), 247-252.

Kos, E., and Stoll, F. (2008). Engineered sandwich cores: Vehicular bridge deck applications. *SAMP J*, 44(4), 36-42.

Lake, S., Saunders, M., and Anderson, J. (2007). *Shear wrinkling of composite sandwich stiffener webs*. SAMPE-2007, Baltimore, MD.

Lecieux, Y., and Bouzidi, R. (2010). Experimental analysis on membrane wrinkling under biaxial load - Comparison with bifurcation analysis. *Int J Solid Struct*, 47, 2459-2475.

Lee, S.C., Davidson, J.S., and Yoo, CH. (1996). Shear buckling coefficients of plate girder web panels**.** *Comput Struct*, 59 (5), 789-795.

Leissa, A.W. (1983). Buckling of composite plates. *Compos Struct*, 1(1), 51-66.

Leissa, A.W. (1985). *Buckling of laminated composite plates and shell panels*. AFWAL-TR 853069, Air Force Wright Aeronautical Lab, Wright Patterson Air Force Base, OH.

Lekhnitskii, S,G., Tsai, S.W., and Cheron, T. (1968). *Anisotropic plates*. Gordon and Breach, Science Publishers Inc., New York.

Ley, R.P., Lin, W., and Mbanefo, U. (1999). *Facesheet wrinkling in sandwich structures*. NASA: Langley Research Center.

Nemeth, M.P. (1997). *Buckling behavior of long symmetrically laminated plates subjected to shear and linearly varying axial edge loads*. TP 3659: NASA.

Pflug, J., and Verpoest, I. (2006). Sandwich materials selection charts. *J Sandw Struct Mater*, 8, 407-421.

Petras, A., and Sutcliffe, M.P.F. (1999). Failure mode maps for honeycomb sandwich panels. *Compos Struct*, 44 (4), 237-252.

Plantema, F.J. (1966). *Sandwich construction*. New York: John Wiley & Sons Inc.

Reddy, J.N. (1997). *Mechanics of laminated composite plates: theory and analysis*. Boca Raton: CRC Press.

Rion, J. (2008). *Ultra-Light Photovoltaic composite Sandwich Structures*. Doctorate Thesis, EPFL, Switzerland.

Robinson, M.J., and Kosmatka, J.B. (2008). Light-weight fiber-reinforced polymer composite deck panels for extreme applications. *J Compos Constr*, 12(3), 344-354.

Romeo, G., and Ferrero, G. (2001). Analytical/experimental behavior of anisotropic rectangular panels under linearly varying combined loads. *AIAA J*, 39(5), 932-941.

Romeo, G., and Frulla, G. (1994). Nonlinear analysis of anisotropic plates with initial imperfections and various boundary conditions subjected to combined biaxial compression and shear loads. *Int. J. Solids Struct,* 31(4), 763-783.

Romeo, G., and Frulla, G. (1997). Post-buckling behavior of graphite/epoxy stiffened panels with initial imperfections subjected to combined biaxial compression loading. *Int J Nonlin Mech*, 32(6), 1017-1033.

Segedin, RH., Collins, I.F., and Segvoin, C.M. (1988). The elastic wrinkling of rectangular sheets. *Int J Mech Sci*, 30(10), 719-732.

Shufrin, I., Rabinovitch, O., and Eisenberger, M. (2008). Buckling of symmetrically laminated rectangular plates with general boundary conditions – A semi analytical approach. *Compos Struct*, 82(4), 521–531.

Singer, J., Arbocz, J., and Weller, T. (1998). *Buckling experiments: experimental methods in buckling of thin-walled structures-volume I*. John Wiley & Sons Inc., New York.

Singer, J., Arbocz, J., and Weller, T. (2002). *Buckling experiments: experimental methods in buckling of thin-walled structures-volume II*. John Wiley & Sons Inc., New York.

Spencer, H.J., and Walker, A.C. (1975). Critique of Southwell plots with proposals for alternative methods. *Exp Mech*, 15(8), 303-310.

Sullins, R.T. Smith, G.W., and Spier, E.E. (1969). *Manual for structural stability analysis of sandwich plates and shells*. NASA-Contractor Report No. 1467.

Thielemann, W. (1950). *Contribution to the problem of buckling of orthotropic plates with special reference to plywood*. NACA. TM. 1263.

Timoshenko, S.P. (1935). *Stability of webs of plate girders*. *Engineering-London*, 238, 207.

Timoshenko S., and Goodier, J.N. (1951). *Theory of elasticity*. New York, 2nd edn. McGraw-Hill.

Timoshenko, S.P., and Gere, J.M. (1963). *Theory of elastic stability*. 2nd Ed. McGraw-Hill Int., New York.

Tomita, Y., and Shindo, A. (1988). Onset and growth of wrinkles in thin square plates subjected to diagonal tension. *Int J Mech Sci*, 30(12), 921-931.

Triantafillou, T.C., and Gibson, L.J. (1987). Failure modes map for foam core sandwich beams. *Mater Sci Eng*, 5 (1), 37-53.

Tuttle, M., Singhatanadgid, P., and Hinds, G. (1999). Buckling of composite panels subjected to biaxial loading. *Exp Mech*, 39(3), 191-201.

Ungbhakorn, V., and Singhatanadgid, P. (2006). Buckling analysis of symmetrically laminated composite plates by the extended Kantorovich method. *Compos Struct*, 73(1), 120-128.

Upadyay, A., and Kalyanaraman, V. (2003). Simplified analysis of FRP box-girders. *Compos Struct*, 59(2), 217–225.

Veres I., and Kollár, L.P. (2001). Buckling of orthotropic plates with different edge supports. *J Compos Mater*, 35, 625-635.

Vinson, J. R. (1995). *The behavior of sandwich structures of isotropic and composite materials*. Technomic Publishing Company, Lancaster, PA.

Vonach, W.K., and Rammerstorfer, F.G. (2000-a). Wrinkling of thick orthotropic sandwich plates under general loading conditions. *Arch Appl Mech*, 70(5), 338-348.

Vonach, W.K., and Rammerstorfer, F.G. (2000-b). The effects of in-plane core stiffness on the wrinkling behavior of thick sandwich. *Acta Mech*, 141, 1-10.

Vonach, W.K. (2001). *A general solution to the wrinkling problem of sandwiches*. VDI Verlag, Düsseldorf.

Wagner, H. (1931). *Flat sheet metal girder with very thin metal web*. Tech Memorandum 604–606, National Advisory Committee for Aeronautics (NACA), Hampton, Va.

Weaver, P.M., and Nemeth, M.P. (2008). Improved design formulas for buckling of orthotropic plates under combined loading. *AIAA J*, 46 (9), 2391-2396.

Webber, J.P.H., Kyriakides, S., and Lee, C.T. (1976). Wrinkling of honeycomb sandwich columns with laminated cross-ply faces. *Aeronaut J*, 80 (786), 264-272.

Wiedemann, J. (1996). *Leichtbau 1: Elemente*. Springer Berlin, Heidelberg, ISBN 3-540-60746-3, 430 pages.

Williams, D. (1947). *Sandwich construction: A practical approach for the use of designers.* RAE Report No. Structures 2.

Williams, B., Shehata, E., and Rizkalla, S. (2003). Filament-wound glass fiber reinforced polymer bridge deck modules. *J Compos Constr*, 7(3), 266–273.

Williams, D., Legget, D.M.A., and Hopkins, H.G. (1941). *Flat sandwich panels under compressive end loads*. Royal Aircraft Establishment Report No. A.D. 3174.

Wilson, J.M. (1886). On specifications for strength of iron bridges. *Trans Am Soc Civ Eng*, 15 (1), 401–403 489–490.

Wong, Y., and Pellegrino, S. (2006). Wrinkled membranes part I: experiments. *J Mech Mater Struct*, 1, 1-23.

Xu Y., and Yu, T.X. (1990). The elastic-plastic wrinkling of rectangular plates subjected to locally uniform tension. *Int J Mech Sci*, 32(10), 829-842.

Yoshida, K., Hayashi, S., Miyauchi, K., Yamato, Y., Abe, K., Usuda, I., Ishida, R., and Oike, Y. (1974). *The effects of mechanical properties of sheet metals on the growth and removing of buckles due to non uniform stretching*. Scientific Papers of the Institute of Physical and Chemical Research, 68, 85-93.

Yusuff, S. (1960). Face wrinkling and core strength in sandwich construction. *J R Aeronaut Soc*, 64, 164-167.

Zenkert, D. (1995). *An introduction to sandwich construction*. Engineering Materials Advisory Services Ltd, Solihull, UK.

Zureick, A., Shih, B., and Munley, E. (1995). Fiber-reinforced polymeric bridge decks. *Struct Eng Rev*, 7(3), 257-266.

Curriculum Vitae

BEHZAD DEHGHAN MANSHADI

Date of Birth:	August 09, 1980 in Karaj/Tehran, Iran
Nationality:	Iranian
E-mail:	behzad.dehghan@epfl.ch

Education

April 2008- Sept. 2011	**Ph.D.** Student at Composite Construction Laboratory CCLab, Civil and Environmental Engineering EDCE, École Polytechnique Fédérale de Lausanne EPFL, Lausanne, Switzerland.
Sept. 2005- Sept. 2007	**M.Sc.** Aerospace Engineering, Sharif University of Technology, Tehran, Iran.
Sept. 1998- July 2003	**B.Sc.** Aerospace Engineering, Sharif University of Technology, Tehran, Iran.

Work experience

April 2008– Sept. 2011	Research Assistant, Composite Construction Laboratory CCLab, École Polytechnique Fédérale de Lausanne EPFL, Switzerland.
Nov. 2002–March 2008	Structural Designer, Zamyad Co. (Iranian Commercial Vehicle Manufacturing Co.), Tehran, Iran.
June 2004–Sept. 2005	Coordinator of Composite Lab., Sharif University of Technology, Tehran, Iran.
Dec. 2001–July 2002	Mechanical Designer, Iran-khodro Clutch Manufacturing Co., Tehran, Iran.

Publications

Journal Papers

1. Behzad D. Manshadi, Anastasios P. Vassilopoulos, Julia de Castro, Thomas Keller, "*Modeling of buckling and wrinkling behavior in GFRP plate and sandwiches subjected to biaxial compression–tension loading*", ASCE's Journal of Composites for Construction, 2011 (under review).

2. Behzad D. Manshadi, Anastasios P. Vassilopoulos, Julia de Castro, Thomas Keller, "*An analytical model for lateral contraction of composite laminates subjected to partially uniform tension*", International Journal of Mechanical Sciences, 2011 (under review).

3. Behzad D. Manshadi, Anastasios P. Vassilopoulos, Julia de Castro, Thomas Keller, "*Contribution to shear wrinkling of GFRP webs in cell-core sandwiches*", ASCE's Journal of Composites for Construction, 2011 (accepted, doi:10.1061/(ASCE)CC.1943-5614.0000212).

4. Behzad D. Manshadi, Anastasios P. Vassilopoulos, Thomas Keller, "*Shear buckling resistance of GFRP plate girders*", ASCE's Journal of Composites for Construction, Vol. 15, No. 3, pp. 431-440, 2011.

5. Thomas Keller, Anastasios P. Vassilopoulos, Behzad D. Manshadi, "*Thermo-mechanical behavior of multifunctional GFRP sandwich structures with encapsulated photovoltaic cells*", ASCE's Journal of Composites for Construction, Vol. 14, No. 4, pp. 470-478, 2010.

6. Anastasios P. Vassilopoulos, Roohollah Sarfaraz, Behzad D. Manshadi, Thomas Keller, "*A computational tool for the life prediction of GFRP laminates under irregular complex stress states: influence of the fatigue failure criterion*", Computational Materials Science, Vol. 49, No. 3, pp. 483-491, 2010.

7. Anastasios P. Vassilopoulos, Behzad D. Manshadi, Thomas Keller, "*Piecewise non-linear constant life diagram formulation for FRP composite materials*", International Journal of Fatigue, Vol. 32, pp. 1731–1738, 2010.

8. Anastasios P. Vasilopoulos, Behzad D. Manshadi, Thomas Keller, "*Influence of the constant life diagram formulation on the fatigue life prediction of composite materials*", International Journal of Fatigue, Vol. 32, No. 4, pp. 659–669, 2010.

9. Kazem Fayazbakhsh, Ali Abedian, Behzad D. Manshadi, Roohollah Sarfaraz, "*Introducing a novel method for materials selection in mechanical design using Z-transformation in statistics for normalization of material properties*", Materials & Design, Vol. 30, No. 10, pp. 4396-4404, 2009.

10. Roohollah Sarfaraz, Behzad D. Manshadi, Ali Abedian, "*Nonlinear analysis of FGM plates under pressure loads using the higher-order shear deformation theories*", Composite Structures, Vol. 89, No. 3, pp. 333-496, 2009.

11. Roohollah Sarfaraz, Behzad D. Manshadi, Ali Abedian, Reza Mahmudi, "*A simplified fuzzy logic approach for materials selection in mechanical engineering design*", Materials & Design, Vol. 30, No. 3, pp. 687-697, 2009.

12. Behzad D. Manshadi, Hamed Mahmudi, Ali Abidian, Reza Mahmudi, "*A novel method for materials selection in mechanical design: combination of non-Linear normalization and a modified digital logic methods*", Materials & Design, Vol. 28, No. 1, pp. 8-15, 2007.

13. Ali Abedian, Hossein Ghiasi, Behzad D. Manshadi, "*An introduction to a new criterion proposed for stopping GA optimization process of a laminated composite plate*", Journal of Aerospace Science and Technology (JAST), Vol. 3, No. 4, pp. 167-176, 2007.

14. Hossein Ghiasi, Behzad D. Manshadi, Ali Abedian, "*Effects of a linear-exponential penalty function on the GA's efficiency in optimization of a laminated composite panel*", International Journal of Computational Intelligent (IJCI), Vol. 2, pp. 5-11, 2005.

Conference Papers

1. Behzad D. Manshadi, Anastasios P. Vassilopoulos, Julia de Castro, Thomas Keller, "*Shear wrinkling in glass fiber-reinforced polymer sandwich webs*", 9th International Conference on Sandwich Structures ICSS–9, California Institute of Technology, Pasadena, California, USA (June 14-16, 2010).

2. Anastasios P. Vassilopoulos, Behzad D. Manshadi, Thomas Keller, "*PNL constant life diagram formulation for FRP composite materials*", 14th European Conference on Composite Materials ECCM–14, Budapest, Hungary (June 7-10, 2010).

3. Behzad D. Manshadi, Anastasios P. Vassilopoulos, Thomas Keller, "*Shear buckling of GFRP beam webs*", 5th International Conference on FRP Composites in Civil Engineering CICE–2010, Beijing, China (September 27-29, 2010).

4. Behzad D. Manshadi, Anastasios P. Vassilopoulos, Julia de Castro, Thomas Keller, "*Shear wrinkling of GFRP webs in cell-core sandwiches*", 5th International Conference on FRP Composites in Civil Engineering CICE–2010, Beijing, China (September 27-29, 2010).

5. Behzad D. Manshadi, Anastasios P. Vassilopoulos, Thomas Keller, "*A computational tool for the fatigue life prediction of composite materials*", Proceedings of the 2nd International conference on material and component performance under variable amplitude loading, pp. 585-594, Darmstadt, Germany (March 2009).

6. Roohollah Sarfaraz, Behzad D. Manshadi, Ali Abedian, Reza Mahmudi , "*Materials selection for spar of a Human Powered Aircraft (HPA) using a simplified fuzzy logic approach*", Proceedings of the 7th Iranian Aerospace Society Conference, Vol. 2, pp. 55-56, Sharif University of Technology, Tehran, Iran (February 2008).

7. Mostafa Shafigh, Behzad D. Manshadi, Behrooz Khosravi, "*Using genetic algorithm in shape optimization of front axle bump stop for a new pickup vehicle (ZAMYAD-24F)*", Proceedings of the 9th International Conference on Computer Aided Optimum Design in Engineering OPTI'2005 (WIT Transactions), Vol. 80, pp. 311-320, Skiathos, Greece (May 2005).

8. Ali Abedian, Hossein Ghiasi, Behzad D. Manshadi, "*Comparison of static and dynamic penalty factors on efficiency of GA in optimization of stiffened composite panels*", 8th International & 12th Annual Mechanical Engineering Conference ISME'2004, Tehran, Iran (May 2004).

9. Ali Abedian, Hossein Ghiasi, Behzad D. Manshadi, "*Influence of external penalty functions in optimization of stiffened composite panels using genetic algorithm*", Proceedings of the 2nd International & 5th National Conference of Aerospace Engineering AERO'2004, pp. 351-360, Isfahan, Iran (February 2004).

10. Ali Abedian, Hossein Ghiasi, Behzad D. Manshadi, "*Application of genetic algorithms (GAs) to the design of laminated composite*", Proceedings of the 7th International & 11th Annual Conference of Mechanical Engineering ISME'2003, Vol. 6, pp. 402-409, Mashhad, Iran (May 2003).

11. Mohammad Daghigh, Behzad D. Manshadi, "*Prediction of ultimate load carrying capacity of Nissan Junior axle beam using elasto-plastic analysis procedure*", Proceedings of the 5th International & 9th Annual Conference of Mechanical Engineering ISME'2001, Vol. 4, pp. 45-52, Tehran, Iran (May 2001).

12. Reza Mahmudi, Behzad D. Manshadi, Hamed Mahmudi, "*Plane-strain tension testing of sheet metals",* Proceedings of the 9th Amsler Symposium (World of Dynamic Testing), Vol. 4, pp. 67-76, Gottmadingen, Germany (May 2001).

13. Hamed Mahmudi, Behzad D. Manshadi, Reza Mahmudi, "*Materials selection for the wing structure of a Human Powered Aircraft (HPA)*", Proceedings of the 1st International & 3rd Biennial of Conference of Aerospace Engineering AERO'2000, Vol. 3, pp. 1405-1413, Tehran, Iran (January 2000).

Appendix A: Determination of stress functions

The function $\phi_\circ$, which satisfies the symmetrical boundary conditions given by Eq. (4.12), is defined by Eq. (4.18) as the summation of two terms, $\phi'_\circ$ and $\phi''_\circ$, according to (Goodier 1931). The first term, $\phi'_\circ$, applies when the opposite sides of the rectangular plate are loaded with normal loads distributed symmetrically, see Figure A.1 which shows loads of $F'(x)$ and $G'(y)$ applied on the two opposite sides at $y=\pm b$ and $x=\pm a$, respectively. This can be expressed as:

$$
\begin{aligned}
&y = \pm b \rightarrow \frac{\partial^2 \phi'_\circ}{\partial x^2} = F'(x) \\
&x = \pm a \rightarrow \frac{\partial^2 \phi'_\circ}{\partial x^2} = G'(x) \\
&x = \pm a, \text{ and } y = \pm b \rightarrow \frac{\partial^2 \phi'_\circ}{\partial x \partial y} = 0
\end{aligned}
\tag{A.1}
$$

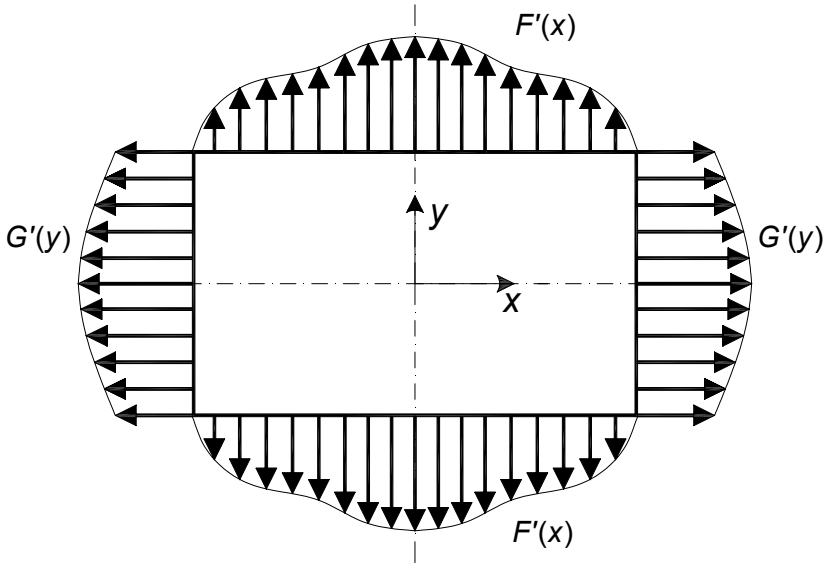

Figure A.1. Opposite edges of rectangular plate subjected to normal loads.

In all the cases occurring subsequently, $\phi_{\circ}'$ is obtained by:

$$\phi_{\circ}' = \iint F'(x)dxdx + \iint G'(y)dydy \tag{A.2}$$

with $\frac{\partial^2 \phi_{\circ}'}{\partial x^2} = F'(x)$, $\frac{\partial^2 \phi_{\circ}'}{\partial x^2} = G'(y)$ and $\frac{\partial^2 \phi_{\circ}'}{\partial x \partial y} = 0$.

The second term, $\phi_{\circ}''$, is used when shearing forces are applied. For a stress system as shown in Figure A.2, the intensity of the shearing forces on the boundary $y=+b$ will be an odd function of x, $F''(x)$, and on $y= -b$ it will be $-F''(x)$. Similarly a distribution $G''(y)$ on $x=+a$ and $-G''(y)$ on $x= -a$ are considered. The boundary conditions for $\phi_{\circ}''$ are then:

$$-\frac{\partial^2 \phi_{\circ}''}{\partial x \partial y} = \begin{cases} F''(x) : y = +b \\ -F''(x) : y = -b \\ G''(y) : x = +a \\ -G''(y) : x = -a \end{cases}$$

$$y = \pm b \rightarrow \frac{\partial^2 \phi_{\circ}''}{\partial x^2} = 0 \tag{A.3}$$

$$x = \pm a \rightarrow \frac{\partial^2 \phi_{\circ}''}{\partial y^2} = 0$$

$\phi_{\circ}''$ is initially defined as:

$$\phi_{\circ}'' = \left(x^2 - a^2\right) g''(y) + \left(y^2 - b^2\right) f''(x) \tag{A.4}$$

where $g''(y)$ is an even function of y only, and $f''(x)$ is an even function of x only. The second derivative of Eq. (A.4) with respect to x is:

$$\frac{\partial^2 \phi_{\circ}''}{\partial x^2} = 2g''(y) + \left(y^2 - b^2\right) \frac{\partial^2 f''(x)}{\partial x^2} \tag{A.5}$$

At $y=\pm b$, Eq. (A.5) has the constant value of $2g''(b)$. Similarly

$$\frac{\partial^2 \phi_{\circ}''}{\partial x^2} = \left(x^2 - a^2\right) \frac{\partial^2 g''(x)}{\partial x^2} + 2f''(x) \tag{A.6}$$

has the constant value $2f''(a)$ at $x=\pm a$. These constant boundary values are eliminated by adding $-x^2 g(b) - y^2 f(a)$ to the Eq. (A.4). $\phi_{\circ}''$ takes the following form:

$$\phi_{\circ}'' = \left(x^2 - a^2\right) g''(y) + \left(y^2 - b^2\right) f''(x) - x^2 g''\left(b\right) - y^2 f''\left(a\right) \tag{A.7}$$

Further, differentiating Eq. (A.7) with respect to x and y gives

$$-\frac{\partial^2 \phi_{\circ}''}{\partial x \partial y} = -2x\frac{\partial g''(y)}{\partial y} - 2y\frac{\partial f''(x)}{\partial x} \tag{A.8}$$

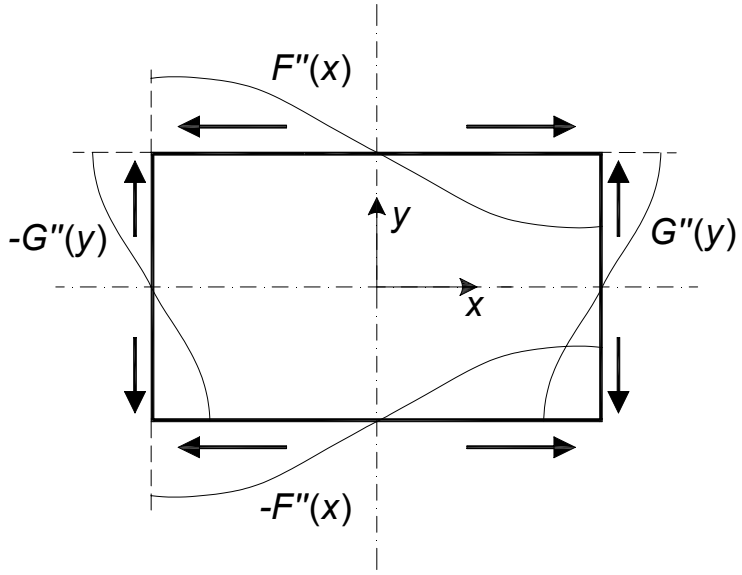

Figure A.2. Symmetrical shearing forces on rectangular plate.

According to Eq. (A.3), Eq. (A.8) is an odd function in both x and y, which means that this function is $\pm F(x)$ at $y=\pm b$ and $\pm G(y)$ at $x=\pm a$. It follows:

$$2b\frac{\partial f''(x)}{\partial x}\Big|_{x=a} = 2a\frac{\partial g''(y)}{\partial y}\Big|_{y=b} = -\frac{1}{2}F''(a) = -\frac{1}{2}G''(b) \tag{A.9}$$

Eqs. (A.8) and (A.9) result in

$$\begin{aligned} f''(x) &= \frac{1}{2b}\int\left(-F''(x) + \frac{x}{2a}F''(a)\right)dx \\ g''(y) &= \frac{1}{2a}\int\left(-G''(y) + \frac{y}{2b}G''(b)\right)dy \end{aligned} \tag{A.10}$$

Substituting Eq. (A.10) into Eq. (A.7), $\phi_{\circ}''$ is obtained by

$$\phi_{\circ}'' = \frac{(x^2 - a^2)}{2a} \int \left(-G''(y) + \frac{y}{2b} G''(b) \right) dy - x^2 g''(b) + \frac{(y^2 - b^2)}{2b} \int \left(-F''(x) + \frac{x}{2a} F''(a) \right) dx - y^2 f''(a) \tag{A.11}$$

which can be reformed by using Eq. (A.10) as follows:

$$\phi_{\circ}'' = \frac{(x^2 - a^2)}{2a} \int_b^y \left(-G''(y) + \frac{y}{2b} G''(b) \right) dy + \frac{(y^2 - b^2)}{2b} \int_a^x \left(-F''(x) + \frac{x}{2a} F''(a) \right) dx \tag{A.12}$$

Appendix B: Experimental report

B.1. Biaxial buckling of GFRP plates

B.1.1. $[0/90]_S$ specimens

B.1.1.1. 0-kN Tension

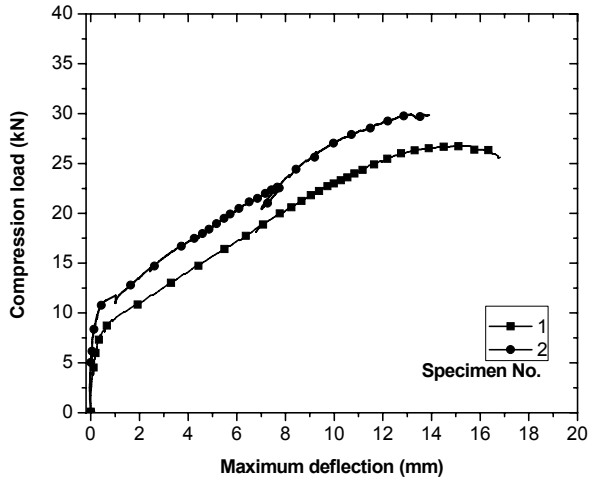

Figure B.1. Load vs. maximum out-of-plane displacement responses.

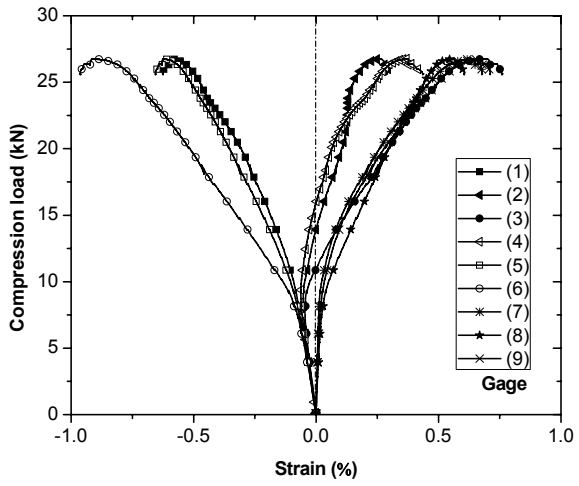

Figure B.2. Compression load vs. strain responses of specimen#1.

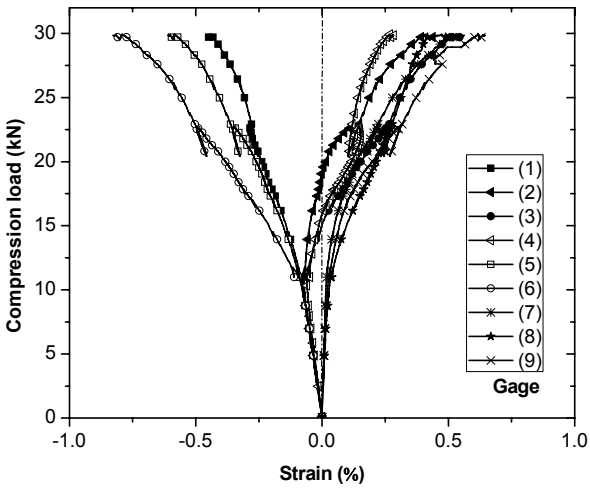

Figure B.3. Compression load vs. strain responses of specimen#2.

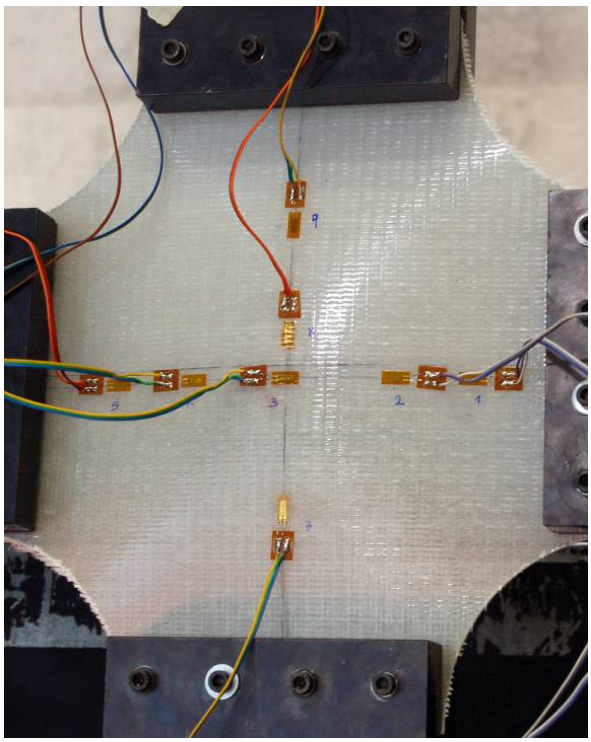

Figure B.4. Buckling mode shape of specimen#1.

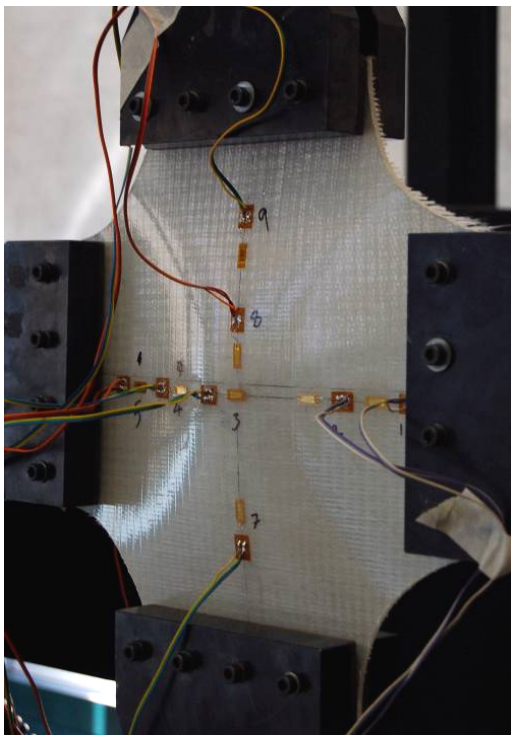

Figure B.5. Buckling mode shape of specimen#2.

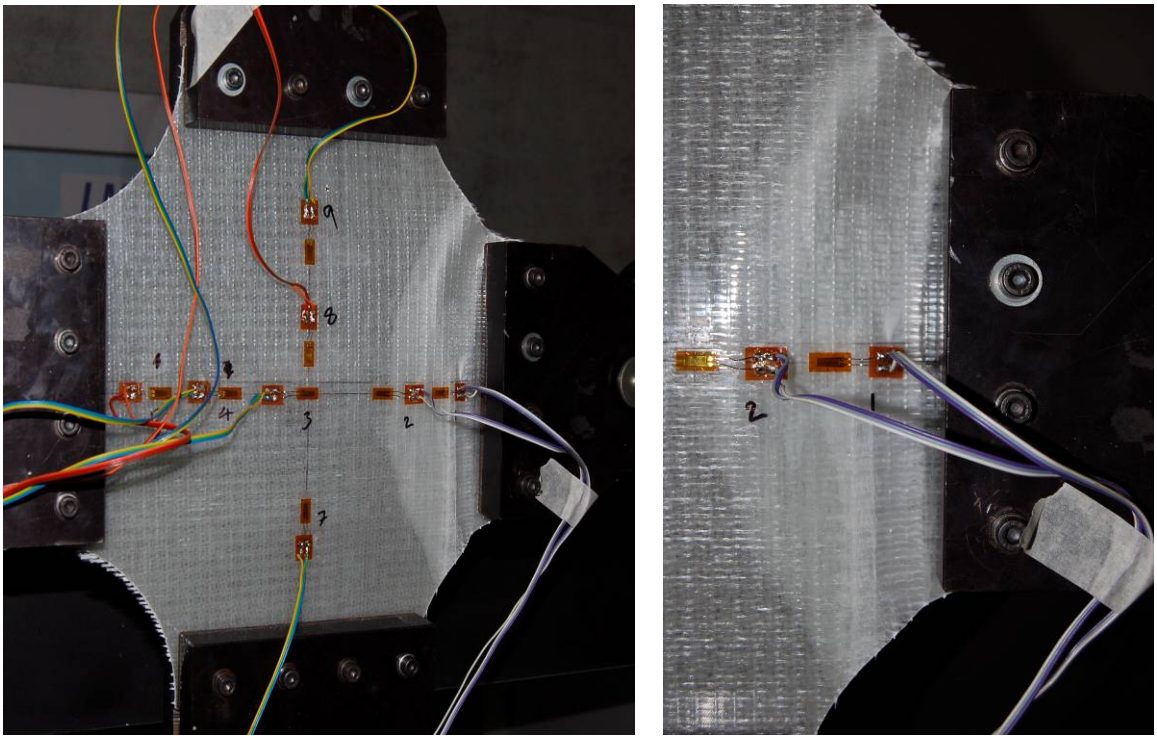

(a) (b)

Figure B.6. Failure mode of specimen#2.

B.1.1.2. 5-kN Tension

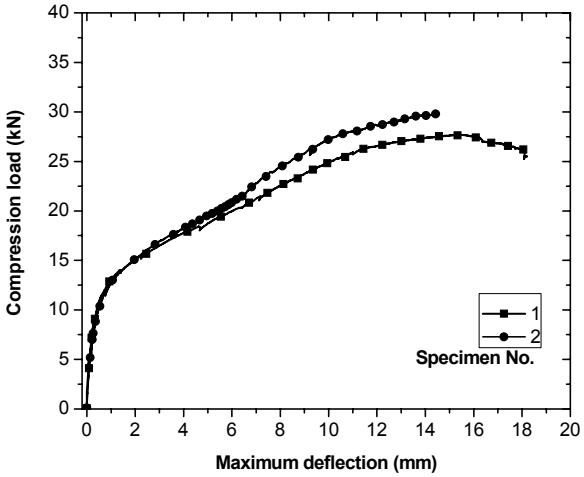

Figure B.8. Load vs. maximum out-of-plane displacement responses.

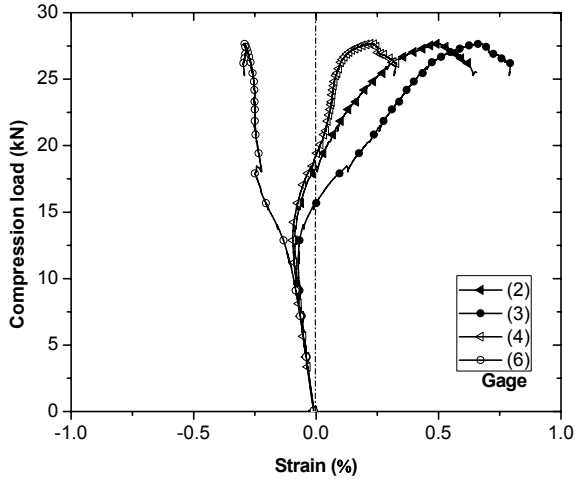

Figure B.9. Compression load vs. strain responses of specimen#1.

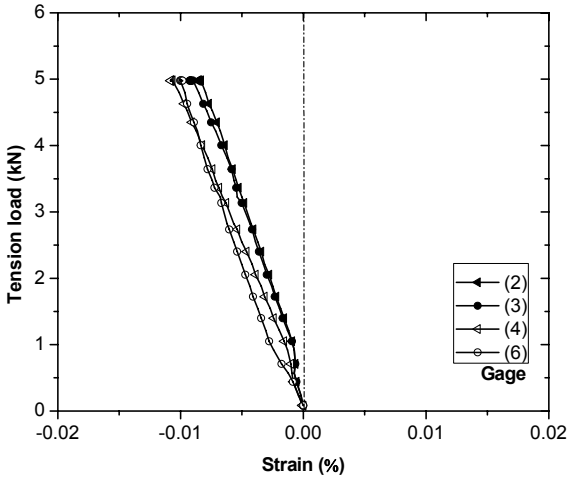

Figure B.10. Tension load vs. strain responses of specimen#1.

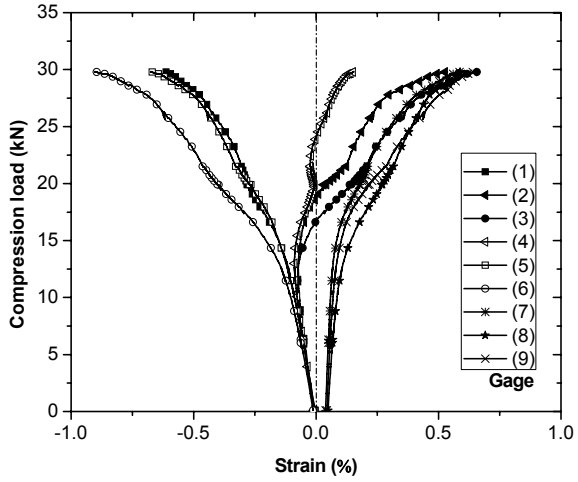

Figure B.11. Compression load vs. strain responses of specimen#2.

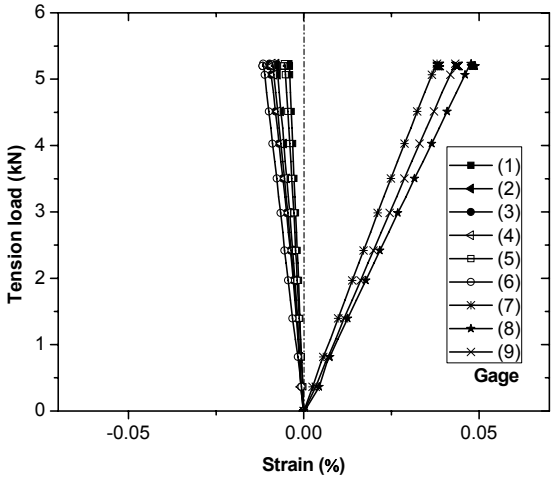

Figure B.11. Tension load vs. strain responses of specimen#2.

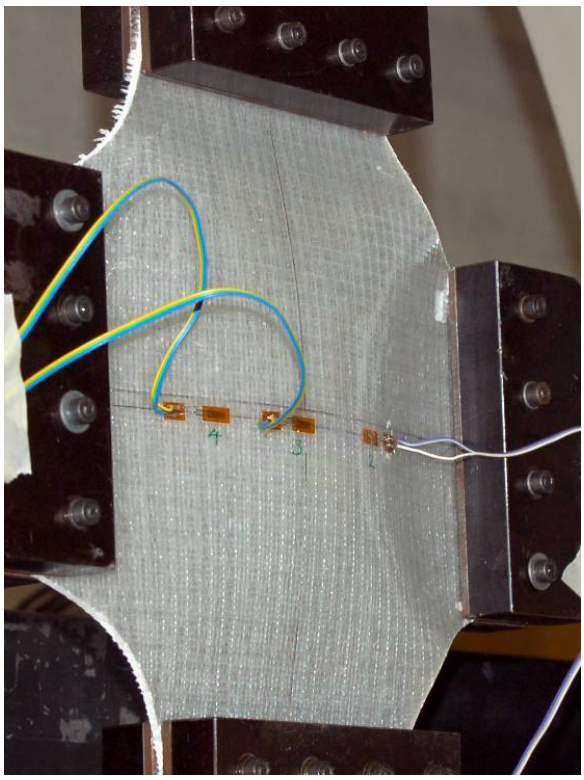

Figure B.12. Buckling mode shape of specimen#1.

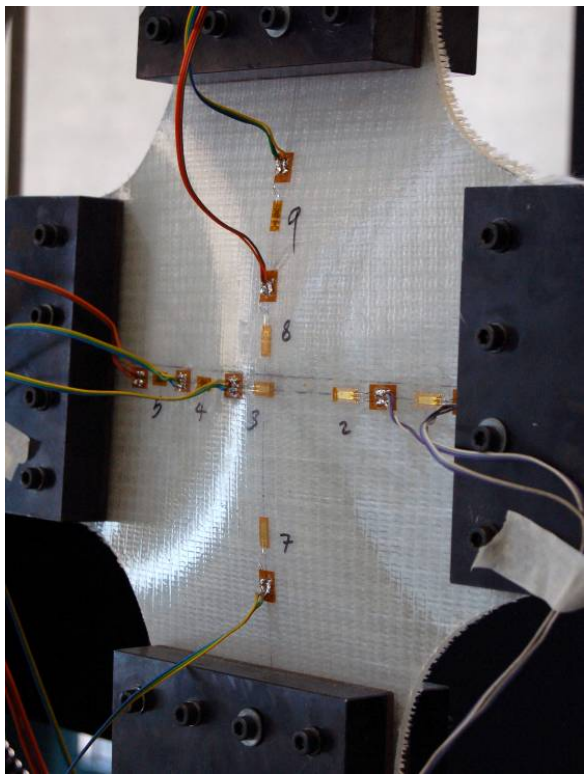

Figure B.13. Buckling mode shape of specimen#2.

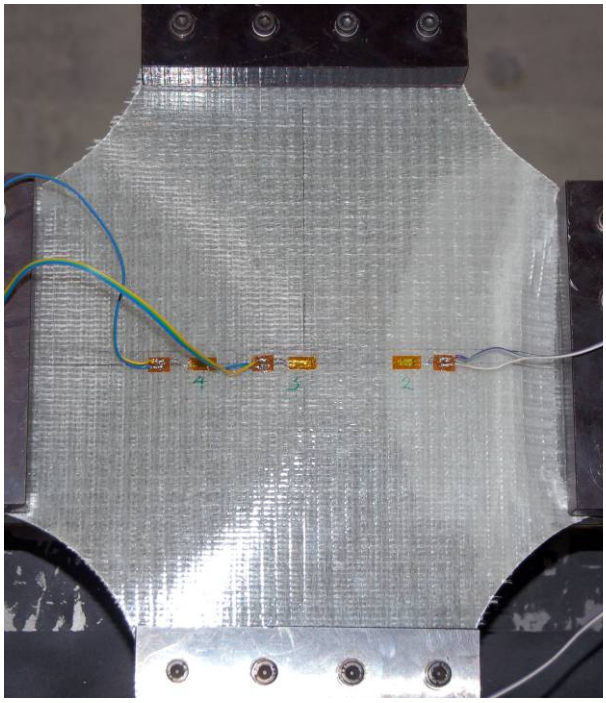

Figure B.14. Failure mode of specimen#1.

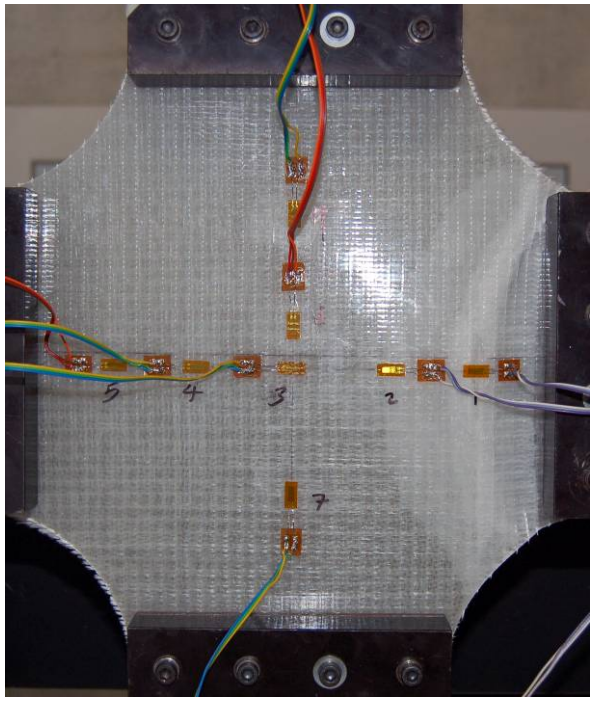

Figure B.15. Failure mode of specimen#2.

B.1.1.3. 10-kN Tension

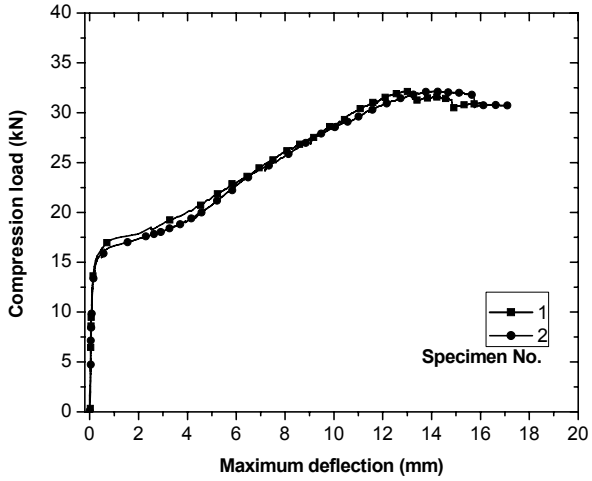

Figure B.16. Load vs. maximum out-of-plane displacement responses.

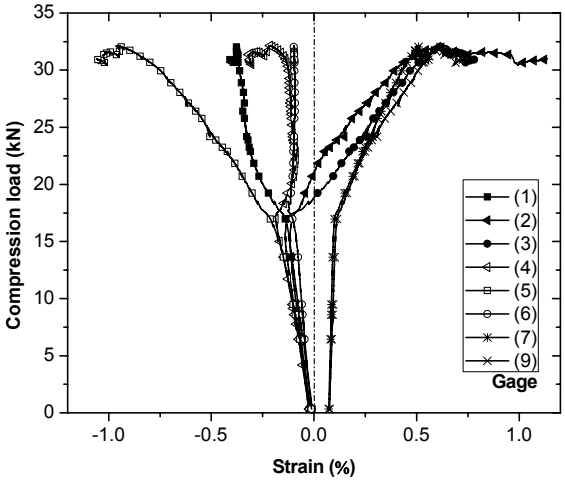

Figure B.17. Compression load vs. strain responses of specimen#1.

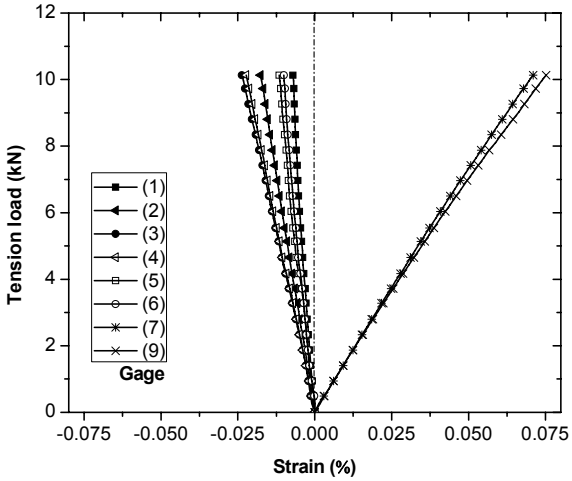

Figure B.18. Tension load vs. strain responses of specimen#1.

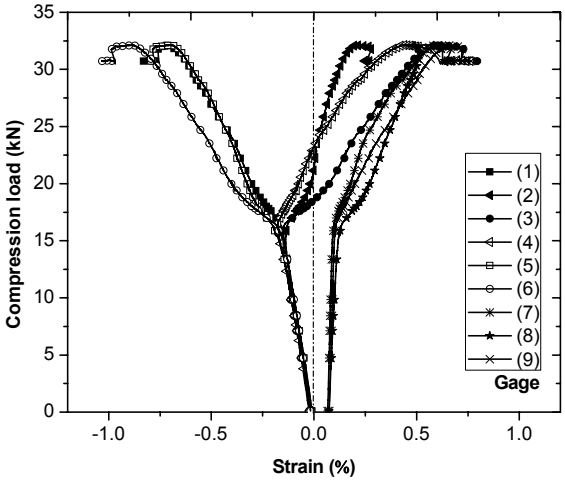

Figure B.19. Compression load vs. strain responses of specimen#2.

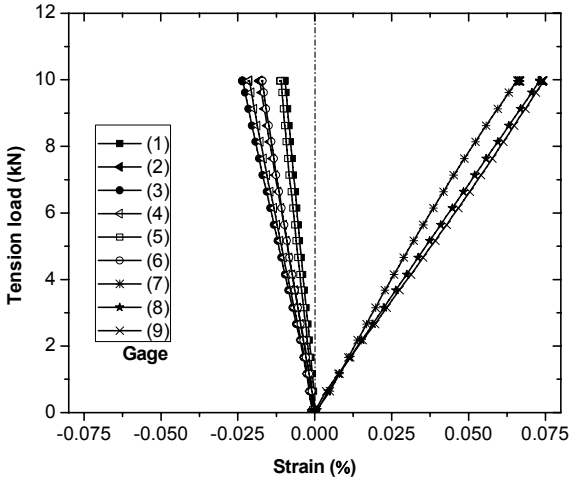

Figure B.20. Tension load vs. strain responses of specimen#2.

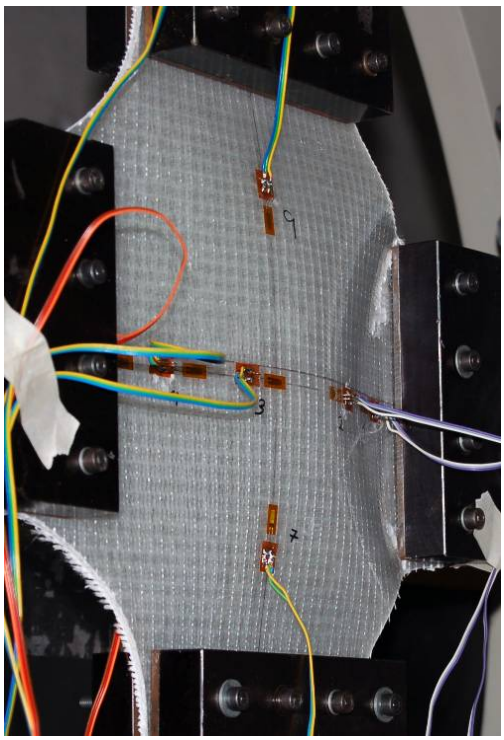

Figure B.21. Buckling mode shape of specimen#1.

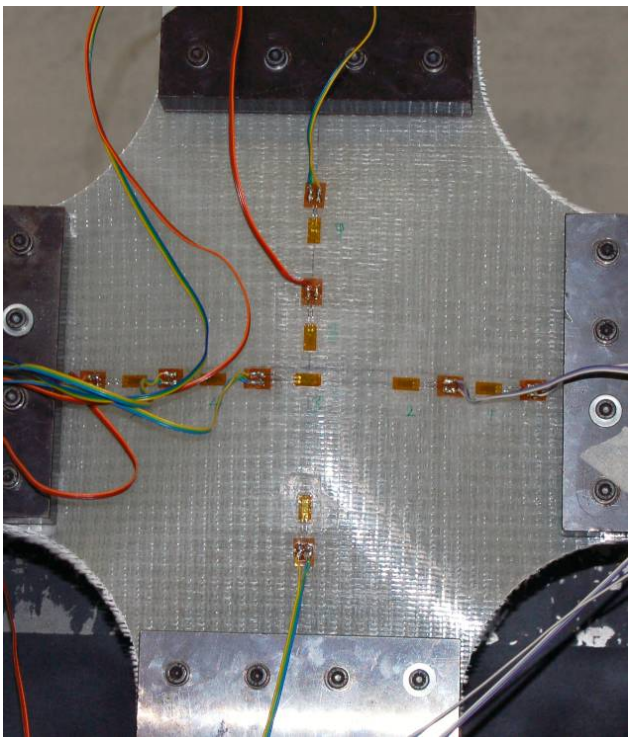

Figure B.22. Buckling mode shape of specimen#2.

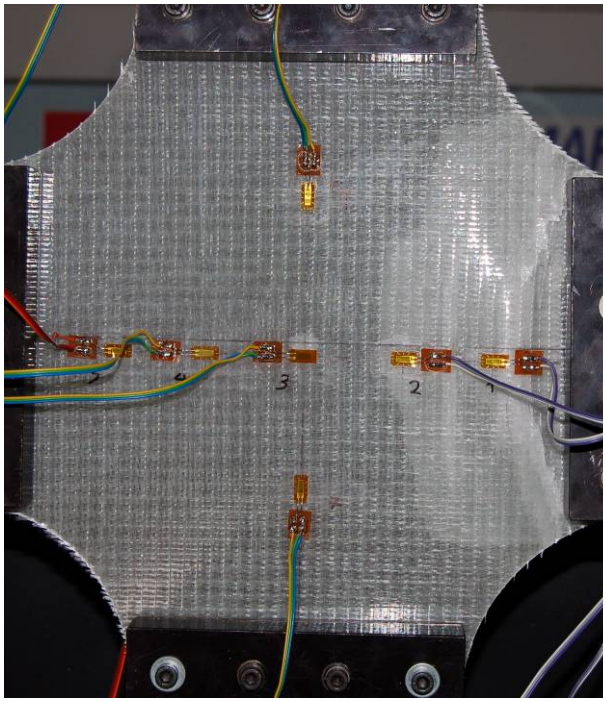

Figure B.23. Failure mode of specimen#1.

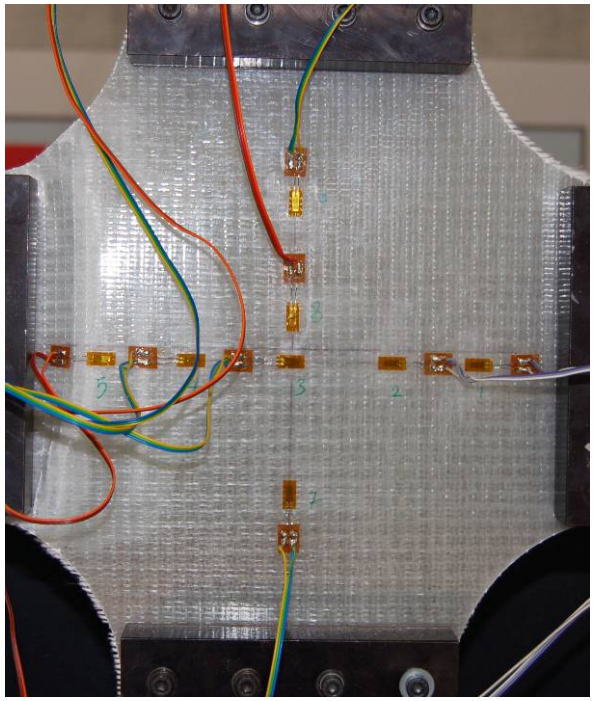

Figure B.24. Failure mode of specimen#2.

B.1.1.4. 15-kN Tension

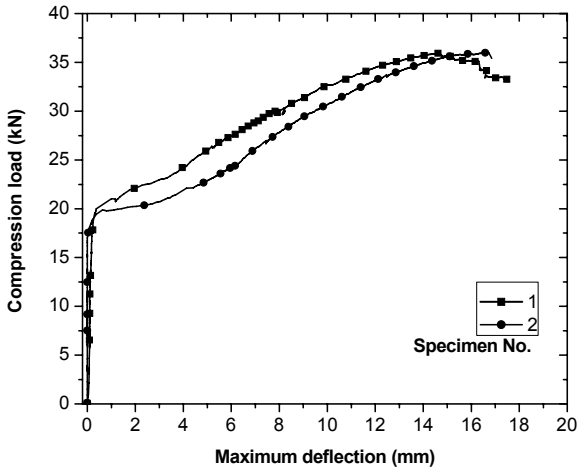

Figure B.25. Load vs. maximum out-of-plane displacement responses.

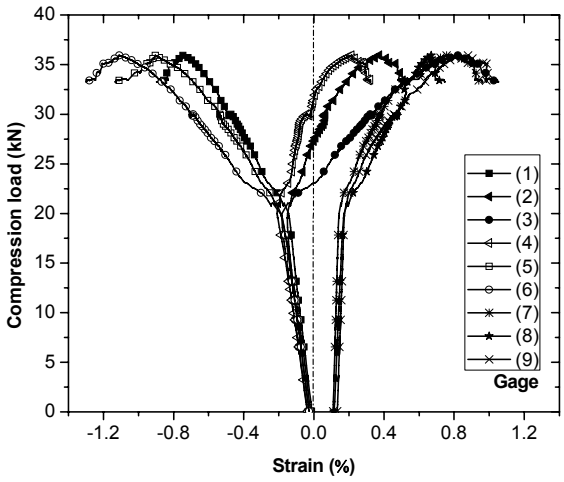

Figure B.26. Compression load vs. strain responses of specimen#1.

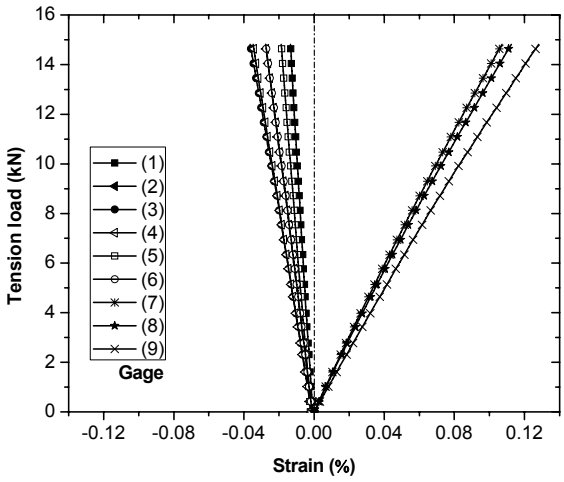

Figure B.27. Tension load vs. strain responses of specimen#1.

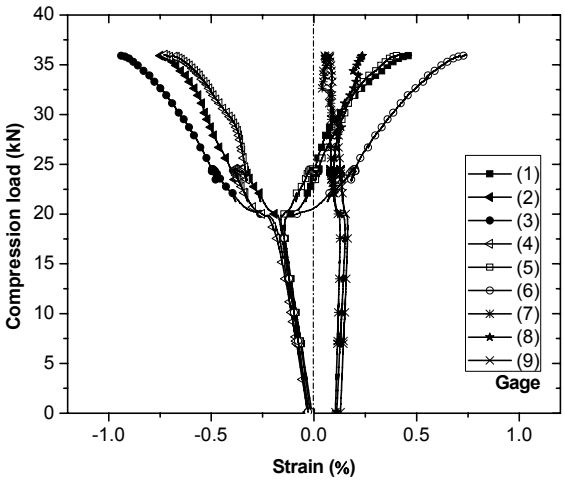

Figure B.28. Compression load vs. strain responses of specimen#2.

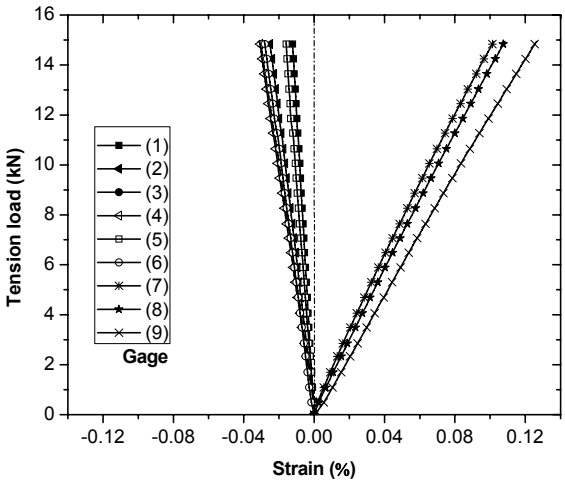

Figure B.29. Tension load vs. strain responses of specimen#2.

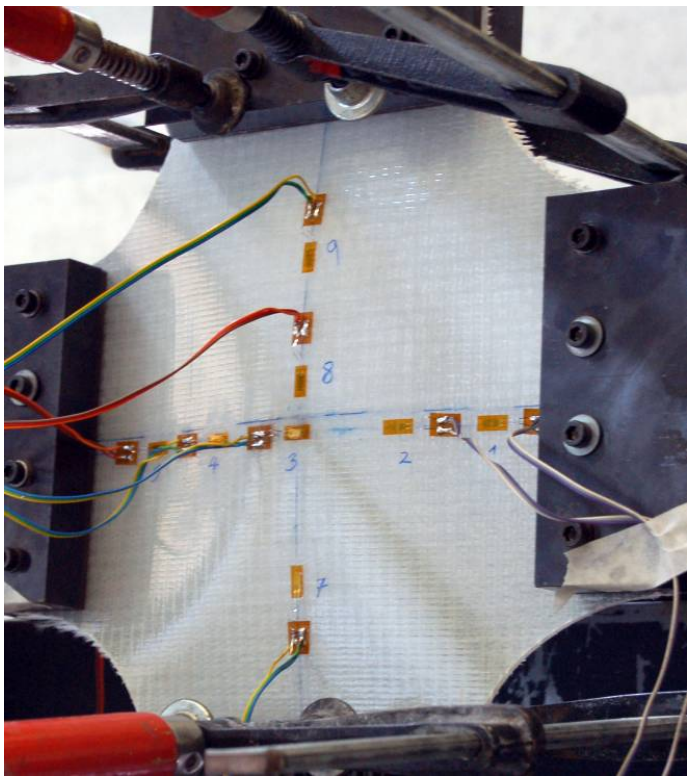

Figure B.30. Buckling mode shape of specimen#1.

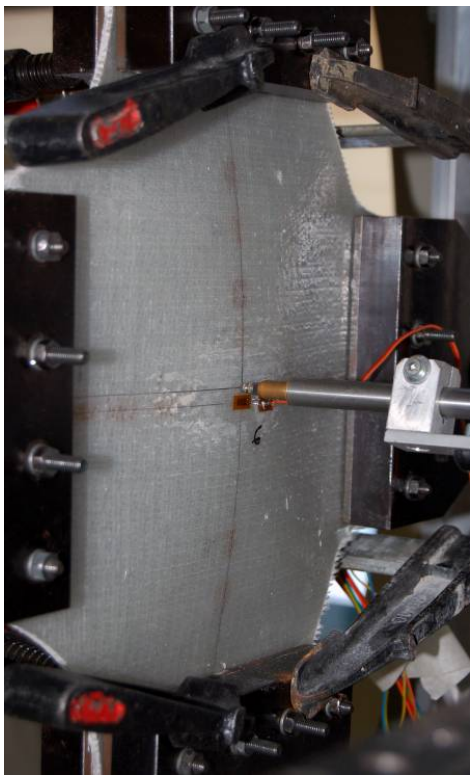

Figure B.31. Buckling mode shape of specimen#2.

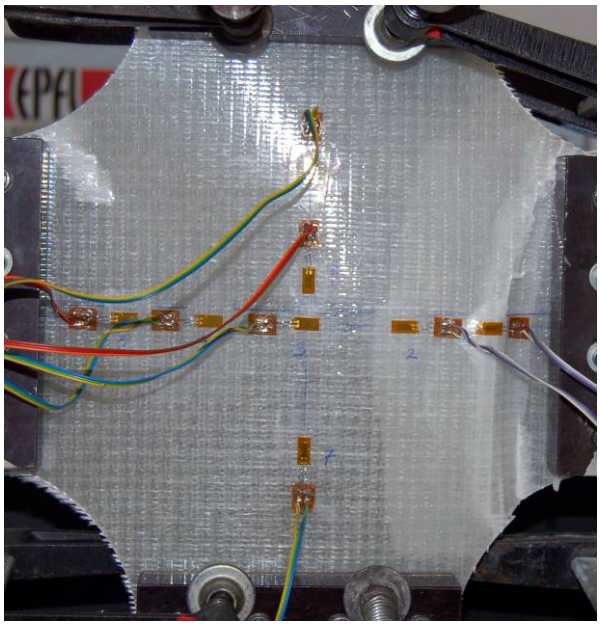

Figure B.32. Failure mode of specimen#1.

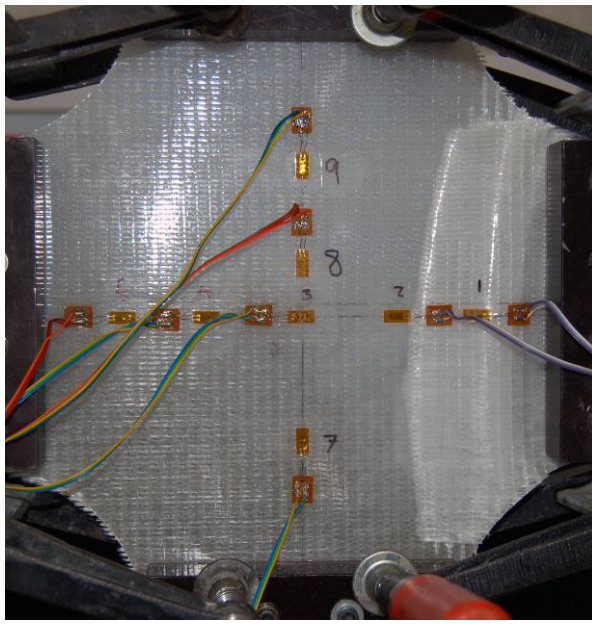

Figure B.33. Failure mode of specimen#2.

B.1.1.5. 20-kN Tension

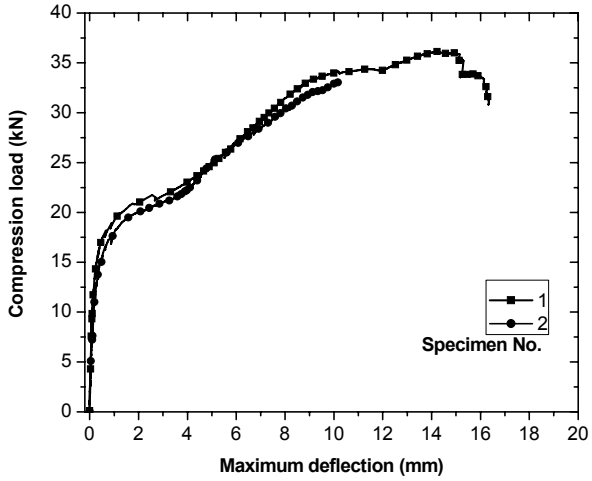

Figure B.34. Load vs. maximum out-of-plane displacement responses.

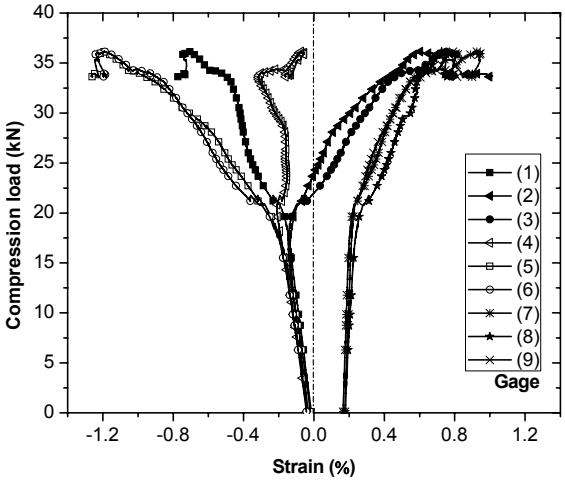

Figure B.35. Compression load vs. strain responses of specimen#1.

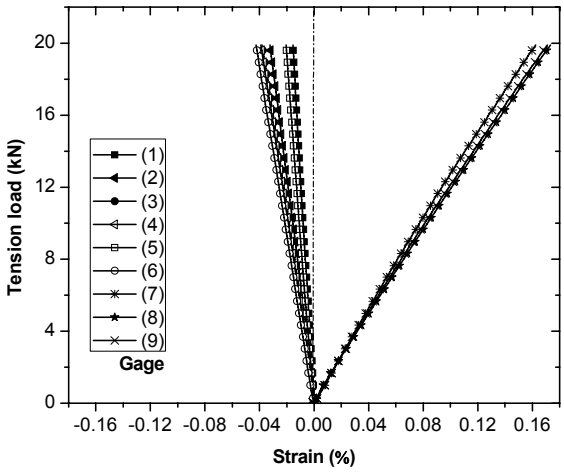

Figure B.36. Tension load vs. strain responses of specimen#1.

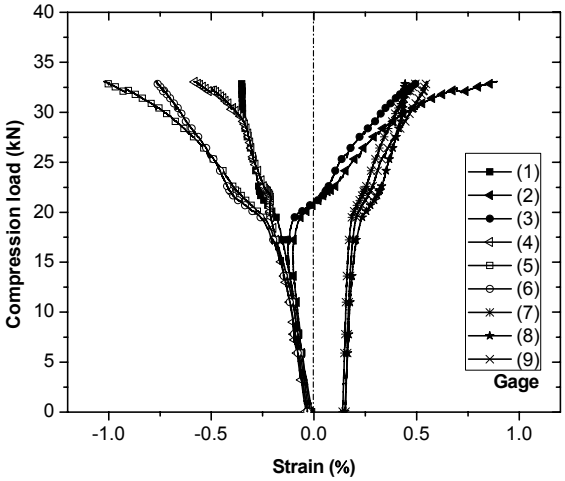

Figure B.37. Compression load vs. strain responses of specimen#2.

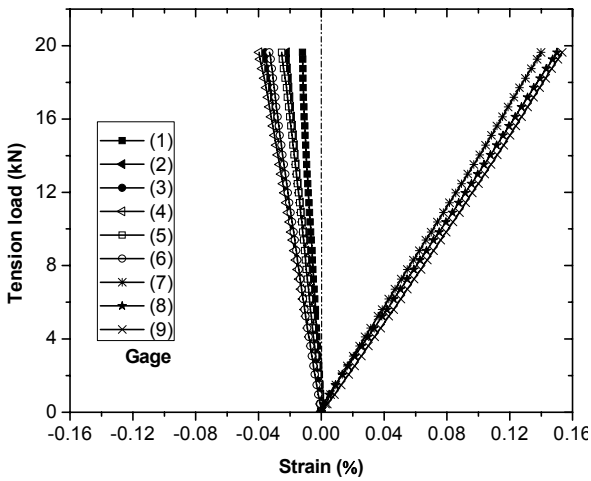

Figure B.38. Tension load vs. strain responses of specimen#2.

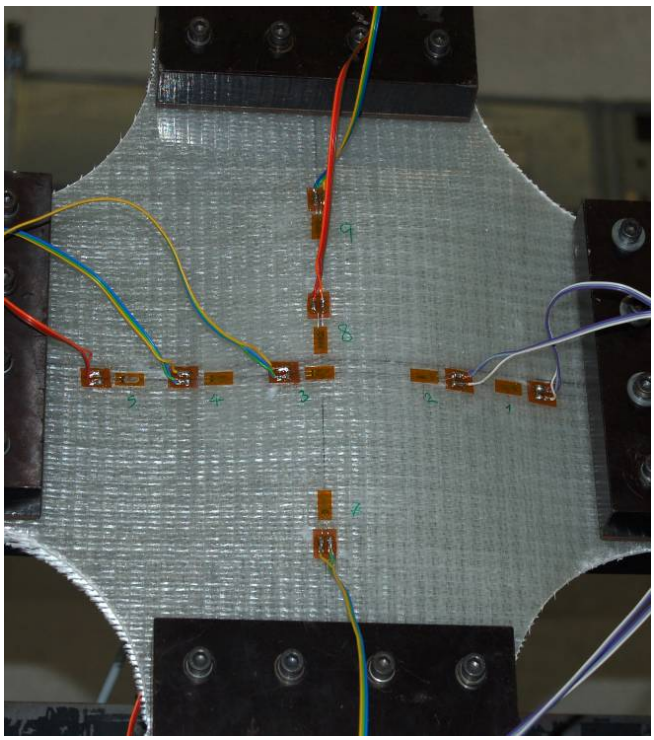

Figure B.39. Buckling mode shape of specimen#1.

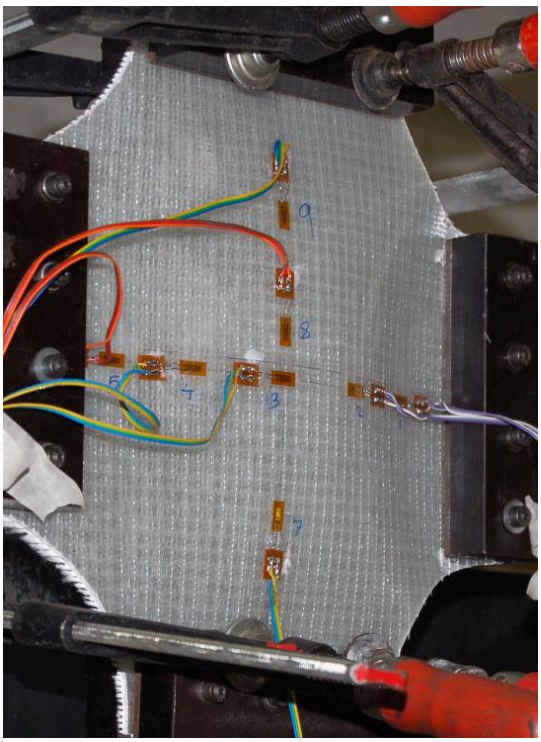

Figure B.40. Buckling mode shape of specimen#2.

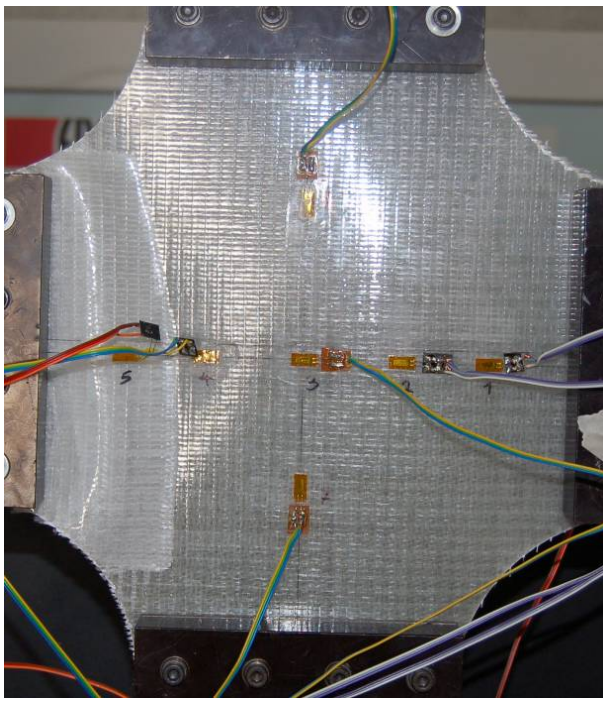

Figure B.41. Failure mode of specimen#1.

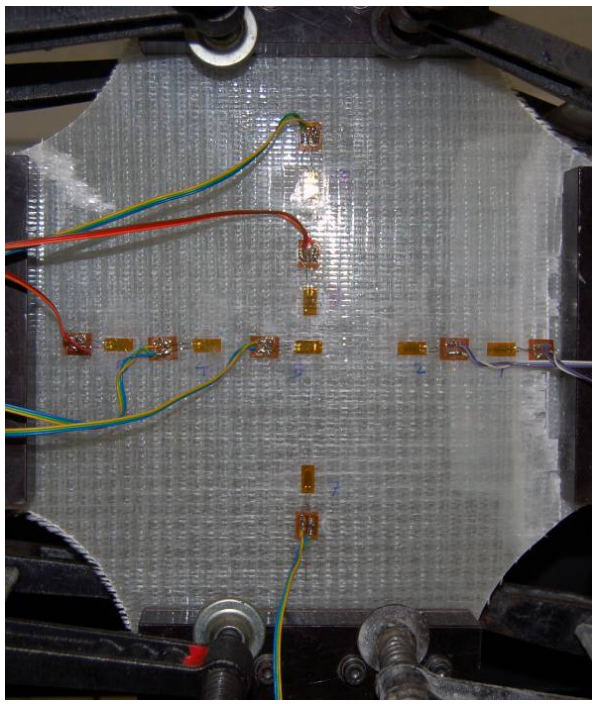

Figure B.42. Failure mode of specimen#2.

B.1.1.6. 25-kN Tension

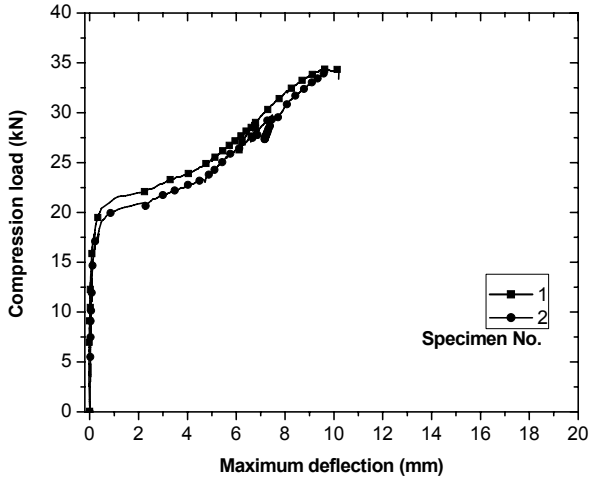

Figure B.43. Load vs. maximum out-of-plane displacement responses.

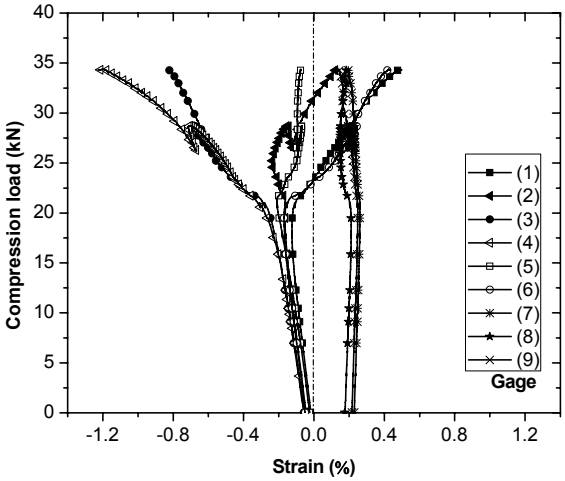

Figure B.44. Compression load vs. strain responses of specimen#1.

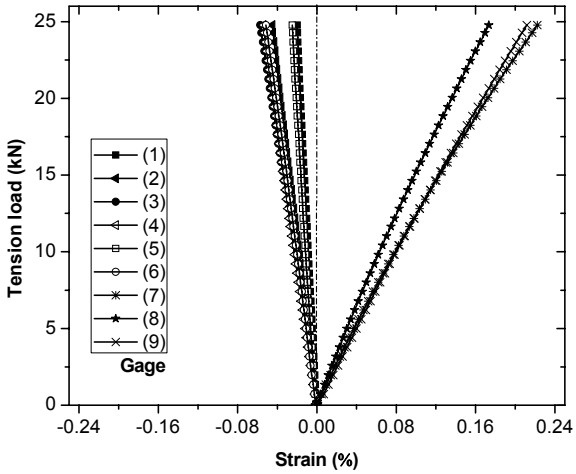

Figure B.45. Tension load vs. strain responses of specimen#1.

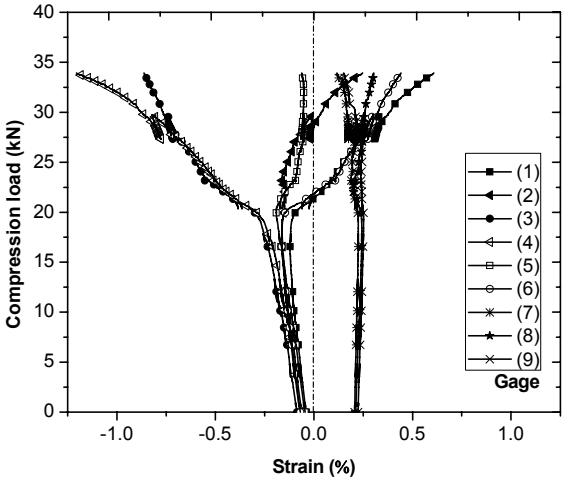

Figure B.46. Compression load vs. strain responses of specimen#2.

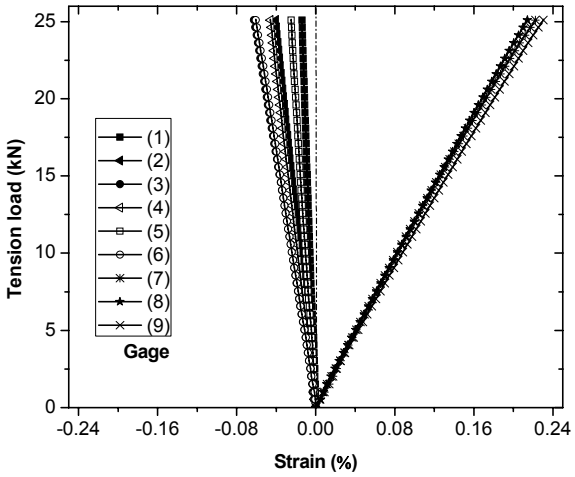

Figure B.47. Tension load vs. strain responses of specimen#2.

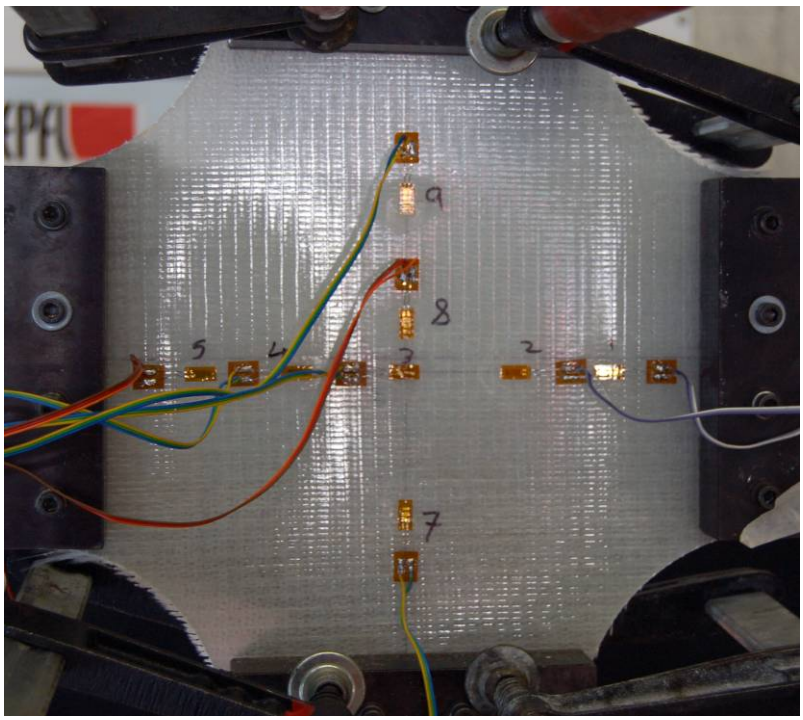

Figure B.48. Buckling mode shape of specimen#1.

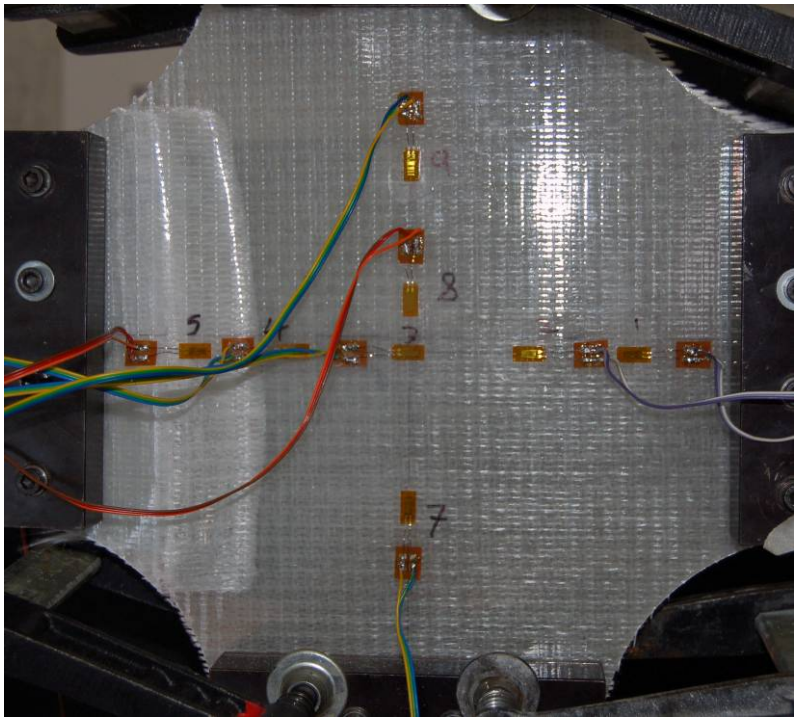

Figure B.49. Failure mode of specimen#1.

B.1.1.7. 30-kN Tension

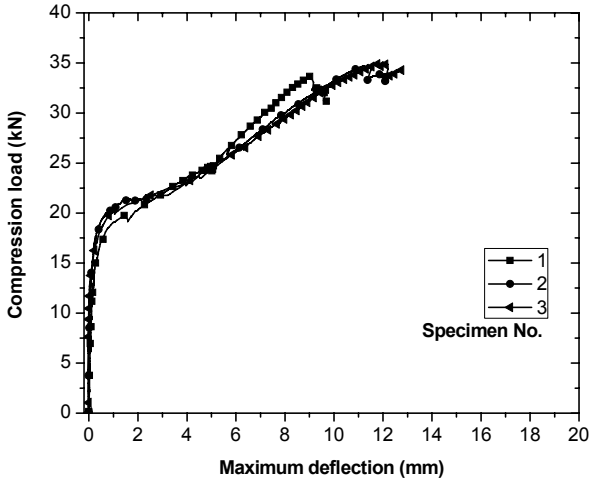

Figure B.50. Load vs. maximum out-of-plane displacement responses.

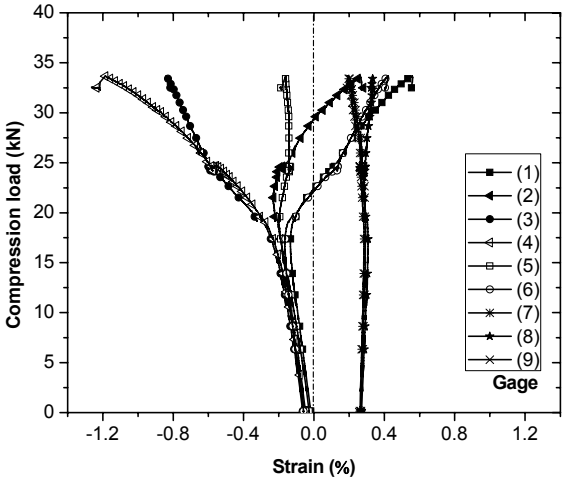

Figure B.51. Compression load vs. strain responses of specimen#1.

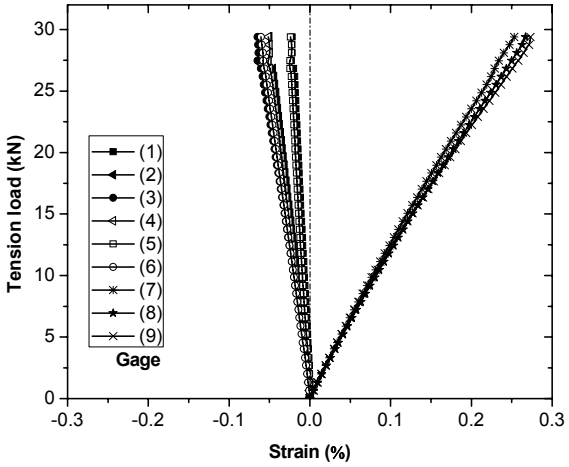

Figure B.52. Tension load vs. strain responses of specimen#1.

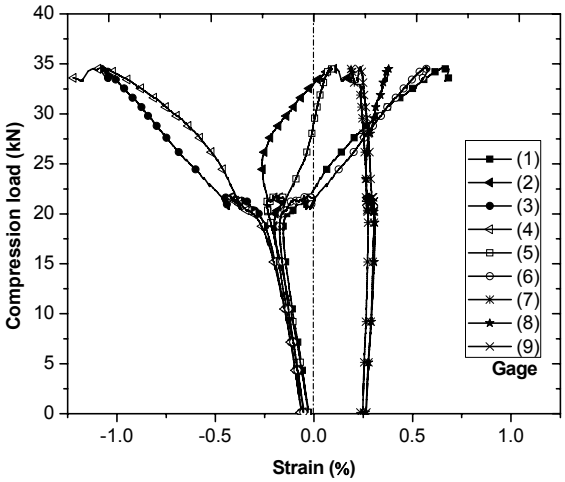

Figure B.53. Compression load vs. strain responses of specimen#2.

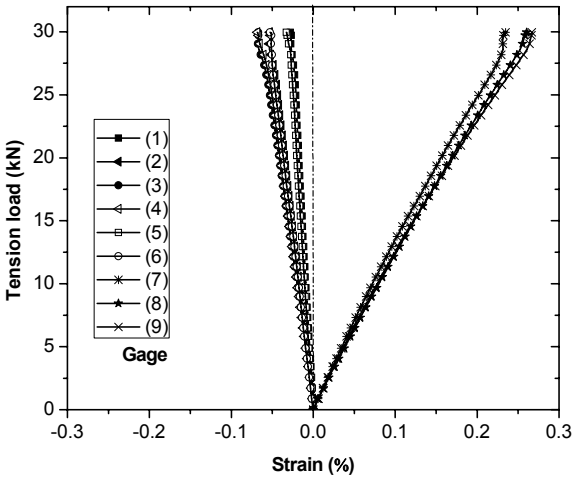

Figure B.54. Tension load vs. strain responses of specimen#2.

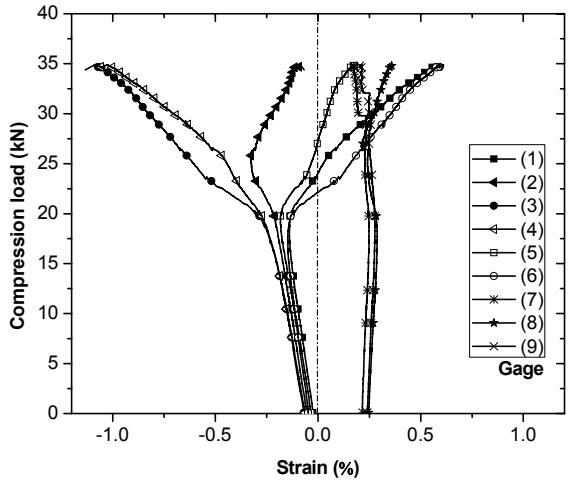

Figure B.55. Compression load vs. strain responses of specimen#3.

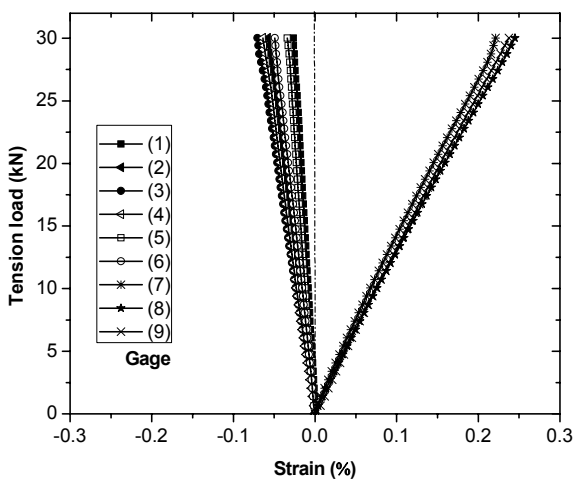

Figure B.56. Tension load vs. strain responses of specimen#3.

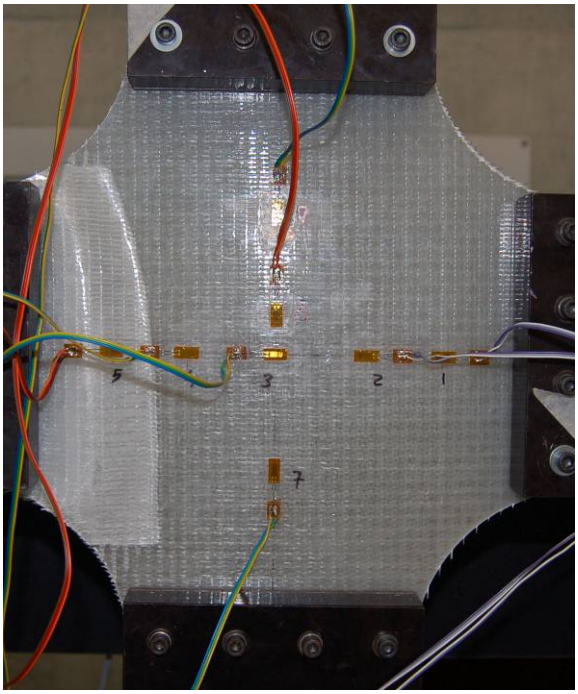

Figure B.57. Failure mode of specimen#1.

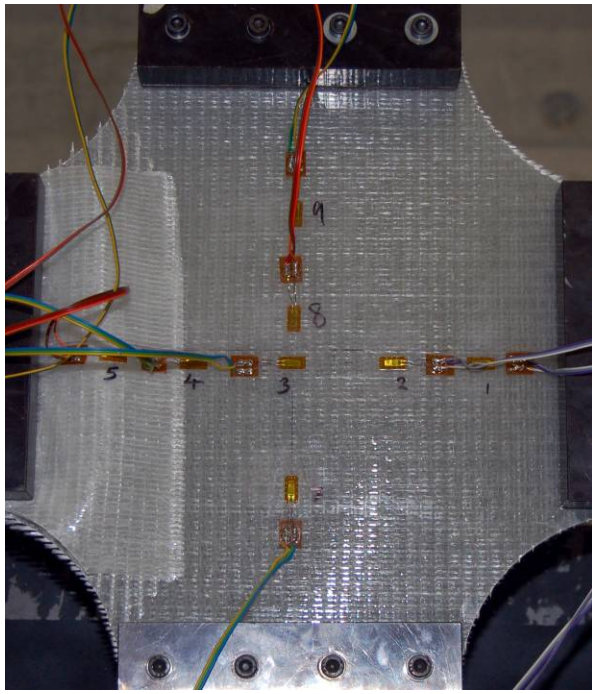

Figure B.58. Failure mode of specimen#2.

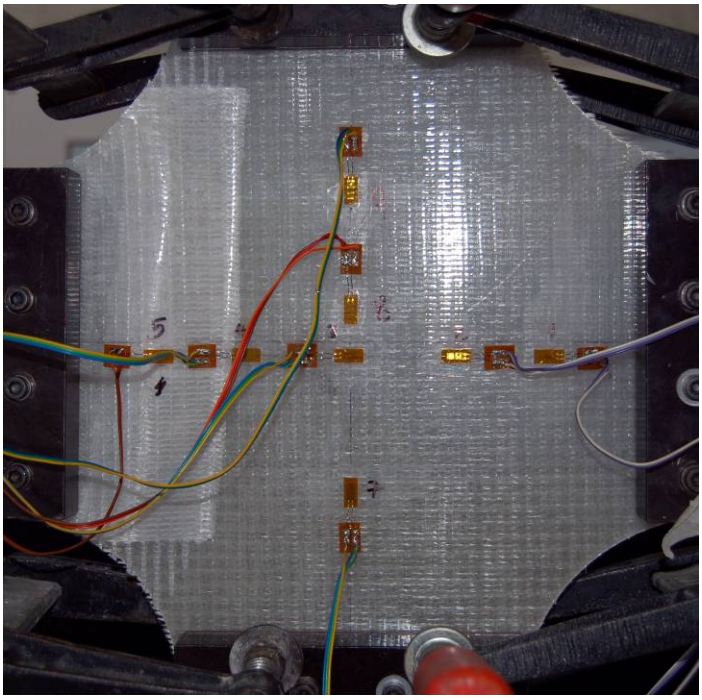

Figure B.59. Failure mode of specimen#3.

B.1.1.8. SCT

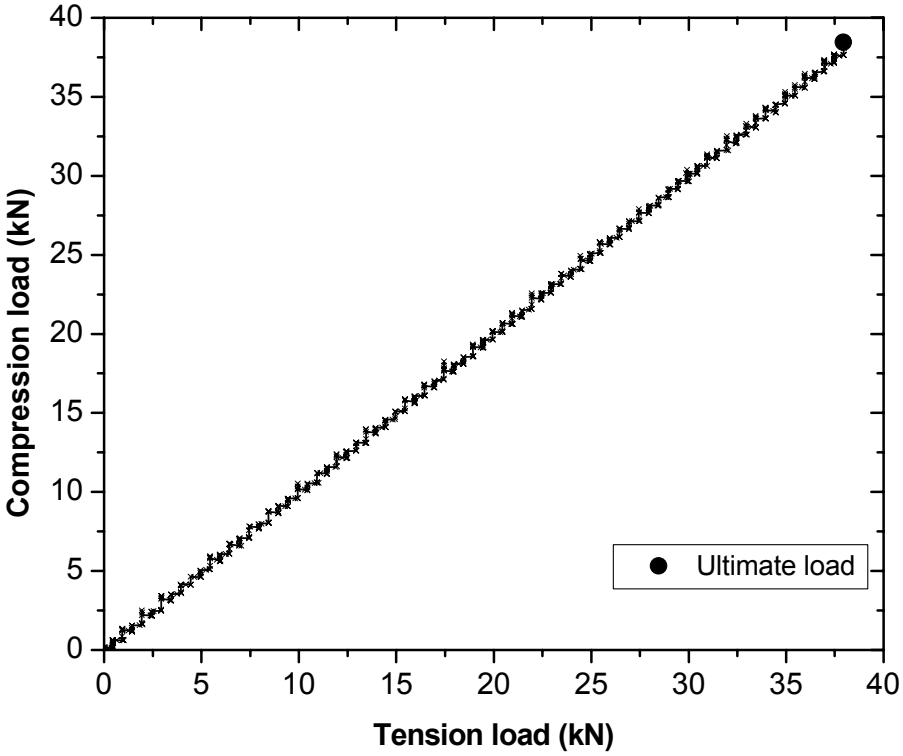

Figure B.60. Compression load vs. tension load.

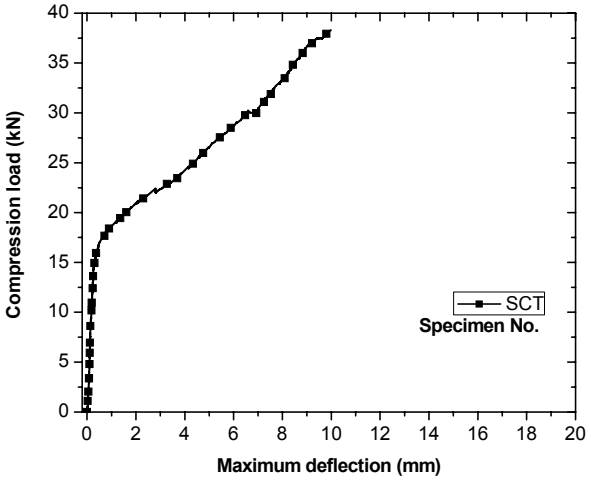

Figure B.61. Load vs. maximum out-of-plane displacement responses.

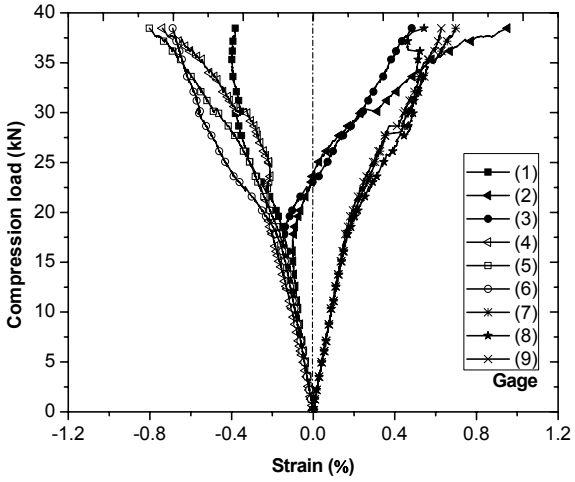

Figure B.62. Compression load vs. strain responses.

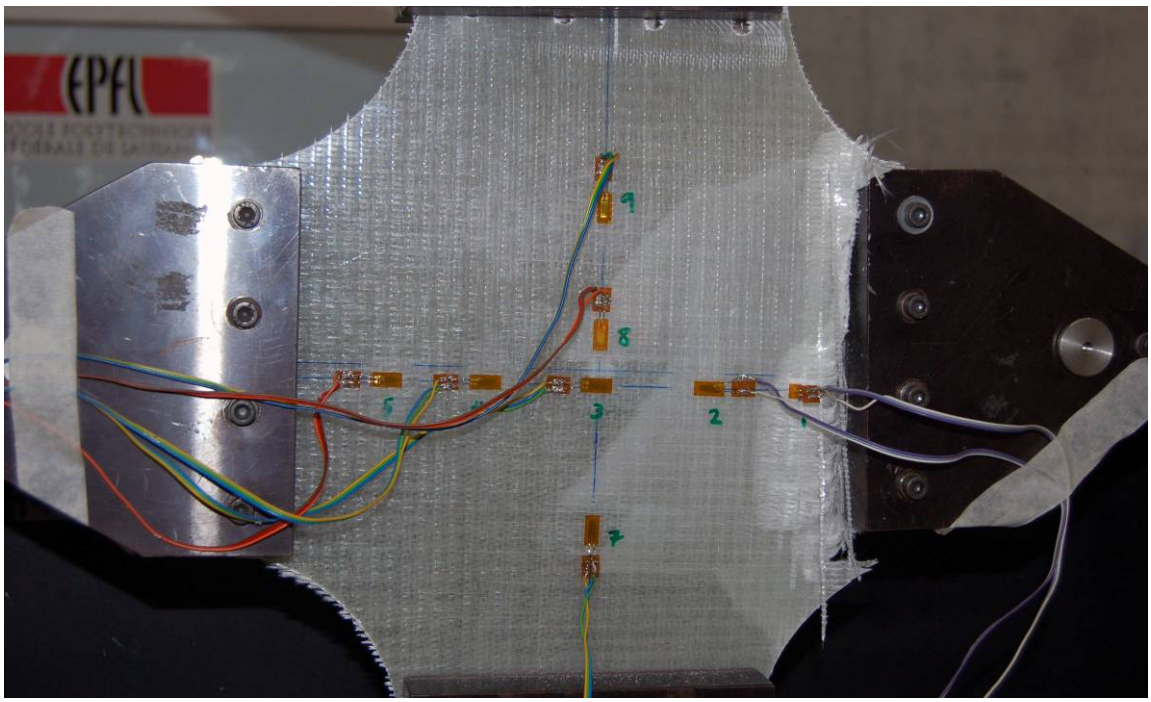

Figure B.63. Failure mode of specimen.

B.1.2. $[90/0]_S$ specimens

B.1.2.1. 0-kN Tension

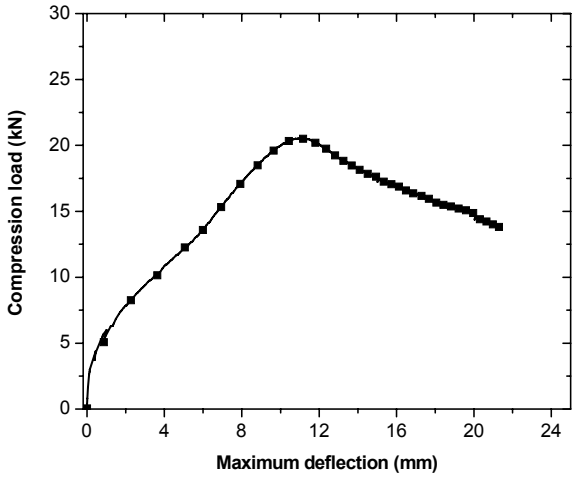

Figure B.64. Load vs. maximum out-of-plane displacement responses.

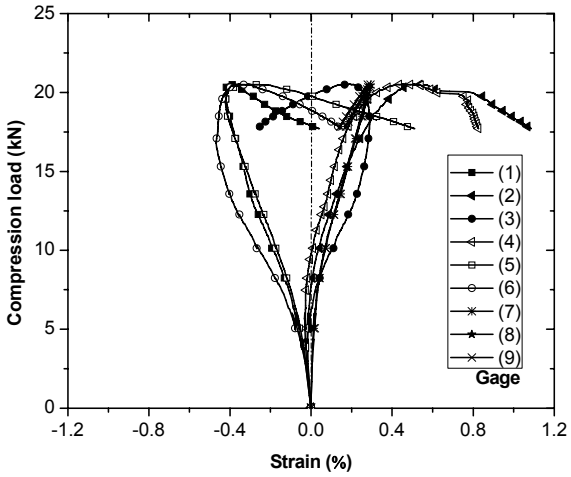

Figure B.65. Compression load vs. strain responses.

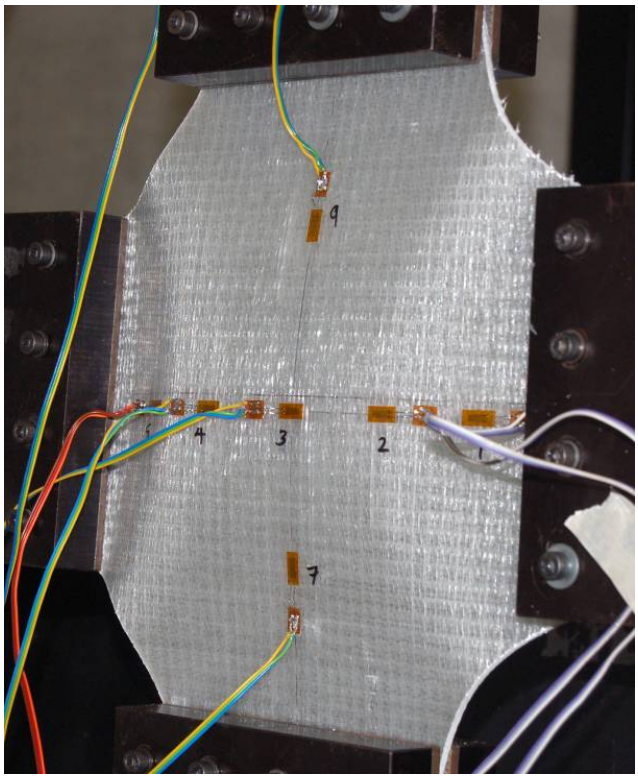

Figure B.66. Buckling mode shape.

B.1.2.2. 5-kN Tension

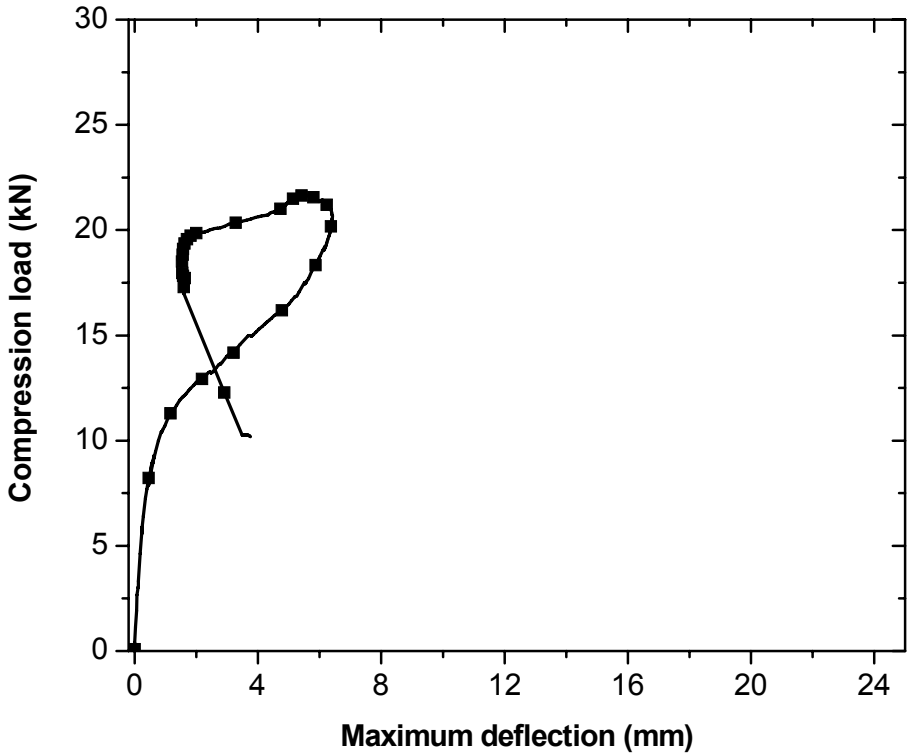

Figure B.67. Load vs. maximum out-of-plane displacement responses.

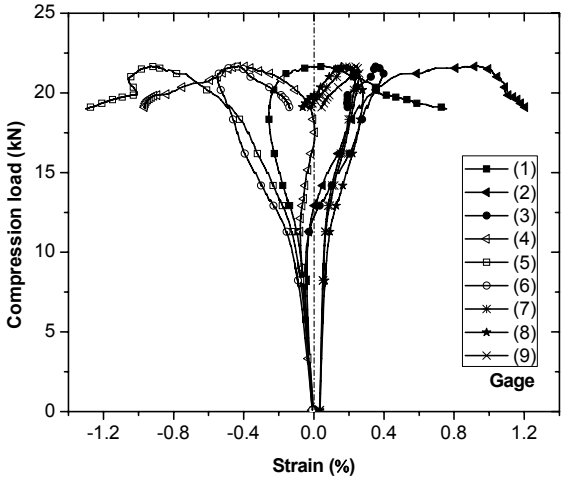

Figure B.68. Compression load vs. strain responses.

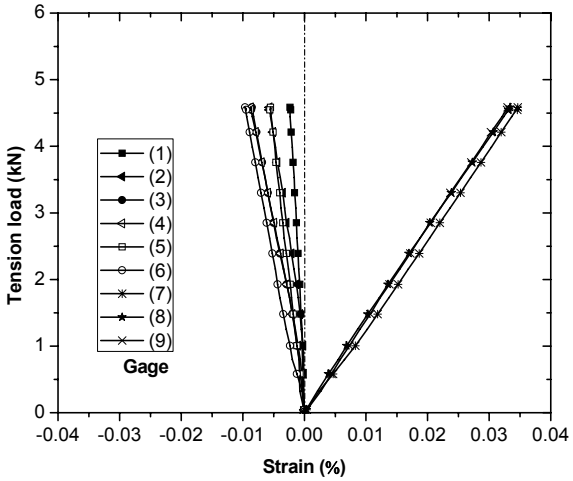

Figure B.69. Tension load vs. strain responses.

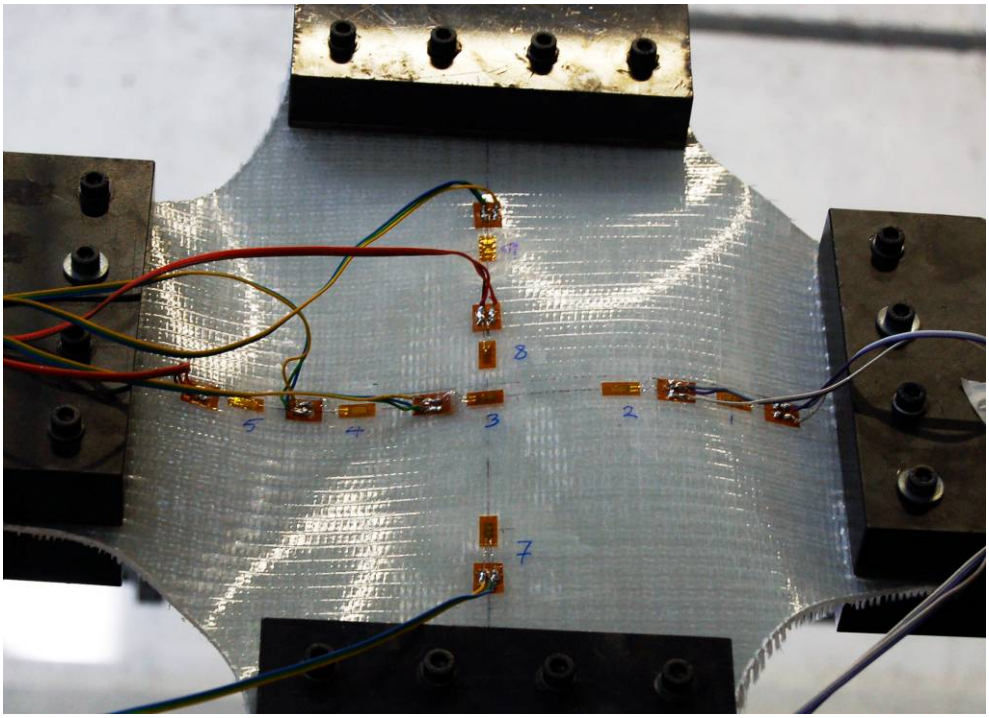

Figure B.70. Buckling mode shape.

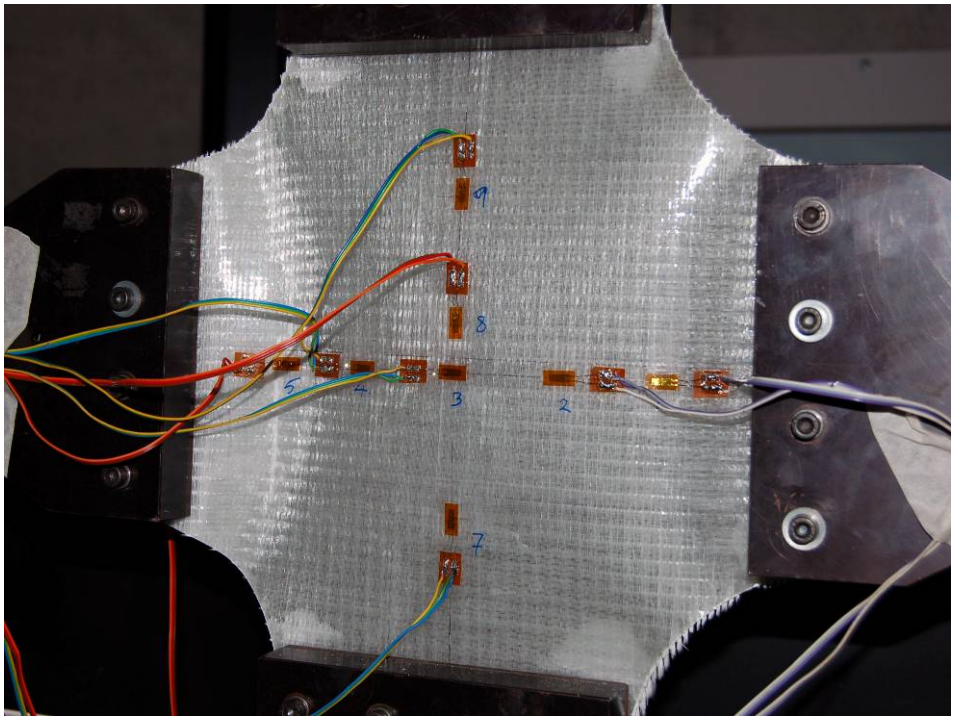

Figure B.71. Failure mode of specimen.

B.1.2.3. 10-kN Tension

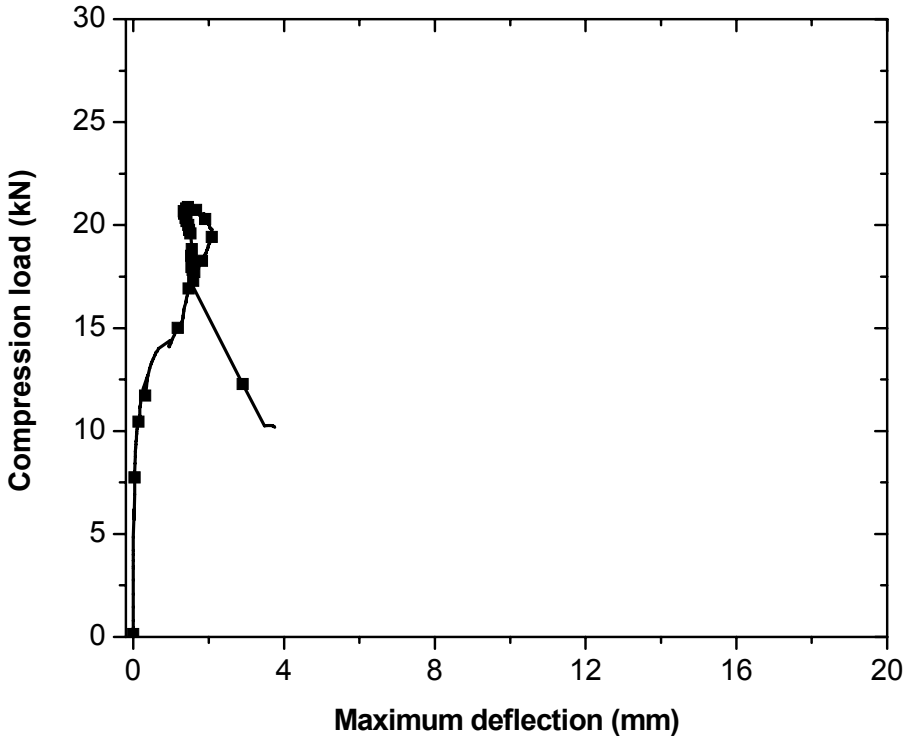

Figure B.72. Load vs. maximum out-of-plane displacement responses.

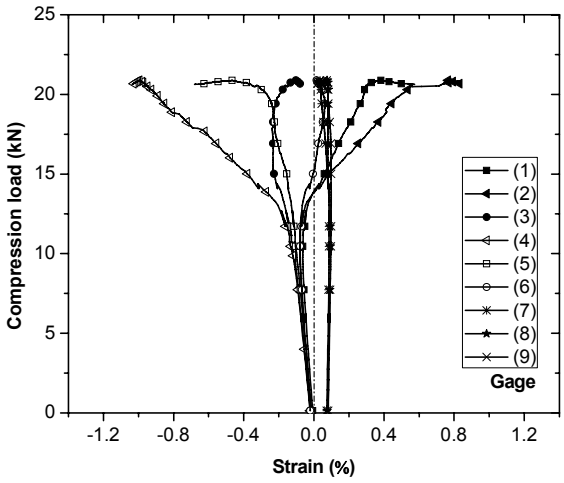

Figure B.73. Compression load vs. strain responses.

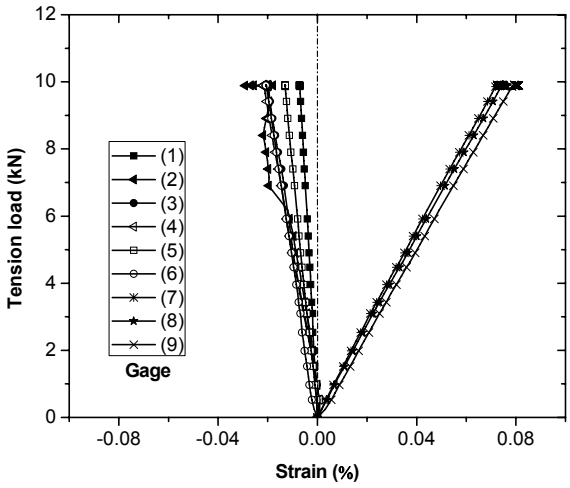

Figure B.74. Tension load vs. strain responses.

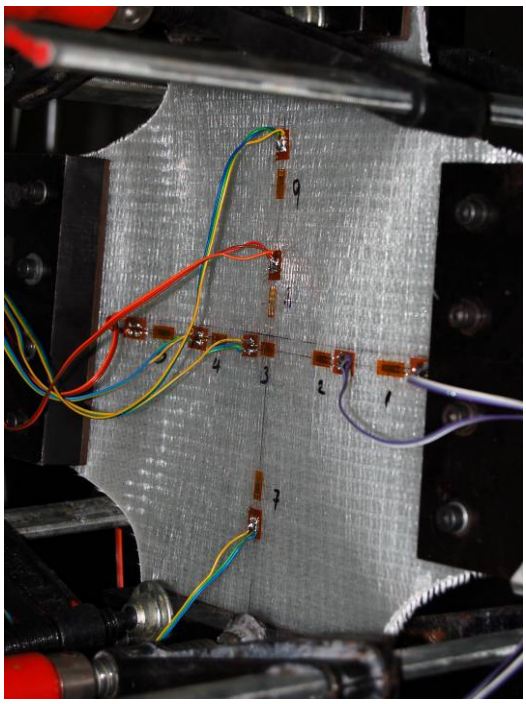

Figure B.75. Buckling mode shape.

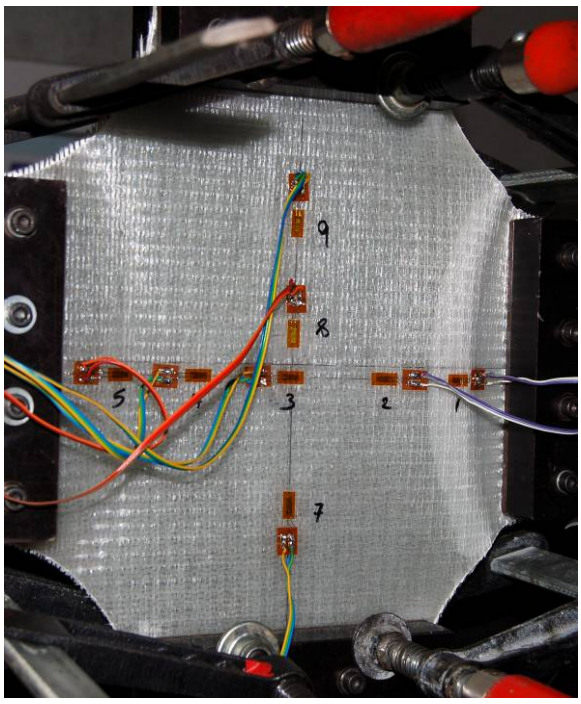

Figure B.76. Failure mode of specimen.

B.1.2.4. 15-kN Tension

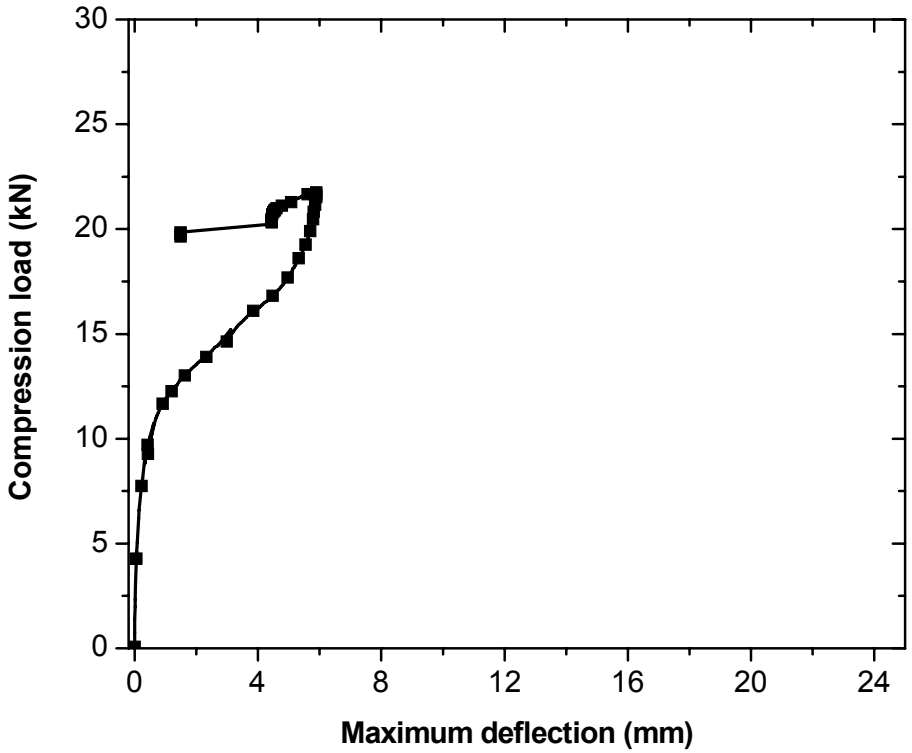

Figure B.77. Load vs. maximum out-of-plane displacement responses.

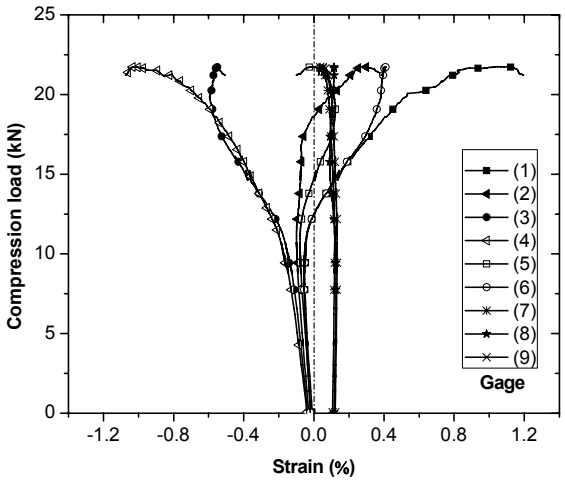

Figure B.78. Compression load vs. strain responses.

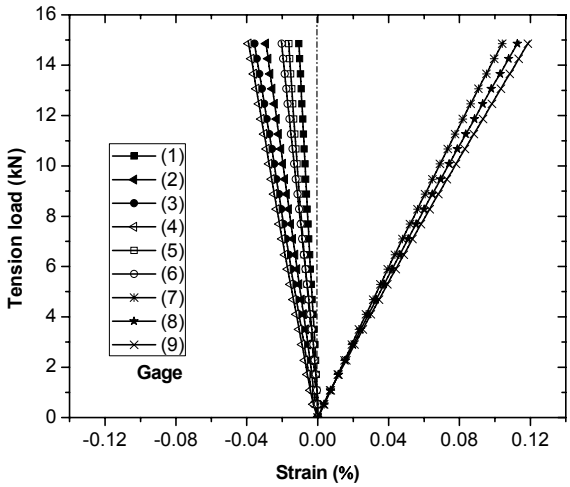

Figure B.79. Tension load vs. strain responses.

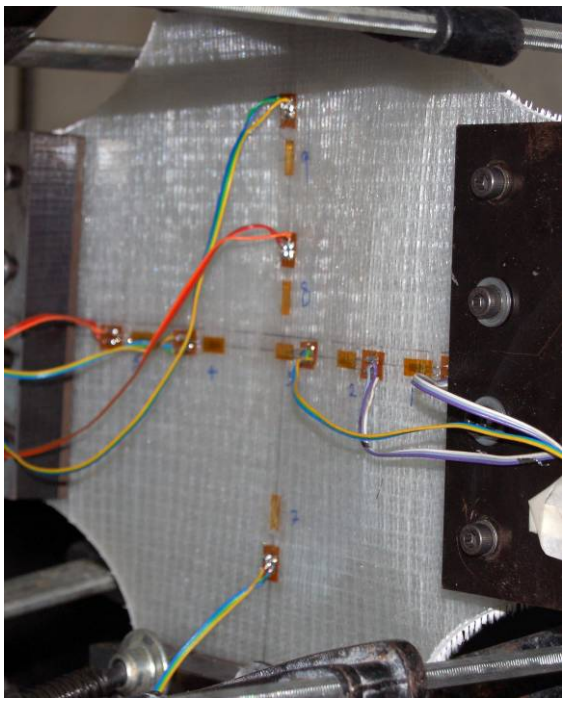

Figure B.80. Buckling mode shape.

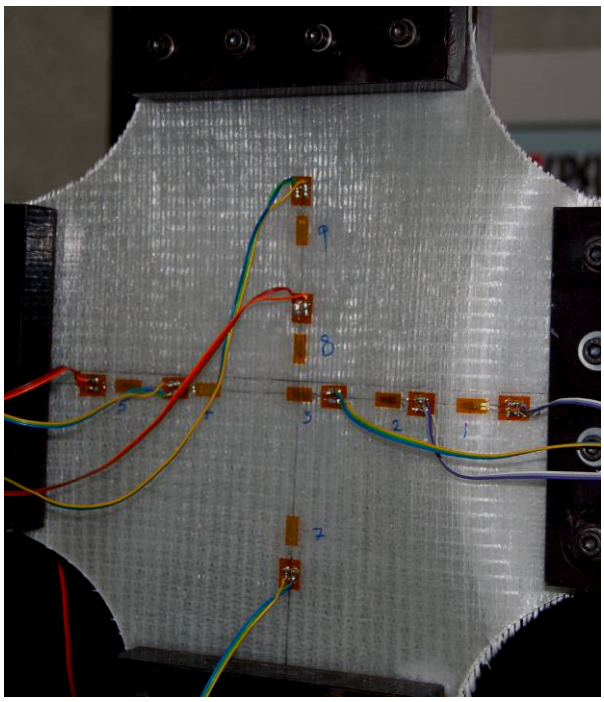

Figure B.81. Failure mode of specimen.

B.1.2.5. 20-kN Tension

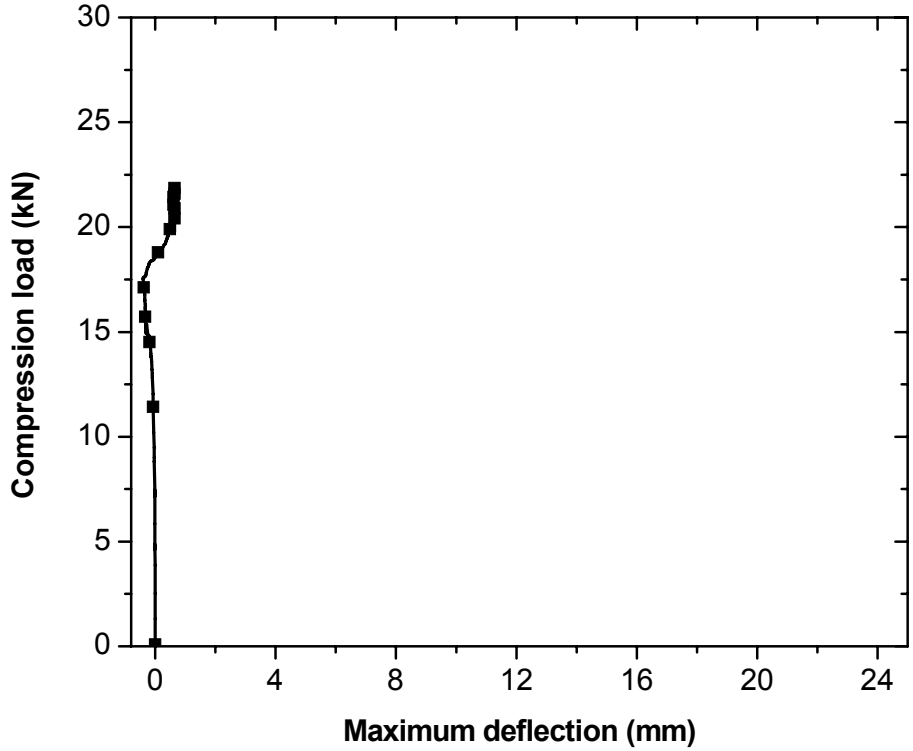

Figure B.82. Load vs. maximum out-of-plane displacement responses.

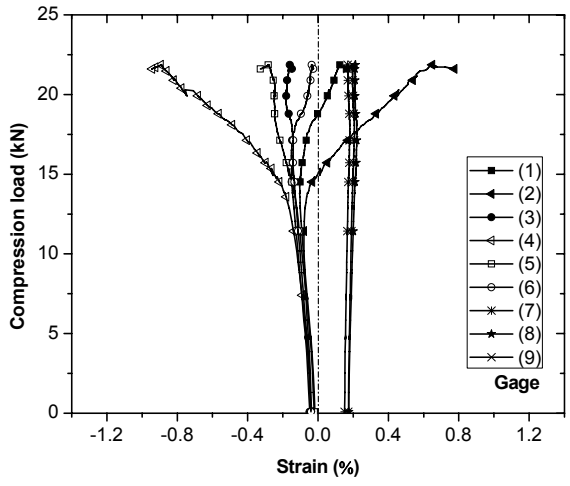

Figure B.83. Compression load vs. strain responses.

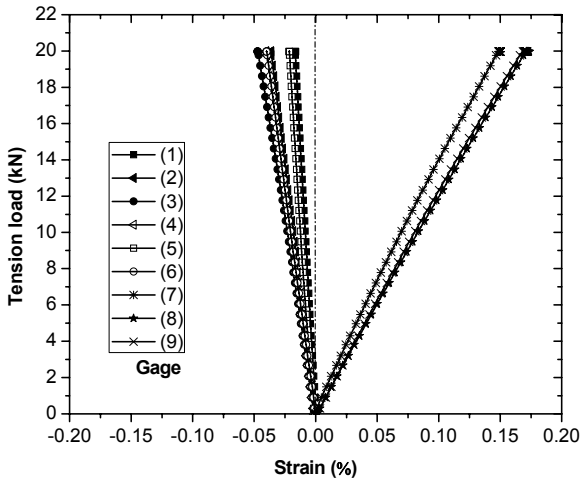

Figure B.84. Tension load vs. strain responses.

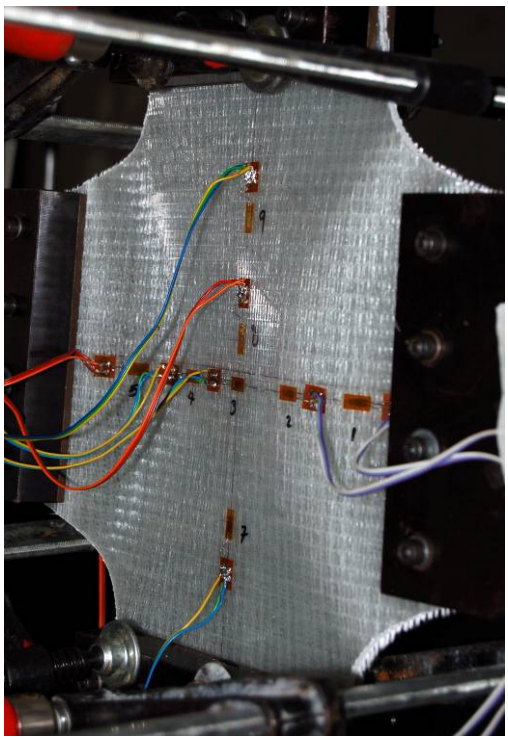

Figure B.85. Buckling mode shape.

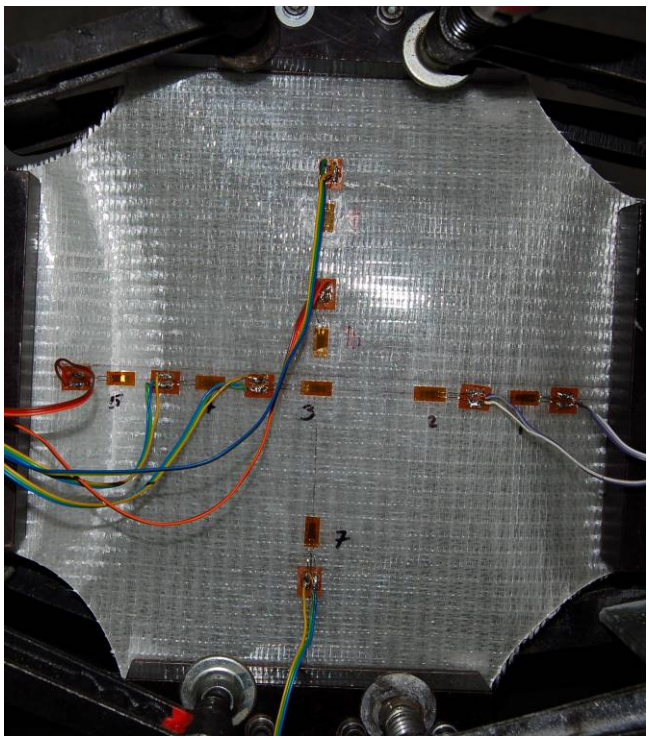

Figure B.86. Failure mode of specimen.

B.1.2.6. 25-kN Tension

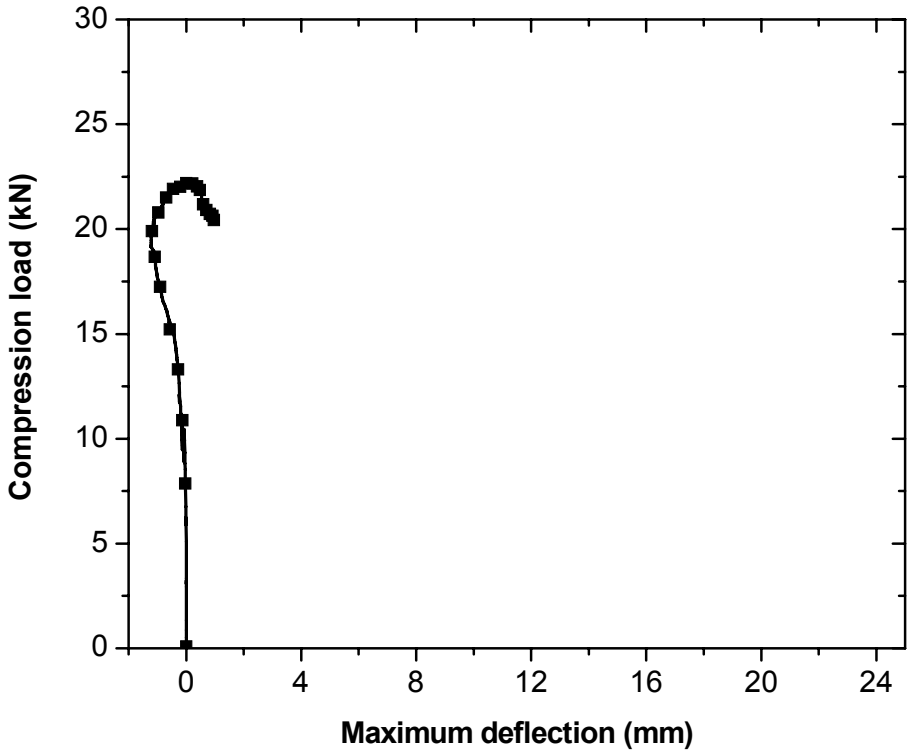

Figure B.87. Load vs. maximum out-of-plane displacement responses.

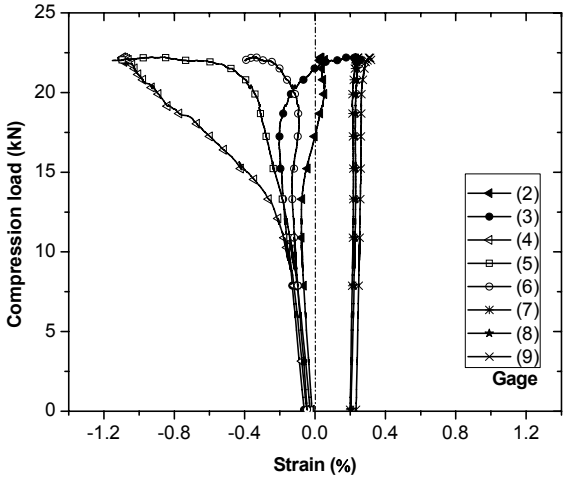

Figure B.88. Compression load vs. strain responses.

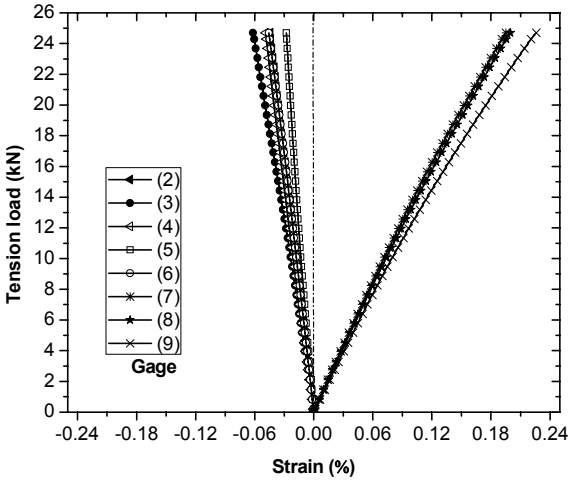

Figure B.89. Tension load vs. strain responses.

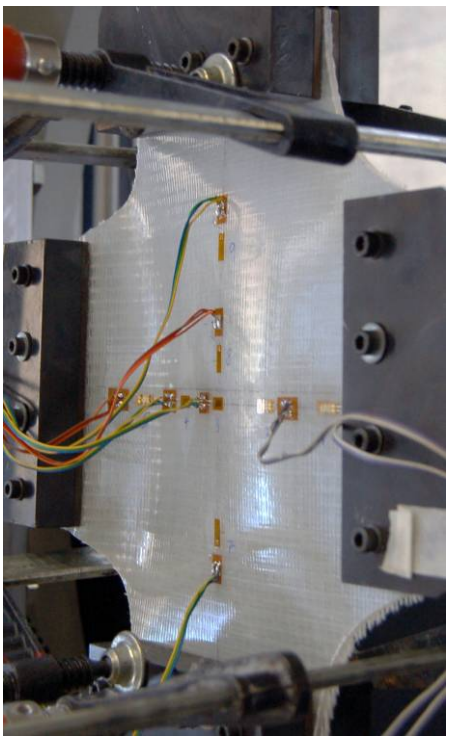

Figure B.90. Buckling mode shape.

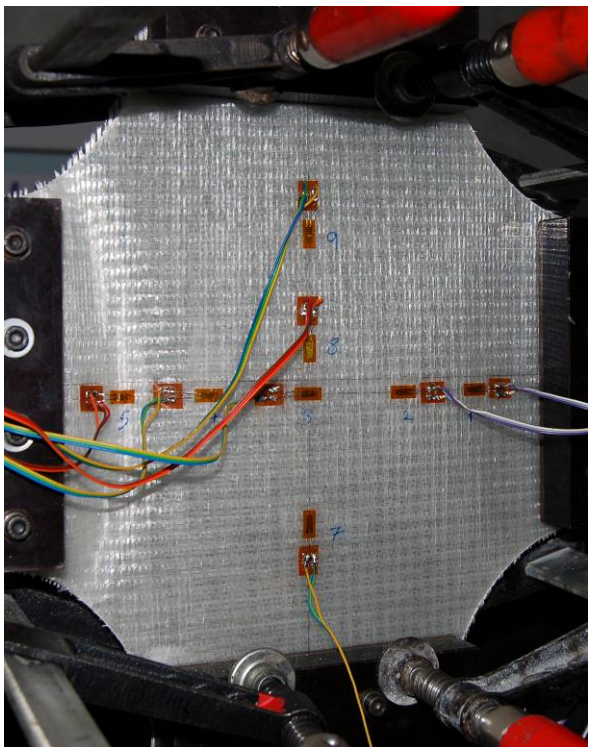

Figure B.91. Failure mode of specimen.

B.1.2.7. 30-kN Tension

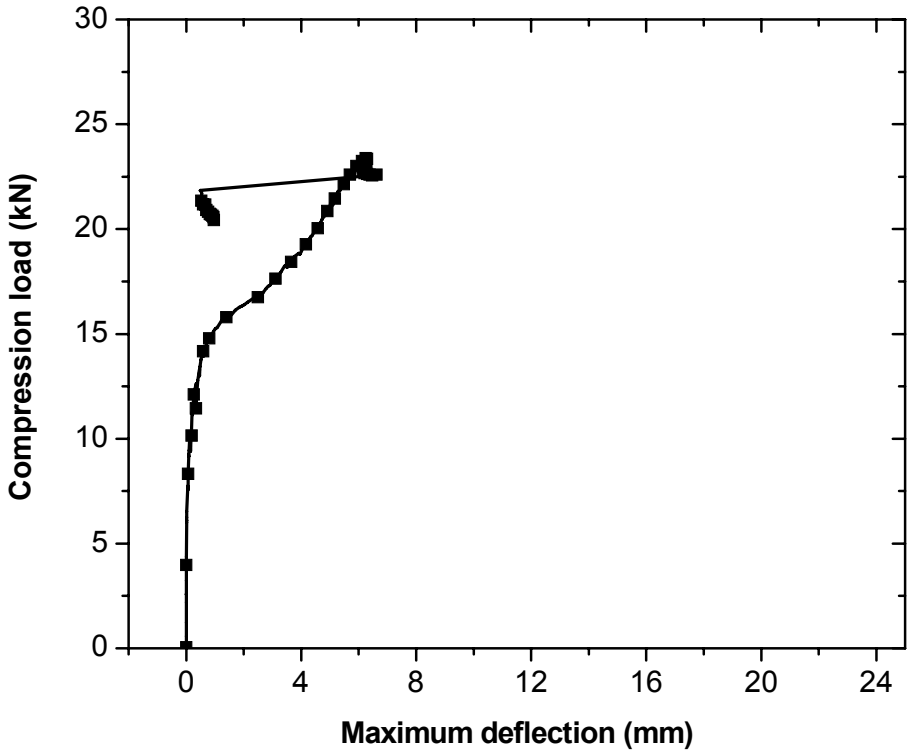

Figure B.87. Load vs. maximum out-of-plane displacement responses.

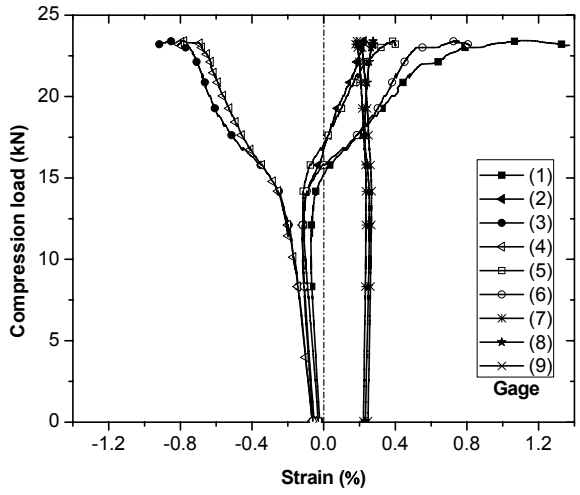

Figure B.88. Compression load vs. strain responses.

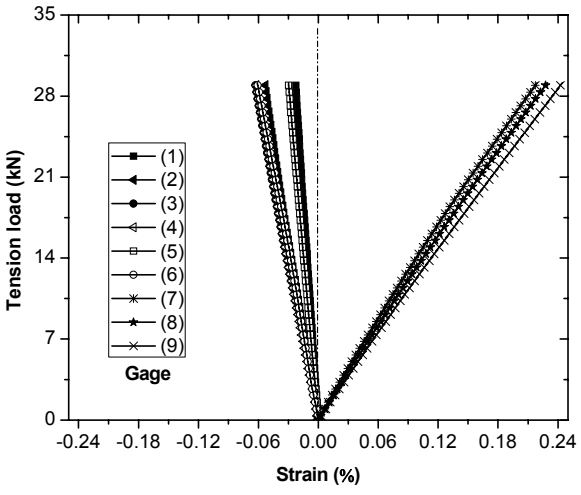

Figure B.89. Tension load vs. strain responses.

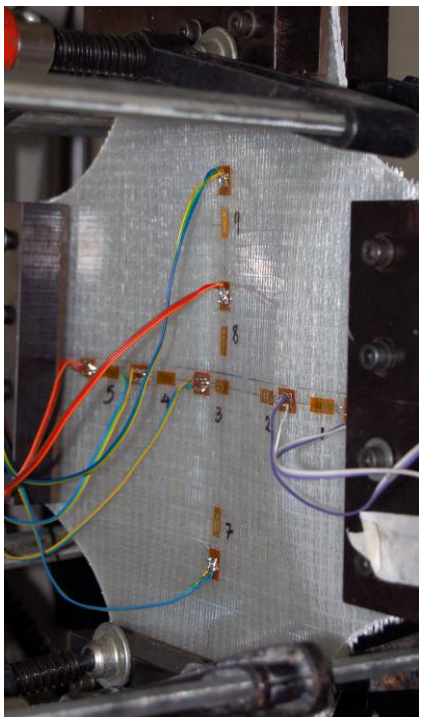

Figure B.90. Buckling mode shape.

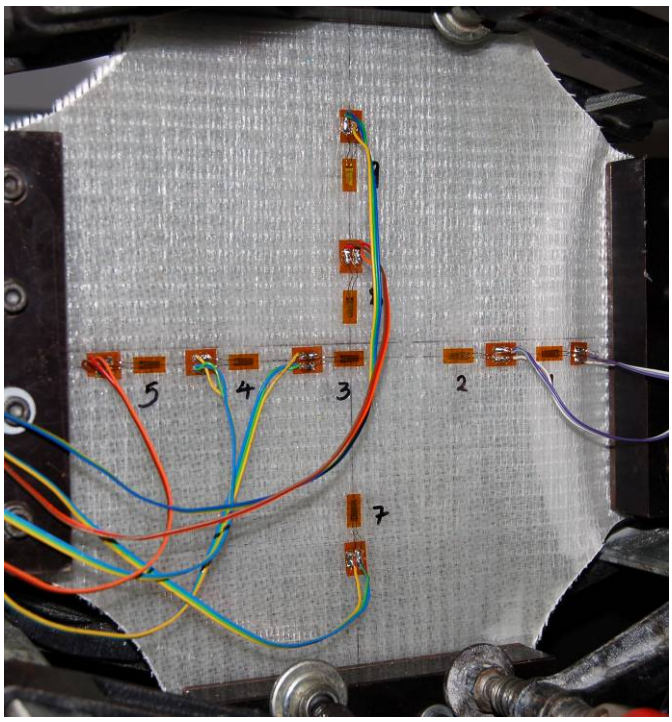

Figure B.91. Failure mode of specimen.

B.1.3. $[\pm 45]_S$ specimens

B.1.3.1. 0-kN Tension

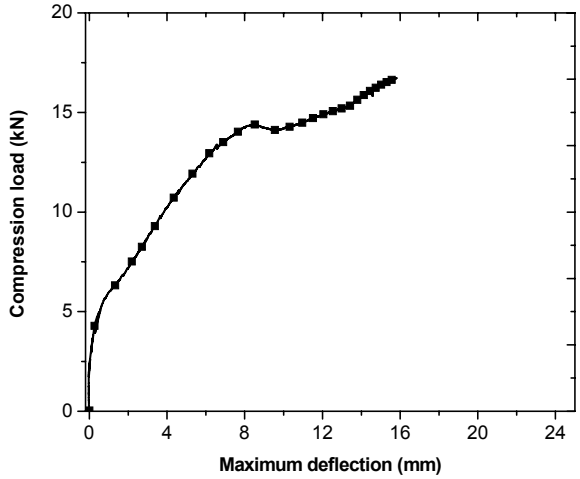

Figure B.92. Load vs. maximum out-of-plane displacement responses.

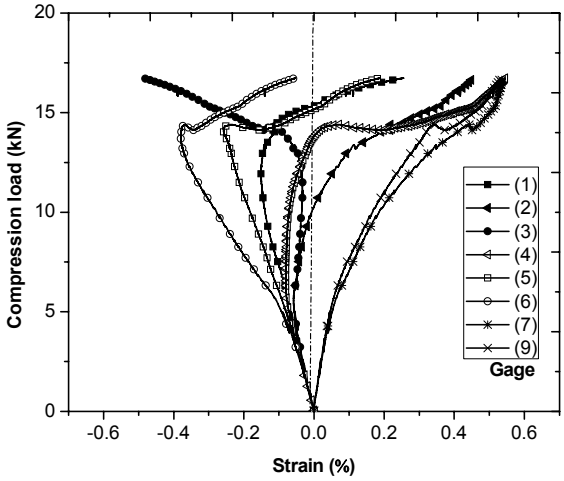

Figure B.93. Compression load vs. strain responses.

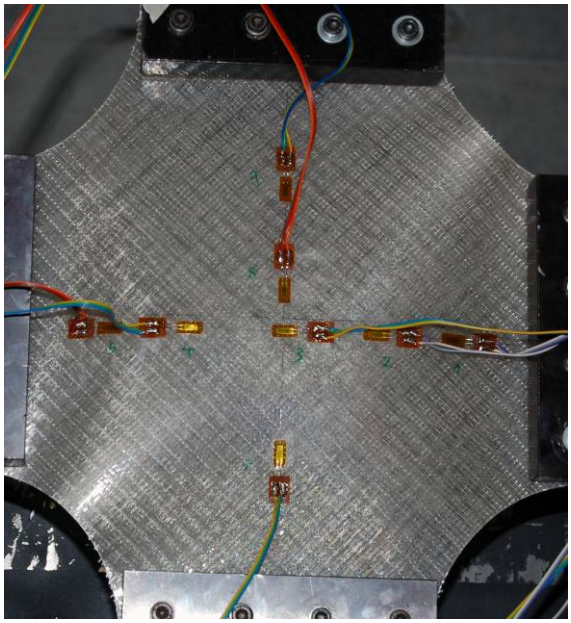

Figure B.94. Buckling mode shape.

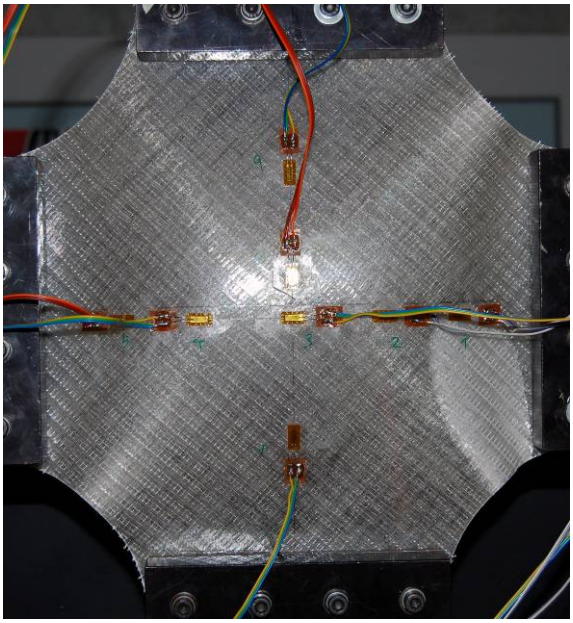

Figure B.95. Failure mode of specimen.

B.1.3.2. 5-kN Tension

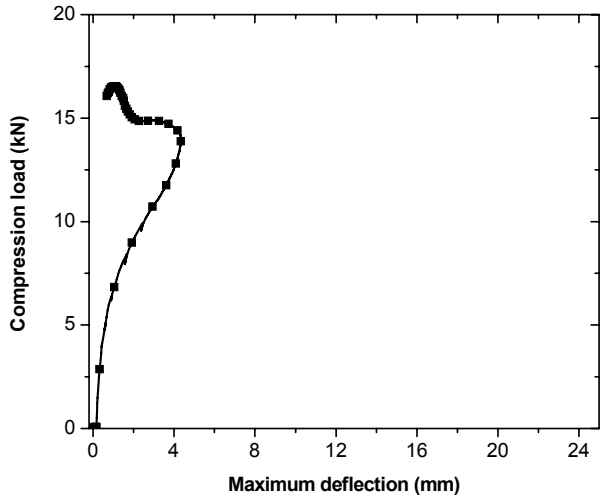

Figure B.96. Load vs. maximum out-of-plane displacement responses.

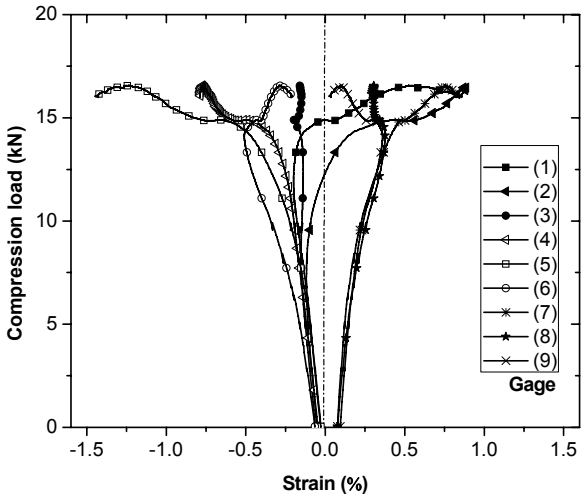

Figure B.97. Compression load vs. strain responses.

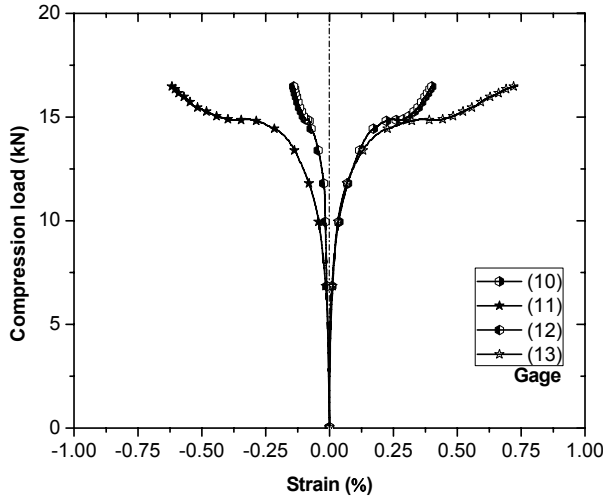

Figure B.98. Compression load vs. strain responses.

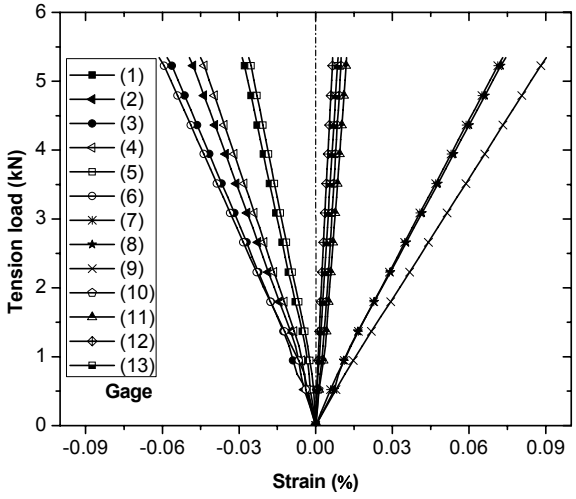

Figure B.99. Tension load vs. strain responses.

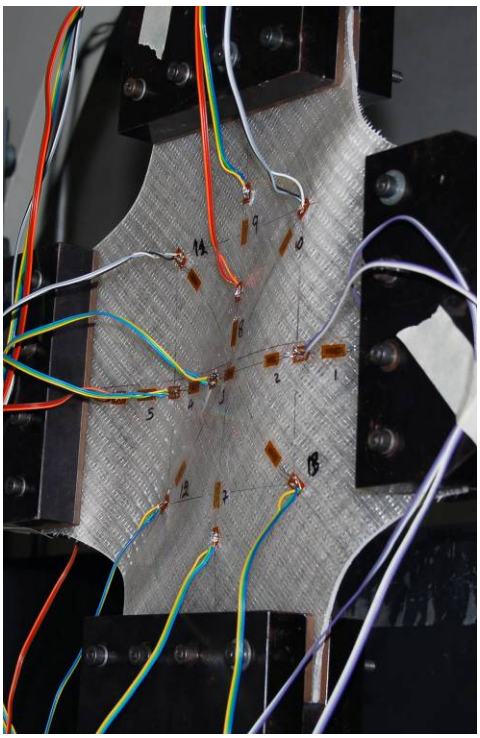

Figure B.100. Buckling mode shape.

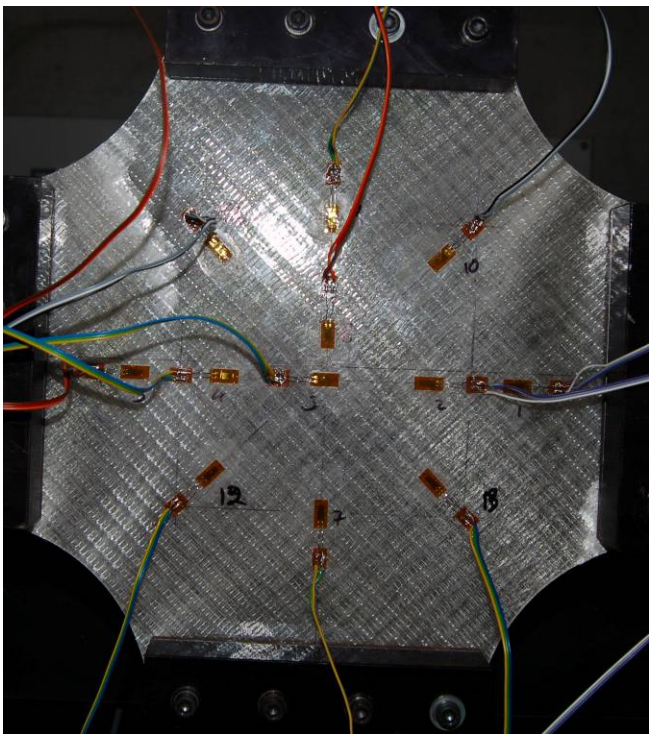

Figure B.101. Failure mode of specimen.

B.1.3.3. 10-kN Tension

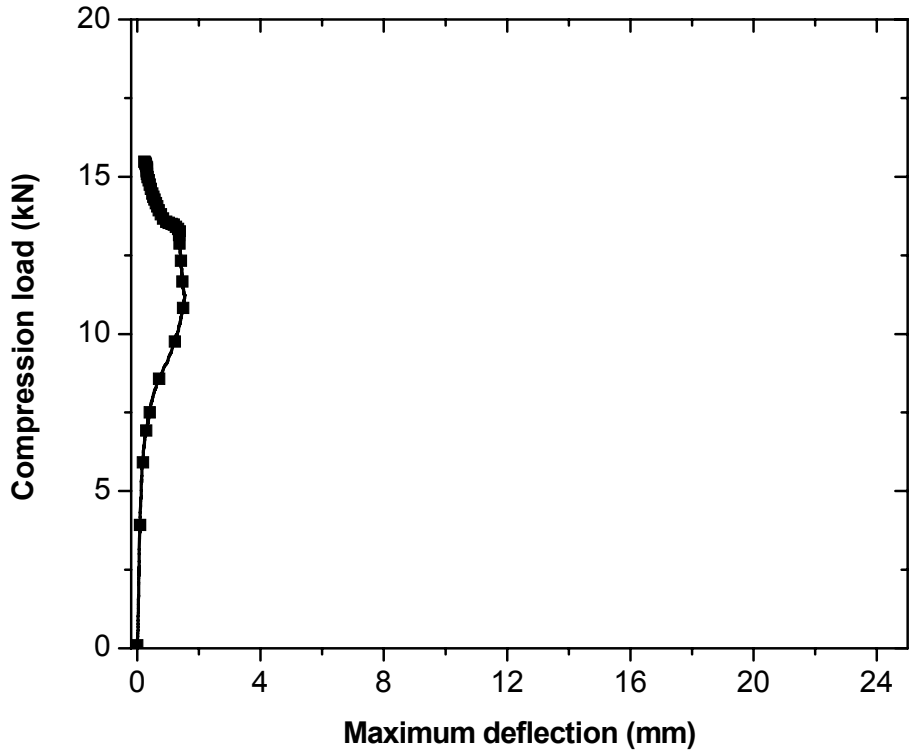

Figure B.102. Load vs. maximum out-of-plane displacement responses.

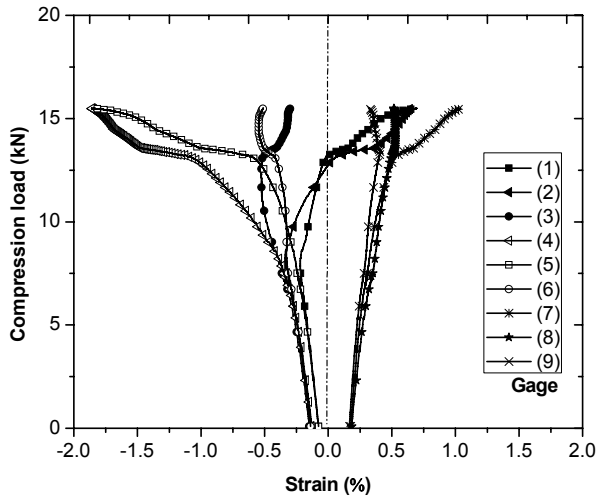

Figure B.103. Compression load vs. strain responses.

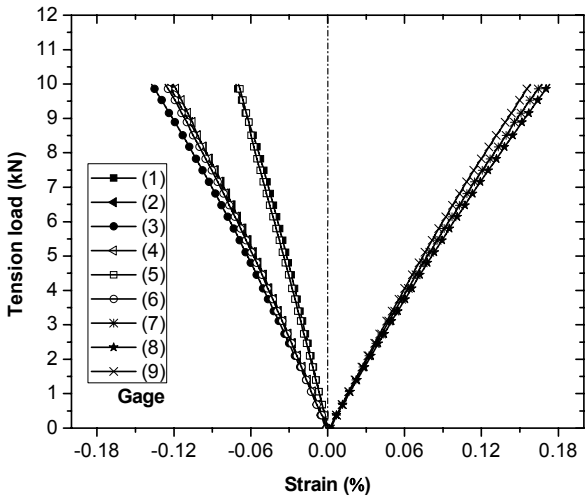

Figure B.104. Tension load vs. strain responses.

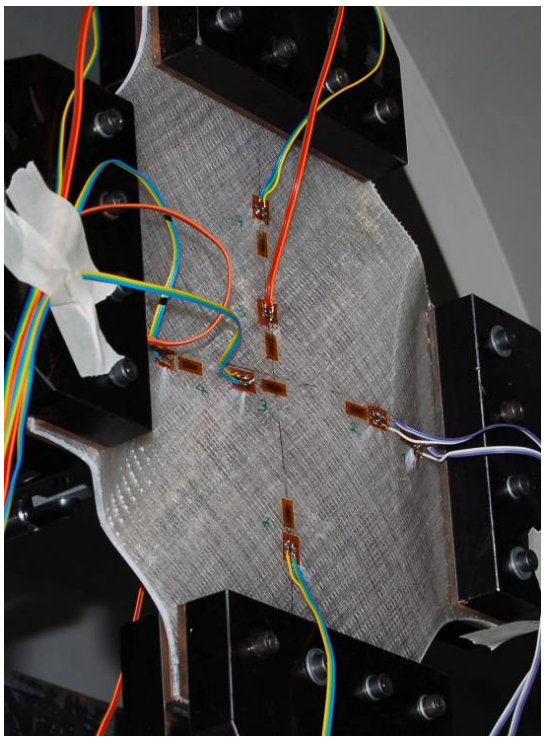

Figure B.105. Buckling mode shape.

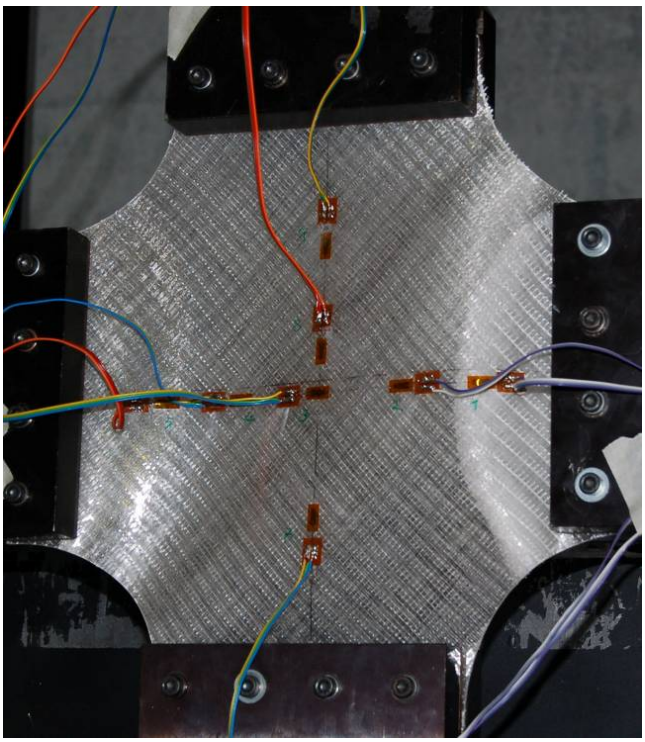

Figure B.106. Failure mode of specimen.

B.1.3.4. 15-kN Tension

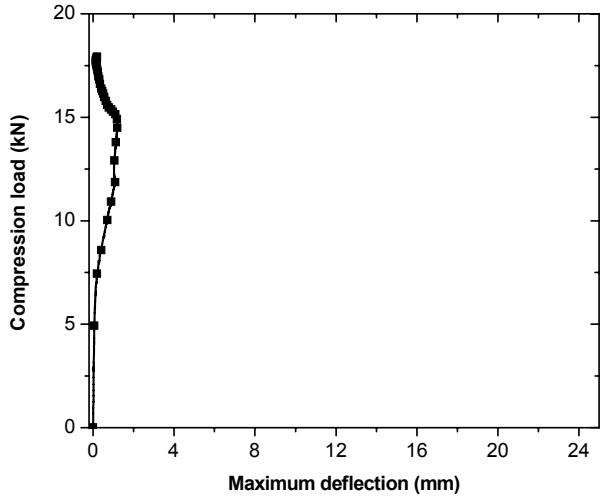

Figure B.107. Load vs. maximum out-of-plane displacement responses.

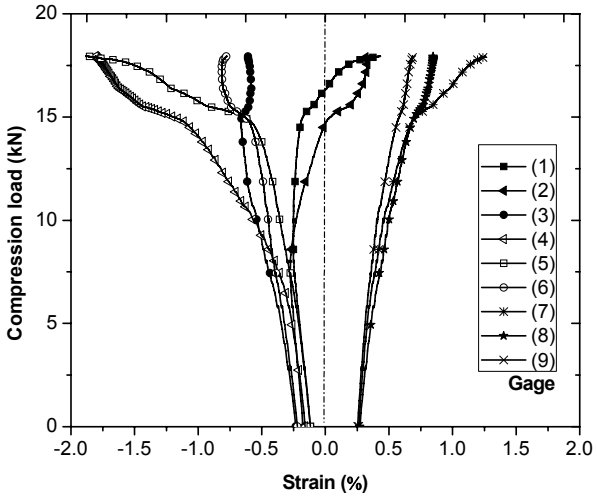

Figure B.108. Compression load vs. strain responses.

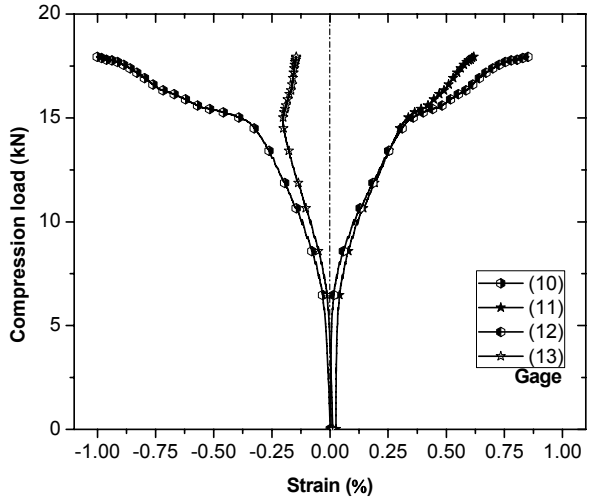

Figure B.109. Compression load vs. strain responses.

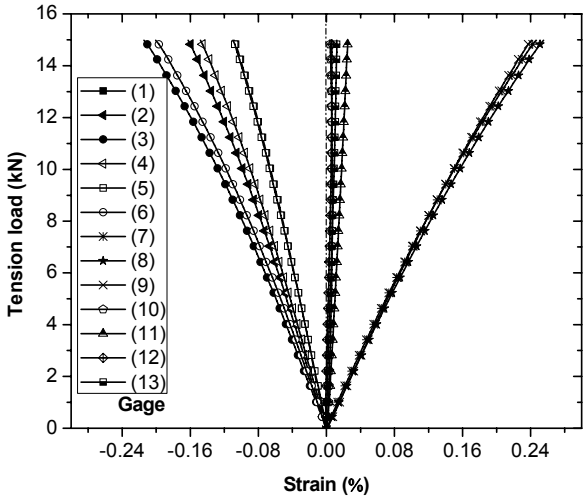

Figure B.110. Tension load vs. strain responses.

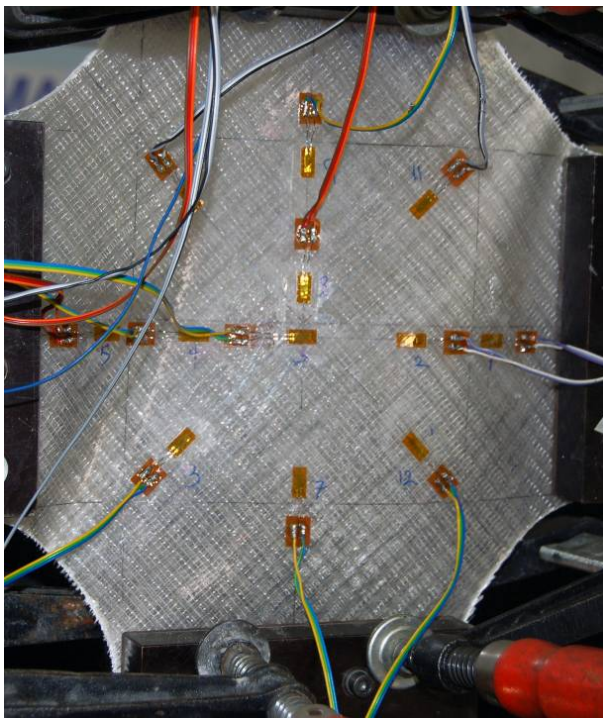

Figure B.111. Buckling mode shape.

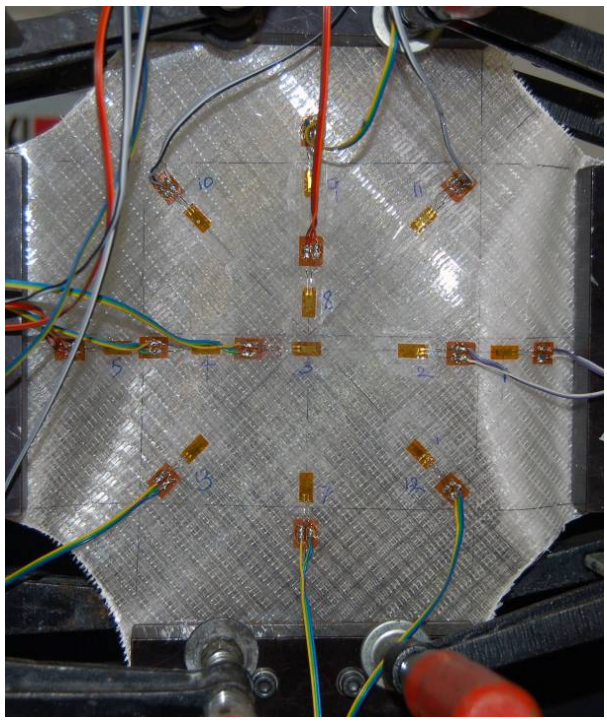

Figure B.112. Failure mode of specimen.

B.1.3.5. 20-kN Tension

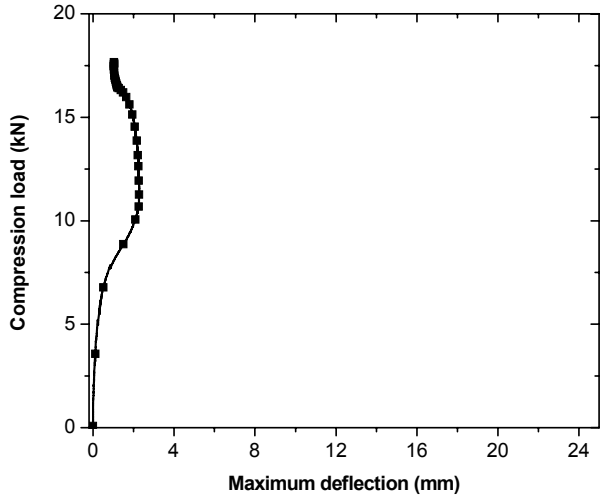

Figure B.113. Load vs. maximum out-of-plane displacement responses.

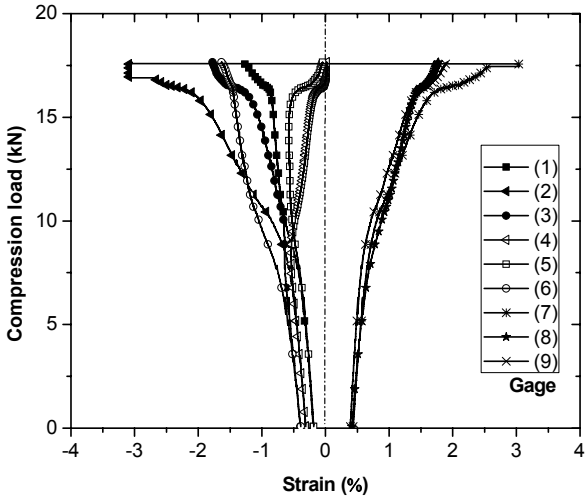

Figure B.114. Compression load vs. strain responses.

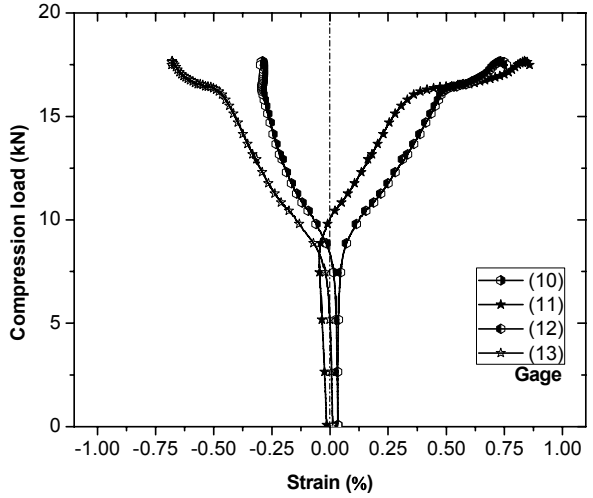

Figure B.115. Compression load vs. strain responses.

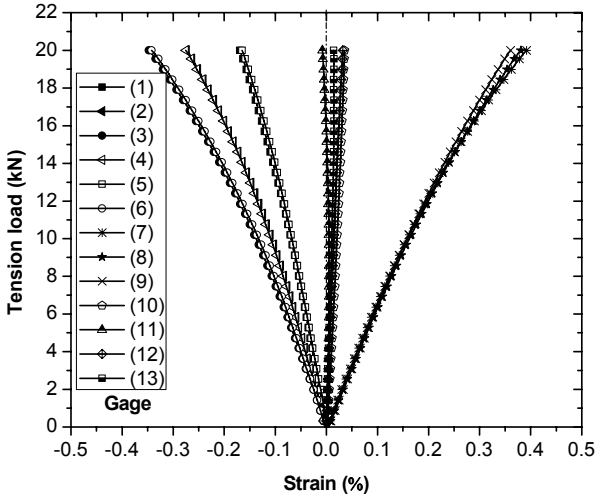

Figure B.116. Tension load vs. strain responses.

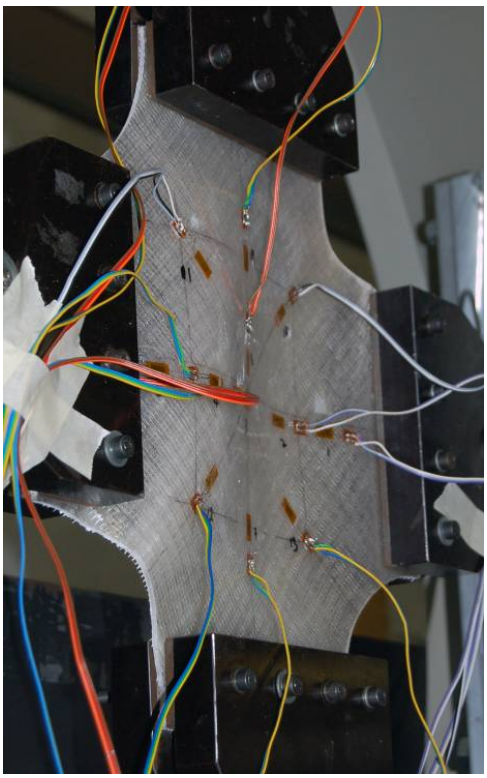

Figure B.117. Buckling mode shape.

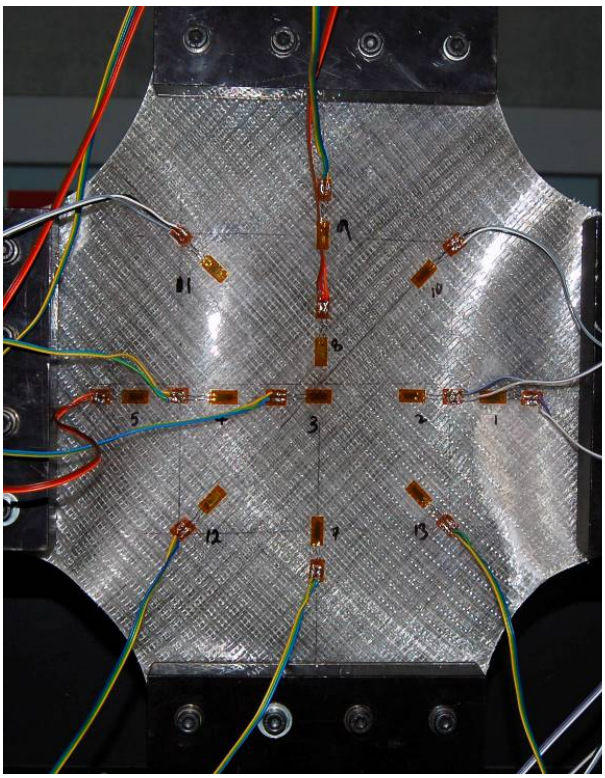

Figure B.118. Failure mode of specimen.

B.1.3.6. 25-kN Tension

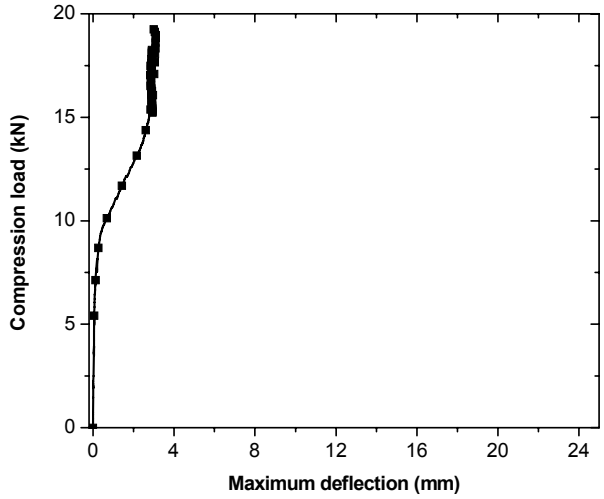

Figure B.119. Load vs. maximum out-of-plane displacement responses.

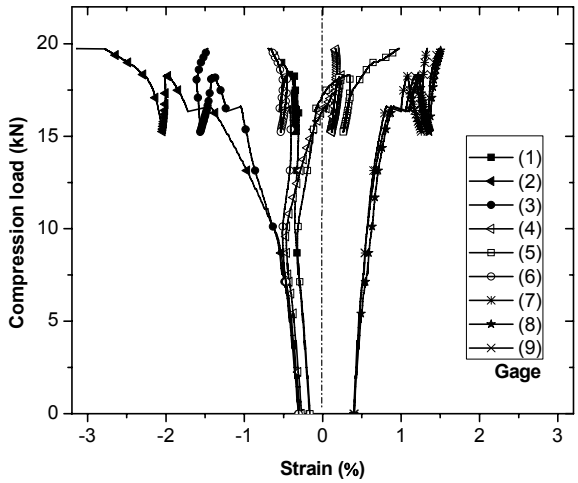

Figure B.120. Compression load vs. strain responses.

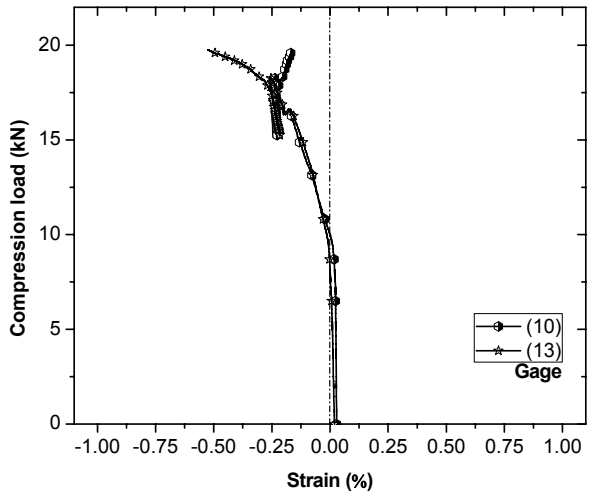

Figure B.121. Compression load vs. strain responses.

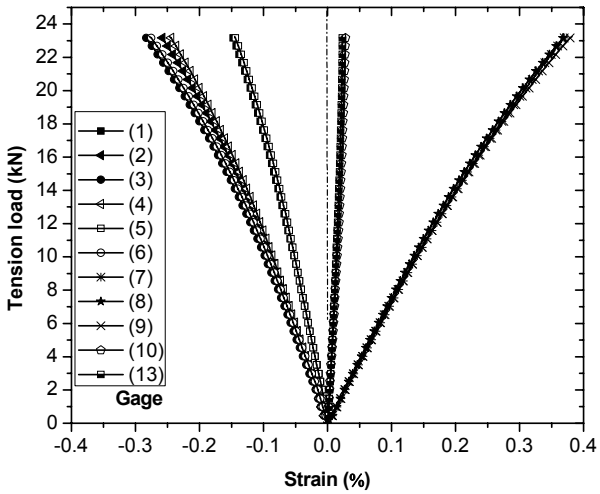

Figure B.122. Tension load vs. strain responses.

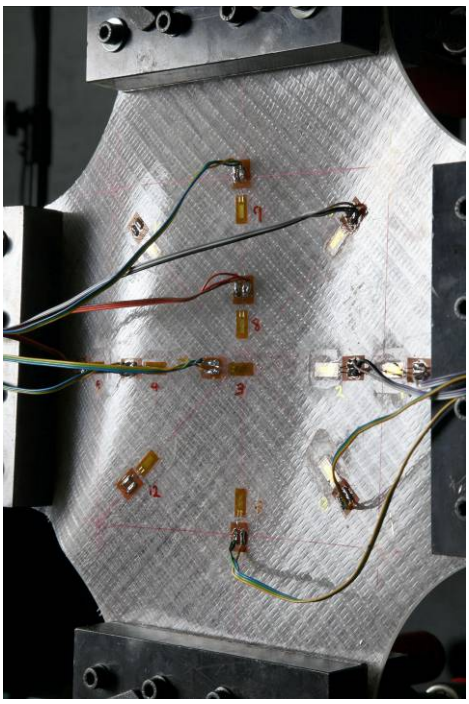

Figure B.123. Buckling mode shape.

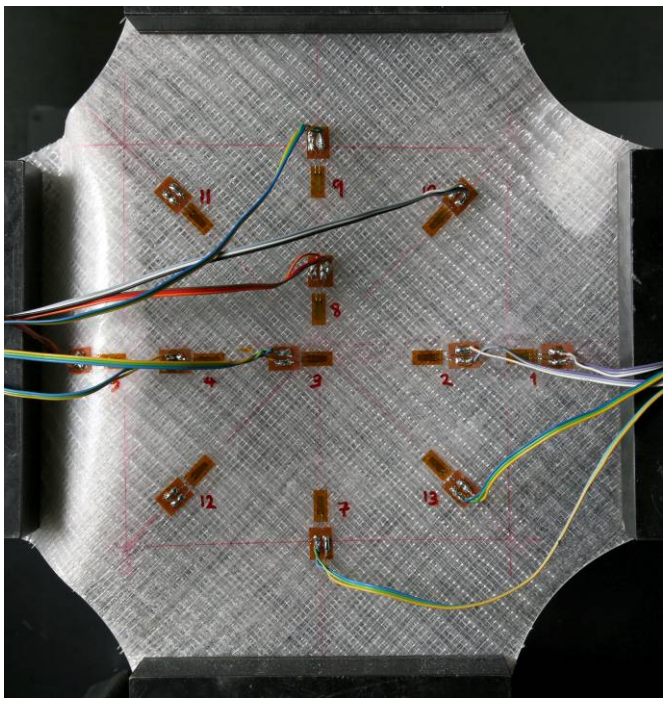

Figure B.124. Failure mode of specimen.

B.1.3.7. SCT

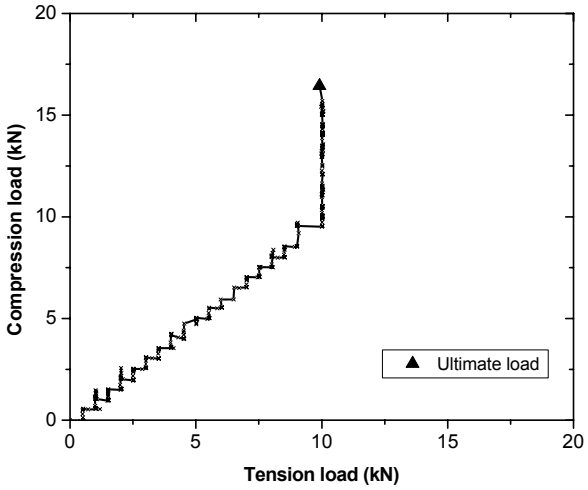

Figure B.125. Compression load vs. tension load.

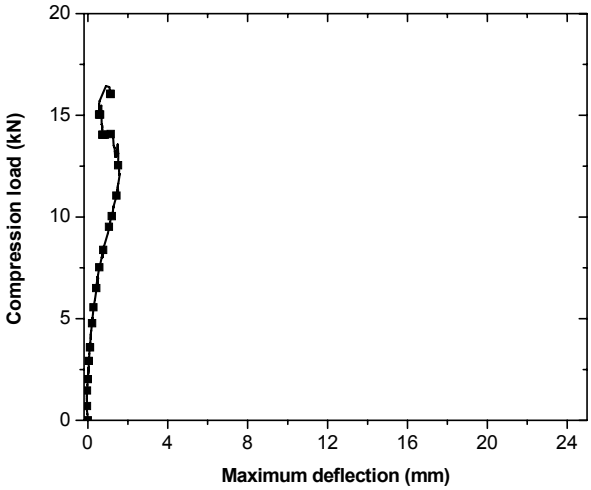

Figure B.126. Load vs. maximum out-of-plane displacement responses.

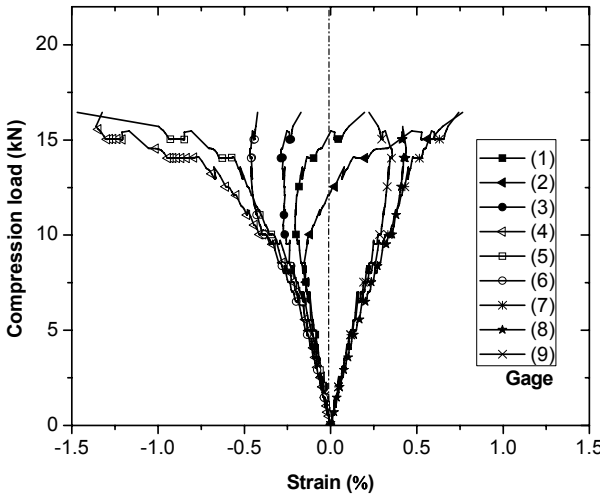

Figure B.127. Compression load vs. strain responses.

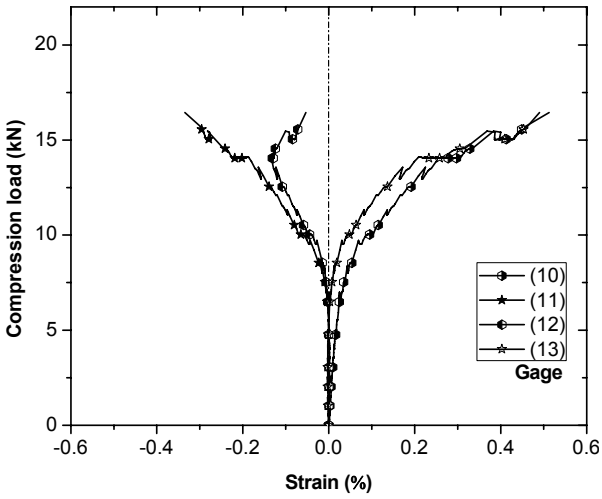

Figure B.128. Compression load vs. strain responses.

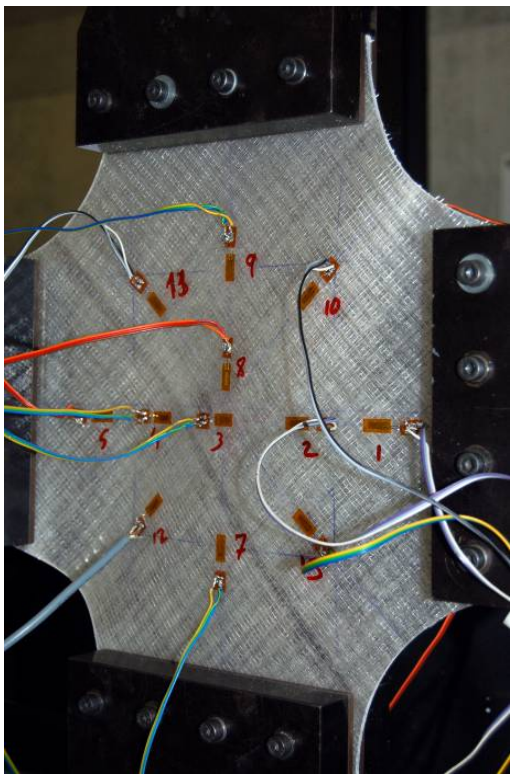

Figure B.129. Buckling mode shape.

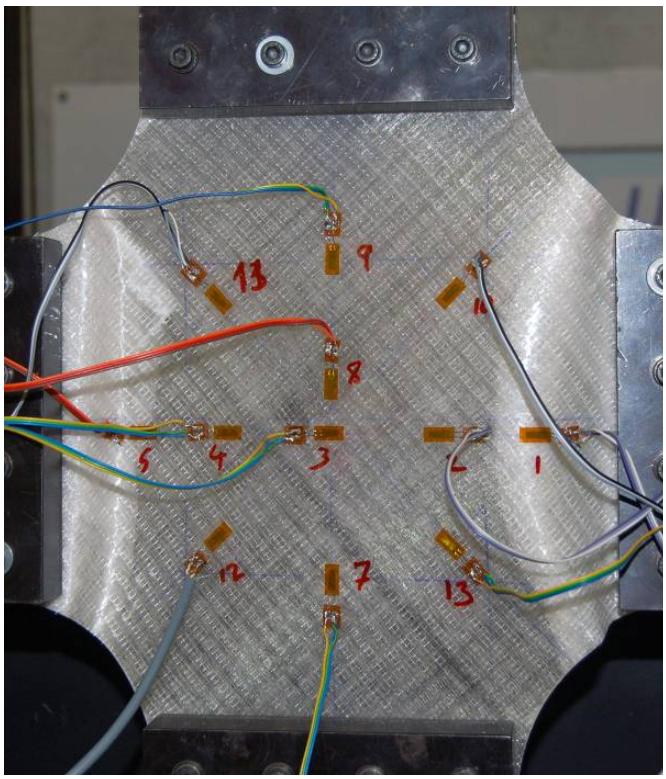

Figure B.130. Failure mode of specimen.

B.2. Biaxial wrinkling of GFRP sandwiches

B.2.1. [90/0] specimens

B.2.1.1. CT 0-kN

The first specimen at 0-kN tension load was equipped with three strain gage located, as shown in Figure B.134. The gage (2) was located at the center point and gages (1) and (3) were located on the left and right sides of the gage (2), respectively, with 3 cm distance.

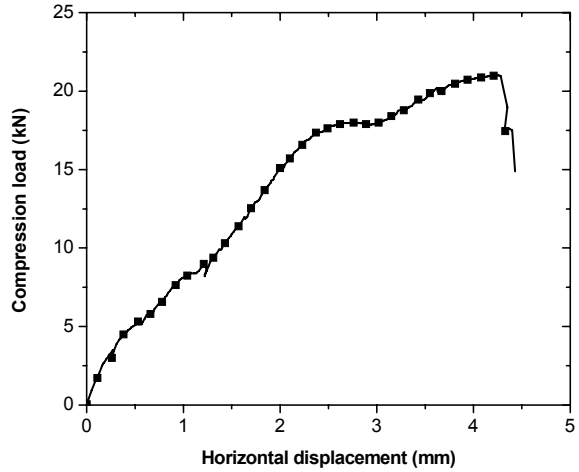

Figure B.131. Compression load vs. horizontal displacement of specimen#1.

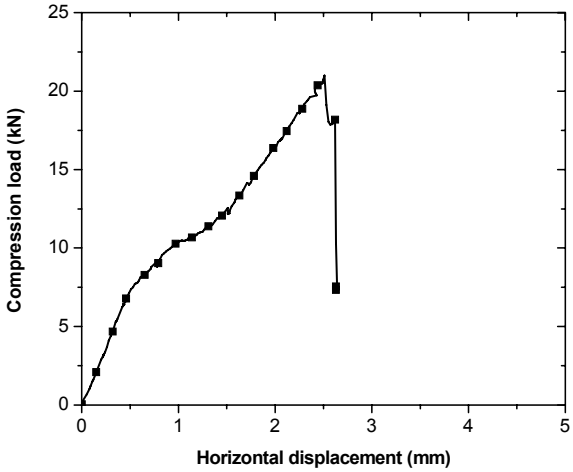

Figure B.132. Compression load vs. horizontal displacement of specimen#2.

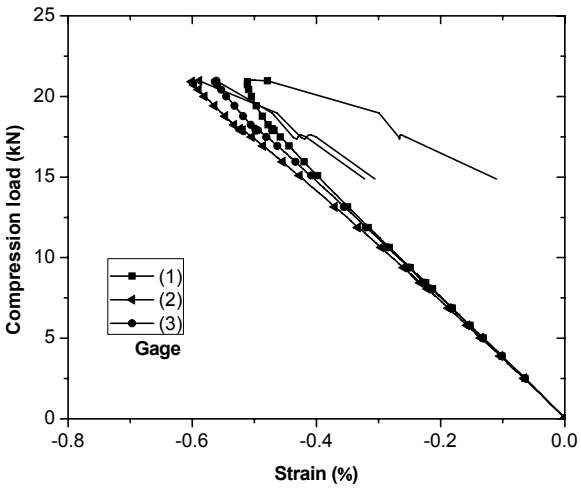

Figure B.133. Compression load vs. strain responses of specimen#1.

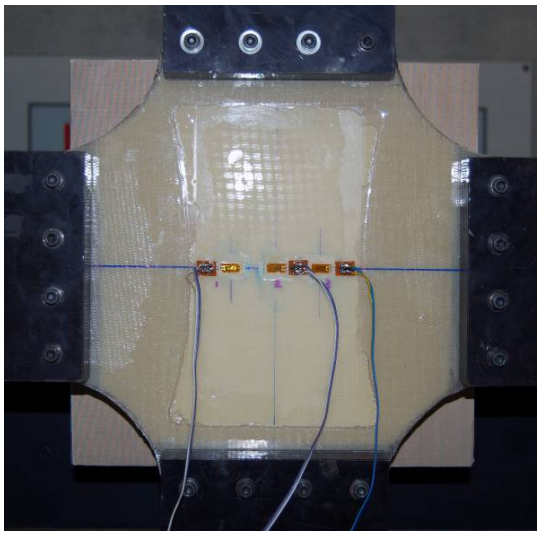

Figure B.134. Configuration of gages on specimen#1.

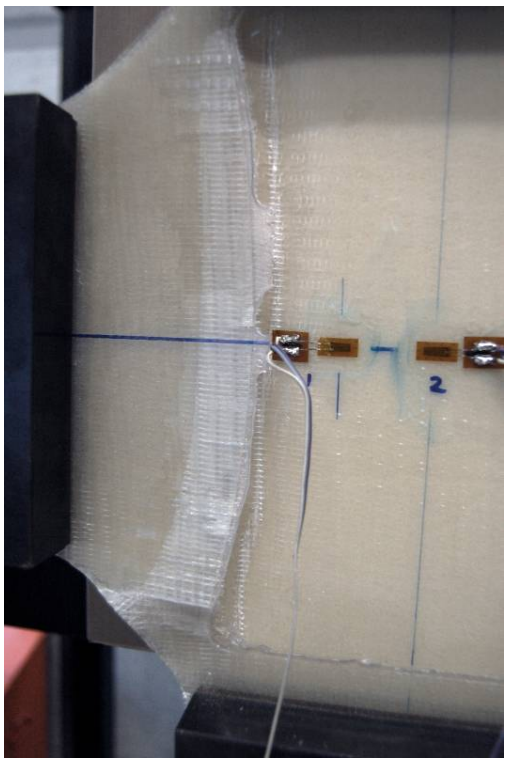

Figure B.135. Wrinkling failure mode of specimen#1.

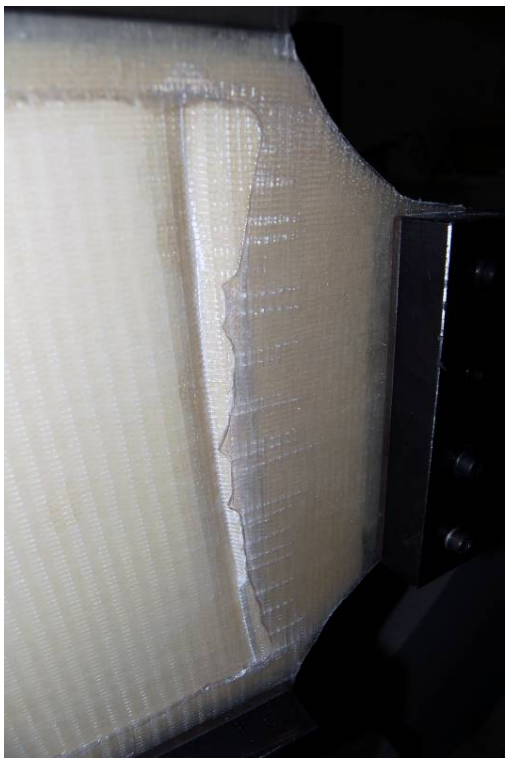

Figure B.136. Wrinkling failure mode of specimen#2.

B.2.1.2. CT 3-kN

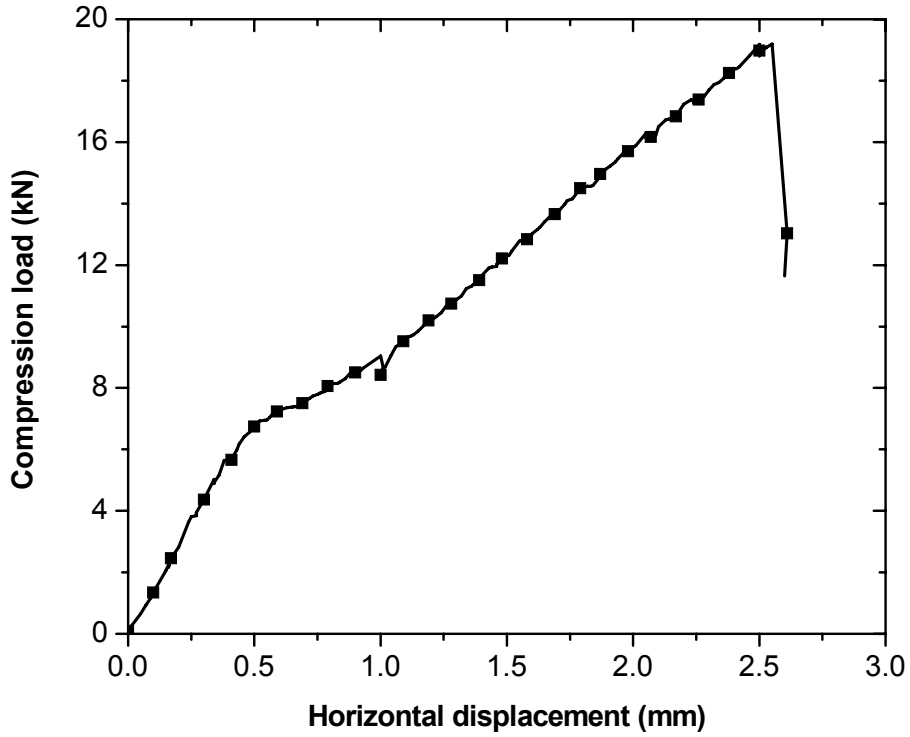

Figure B.137. Compression load vs. horizontal displacement.

Figure B.138. Foam failure occurred by wrinkling failure.

B.2.1.3. CT 5-kN

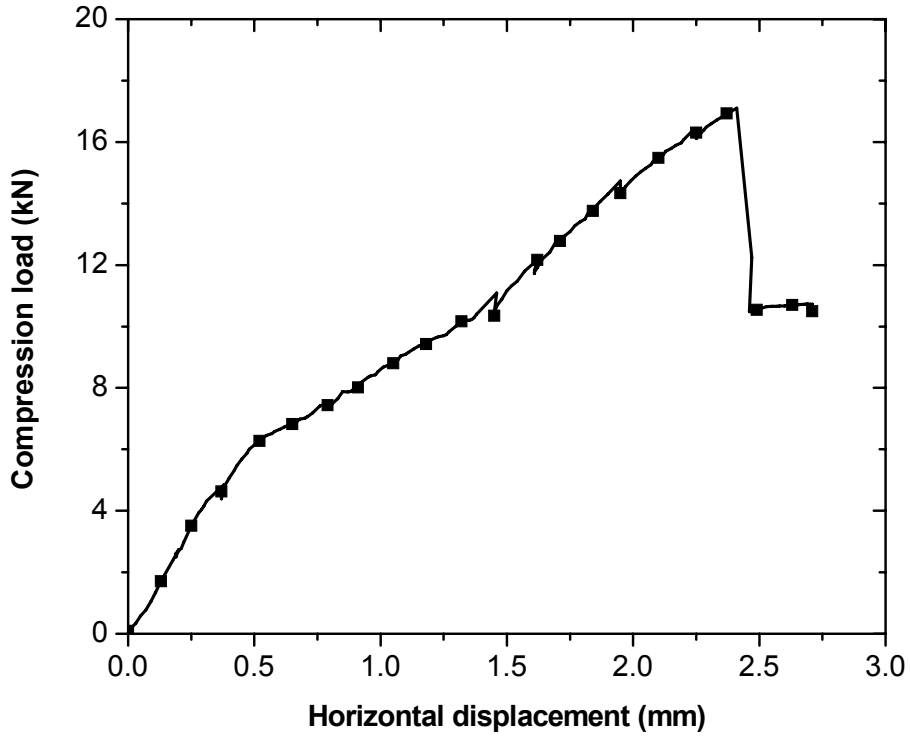

Figure B.139. Compression load vs. horizontal displacement.

Figure B.140. Wrinkling failure mode.

B.2.1.4. CT 10-kN

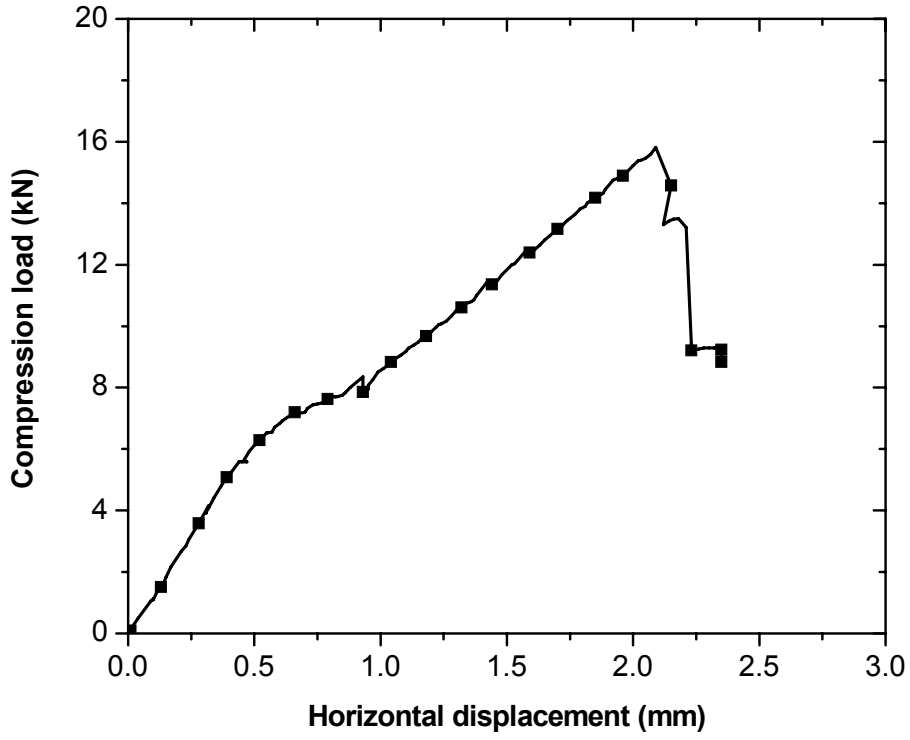

Figure B.141. Compression load vs. horizontal displacement.

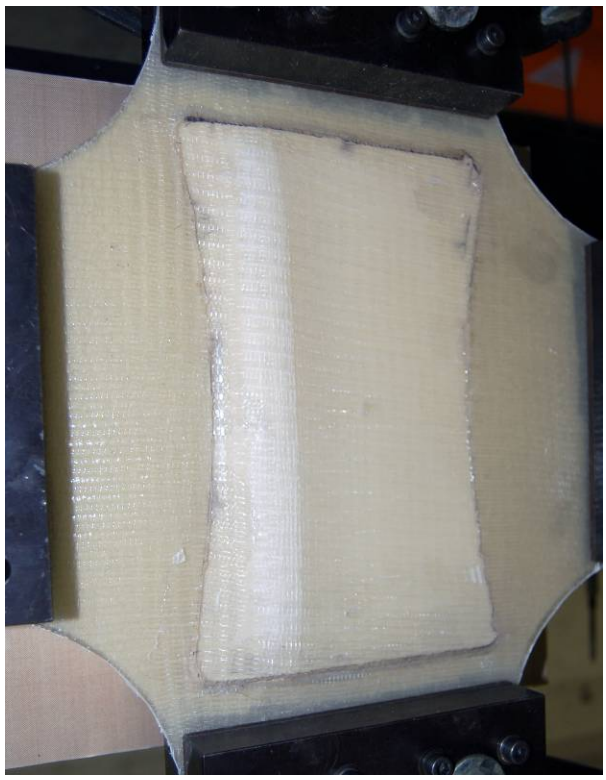

Figure B.142. Wrinkling failure mode.

B.2.1.5. CT 11.3-kN

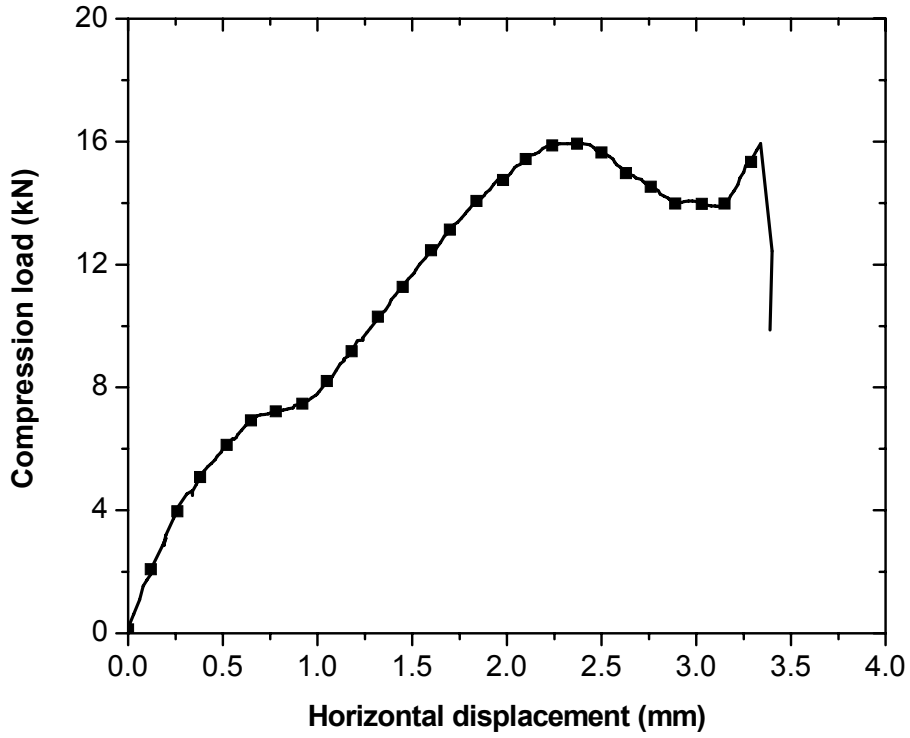

Figure B.143. Compression load vs. horizontal displacement.

Figure B.144. Wrinkling failure mode.

B.2.1.6. CT 17.7-kN

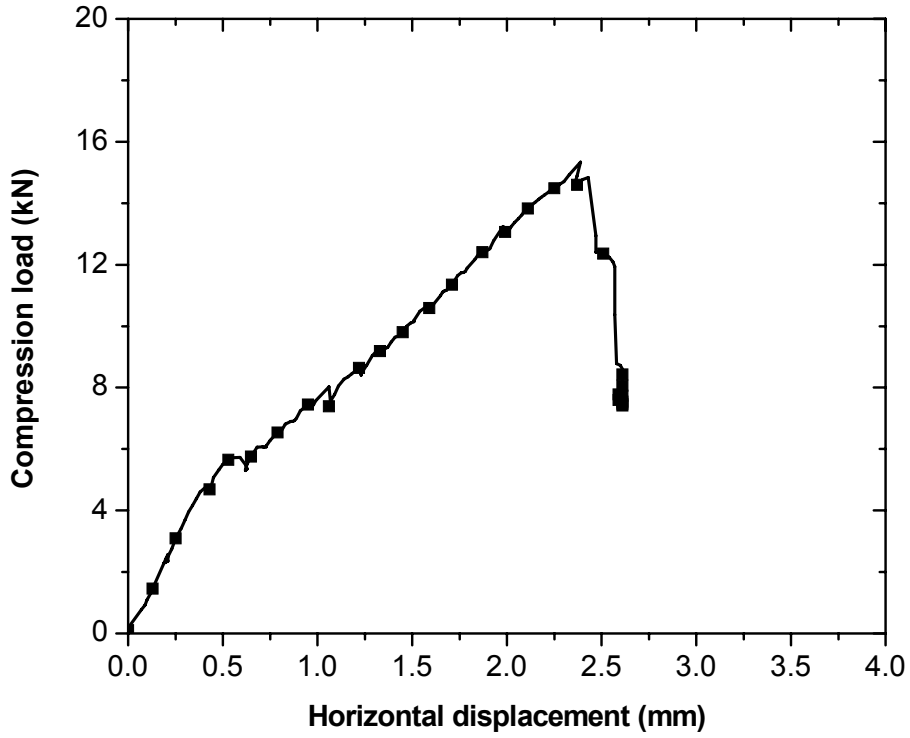

Figure B.145. Compression load vs. horizontal displacement.

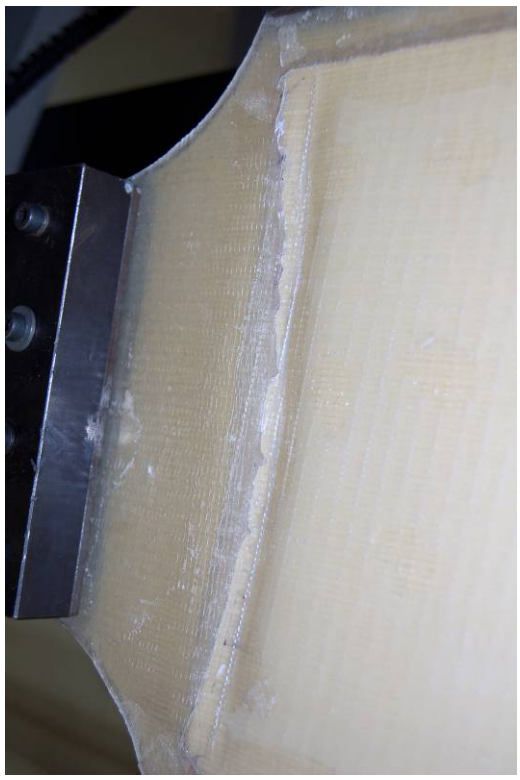

Figure B.146. Wrinkling failure mode.

B.2.1.7. CT 19.8-kN

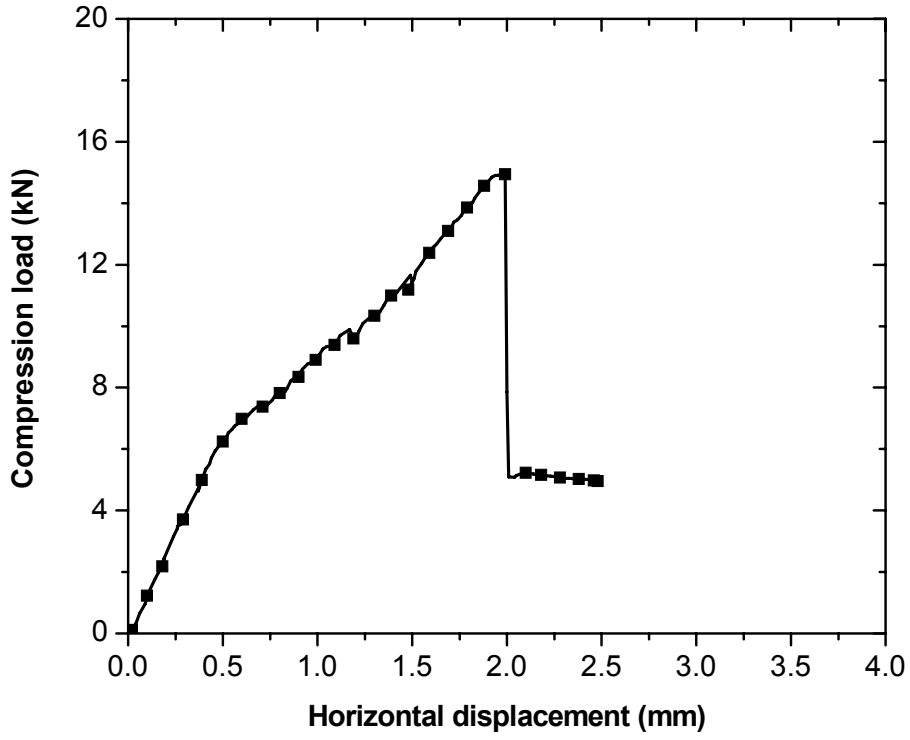

Figure B.147. Compression load vs. horizontal displacement.

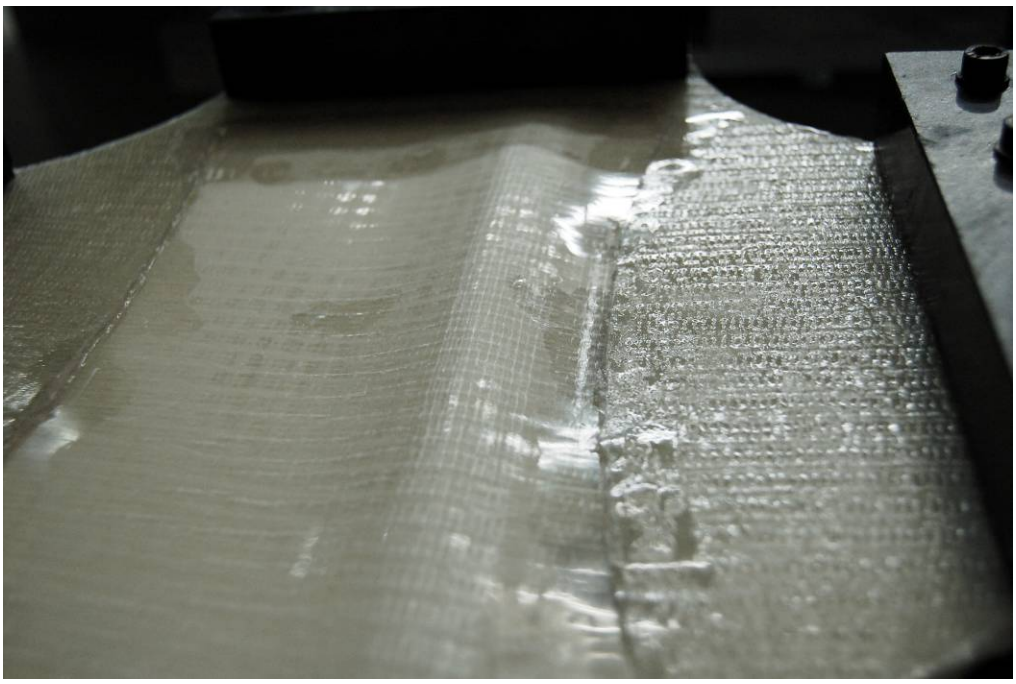

Figure B.148. Wrinkling failure mode.

B.2.1.8. CT 20-kN

The specimen at 20-kN tension load was equipped with one biaxial strain gage and two omega-shaped extensometers (designated as omega gage) located at the center point, as shown in Figure B.150; however, accurate results were not provided using the omega gages.

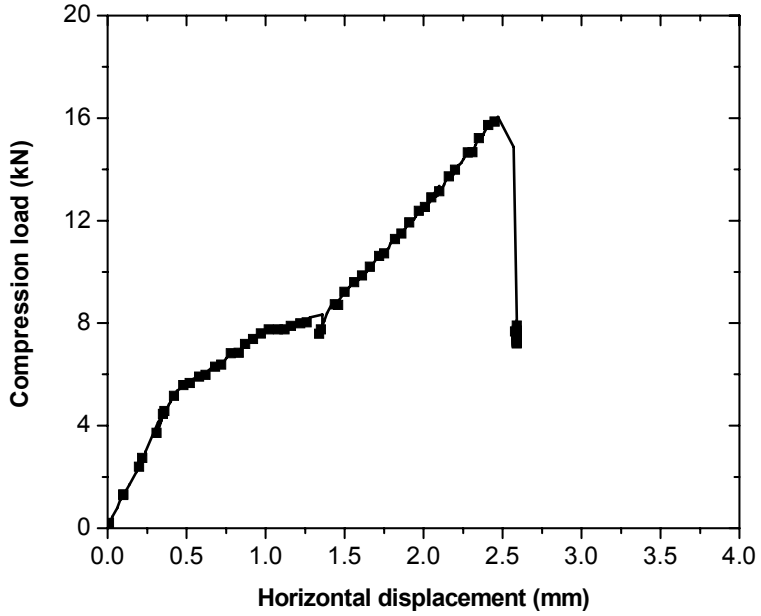

Figure B.149. Compression load vs. horizontal displacement.

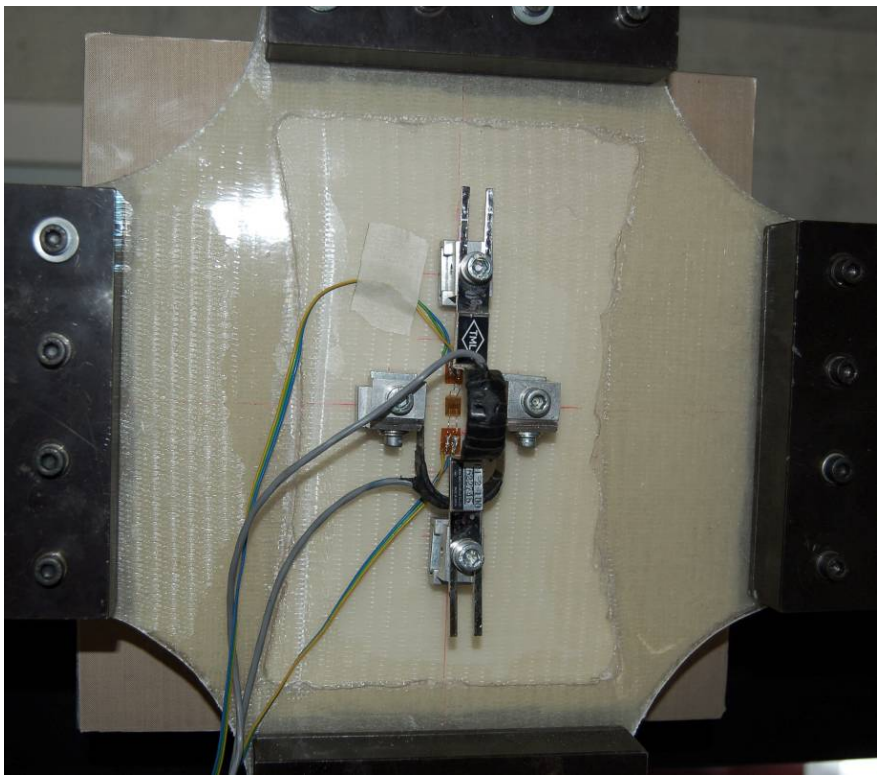

Figure B.150. Wrinkling failure mode and instrumentation.

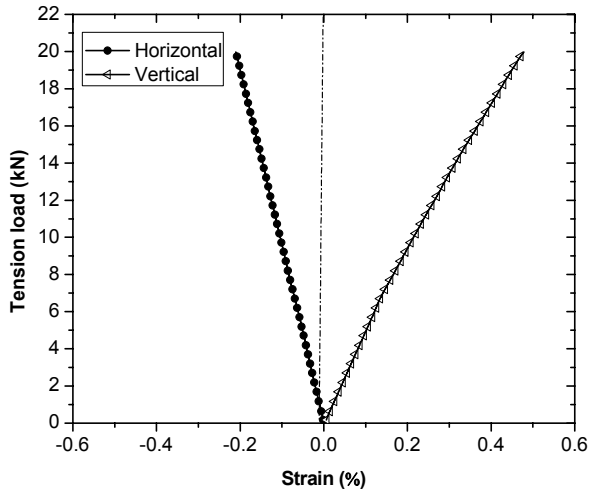

Figure B.151. Tension load vs. biaxial strain responses.

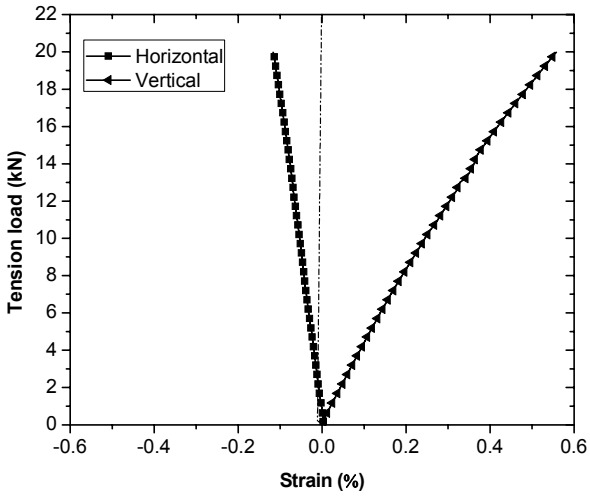

Figure B.152. Tension load vs. strain responses of omega gages.

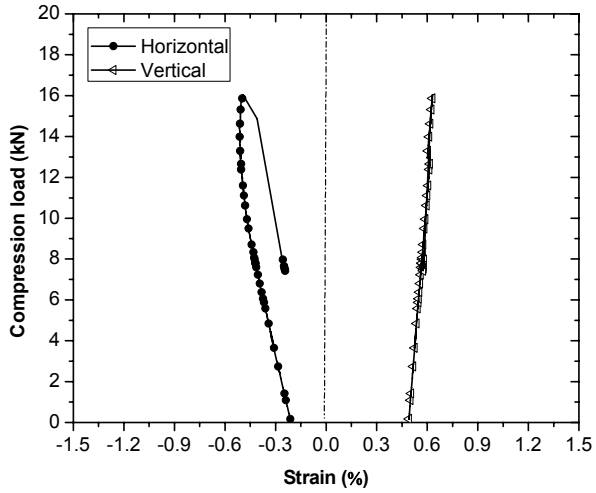

Figure B.153. Compression load vs. biaxial strain responses

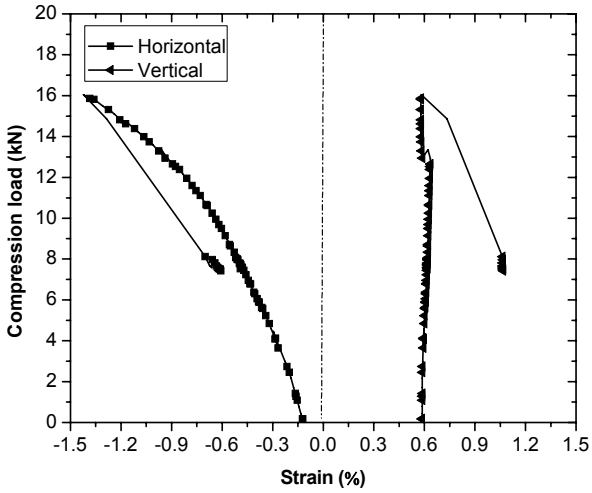

Figure B.154. Compression load vs. strain responses of omega gages.

B.2.1.9. SCT ϕ = 30°

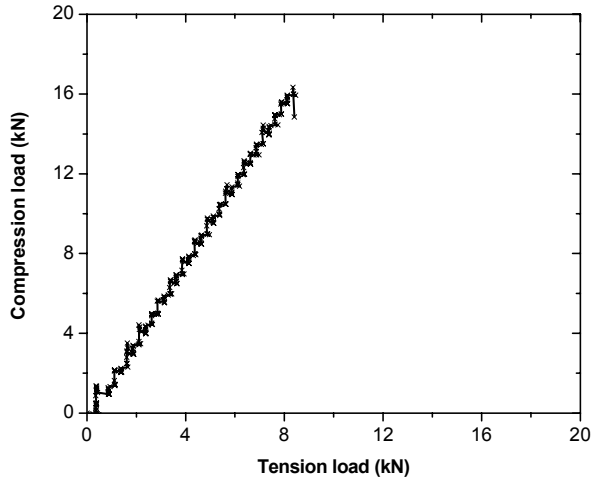

Figure B.155. Compression load vs. tension load.

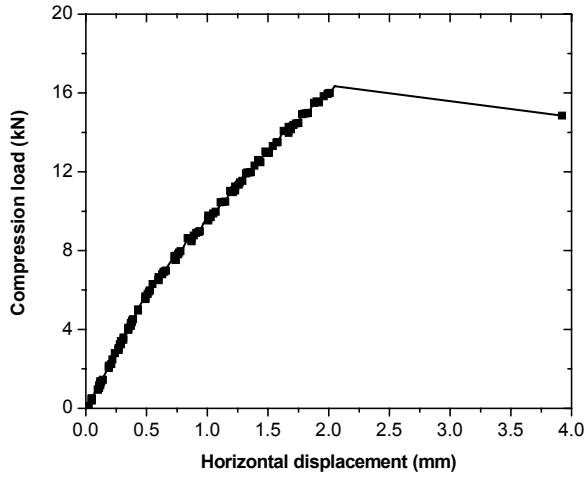

Figure B.156. Compression load vs.

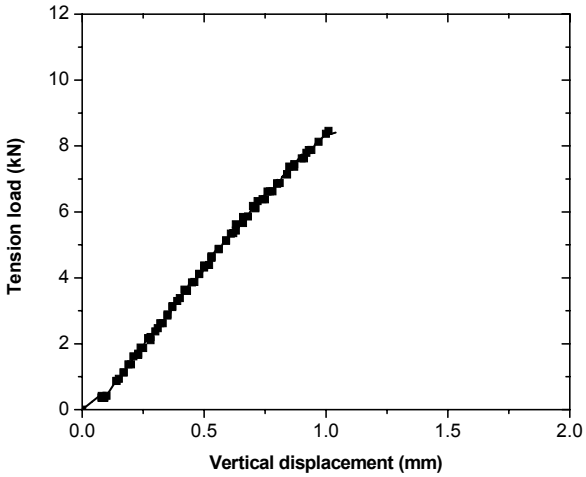

Figure B.157. Tension load vs. vertical

horizontal displacement. displacement.

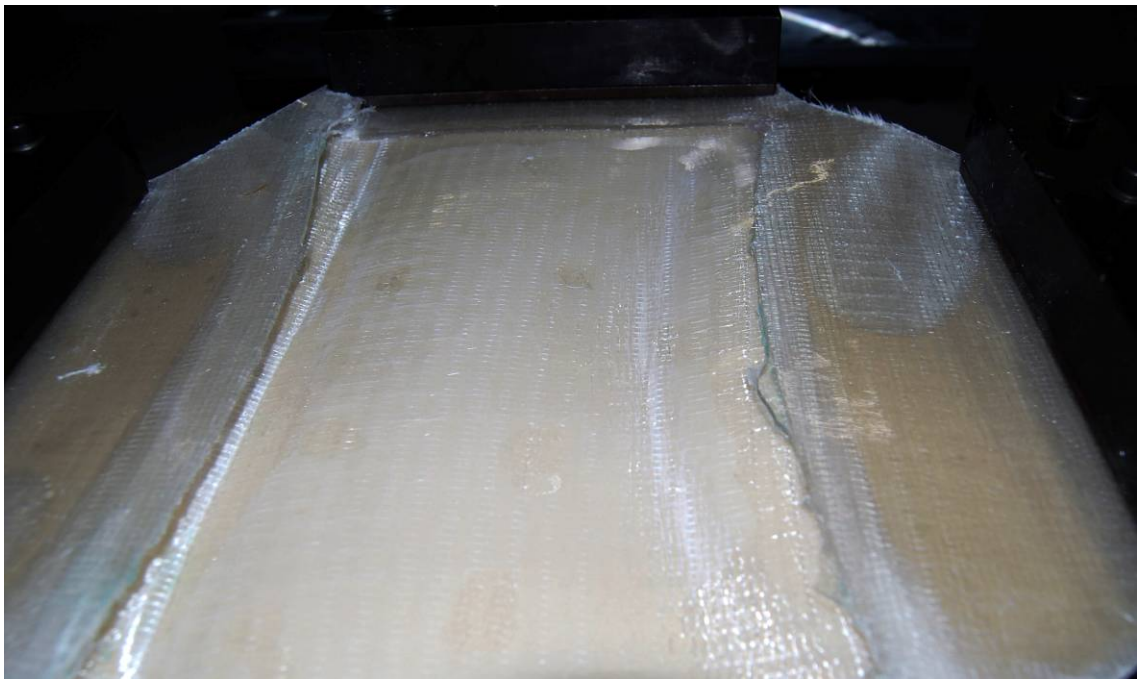

Figure B.158. Wrinkling failure mode.

B.2.1.10. SCT $\phi = 45°$

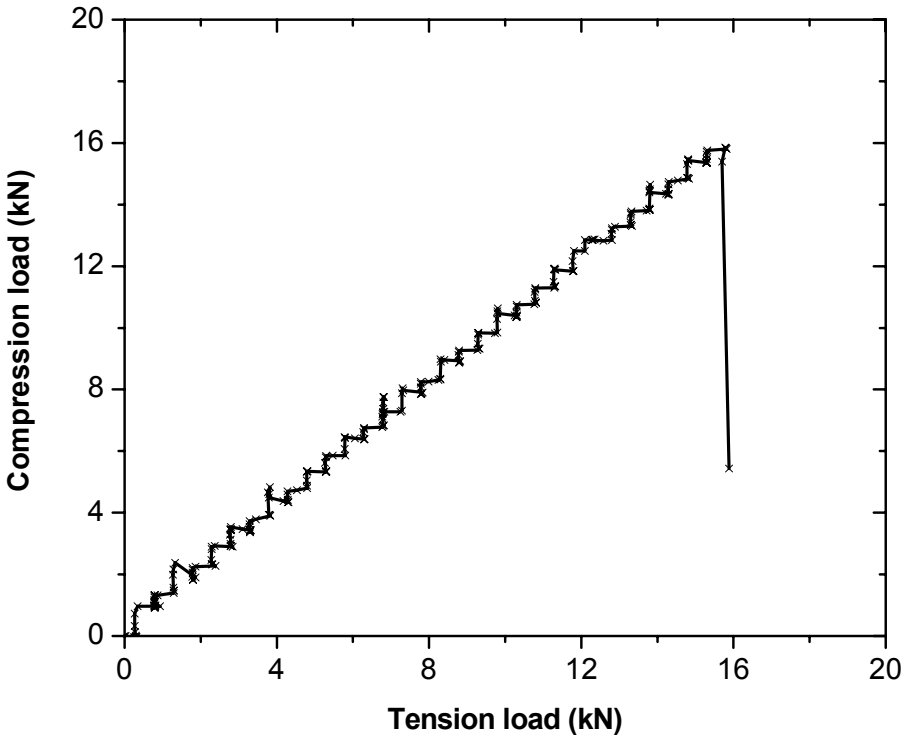

Figure B.159. Compression load vs. tension load.

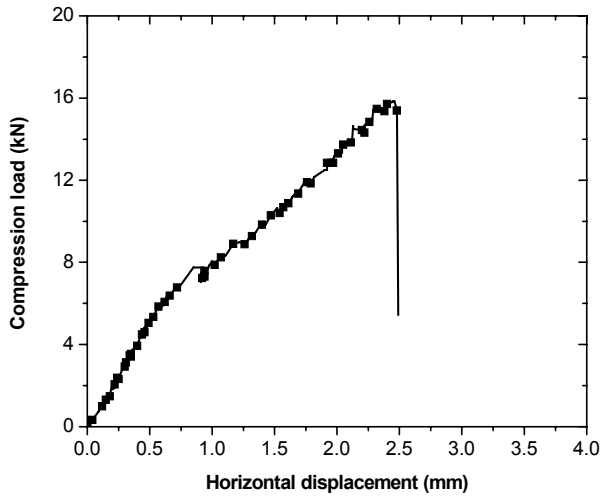

Figure B.160. Compression load vs. horizontal displacement.

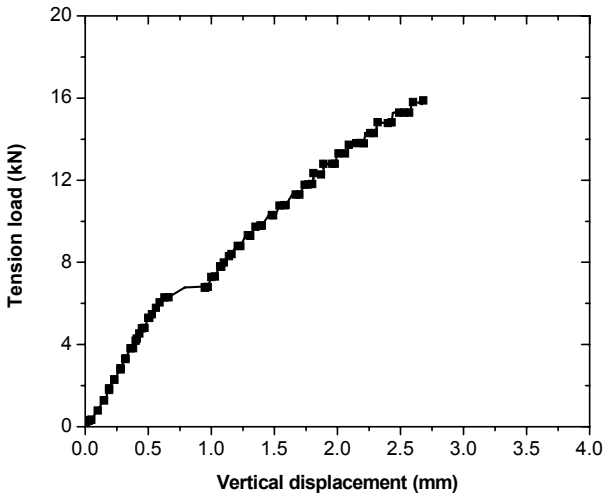

Figure B.161. Tension load vs. vertical displacement.

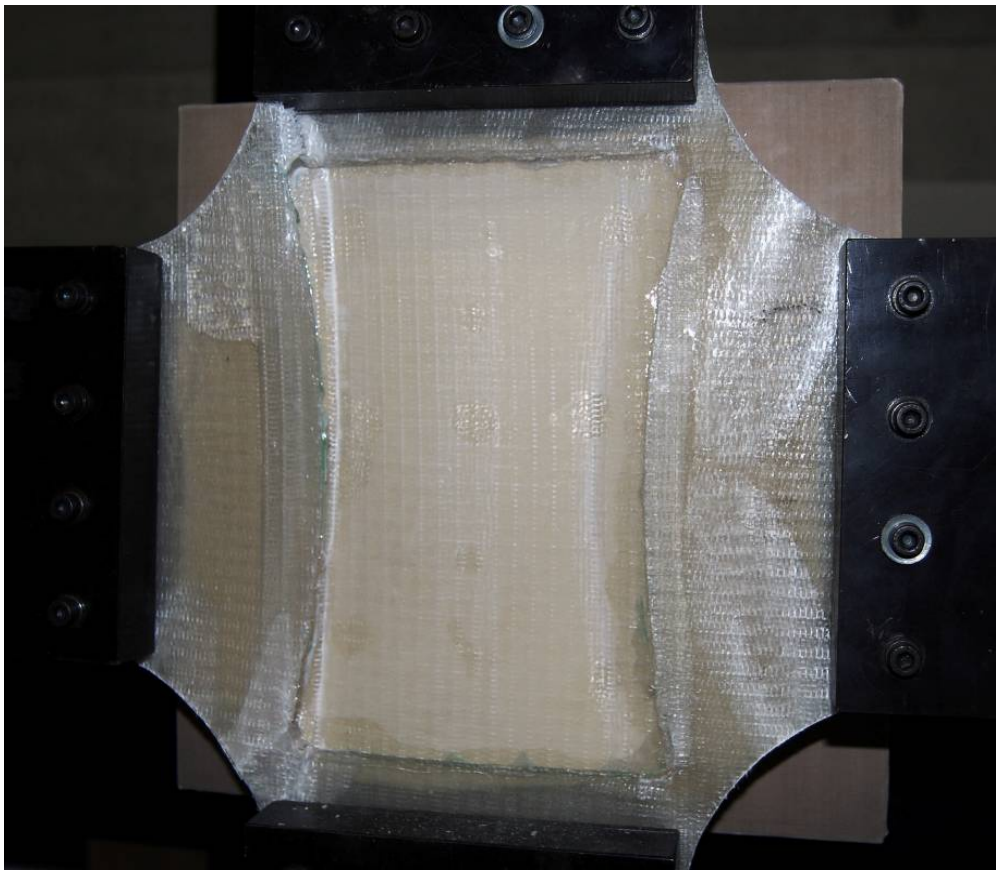

Figure B.162. Wrinkling failure mode.

B.2.2. [±45] specimens

B.2.2.1. CT 0-kN

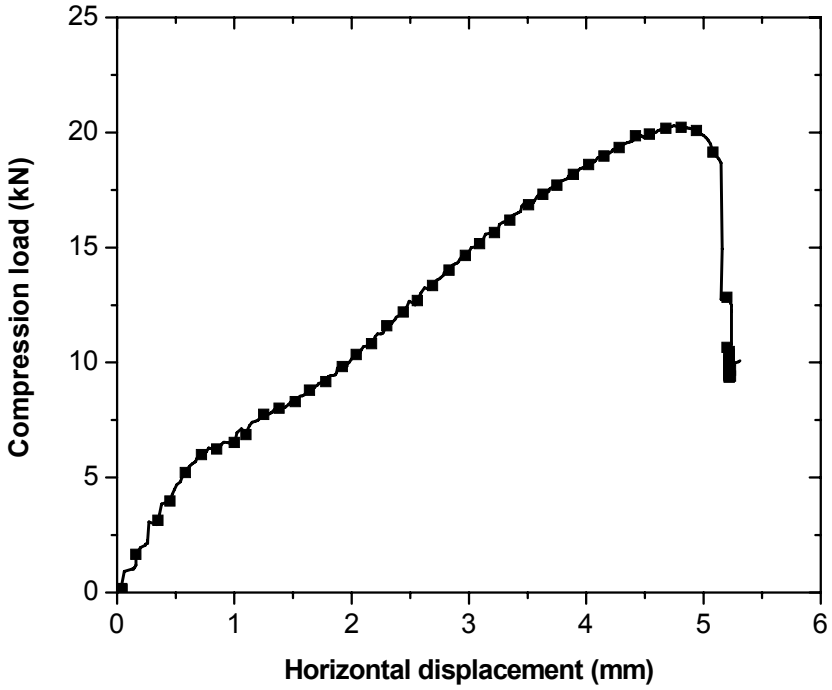

Figure B.163. Compression load vs. horizontal displacement.

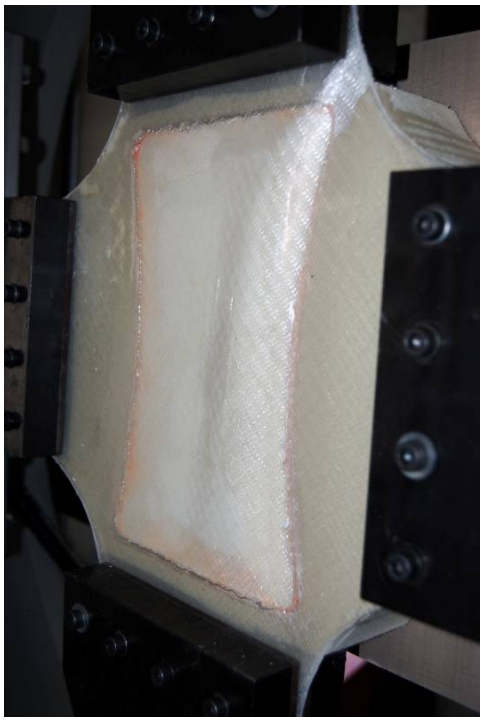

Figure B.164. Wrinkling failure mode.

B.2.2.2. CT 5-kN

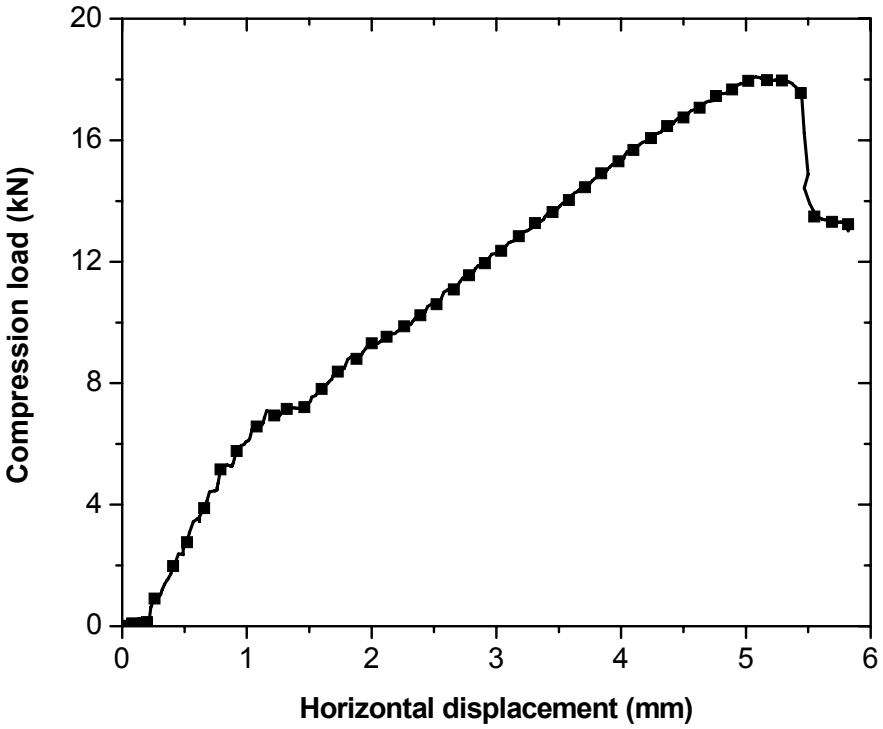

Figure B.165. Compression load vs. horizontal displacement.

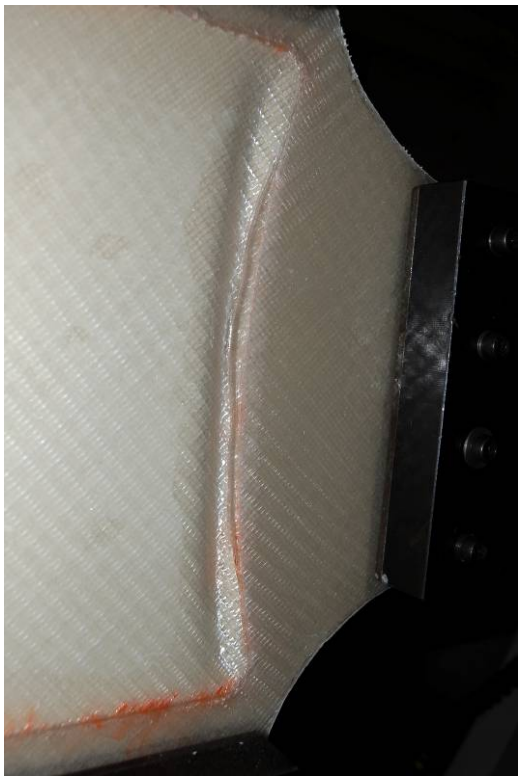

Figure B.166. Wrinkling failure mode.

B.2.2.3. CT 10-kN

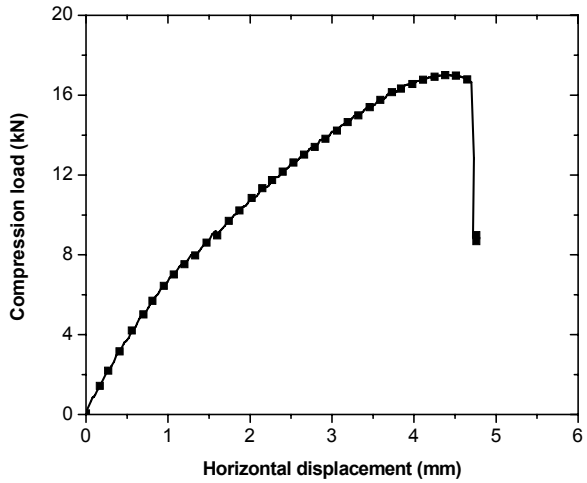

Figure B.167. Compression load vs. horizontal displacement of specimen#1.

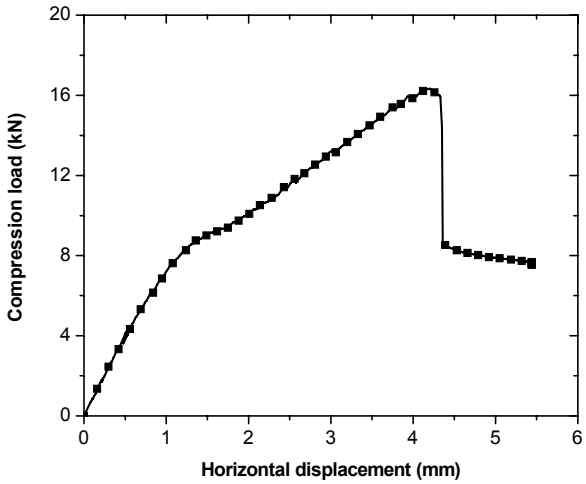

Figure B.168. Compression load vs. horizontal displacement of specimen#2.

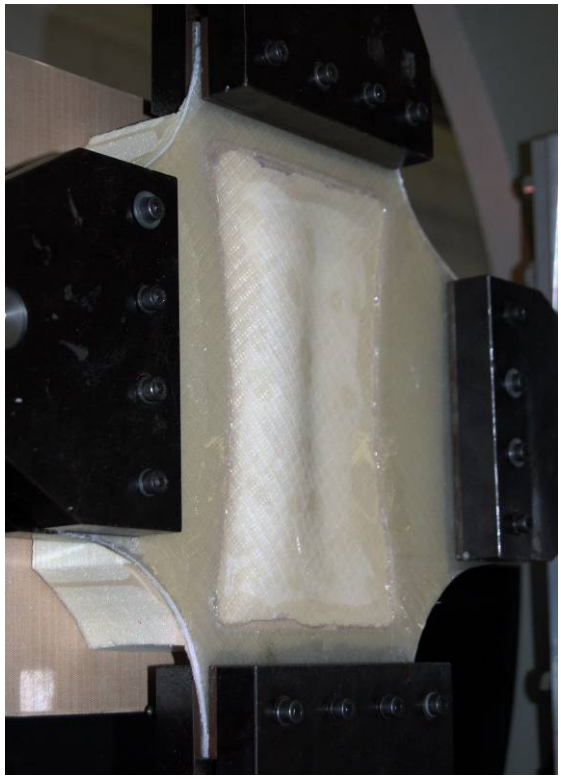

Figure B.169. Wrinkling failure mode of specimen#1.

Figure B.170. Wrinkling failure mode of specimen#2.

B.2.2.4. CT 13.5-kN

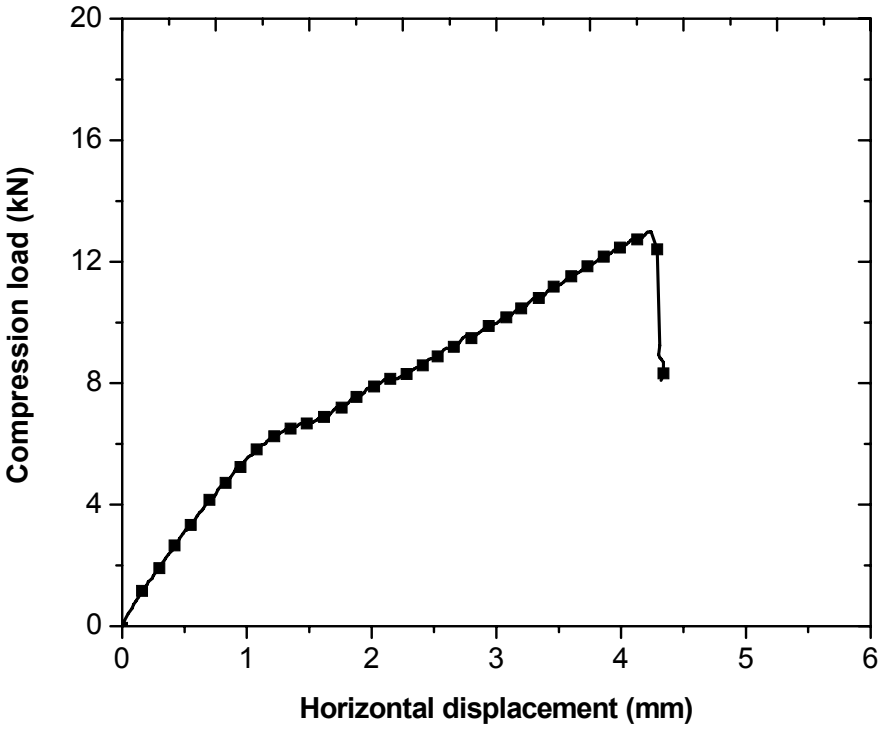

Figure B.171. Compression load vs. horizontal displacement.

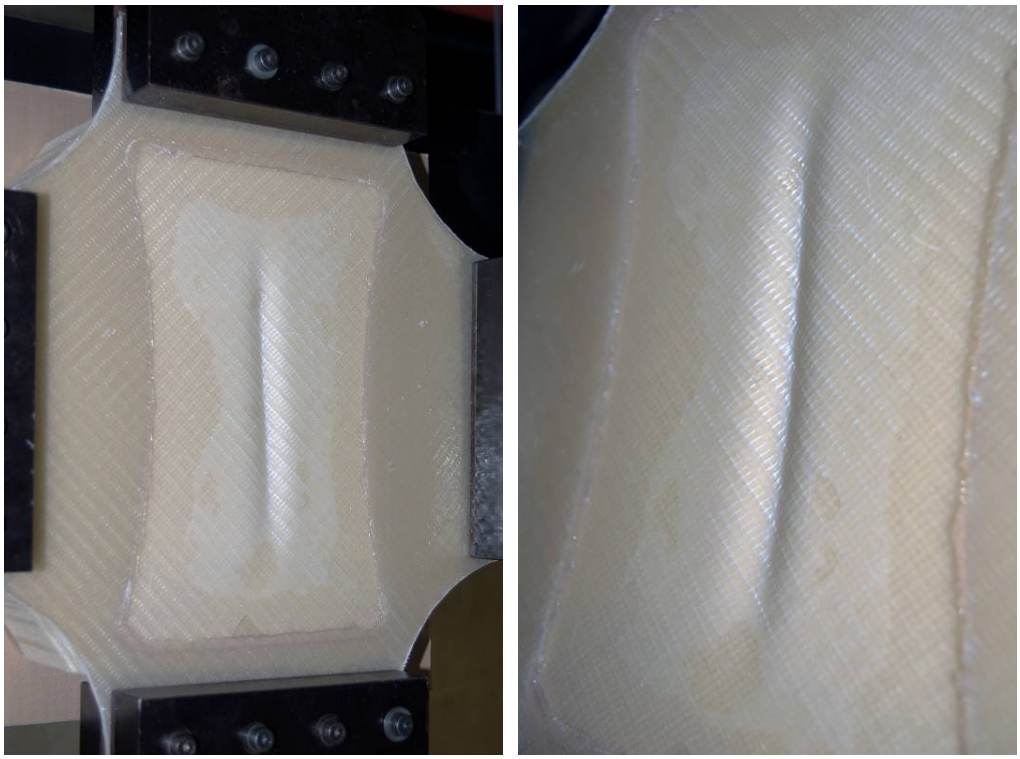

(a) (b)

Figure B.172. Wrinkling failure mode.

B.2.2.5. CT 16.6-kN

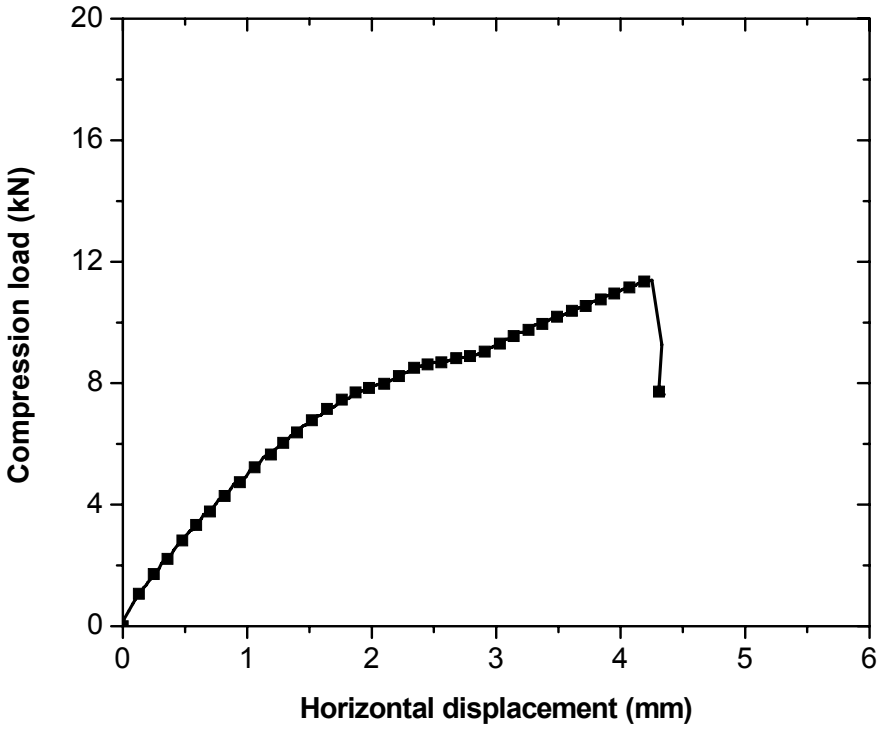

Figure B.173. Compression load vs. horizontal displacement.

(a) (b)

Figure B.174. Wrinkling failure mode.

B.2.2.6. CT 20-kN

In a similar way explained in the section B.2.1.8, the specimen at 20-kN tension load was equipped with one biaxial strain gage and two omega gages located at the center point, see Figure B.176. The results of omega gages were not accurate.

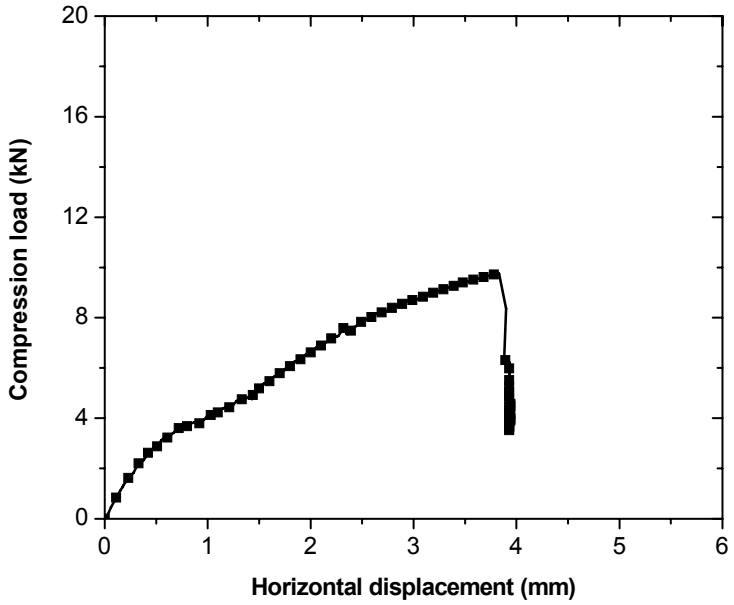

Figure B.175. Compression load vs. horizontal displacement.

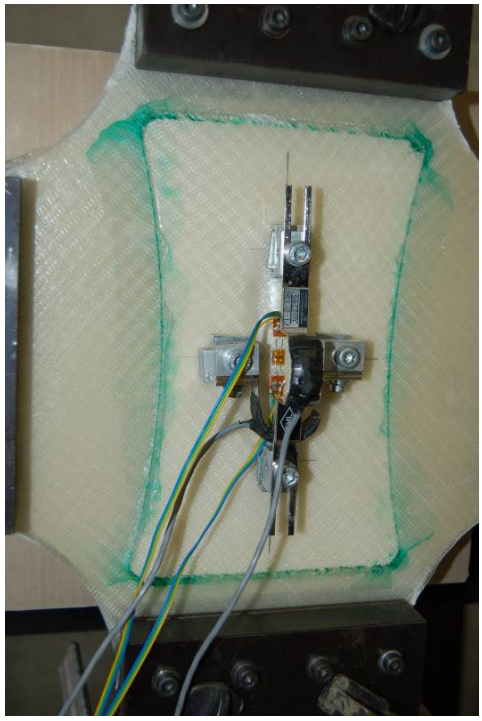

Figure B.176. Wrinkling failure mode and instrumentation.

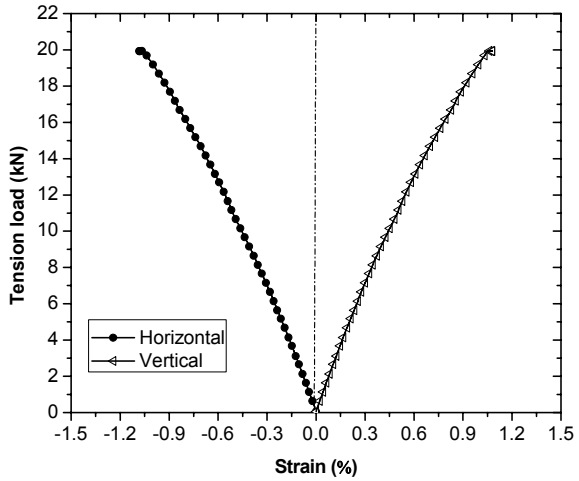

Figure B.177. Tension load vs. biaxial strain responses.

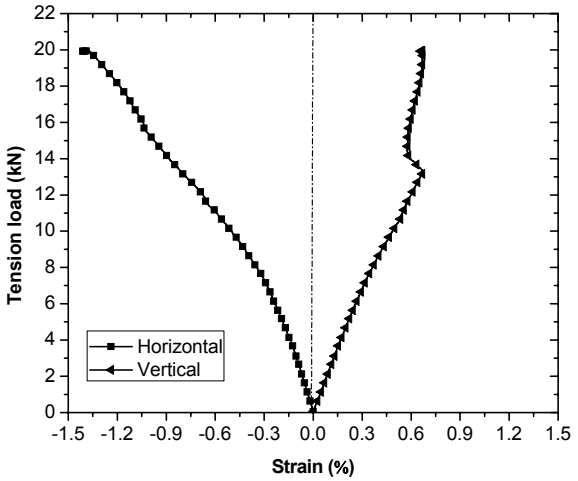

Figure B.178. Tension load vs. strain responses of omega gages.

B.2.2.7. SCT ϕ = 30°

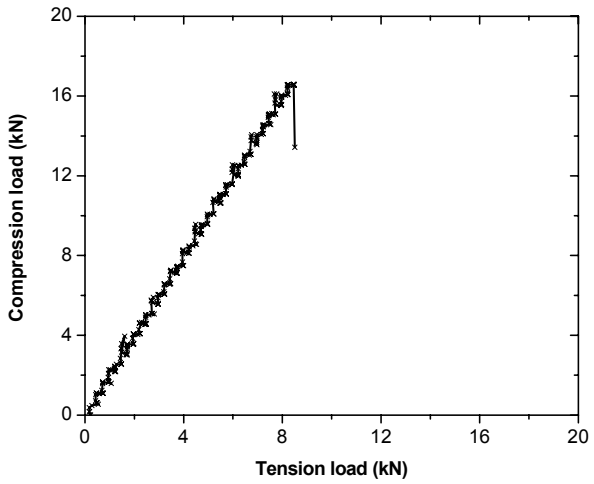

Figure B.179. Compression load vs. tension load.

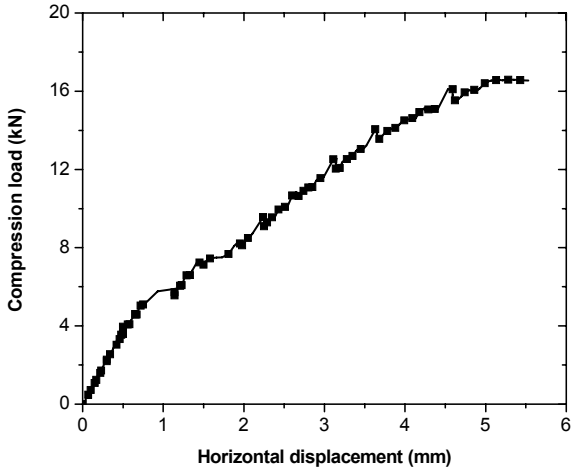

Figure B.180. Compression load vs. horizontal displacement.

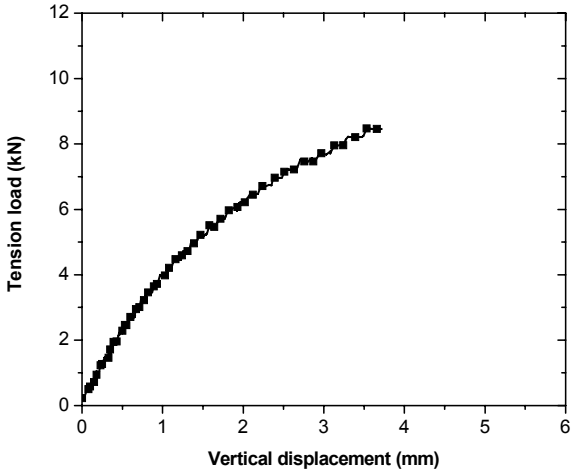

Figure B.181. Tension load vs. vertical displacement.

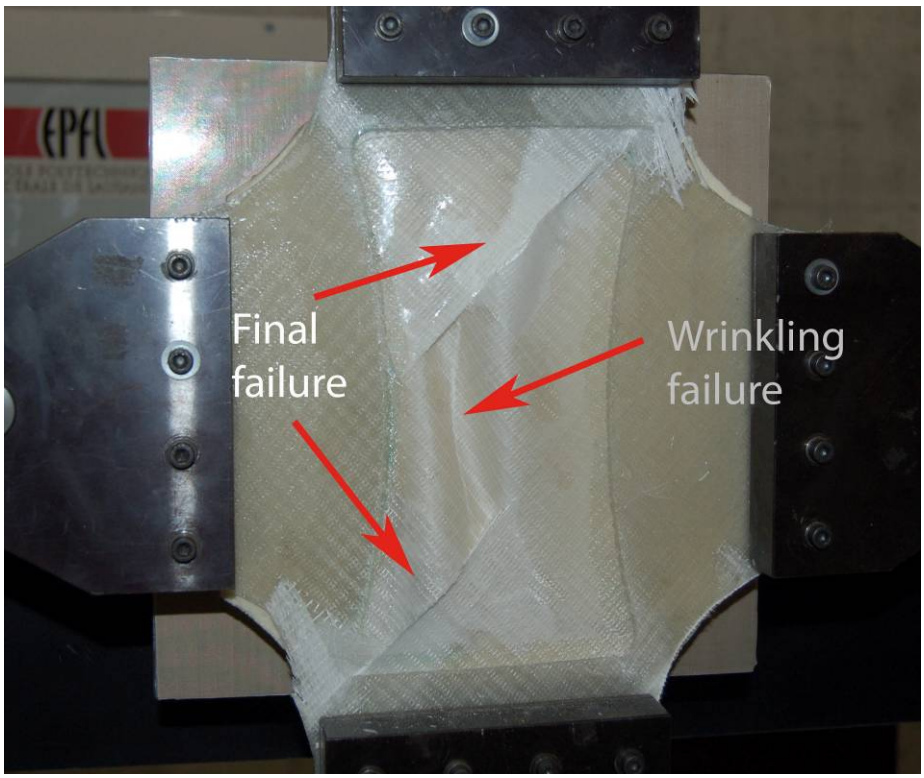

Figure B.182. Wrinkling failure mode.

B.2.2.8. SCT ϕ = 45°

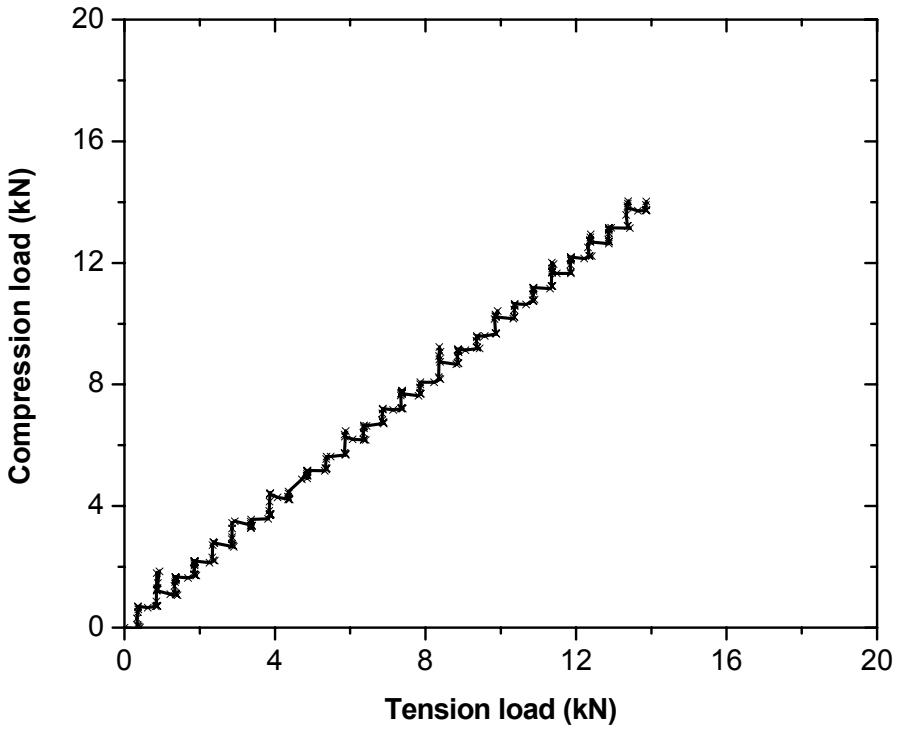

Figure B.183. Compression load vs. tension load.

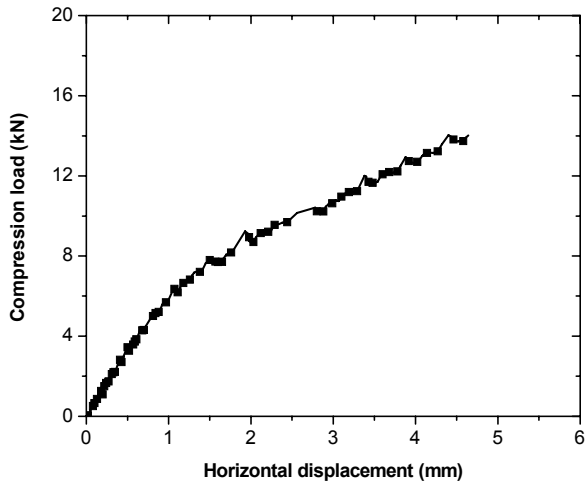

Figure B.184. Compression load vs. horizontal displacement.

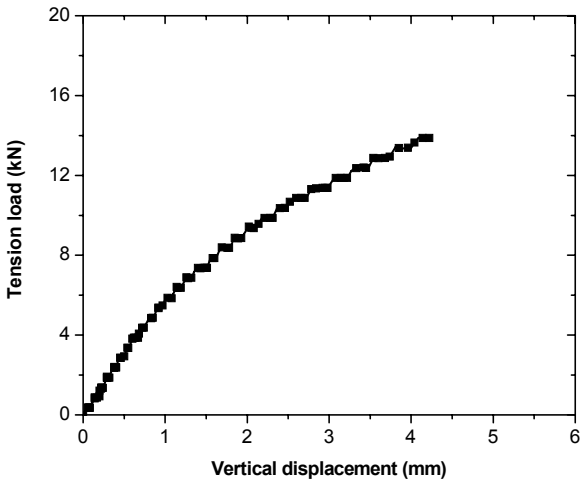

Figure B.185. Tension load vs. vertical displacement.

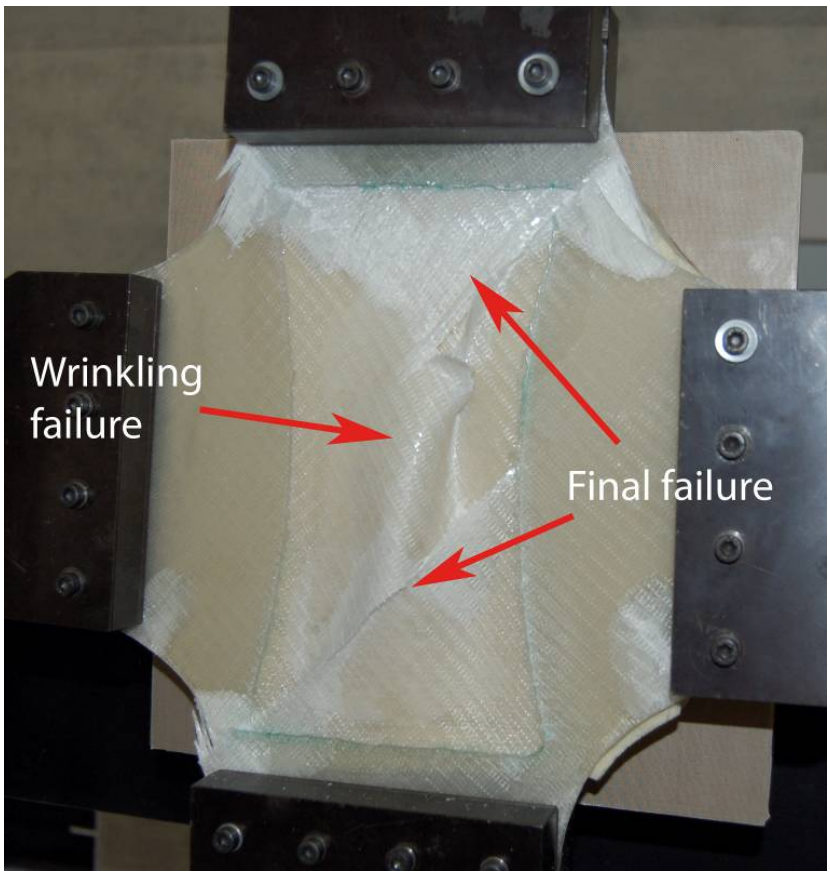

Figure B.186. Wrinkling failure mode.

B.2.2.9. SCT $\phi = 60°$

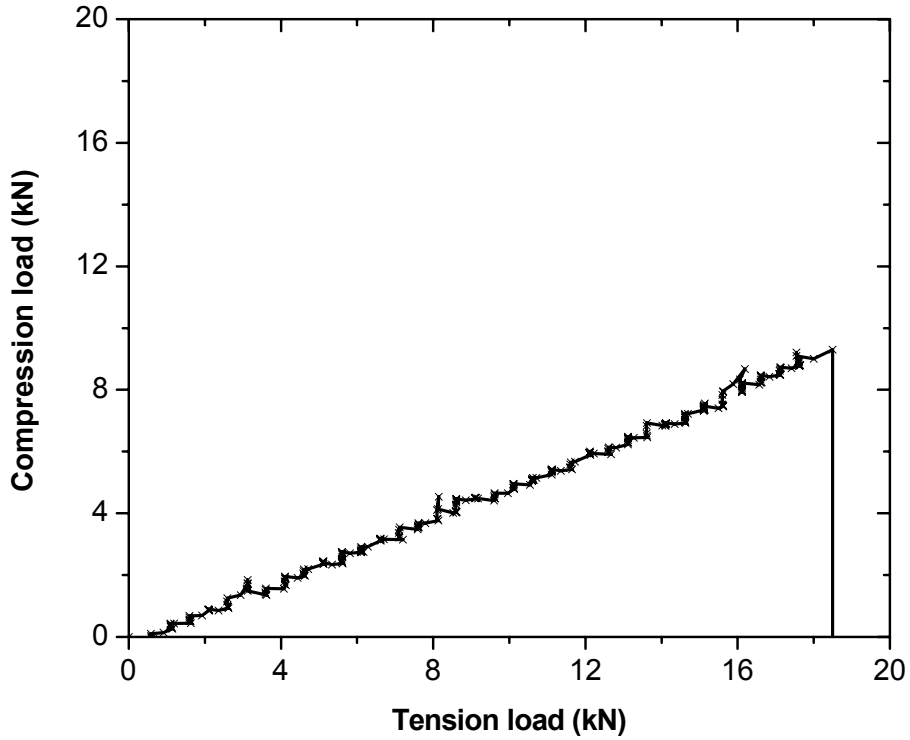

Figure B.187. Compression load vs. tension load.

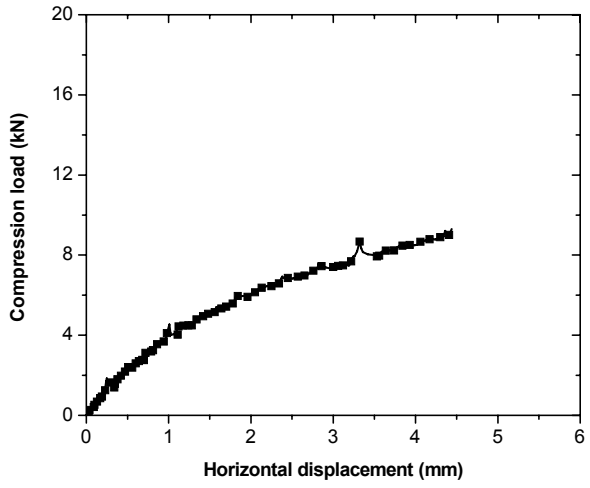

Figure B.188. Compression load vs. horizontal displacement.

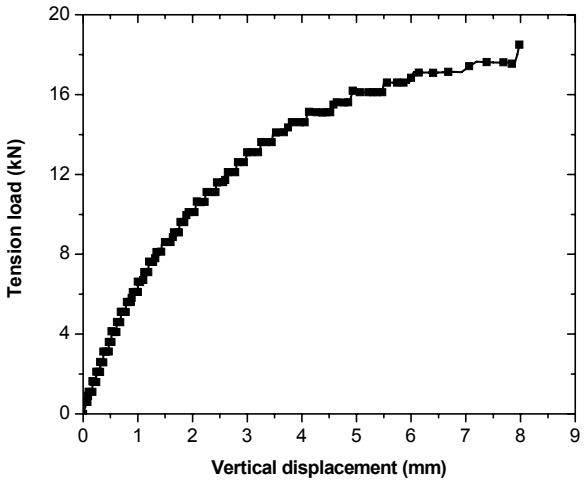

Figure B.189. Tension load vs. vertical displacement.

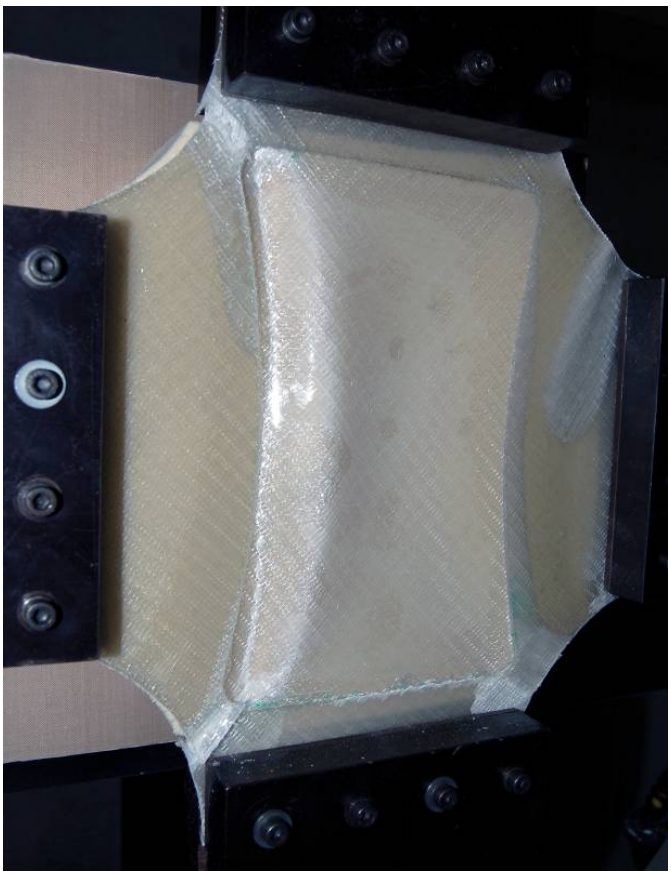

Figure B.190. Wrinkling failure mode.